LEABHARLANN CHOLÁISTE NA TRÍONÓIDE, BAILE ÁTHA CLIATH
Ollscoil Átha Cliath

TRINITY COLLEGE LIBRARY DUBLIN
The University of Dublin

Terms and Conditions of Use of Digitised Theses from Trinity College Library Dublin

Copyright statement

All material supplied by Trinity College Library is protected by copyright (under the Copyright and Related Rights Act, 2000 as amended) and other relevant Intellectual Property Rights. By accessing and using a Digitised Thesis from Trinity College Library you acknowledge that all Intellectual Property Rights in any Works supplied are the sole and exclusive property of the copyright and/or other IPR holder. Specific copyright holders may not be explicitly identified. Use of materials from other sources within a thesis should not be construed as a claim over them.

A non-exclusive, non-transferable licence is hereby granted to those using or reproducing, in whole or in part, the material for valid purposes, providing the copyright owners are acknowledged using the normal conventions. Where specific permission to use material is required, this is identified and such permission must be sought from the copyright holder or agency cited.

Liability statement

By using a Digitised Thesis, I accept that Trinity College Dublin bears no legal responsibility for the accuracy, legality or comprehensiveness of materials contained within the thesis, and that Trinity College Dublin accepts no liability for indirect, consequential, or incidental, damages or losses arising from use of the thesis for whatever reason. Information located in a thesis may be subject to specific use constraints, details of which may not be explicitly described. It is the responsibility of potential and actual users to be aware of such constraints and to abide by them. By making use of material from a digitised thesis, you accept these copyright and disclaimer provisions. Where it is brought to the attention of Trinity College Library that there may be a breach of copyright or other restraint, it is the policy to withdraw or take down access to a thesis while the issue is being resolved.

Access Agreement

By using a Digitised Thesis from Trinity College Library you are bound by the following Terms & Conditions. Please read them carefully.

I have read and I understand the following statement: All material supplied via a Digitised Thesis from Trinity College Library is protected by copyright and other intellectual property rights, and duplication or sale of all or part of any of a thesis is not permitted, except that material may be duplicated by you for your research use or for educational purposes in electronic or print form providing the copyright owners are acknowledged using the normal conventions. You must obtain permission for any other use. Electronic or print copies may not be offered, whether for sale or otherwise to anyone. This copy has been supplied on the understanding that it is copyright material and that no quotation from the thesis may be published without proper acknowledgement.

Numerical Vibro/Acoustic Analysis at Higher Frequencies

Gabriel Ruiz

Submitted in partial fulfilment of the requirements for the award of the degree of Doctor of Philosophy to the University of Dublin, 24^{th} October, 2002.

The work presented in this thesis was conducted at the Department of Mechanical and Manufacturing Engineering, Trinity College Dublin, Ireland.

Declaration

I declare that the present work has not been submitted, in whole or in part, to any other university or college for any degree or qualification. This thesis consists entirely of my own work, unless otherwise referenced.

I authorise the library of Trinity College Dublin, to lend or copy this thesis upon request.

Gabriel Ruiz

Acknowledgements

I would like to thank the Irish Centre for High Performance Computing at Trinity College, which provided the financial assistance to support this work. I am particularly indebted to my supervisor Henry Rice and his family: Jean, Maura, Emily, Anna and little Lucy for their help and encouragement.

Special thanks to Conor for his unconditional support (and patience with my tennis game), and to all the people at Materials Ireland Centre: Michael, Ray, Toman and Gavin for uncountable hours of help and fun. Thanks are due to Craig, Joan and all the technicians and postgraduate students for all their help.

I would like to thank my family who, despite the difficult times, has always encouraged me to persevere in my work. Their support has greatly inspired me throughout this thesis.

Finalmente, quisiera dedicar esta tesis a Antonietta -mi esposa y compañera- quien durante estos cuatro años ha compartido mis miedos, ansiedades y obsesión por el trabajo, dándome siempre apoyo y aliento. Gracias, tana.

Abstract

Accurate modelling of steady-state acoustic and elastic wave phenomena at higher frequencies, represents a major challenge for current numerical tools. Due to the large amount of computational effort and memory resources involved with the application of these methods, their use is practically restricted to low-frequency dynamic analysis.

The overall objective of this study is to overcome the computational limitations associated to conventional numerical methods for modelling vibro/acoustic problems at higher frequencies. A relatively new approach, known as the Wave Expansion Discretisation Method (WED), is comprehensively assessed as a viable alternative scheme.

For validation purposes, the method is applied to several acoustic problems in two and three dimensions, including homogeneous and inhomogeneous flow conditions within the continuum domain. In addition, the accuracy of the WED method for modelling linear (isotropic) elastic waves in two and three dimensions and plate vibration analysis is also explored.

For the acoustic case, it is shown that accurate results can be obtained near the bi-nodal/wavelength limit. Furthermore, the method shows also a comparable accuracy for two-dimensional (plain strain) elastic problems and plate vibration analysis. This represents a major accuracy improvement in comparison to the existing techniques, reducing significantly the size of the model. Under the present formulation, however, the implementation for three-dimensional elastic problems faces a serious practical limitation.

Nomenclature

c	speed of sound [m/s]
c_L	speed of propagation of elastic dilatational waves [m/s]
c_T	speed of propagation of elastic equivoluminal waves [m/s]
D	derivative operator
E	modulus of elasticity [Pa]
f	frequency [Hz]
G	Green's kernel function
h	maximum nodal spacing in the mesh [m]
$H_0^{(2)}$	zero-order Hankel function of the second kind
k	acoustic wavenumber [1/m]
k_L	elastic dilatational wavenumber [1/m]
k_T	elastic equivoluminal wavenumber [1/m]
$\mathcal{K}$	adiabatic bulk modulus [Pa]
m_{ns}	torsional moment per unit length about the direction n [N]
M_n	bending moment per unit length [N]
$\mathbf{n}$	normal vector
p	acoustic pressure [Pa]
$\mathbf{q}$	unit vector oriented in the direction of propagation of the plane wave
Q_n	plate shear force per unit length [N/m]
$\mathbf{u}$	displacement vector [m]
$\mathbf{v}$	fluid velocity vector [m/s]
$\mathbf{x}$	general field position vector [m]
$\mathbf{x}_b$	general boundary position vector [m]
Z	impedance [kg/m^{2}s]

δ	Kronecker delta
ε_n	normal strain components
γ	strength of a plane wave
γ_{ij}	tangential strain components
Γ_A	acoustic boundary
Γ_C	clamped elastic boundary (one or more components of the displacement vector are zero)
Γ_D	acoustic boundary surface with a prescribed pressure distribution
Γ_E	elastic boundary
Γ_F	free elastic boundary surface (normal and tangential traction forces are zero)
Γ_N	acoustic boundary surface with a prescribed normal velocity
Γ_R	acoustic boundary surface with a prescribed normal impedance distribution
Γ_S	simple supported elastic boundary surface
ι	imaginary unit
λ	wavelength [m]
λ_e	second Lame's elastic constant
μ	first Lame's elastic constant [N/m^2]
ν	Poisson's coefficient
θ_n	normal rotational displacement [rad]
ρ_0	ambient mass density of the fluid [kg/m^3]
ρ	structural mass density [kg/m^3]
σ_n	normal stress components (related to normal traction forces)
τ_{ns}	tangential stress components (related to shear traction forces)
ω	circular frequency [rad/s]
Ω_A	acoustic domain
Ω_E	isotropic elastic domain

∇	gradient operator
∇^2	Laplace operator
$^+$	generalised pseudo-inverse

Contents

Chapter 1

Introduction

1.1 Importance of efficient numerical methods for modelling vibro/acoustic problems

Numerical modelling methods are, in essence, predictive tools primarily used in the design stages of the engineering process. Their use in acoustic applications include, for example, traffic noise control, interior car and aircraft cabin insulation and turbofan noise simulation. The use of numerical methods for problems related to vibration and general elastic wave propagation, may be found for example, in the vibration control and fault detection of structures and machinery, seismic wave modelling and material property identification.

Numerical methods give always an approximate solution to the real problem. Thus, their ultimate efficiency as predictive tools is assessed in terms of the *accuracy* of the numerical solution and the *computational cost* required to obtain the desired solution. The accuracy will determine the reliability of the method, whilst the computational cost will determine the viability of the numerical scheme.

Commercial numerical tools for modelling wave phenomena, have failed in many cases to provide accurate solutions at a reasonable computational cost, rendering some important applications practically unsolvable. Problems such as interior car and aircraft cabin insulation can only be efficiently modelled at lower frequencies. However, these are often not the frequencies for which the acoustic pressure is maximum in the real problem, nor those which are the most sensitive to human hearing. The research efforts devoted to circumvent the drawbacks associated to standard numerical methods, may be traced back over several decades. Over the last few years, however, there has been a steadily increasing demand for an efficient simulation tool for wave propagation phenomena, in particular for acoustic applications. This has been mainly prompted by higher customer requirements regarding acoustic performance along with new regulations in noise emission. As a consequence, solutions over a broad band frequency range in large domains are often required.

The remarkable advance in the computing technology in recent times, has given the opportunity to increase significantly the computational resources, allowing the standard commercial packages to solve more problems of interest. These advances are nonetheless, insufficient to compensate for the poor efficiency of the conventional approaches.

In order to fully incorporate predictive criteria in the design process, there is also a strong need for numerical simulation methods to provide insight in the physical phenomena which govern the wave behaviour.

1.2 Definition of the acoustic and elastic wave problems

1.2.1 Acoustic problems

Assuming only small dynamic perturbations and that, the air density $\rho(\mathbf{x})$ and bulk modulus $\mathcal{K}(\mathbf{x})$ where $\mathbf{x}$ is a general position vector, remain relatively constant within the continuum, so that $\rho(\mathbf{x}) = \rho_0$, the propagation of acoustic waves is governed by the general *wave equation* [1]

$$\nabla^2 p(\mathbf{x},t) = \frac{1}{c^2}\frac{\partial^2 p(\mathbf{x},t)}{\partial t^2}, \tag{1.1}$$

where c is the sound speed and $p(\mathbf{x},t)$ is the acoustic pressure at a time t and position $\mathbf{x}$.

For modelling purposes, the use of equation 1.1 requires not only a spatial discretisation but also a time step discretisation. An important simplification in the formulation is obtained if only the steady-state pressure $p(\mathbf{x})$ is considered (see Appendix A). Equation 1.1 then reduces to the *Helmholtz equation*

$$\nabla^2 p(\mathbf{x}) = -\left(\frac{\omega}{c}\right)^2 p(\mathbf{x}), \tag{1.2}$$

where $\omega = 2\pi f$ is the circular frequency. The ratio $k = \frac{\omega}{c}$ is the wavenumber, which gives the spatial phase behaviour of the wave solutions.

A boundary value problem with a unique solution then results, provided that one boundary condition is specified at each point on the boundary of the problem domain. Given a general acoustic domain Ω_A with boundary $\Gamma_A = \Gamma_D \cup \Gamma_N \cup \Gamma_R$, three conditions are usually considered:

- imposed pressure (Dirichlet condition)

  $$p(\mathbf{x}_b) = \overline{p}(\mathbf{x}_b), \;\; \mathbf{x}_b \in \Gamma_D, \tag{1.3}$$

  where $\overline{p}(\mathbf{x})$ is a prescribed pressure function

- imposed normal velocity (Neumann condition)

  $$\mathbf{v}_n(\mathbf{x}_b) = \frac{\iota}{\rho_0 \omega}\frac{\partial p(\mathbf{x}_b)}{\partial \mathbf{n}} = \overline{v}_n, \;\; \mathbf{x}_b \in \Gamma_N, \tag{1.4}$$

  where $\iota = \sqrt{-1}$, $\overline{v}_n$ is a prescribed normal velocity function and $\mathbf{n}$ is the boundary outward normal. For a perfectly reflective condition, $\overline{v} = 0$.

- imposed impedance (radiation or mixed boundary condition)

  $$\frac{\partial p(\mathbf{x}_b)}{\partial \mathbf{n}} = -\iota \frac{\rho_0 \omega}{Z} p(\mathbf{x}_b) = -\iota \rho_0 \omega \mathbf{v}_n, \;\; \mathbf{x}_b \in \Gamma_R \tag{1.5}$$

  where $Z = p/\mathbf{v}_n$ is the normal specific acoustic impedance.

Although the Helmholtz equation 1.2 is only a steady-state approximation of the general (time-domain) differential wave equation, it generally gives a useful insight into the behaviour of the numerical model, whilst avoiding the complications of analysing the transient effects. Nonetheless, it requires a significant computational effort as the entire domain must be discretized with the same level of mesh refinement. For illustration purposes, consider a point source located in an infinite, reflective baffle pulsating at $600Hz$. The steady-state linear pressure distribution in a homogeneous, two-dimensional square domain of $20m$ edge length, is shown in figure 1.1.

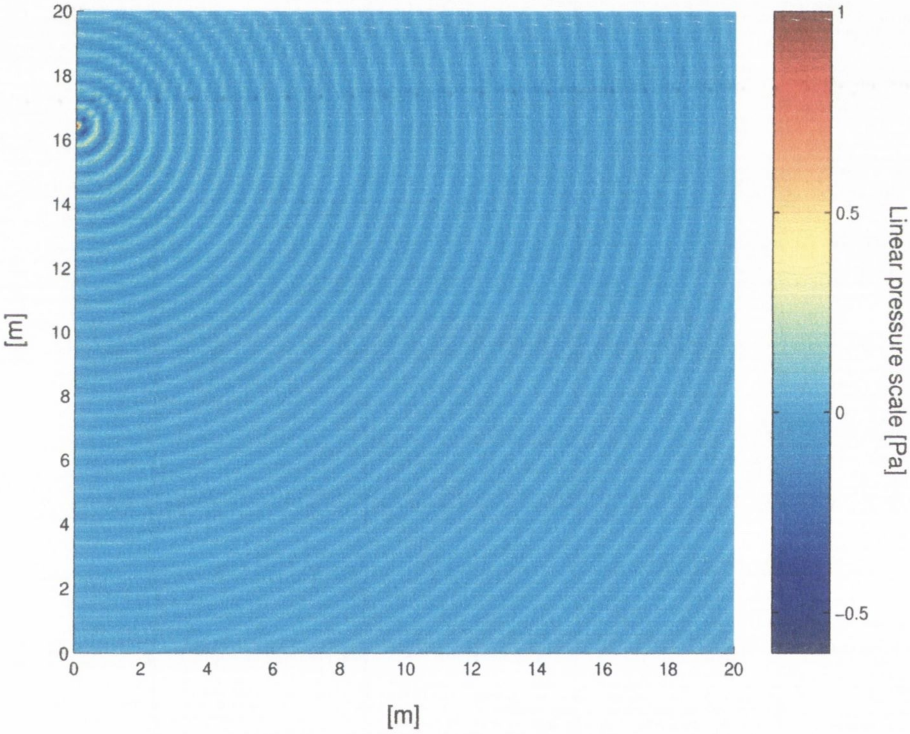

Figure 1.1: Point source in an infinite baffle.

As the frequency f increases, the spatial variations in the pressure distribution decrease proportionally, as defined by the wavelength $\lambda = c/f$.

The performance of the numerical methods is usually assessed in terms of the number of discretisation points per wavelength ratio (ppw) required to obtain an accurate solution. The ppw is defined as

$$ppw = \frac{c}{h \cdot f} , \tag{1.6}$$

where h is the maximum nodal spacing in the mesh.

From the Nyquist theory of signal processing analysis it is known that, in order to avoid aliasing effects, the sampling rate must be at least twice of the highest frequency to sample (see e.g. [2]). Thus a minimum of two points per wavelength is required. Standard numerical schemes, like finite differences (FD), finite elements (FE) or boundary element (BE) methods require between 6-10 points per wavelength in order to give an accurate solution [3].

Consider for example, modelling 20 wavelengths of a 1000Hz sine wave. The number of nodal points required by an 'ideal' (2 points per wavelength) method and the standard approaches mentioned above in one, two and three dimensions is listed in table 1.1. As shown, for two and three dimensions the difference in the number of discretisation points is substantial. Note that the actual domain considered in table 1.1 is relatively small in comparison to most acoustic applications (20 wavelengths for a 1000Hz sinusoidal wave cover a distance of $6.8m$ in each spatial direction). At larger domains and/or higher frequencies, the computational requirements of the standard methods will rapidly overwhelm current computational resources.

	1D	2D	3D
ideal	40	1,600	64,000
standard	120-200	14,400-40,000	1,728,000-8,000,000

Table 1.1: Accuracy comparison between an 'ideal' method and the standard numerical schemes.

1.2.2 Elastic problems

Steady-state elastic waves in isotropic media, may be also reduced to a system of Helmholtz equations (see Appendix B)

$$\nabla^2\mathbf{u}(\mathbf{x}) + k_L^2\mathbf{u}(\mathbf{x}) = 0 \tag{1.7}$$

and

$$\nabla^2\mathbf{u}(\mathbf{x}) + k_T^2\mathbf{u}(\mathbf{x}) = 0, \tag{1.8}$$

where

$$\mathbf{u}(\mathbf{x}) = \begin{pmatrix} u_1(\mathbf{x}) \\ u_2(\mathbf{x}) \\ u_3(\mathbf{x}) \end{pmatrix} \tag{1.9}$$

is the vector displacement with components $u_1(\mathbf{x})$, $u_2(\mathbf{x})$ and $u_3(\mathbf{x})$, and $k_L = \omega/c_L$ and $k_T = \omega/c_T$ are the dilatational and equivoluminal wave numbers, respectively[1]. Dilatational waves are associated with compressional and dilatational changes in the volume of the elastic domain whilst equivoluminal waves produce a shear displacement, where the shape of the domain is changed but not its volume. Given a general isotropic elastic domain Ω_E with boundary $\Gamma_E = \Gamma_C \cup \Gamma_F$, two boundary conditions are generally considered

- clamped condition

$$\mathbf{u}(\mathbf{x}_b) = 0, \;\; \mathbf{x}_b \in \Gamma_C \tag{1.10}$$

- free condition

$$\sigma_n = \tau_{ns} = 0 \; \mathbf{x}_b \in \Gamma_F, \tag{1.11}$$

  where σ_n and τ_{ns} are the normal and tangential edge stress components, respectively.

---

[1] For two-dimensional problems, a *plain strain* condition is assumed by making $u_3 = 0$. Thus, the strain tensor components in the x_3 general coordinate direction vanish identically, i.e., $\varepsilon_3 = \gamma_{13} = \gamma_{23} = 0$, with σ_3, τ_{13}, $\tau_{23} \neq 0$. Alternatively, a *plain stress* solution may be obtained by restraining the stress components in the x_3-direction, i.e., $\sigma_3 = \tau_{13} = \tau_{23} = 0$, with $u_3 \neq 0$.

Since the speed of propagation of elastic waves is in general significantly higher than that of acoustic waves, the efficiency of the standard numerical methods at higher frequencies is improved. However, at each discretisation point, there are two (2D) and three (3D) degrees of freedom associated to the displacement vector field.
Thus, the overall computational cost is, in general, even higher than that required for acoustic problems, which imposes severe practical computational limitations on the size of the solution domain and/or frequency modelling.

1.3 Structure of the thesis

Chapter 2 gives a detailed review of the numerical modelling schemes applicable to the solution of the Helmholtz equation. A brief discussion on conventional methods, i.e., the finite differences method (FDM), the finite element method (FEM) and the boundary element method (BEM), is also included for completeness (for a more detailed discussion, the reader is referred to, e.g., references [4–6]).
The review is centred in the discussion of the alternative numerical techniques proposed in recent years, which are aimed at overcome the accuracy problems associated with the standard methods. Some of these new schemes have many attractive features, and have, in general, a better accuracy in comparison to the standard methods. However, in addition to the accuracy, there are other several important properties that have to be considered in order to determine whether a particular approach has a better overall performance. Based on this criteria, a relatively new and unknown method, called the Wave Expansion Discretisation (WED), was selected.
The formulation and methodology of the WED is discussed in chapter 3. Following a similar procedure as described by Caruthers *et al.* [7], the accuracy and conditioning of the WED for two- and three-dimensional acoustic problems is investigated. Particular emphasis is given to the implementation of the radiation boundary condition, for which an alternative formulation is derived.
The application of the wave expansion technique for two- and three-dimensional

acoustic problems is described in chapter 4. The modelling results for several illustrative examples, including non-uniform inhomogeneities within the computational domain, are also discussed.

Chapter 5 describes the application of the WED method in elastodynamics. For validation, the results of the proposed scheme for a two-dimensional (plane strain) problem are compared against a finite element model, using similar computer resources. The implementation of the WED for three-dimensional problems is also explored.

Chapter 6 presents the general conclusions and suggests future work in the development of the wave expansion discretisation technique, which should lead towards a versatile and generally applicable modelling scheme.

Chapter 2

Review of numerical methods applicable to the Helmholtz equation

2.1 Introduction

For most acoustic and elastic wave problems, the solution of the partial differential equations cannot be found in closed analytical form, due to the complexity of the geometry and the boundary conditions. Therefore, an approximation of the exact solution is searched for by transforming the mathematical model into a set of approximated (algebraic) equations, which are amenable to numerical solution procedures. These equations have the form

$$\mathbf{A}\mathbf{x} = \mathbf{b}, \tag{2.1}$$

where **A** is a square matrix which can be sparse or dense, and **b** is the forcing vector, determined by the boundary conditions and loadings applied on the physical domain.

Numerical commercial tools are usually based on some variation of traditional finite differences (FD), finite element (FEM) or boundary element (BEM) schemes. These approaches are briefly discussed in sections 2.2 and 2.3. Despite the fact that these methods have been widely used for many years, their efficiency is limited only to lower frequency solutions. At higher frequencies, the computational cost required to obtain accurate solutions rapidly consumes available computational resources.

In an effort to overcome these drawbacks, a myriad of alternative techniques have been developed in recent years. Some of these 'new' approaches have incorporated the idea of using solutions of the governing differential equation to interpolate the pressure field. These numerical schemes, discussed in section 2.4, fall into the group of Trefftz methods. The results obtained with these techniques, though still rather simple academic problems, have shown a much better accuracy in the solution in comparison to the standard methods.

This chapter does not aim at giving an exhaustive account of every possible numerical scheme that may give an approximate solution for acoustic and elastic waves. The discussion is centred on those approaches that have been developed, investigated and used for acoustic and elastic wave problems in recent years.

Given the relevance of the implementation of the free field boundary conditions in the modelling of acoustic problems, a brief review on the available techniques is given in section 2.5. These methods provide the base from which a solution to the radiation problem in the Wave Expansion Discretisation (WED) method is derived in the subsequent chapters.

2.2 Basic concepts and properties of FDM and FEM

The Finite Difference Method (FD) and the Finite Element Method (FEM) are full field domain discretisation techniques. That is, the domain is discretized in its entirety, unlike boundary discretisation techniques in which the discretisation is performed only in the boundary of the computational domain. These methods reduce the problem to a system of equations

$$(\mathbf{K} + j\omega\mathbf{C} - \omega^2\mathbf{M})\mathbf{p} = \mathbf{f}, \tag{2.2}$$

where the matrices **K**, **C** and **M** are the acoustic stiffness, damping and mass matrices, respectively. The mass matrix **M** and **K** matrix model reactive effects. The damping matrix **C** results from the impedance boundary conditions and other losses within the computational domain.

The stiffness and mass matrices, **K** and **M**, as given in equation 2.2, are independent of the frequency. This allows the use of standard eigenvalue solvers for the calculation of the undamped natural frequencies and mode shapes of acoustic and elastic systems.

The properties of the finite differences and finite element methods are outlined below. Though the formulation in both cases is related[1], the concept behind the interpolation procedure is different for both methods. A summary of the properties related to the FD and FE methods is given in section 2.2.3.

2.2.1 Finite difference method (FD)

The finite difference method is a discrete domain technique, in which the governing differential equation is approximated at a finite number of points located within the continuum domain. In the traditional formulation, the derivatives of the governing equation are replaced by finite difference operators formulated in terms of the field values at neighbouring points. A difference equation at each point results directly, for which the associated approximation error may be readily determined.

For first order derivatives, the finite difference operator may be formulated considering the precedent or the following field nodes, in which case, is called *backward difference* and *forward difference* approximation, respectively. For second order derivatives, a *central difference* approximation is generally determined using the

---

[1] It can be readily demonstrated that the finite element method may be reduced to finite differences should δ (Kronecker delta) interpolating functions are used.

precedent and following discretisation points, based on the Taylor expansion of the differential operator.

To illustrate the concept, consider the Helmholtz equation 1.2 in one dimension

$$D_{xx}p(x) + k^2 p(x) = 0, \tag{2.3}$$

where D_{xx} is the second order derivative operator. The central difference approximation of equation 2.3 at a general discretisation point x then yields

$$\frac{p(x+h) - 2p(x) + p(x-h)}{h^2} + k^2 p(x) = 0 \tag{2.4}$$

where h is the nodal spacing.

Applying the approximation 2.4 for each discretisation point and its neighbours, an overlapping stencil then results. The stiffness (**K**) and damping (**C**) matrices in the system of equations 2.2 are banded, with a band size determined by the number of neighbouring nodes in the stencil. The mass matrix (**M**) is diagonal. The final solution for the unknown nodal values may then be obtained from efficient sparse matrix solvers.

The approximation 2.4 may be readily extended to include also the time variable for the solution of the general wave equation [8].

$$D_{xx}p(x,t) - \frac{1}{c^2}\frac{\partial^2 p(x,t)}{\partial t^2} = 0, \tag{2.5}$$

where c is the sound speed.

This form of the finite difference method, known as the *finite difference time-domain* (FDTD), has been applied to radiation and scattering acoustics problems [9–11], elastic waves and seismic analysis [12, 13] and electromagnetic waves [14]. In this methods, time could be discretized by using a central difference expansion of the form

$$\frac{\partial^2 p(x,t)}{\partial t^2} = \frac{p(x,t+\triangle) - 2p(x,t) + p(x,t-\triangle)}{\triangle^2}, \tag{2.6}$$

where $\triangle$ is the time step. The finite difference approximation of equation 2.5 then yields,

$$\frac{p(x+h,t)-2p(x,t)+p(x-h,t)}{h^2}-\frac{1}{c^2}\left(\frac{p(x,t+\triangle)-2p(x,t)+p(x,t-\triangle)}{\triangle^2}\right)=0. \tag{2.7}$$

Unfortunately, equation 2.7 will not be stable so McCormack/Lax predictor/corrector forward difference methods are generally used. Other alternatives formulations include, for example, Chebyshev polynomials [15] and Runge-Kutta discretisation techniques [16].

The concepts outlined above may be summarised as follows:

- discretisation of the domain into a finite number of points uniformly distributed within the domain.
- approximation of the derivatives of the governing equation by interpolating polynomials, formulated in terms of surrounding points in the grid.
- solution of a system of equations of the form $\mathbf{Ax} = \mathbf{b}$, where $\mathbf{x}$ is the approximated field variable at each discretisation point, and $\mathbf{A}$ is a banded matrix formed by the stiffness, mass and damping system matrices.

2.2.1.1 Consistency conditions and approximation errors

The consistency of a finite difference approximation refers to the convergence of the approximated algebraic equation to the desired differential equation as the maximum nodal spacing $h \to 0$. Whilst in general this condition is satisfied, it is possible to find approximations that in the limit $h \to 0$, may not converge to the desired differential equation (see, e.g. [17, section 2.8]).

Note that, for the solution of the general (time domain) wave equation using the FDTD method, the consistency conditions are significantly more stringent. The consistency conditions require not only convergence as h varies at a fixed time, but also, that the accumulated error remains bounded for successive steps with h fixed. When this situation is present, the solution is said to be *stable*.

The accumulated local errors can produce diffusion effects in the numerical solution, i.e. waves of different frequencies will propagate at different speeds through the grid [18]. Thus, in order for the finite difference solution to converge to the true solution it is essential to determine the nodal distance and the time step accordingly. The nodal distance is directly related to the truncation error of the finite difference operator. Popular low-order schemes that use five-point stencils (equation 2.4), have a local truncation error of $\mathcal{O}(h^2)$ for second derivatives [17]. In this case, the general 'rule of thumb' is to use 10 cells per wavelength ($\lambda = c/f$, where c is the sound speed and f is the frequency). That is, each cell should be $\lambda/10$ at the highest frequency of interest.

A necessary condition for a stable solution of the wave equation is given by [19]

$$ck \leq h, \tag{2.8}$$

where k is the time discretisation step. To understand equation 2.8, called the Courant-Friedrichs-Lewy (CFL) condition, consider a plane wave propagating trough a finite difference grid. In one time step any point on this wave must not pass through more than one cell, because during one time step FDTD can propagate the wave only from one cell to its nearest neighbours.

From the discussion above it is clear that, in order to reduce the dispersion error to an acceptable level, the size of the model as the frequency increases becomes prohibitively large. To circumvent this problem, several high-order finite difference methods have been proposed in the literature.

Min *et al.* [20] derived a high-accuracy difference scheme for elastic wave modelling in the frequency domain. Despite the improved accuracy in comparison to the standard FD approach, the method is based on a 25-point stencil which severely affects the sparsity of the overall assembled matrix. Singer and Turkel [21], proposed a five-point stencil central difference operator formulation with fourth-order accuracy based on the Padé approximation. The results obtained show that, even when the local error is reduced the convergence of higher-order FD approaches is not necessarily improved for higher frequencies.

Note also that the FD approach based on relationship 2.4, is restricted to a unique nodal distance h. Thus, in the standard formulation there is an additional error associated with the approximation of the problem geometry (which clearly depends on the shape of the domain). It is possible to obtain a five-point stencil approximation for more general types of variable spacing [17]. However, this approximation is in general accurate only to $\mathcal{O}(h)$.

Holland [22], generalised the FDTD algorithm (with $\mathcal{O}(h^2)$ accuracy) to general non-orthogonal grids for modelling electromagnetic waves. Lee *et al.* [23] reformulated Holland's method using a series of components of the magnetic field. More recently, Botteldooren [9, 24] proposed an alternative FDTD scheme for acoustic simulation in non uniform (quasi-Cartesian) grids. The formulation is based on non-uniform and non-overlapping finite volumes, usually known as Voronoi cells. Though the accuracy of the standard FDTD method is improved, the overall computational cost may increase for some applications.

It is worth mentioning that new formulations of high-order FDTD in non-uniform grids and closely related finite-volume (FV) time-domain simulation (see, e.g. references [16, 25]) tend to become more similar to recently developed finite element time-domain approaches. The distinction between finite differences and finite elements becomes rather blurred at this point.

2.2.2 Finite element method (FEM)

The finite element method is the most commonly used numerical modelling technique for solving engineering problems. Due to its adaptability and straightforward implementation, the use of finite elements has been extended into many areas of the engineering process.

The method is based on the following concepts:

- transformation of the original problem into an equivalent integral formulation (weighted residual or variational).

- division of the continuum into smaller non-overlapping sub domains called *elements.*
- approximation of the *field variable distributions* and the geometry of the continuum domain, in terms of a set of shape functions, which are locally defined in each element.
- solution of a system of equations of the form $\mathbf{A}\mathbf{x} = \mathbf{b}$, where $\mathbf{x}$ is the approximated field variable at each discretisation point, and $\mathbf{A}$ is a sparse matrix.

An overview of the relevant aspects of the finite element method is given below. A detailed discussion of the fundamental concepts and properties of the method may be found in numerous publications, see e.g. references [5, 26, 27].

Weighted residual approach

The method of weighted residuals provides a conceptual foundation upon to which construct the Galerkin finite element method. In this approach, the field variable is approximated in terms of a set of known linearly independent functions, called *basis* or *shape functions.*

For a given field variable, $\mathbf{u}$ say, a *trial function* $\hat{\mathbf{u}}$ is defined as

$$\hat{\mathbf{u}} = \phi_0(\mathbf{x}) + \sum_{i=1}^{N} u_i \phi_i(\mathbf{x}), \tag{2.9}$$

where the $\phi_i(\mathbf{x})$ are the shape functions, u_i are constants to be determined and $\phi_o(\mathbf{x})$ is a function that satisfies the boundary conditions imposed on $\mathbf{u}(\mathbf{x})$.

Since the approximation is done considering a finite number of terms, $\hat{\mathbf{u}}$ is generally different from the solution $\mathbf{u}$. Thus, substitution of the approximated solution into the differential governing equation will result in a non-zero residual.

The objective of the method of weighted residuals is to select the constants u_i so as to minimise the residual term in some sense. This may be achieved by multiplying the residual term by a set of N weighting functions and setting to zero the integrand of the resulting product. These two procedures force the residual to vanish in a weighted-average sense.

The Galerkin weighted residual method is obtained by selecting the shape functions as the weighting functions. This method leads for several (but not all) continuum problems, to a symmetric matrix equation in the unknown shape function contributions.

The Galerkin finite element method may be regarded as a variant of the Galerkin weighted residual method, in that the concept is applied using shape functions that are only locally defined. The continuum domain is discretized into smaller sub domains ('finite elements'), and a trial function (equation 2.9 with $\phi_0(\mathbf{x}) = 0$) is used to approximate the total number of degrees of freedom at each nodal point in the element.

Variational approach

Many problems possess equivalent variational formulations stating that the solution to the differential governing equation together with the given boundary conditions is a stationary (or "equilibrium") of some functional. The functional is a scalar quantity that results from integrating a function over the continuum domain and integrating another function over the boundary surface.

In the Rayleigh-Ritz method, the solution for each field variable is sought as an expansion in terms of some prescribed trial or shape functions. The contributions of the shape functions to the solution expansion are determined such that the functional of the considered continuum problem is stationary. That is, the functional value remains unaltered for each infinitesimal variation on one of the shape function contributions.

An important property of the functional variation is that it yields always a symmetric system equation in the unknown shape function. The finite element method may be considered as a special case of the Rayleigh-Ritz method in that the solution for each field variable is sought in terms of shape functions, that are locally defined within each element.

2.2.2.1 Implementation

A necessary condition for the implementation of the finite element method is that global conformity must be satisfied, either directly with the shape functions or indirectly, via a conforming auxiliary scheme.

Conforming elements satisfy two conditions: *completeness* and *compatibility*. Whether a finite element model is based upon a weighed residual or a variational formulation, the nodal degrees of freedom result always from a set of equations, in which the coefficients are defined in integral forms. To satisfy the completeness condition, all terms in the integration expression evaluated using the trial functions (equation 2.9), must reach a constant value as the size of the element tends to zero.

The compatibility condition is satisfied if the terms in the integral expression are all finite. This condition is always achieved, if the derivatives of the variable expansion are continuous along inter-element boundaries (see e.g. [5, chapter II]).

Though, in principle, any conforming function may be used as a shape function, the construction of the finite element model becomes particularly simple and straightforward if the element shape functions are obtained from a set of polynomial functions. For the solution of problems governed by the Helmholtz equation (either acoustic or elastic), the integral expression for the variable expansion involves only first order derivatives (see Appendices A and B). Thus, conformity is satisfied with linear polynomial shape functions which ensure C^0-continuity along inter-element boundaries. Each shape function is defined, such that it has a value of unity at the actual node and that it is zero at all the other element nodes.

The most commonly used elements in acoustic and elastic finite element modelling are linear quadrilateral and linear triangular elements for two-dimensional problems and linear hexahedral and linear tetrahedral elements for three dimensional problems. Since the continuum domain will have in general a complex shape, a discretisation of the domain is often constructed using the concept of *parametric mapping*, which enables the use of elements with more complex, distorted geometries. An illustration of this concept is given in Appendix A.

The resulting system of equations 2.2 has the following properties:

- The stiffness (**K**), mass (**M**) and damping (**C**) matrices are very sparse, with only few non-zero entries per row. Furthermore, for acoustic problems, which can be formulated using a variational functional approach, **K**, **M** and **C** are also symmetric. The final solution for the unknown nodal values may then be obtained from efficient matrix solvers.

2.2.2.2 Convergence of the Galerkin FE for the Helmholtz equation - alternative approaches

In principle, for a Galerkin finite element method that consists of conforming elements, the convergence of the numerical solution toward the exact solution is ensured by reducing the nodal spacing h (mesh refining), and/or increasing the order p of the interpolating polynomial. Using a local Taylor expansion of the unknown field variable, the error may be expressed simply as $\mathcal{O}(h^{p+1})$ [5].

For the solution of problems governed by the Helmholtz equation, however, the situation is different. Through several studies [28–30], it has been shown that the accuracy of the solution obtained with the standard Galerkin finite element approach, deteriorates rapidly with increasing wave number k, notwithstanding the conformity condition of the finite element model.

The estimation of the error is generally achieved by following two main procedures [31]. The first is to estimate the error before the actual solution is computed, known as *a priory* error estimates. This type of estimates are not computable because they are given in terms of the unknown exact solution. The second broad class of error estimates is *a posteriori*, which means the error estimate is obtained after the solution is known. These type of estimates are generally used for adaptivity and control of solution error.

Ihlenburg and Babuška [32, 33] proved that an *a priori* accurate error estimator is given by

$$e \leq C_1 \left(\frac{kh}{2p}\right)^2 + C_2 k \left(\frac{kh}{2p}\right)^{2p}, \tag{2.10}$$

where the constants C_1 and C_2 are independent of k, h and p.

The first term in the right hand side of equation 2.10 represents the interpolation error. The second one is the difference between the interpolant and the finite element wave, caused by the indefiniteness of the variational form. Note that this term, usually referred to as the *pollution* effect, goes to infinity with increasing wave number affecting the stability of the FEM solution.

A general used 'rule of thumb', is to refine the mesh so as to keep $n = \lambda/h = const$, where $\lambda = 2\pi/k$ is the wavelength and n is called the resolution of the wave. However, from relationship 2.10, it is seen that if only linear elements ($p = 1$) are considered (called the *h-version* of the FEM), a systematic refinement of the mesh does not necessarily guarantee convergence to the desired solution as k grows [34]. In this case, convergence is ensured independently of k, if hk^2 is constrained [29].

A posteriori error estimators proposed for wave problems fall into three main types: residual [28], based on smoothing [35] (known as the *Super Convergent Patch Recovery*) and based on local computations of *admissible fields* [36].

It has been shown [29, 37] that the Super Convergent Patch Recovery and the local based computed error estimators, can estimate the approximation error but no the pollution term. More recently, Irimie and Bouillard [38] proposed an alternative residual a posteriori error estimator procedure. Though the error is more realistically estimated, the quality of the estimator decreases for increasing wave number.

The effect of the pollution error in the finite element solution is a "phase lag". That is, numerical waves propagate with speed $c^h = \omega/k^h$, where c^h is different from the speed of sound c. To circumvent this problem, several non-standard FEM have been proposed in the literature. In these methods, stabilisation is either attempted directly by modification of the differential operator or indirectly, via improvement of approximability by the use of solutions of the governing equation as trial functions. Some of the most relevant techniques based on direct stabilisation are reviewed below. Schemes formulated by the use of solutions of the governing equation, which fall into the category of Trefftz methods, are discussed in section 2.4.

***Galerkin least-squares* (GLS)**

This method appends residuals of the Euler-Lagrange equations in a least-squares form to the Galerkin variational form using a local mesh parameter. In [39], an estimation of the local mesh parameter that minimises the phase lag, $k^h - k$, for the Helmholtz equation in one dimension was determined. For two and three dimensions, however, the determination of the local mesh parameter is cumbersome [40].

An alternative to the GLS is the *Galerkin gradient least-squares* (GGLS) [41], in which the least-squares terms contain residuals of the gradient of the governing equation. A recent comparison between these methods and the standard Galerkin formulation for elastic waves, shows that only the GGLS gives acceptable accuracy in phase and magnitude for longitudinal and transverse waves [42].

***Generalised Finite Element Method* (GFEM)**

Using the phase lag difference $k^h - k$, Babuška *et al.* [43], derived a stabilised finite element method (SFEM) which has no pollution for one-dimensional problems. They also demonstrated that there is no numerical method that can eliminate the entire phase error in two dimensions, independently of the direction of the wave.

Based on this result, they proposed a generalised finite element method (GFEM), which defines a matrix $\mathbf{A}$ and a linear mapping $\mathcal{L}$ which maps the prescribed boundary values at the external surface of the domain onto the vector of the right hand side $\mathbf{b}$. The solution of the linear system

$$\mathbf{A}\mathbf{u} = \mathbf{b} \tag{2.11}$$

is then identified with a finite element function by approximating the unknown field variable $\mathbf{u}$ using a standard basis function. The matrix $\mathbf{A}$ is then individually defined for interior, edge and corner points.

The resulting method is in essence a finite difference approach, where each point in the grid is associated with one equation. It was shown for two-dimensional acoustic problems, that the GFEM has minimal pollution error, equivalently minimal phase error. It is not clear, however, whether this approach (being in essence a finite difference scheme) can be implemented in unstructured meshes and extended to three dimensional problems.

Subgrid Finite Element Method **(SFEM)**

In this approach, the solution is decomposed into a part which is resolvable by the grid and a part which is unresolvable, and is solved for analytically. This method was first proposed by Oberai and Pinsky [44] based on the multiscale variational formulation of Hughes [45]. For problems in two dimensions, the SFEM shows less pollution than the Galerkin solution but is worse than the GLS solution [44]. The accuracy of the method is dependent on the direction of propagation of the wave.

More recently, Oberai and Pinsky [46] derived a residual-based approach that takes into account not only the residual on element interiors but on inter-element boundaries as well. The method is formulated following a variational multiscale scheme. However, the precise values of the parameters in the variational formulation, are determined from a discrete dispersion analysis. The proposed approach displays minimal phase error in structured and unstructured meshes.

Spectral Element Method

The spectral element method is a finite element method, in which high order polynomial functions are used as parent element shape functions. In the original formulation introduced by Patera [47], the nodal points in each element are collocated using a cosine function, giving a more concentrated nodal density at the corners of the element. Once the nodal points are determined, the interpolation is performed using Lagrangian polynomials.

The application of the spectral method in acoustic and elastic waves is mainly due to Seriani *et al.* [48,49]. They proposed a collocation approach based on the Chebyshev-Gauss-Lobatto quadrature rule, and established later a somewhat subjective measure of accuracy for the method [50]. Zampieri and Tagliani [51] and Komatitsch *et al.* [52], proposed the use of different location of points and quadrature rules for modelling elastic wave problems. By comparing these approaches, the accuracy was shown to depend strongly on the choice of the collocation points.

More recently, Dauksher and Emery [53, 54] investigated the dispersion error of the method for the solution of the time-dependent acoustic and elastic waves, using the phase and group velocities. In comparison to the Galerkin low-order isoparametric finite element method, the spectral element method shows a better convergence and accuracy.

Waveguide Method

The waveguide method, also known as the spectral finite element method [55] (but unrelated to the method outlined above), is applicable to continuum problems governed by differential equations in one principal independent spatial variable. Such problems may include railway car structure vibrations and pipe vibration, which can be discretized using one-dimensional elements.

Since the geometrical discontinuities and external excitations occur only at the interfaces between the elements, the field variables within each element are governed by homogeneous ordinary differential equations. The exact solutions may then be expressed in terms of a finite number of frequency dependent local solutions of these equations. The combination of these solutions constitute the base functions.

The waveguide method is a merger of the dynamic stiffness method [56], since a dynamic stiffness matrix can be constructed from the base functions which exactly relates the nodal field variables of the element to the nodal excitations, applied at the endpoints of the elements. Finnveden [57] and Bilodeau and Doyle [58] applied the method to cylindrical pipes. The cross sectional mode shapes were described using standard FE (high order polynomials) shape functions, whilst the propagation in the axial direction was expressed as a combination of exponential terms. A significant reduction in the computational cost in comparison to standard FE approaches was obtained following this procedure.

The waveguide method may be extended to general two and three dimensional problems, provided that the properties of the problem (i.e., material and geometry properties) are piecewise constant in one spatial variable and invariant in the other spatial variables [59,60].

2.2.2.3 Iterative solution techniques

In order to keep a reasonable accuracy in the numerical solution, high-frequency problems governed by the Helmholtz equation require a combination of fine meshes and high-order polynomial functions. For such problems, solving equation 2.2 by a direct method entails memory and CPU requirements that have the capacity to overwhelm even the largest resources that are currently available.

For this reason several iterative algorithms such as Krylov sub-spaces [61–63], multigrid [64–66] and domain decomposition (DD) methods [67–69] have been proposed for the solution of the matrix problem 2.2. The optimal application of these techniques relies on parallel computing, and distributed memory (a comprehensive review is given in reference [70]).

Each of these three classes of methods has its own advantages and disadvantages. One attractive feature of, for example, multigrid methods is its mesh-independent convergence and optimal scalability [64]. However, full multigrid efficiency can only be achieved for problems associated with certain types of partial differential equations, defined on regularly structured domains. Thus, they have a limited applicability.

On the other hand, Krylov subspace methods may not be robust. Thus, the major difficulty in their implementation resides in the indefiniteness of the matrix equation system (equation 2.2) at large wave numbers. In addition, their convergence depends largely on the problem size, in contrast to multigrid schemes. It is well known, that the robustness and efficiency of Krylov sub-spaces can be improved dramatically by using a suitable preconditioner [71–73]. Hence, multigrid and Krylov subspace methods seem to be complementary in which one method's weakness is a strength of the other. Several preconditioning strategies combining multigrid and Krylov sub-spaces were recently proposed by Saad and Zhang [63]. Results show that a robust and efficient iterative solver may result, though further investigation aim to thoroughly assess this methods is needed.

Domain Decomposition methods (DD) reduce the global problem to the iterative resolution of smaller non-overlapping subdomains allowing the direct solution of a smaller problem in each subdomain [74]. This idea leads to an iterative method which converges to the solution of the problem if the solutions in the subdomains are suitably related by means of the boundary conditions at the inter-element interface [67].

Though in most cases, the subdomains are solved using a finite element method [69], a DD scheme based on a finite difference discretisation of the subdomains have been also shown to give good results [75]. Farhat *et al.* [68] proposed a novel regularised DD approach in which an auxiliary second-level problem is solved at each iteration, obtained by projecting the inter-element interface onto a suitable coarse space. They successfully applied the method to the solution of an acoustic scattering problem with more than 1,000,000 discretisation nodes.

2.2.3 Summary of properties for the traditional FD and Galerkin FEM

The resulting system of equations obtained from the conventional finite difference method and the finite element method have similar properties. However, since the FEM may be readily implemented in non-uniform domain discretisations, it has an important practical advantage over finite difference approaches.

A summary of the properties for the traditional FD and the Galerkin FE is given in table 2.1.

	mesh type	non-uniform meshes	numerical integration	equation system
FD	overlapping	difficult	no	banded
FEM	non-overlapping	easy	yes	sparse

Table 2.1: Properties of the traditional FD and the Galerkin FE methods.

2.3 Boundary integral methods

Owing to the significant efforts in the last three decades, the boundary element method has become one of the major methods in numerical analysis for engineering problems (for a review, see e.g. [76]).

The BEM is based on the integral formulation of the considered problem, which may be expressed as a direct or indirect equation [77]. In the more traditional direct approach, the partial differential equation is transformed by means of Green's theorem (or a weighted residual formulation [78]) into a Helmholtz integral formula, in which the unknowns are the primitive variables on the boundary (note the similarities with the direct Trefftz approach of section 2.4.3). For exterior acoustic problems, the Helmholtz integral formula over an acoustic domain Ω_A, is expressed as [79]

$$\epsilon\, p(\mathbf{x}) = \int_{\Gamma_A} \left[p(\mathbf{x}_q) \frac{\partial G(\mathbf{x}, \mathbf{x}_q)}{\partial n_q} - G(\mathbf{x}, \mathbf{x}_q) \frac{\partial p(\mathbf{x}_q)}{\partial n_q} \right] d\Gamma_A(\mathbf{x}_q), \tag{2.12}$$

where $\mathbf{x}$ denotes the field point and $\mathbf{x}_q$ denotes the source point on the surface of the domain, Γ_A. The function $G(\mathbf{x}, \mathbf{x}_q)$ is the Green's kernel function

$$G(\mathbf{x}, \mathbf{x}_q) = \frac{e^{\iota k |\mathbf{x} - \mathbf{x}_q|}}{|\mathbf{x} - \mathbf{x}_q|}, \tag{2.13}$$

for three-dimensional problems, and

$$G(\mathbf{x}, \mathbf{x}_q) = -\frac{\iota}{4} H_0^{(2)} k |\mathbf{x} - \mathbf{x}_q| \tag{2.14}$$

for two dimensional problems, where k is the wave number, $\iota = \sqrt{-1}$, and $H_0^{(2)}$ is the zero-order Hankel function of the second kind. In equation 2.12, the coefficient

ϵ has the value 0 for $\mathbf{x}$ inside surface Γ_A, the value 4π for $\mathbf{x}$ outside surface Γ_A, and the value 4π minus the solid angle of point $\mathbf{x}$ for $\mathbf{x}$ on the boundary surface Γ_A.

The direct boundary integral formulation for interior acoustic problems is similar to the exterior formulation (equation 2.12). Since the direct boundary integral formulation requires that the boundary surface Γ_A is closed, it can only represent either an interior or an exterior pressure or displacement field, but not a combined interior/exterior field. According to the type of boundary conditions of the original boundary problem, equation 2.12 results in an integral equation of the first, second or mixed kind.

A well-known shortcoming of the Helmholtz integral equation for exterior problems, is that it does not have a unique solution at certain characteristic eigenfrequencies associated with the corresponding interior Dirichlet problem [80]. Beginning in the 1960s, many researches tried to find an integral equation approach for the solution of exterior acoustic problems which holds for all frequencies [81]. Schenk [82] (see also references [83, 84]) proposed additional constraints of the Helmholtz integral representation inside the boundary. He suggested a method of overdetermining the system with additional algebraic equations (points located inside the domain) by a combined Helmholtz integral representation (CHIEF).

Another formulation to overcome the non-uniqueness problem was proposed by Burton and Miller [85]. This approach combines the surface Helmholtz integral equation and its associated normal derivative equation, leading to a hypersingular integral formulation. In practise, the hypersingular integral is much more difficult to solve than that of the CHIEF method but the scheme is more robust at higher frequencies. Several authors [86–88], transform the hypersingular integral to reduce the singularity order of kernel and improve the scheme of numerical computation to reduce the execution time.

Brakhage and Miller expressed the solution as a combination of single and double layer integral solutions of the Helmholtz equation, valid for all wave numbers (see e.g. reference [89] and the references therein). This formulation, known as the indirect integral equation, approximates the governing equation in terms of continuous distribution of singular solutions over the boundaries of the problem with unknown fictitious surface densities. The difference in the pressure and the difference in the normal gradient of the pressure across the boundary constitute the primary variables. Thus, the acoustic or elastic model can contain openings and appendages.

For an acoustic domain Ω_A, in which all or part of its boundary surface Γ_A is unbounded, the indirect integral equation is given by [90]

$$p(\mathbf{x}) = \int_{\Gamma_A} \left(G(\mathbf{x}, \mathbf{x}_q)\sigma(\mathbf{x}_q) - \frac{\partial G(\mathbf{x}, \mathbf{x}_q)}{\partial n_q} \delta\sigma(\mathbf{x}_q) \right) d\Gamma_A(\mathbf{x}_q), \ \mathbf{x} \in \Omega_A, \tag{2.15}$$

where

$$\sigma(\mathbf{x}_q) = \frac{\partial p(\mathbf{x}_{q_1})}{\partial n_{q_1}} - \frac{\partial p(\mathbf{x}_{q_2})}{\partial n_{q_2}} \tag{2.16}$$

is the difference in the normal gradient of the pressure (single layer), and

$$\delta\sigma(\mathbf{x}) = (p(\mathbf{x}_{q_1}) - p(\mathbf{x}_{q_2})), \tag{2.17}$$

is the difference in the acoustic pressure across the surface of the boundary (double layer). In equations 2.16 and 2.17, the subscript "1" is associated with the direction opposite to the unit normal on the surface of the boundary , and "2" is associated with the direction of the unit normal. The formulation of the indirect boundary for elastic wave analysis may be obtained following a similar procedure (see e.g. references [77, 91]).

A major difficulty encountered in the indirect integral equation formulation, is the necessity of defining a different formulation for each type of boundary value problem, in order to obtain a uniquely solvable integral equation, which can be used as a basis for a robust numerical scheme [89].

Based on the direct or indirect integral formulation, the boundary element solution is obtained following a two-step procedure:

- solve the boundary integral equation to obtain the distributions of the boundary values.

- obtain the field variable at any point in the domain by integrating the product of the boundary values and the fundamental solution over the boundary.

2.3.1 Direct boundary element method

In this approach, the acoustic pressure and the acoustic velocity constitute the primary variables. The determination of boundary variable values is based on the same modelling concepts as the finite element method. That is, the boundary surface is discretized in a finite number of non-overlapping subsurfaces, called 'boundary elements', and some nodes are defined at particular locations in each element.

The geometry of each element is then approximated by a piecewise polynomial shape function, conveniently mapped onto a local coordinate system. By using isoparametric elements, the boundary variables are represented by the same set of shape functions that are used to represent the geometry (equation 2.9).

The problem of determining the boundary variable distributions is thus turned into a discrete problem of finding the shape function contributions, which represent the pressure values p and its normal derivative $\partial p/\partial \mathbf{n}$. This may be achieved using a weighted residual or a variational formulation, which involves the (sometimes computationally expensive) numerical evaluation of double surface integrals. This drawback is generally circumvented by using a collocation procedure. In this approach, the points p are located at each node location and equation 2.12 is evaluated over the entire boundary on an element-by-element basis (this procedure is exhaustively described in the literature, see e.g. references [80, 92, 93]). Each collocation point p and boundary element combination produces two element coefficient vectors. Upon evaluation over the entire boundary we obtain a matrix equation of the form

$$\mathbf{A}\mathbf{p} = j\rho\omega\mathbf{B}\mathbf{v_n}, \tag{2.18}$$

where, for n_a boundary discretisation points, the $n_a \times n_a$ matrices $\mathbf{A}$ and $\mathbf{B}$, relate the nodal pressure values to the nodal normal velocity values. Equation 2.18 may be rearranged into the known form $\mathbf{A}\mathbf{x} = \mathbf{b}$ by grouping all the boundary unknowns on the left-hand side. Once this equation is solved, the Helmholtz integral equation can be integrated to obtain the sound pressure at any point in the acoustic domain.

2.3.2 Indirect boundary element method

In exactly the same way as in the direct boundary element method, the solutions for the two boundary variables (single and double layer potentials) are approximated in each element surface in terms of a prescribed set of shape functions. In this case, these functions represent the single layer potentials σ_i and double layer potentials $\delta\sigma_i$ at the discrete node locations on the boundary surface.

The use of a collocational procedure for determining the unknown nodal degrees of freedom becomes more difficult in this case. Thus, the single and double potentials are usually obtained from a variational formulation of equation 2.15, which requires the solution of double surface integrals [94, 95]. The stationary condition on the associated functional, yields a symmetric matrix equation for the unknown values

$$\begin{bmatrix} \mathbf{E} & \mathbf{D} \\ \mathbf{D}^{\mathrm{T}} & \mathbf{F} \end{bmatrix} \begin{Bmatrix} \sigma_i \\ \delta\boldsymbol{\sigma}_i \end{Bmatrix} = \begin{Bmatrix} \hat{\mathbf{f}}_{\sigma} \\ \hat{\mathbf{f}}_{\delta\sigma} \end{Bmatrix}, \tag{2.19}$$

where the vectors $\hat{\mathbf{f}}_{\sigma}$ and $\hat{\mathbf{f}}_{\delta\sigma}$ are the imposed pressure and imposed velocity conditions, respectively, whilst imposed impedance conditions appear in matrices **E** and **F**.

At the part of the boundary surface on which a prescribed pressure is imposed, the double layer potential is zero. At the part of the boundary on which a prescribed velocity is imposed, the single layer potential is zero. At the part of the boundary surface on which a prescribed impedance is imposed, a relationship exists between the single and the double layer potential [96].

2.3.3 Error and convergence

In the same way as the finite element method (see Section 2.2.2.1), the boundary element discretisation of the boundary surface is based on the parametric mapping of a geometrically simple parent element discretisation, in which the boundary variables are expressed in terms of polynomial shape functions and of which the convergence toward the exact solution is, in principle, ensured.

The accuracy of the BEM solution improves as the number of elements used to discretise the boundary surface and/or the number of boundary nodes inside each element increases. However, the improvement in accuracy and efficiency that can be obtained by following these procedures, entails a greater cost of computational time. Lin [89] showed that, when the number of discretisation points is doubled, the computational time increases by a factor of about four.

When the close form solution of the problem is available, a straightforward estimation of the BEM solution error can be readily obtained. Tadeu *et al.* [97, 98], analysed the performance of constant, linear and quadratic interpolating functions in a particular acoustic scattering problem. They showed that quadratic elements perform better as the frequency increases.

In most applications, however, the analytical solution is not known a priori. Thus, an accurate estimation of the BEM error is essential in order to implement efficient adaptive refining techniques. For boundary element methods based on a Galerkin procedure, the error e can be bounded by the residual of the boundary integral equation R as [99]

$$c_1||R|| \leq ||e|| \leq c_2||R||, \tag{2.20}$$

where the constants c_1, $c_2 > 0$ are independent of the boundary field value at the discretisation points, and $||\cdot||$ denotes the norm dependent on the subspace of the approximate solution. For the direct BEM based on a collocation procedure, however, equation 2.20 is not proved rigorously but only confirmed by numerical examples. To overcome this difficulty, several alternative error estimation procedures have been proposed (a systematic review of these approaches is given by Kita and Kamiya [100, 101]).

In practise, the estimation of the error is almost as computationally expensive as the initial BEM analysis. Charafi *et al.* [102] used a local reanalysis to obtain a faster estimation of the error. More recently, Rodríguez and Power [103] proposed the use of a local error analysis based on a piecewise polynomial collocation approach, making the method consistent with the collocation BEM.

Based on these error estimators, the error may then be reduced by means of adaptive techniques. Three refinement strategies have gained acceptance, namely, the h-adaptive strategy (e.g. [103, 104]), the p-adaptive strategy (e.g. [105]) and the r-adaptive strategy [101].

Under the h-adaptive scheme, the mesh is refined by subdividing all or some of its elements (see section 2.2.2.2). The p-adaptive process increases the order of the interpolation functions, whilst the r-adaptive method keeps the number and type of elements fixed while repositioning their nodes. Feistauer *et al.* [99], demonstrated that the combined h-p-adaptive Galerkin BEM converges exponentially, in contrast to the h-adaptive Galerkin which converges algebraically.

Once the boundary variables have been computed, the field variable may be estimated at any point in the domain by integrating the product of the boundary values and the fundamental solutions over the boundary (the second step in the BEM procedure). This process involves the use of quadrature integration formulae, giving rise to approximation errors. Furthermore, as the field point is moved close to the surface boundary, the error is significantly increased due to the singularity of the fundamental solution. To circumvent this problem, Tomioka *et al.* [106], proposed the use of a series expansion of the Helmholtz equation, in terms of Hankel functions of the zero- and the first-order. This technique requires, however, that the argument of the fundamental solution be smaller than unity.

2.3.4 Iterative solution techniques

As discussed in the precedent sections, the use of integral equations gives rise to systems of equations of the form

$$\mathbf{A}\mathbf{x} = \mathbf{b}, \tag{2.21}$$

where A is a *dense* matrix of dimension $(N \times N)$, N being the number of surface points. Thus, notwithstanding the convergence of the adaptive schemes discussed above, the storage requirements of matrix A rapidly overwhelm practical computational storage capabilities as the size of the problem increases.

For a system of linear equations of moderate dimension, the solution is generally obtained using direct solvers which, despite requiring $\mathcal{O}(N^3)$ operations, give an exact solution except for round-off errors [107]. When the number of equations becomes large, however, the use of iterative methods, which does not require storage of matrix A, seems unavoidable.

For the direct BEM based on collocation, the matrix A is additionally non-symmetric. The alternative and mathematically attractive Galerkin and variational approaches produce symmetric systems of equations, but are much more difficult to implement (see e.g. reference [108]). For the indirect BEM, on the other hand, the usual procedure is based on a variational formulation giving always a symmetric system. The use of iterative solution techniques is intended to overcome not only the storage problems, but also to give an approximate solution of equation 2.21 in a reasonably small number of iterations. In this context, the difference in the performance of iterative solutions for symmetric and asymmetric systems of equations is important [109].

The iterative methods currently available can be characterised into two groups, namely, stationary and non-stationary methods. The stationary iterative methods refer to classical iterative methods such as Jacobi, Gauss-Seidel and SOR. The non-stationary methods can be framed as Krylov subspace methods. They include the conjugate gradient square (CGS) [110], generalised minimal residual (GMRES) [111], bi-conjugate gradient (Bi-CG) and bi-conjugate gradient stabilised (Bi-CGStab) [112].

The convergence rate of these techniques varies for different type of applications. For a particular type of problem, an iterative solver may or may not converge, or converge more slowly than direct solvers. This situation can be improved greatly by the use of a preconditioner [113, 114]. As long as a competitive iterative solver and a suitable preconditioning scheme can be identified for a particular problem, high efficiencies in solving the linear system of equations can be expected over direct solvers [115–117]. This, however, may be not a simple task and will depend ultimately on the structure of the system matrix **A** for a given problem.

2.4 Trefftz-based methods

2.4.1 Note on Trefftz-type approaches

It is not easy to establish a clear division between the Trefftz-based methods and other numerical modelling procedures. Historically, integral equations go back at least to the work of Green, Poincaré and Fredholm (see e.g. references [118, 119]). The integral approach proposed by Trefftz (based on Green's second identity) is generally regarded as the first *boundary discretisation method.* In addition, the method was originally proposed using non-singular solutions of the governing equation.

Thus, boundary methods in general, are sometimes referred to as "Trefftz-type methods" [5]. However, an approach (not necessarily a boundary solution type) is usually classified as a Trefftz method, when the trial functions are non-singular in the problem domain. That is the criterion adopted in the present analysis.

Modelling methods based on boundary solutions which are singular in the physical domain as, e.g., the Boundary Integral Method (BIM) and the Boundary Element Method (BEM) are reviewed in section 2.3.

2.4.2 Brief historical background

In 1926, Trefftz [120] proposed an alternative approach to the Rayleigh-Ritz method by using non-singular solutions of the homogeneous equation as the weighting functions in a boundary-type solution scheme.

The ideas suggested by Trefftz derived, many years later, in two different boundary method formulations according to the interpolation procedure of the field variable. Namely,

(i) To use an approximation scheme based on a complete (analytically derived) set of non-singular solutions of the homogeneous governing equation

(ii) To use singular solutions as the trial functions in a boundary integral formulation, relating the unknown parameters with some physical properties of the problem at the boundary.

Boundary-type methods based on the boundary integral equation are generally formulated locating the singular sources in the physical boundary of the problem (e.g. various versions of the singular BEM [79]). An alternative approach known as the Method of Fundamental Solutions [121], is to move the sources away from the physical domain, thus obtaining a regular boundary integral scheme [122].

The implementation of modern Trefftz-type methods based on complete solutions was initiated only in the late 1970s. An important contribution to this end was made by Herrera *et al.* [123,124], who performed a systematic study on the different properties of the complete sets of homogeneous solutions, called T(Trefftz)-complete (a brief description of the functions properties is given in [125] and in the references therein).

Trefftz boundary methods based on T-complete functions were subsequently formulated as direct and indirect [126]. The indirect Trefftz method (thought to be the original one presented by Trefftz) has been extensively studied and applied in many fields [127]. The direct method, proposed later by Jin *et al.* [128–130], has received in comparison little attention.

On the other hand, several variational formulations of Trefftz-type schemes as a finite element process were also proposed[2] [131–133]. This led to the hybrid Trefftz and least-squares Trefftz element concepts [134–136], which became increasingly

---

[2] It should be mentioned that this idea was advanced by Trefftz in his original paper, by showing with an example a possible generalisation of the concept to a discretized domain.

popular in the following years (an exhaustive review is given in reference [137]). Recent applications of T-element methods in elastic and acoustic wave modelling may be found in references [138–141].

The Method of Fundamental Solutions (MFS) was originally introduced by Kupradze [121] and investigated later by different authors [142–144] (The method is also known by many other names in the literature. Among these are the *source function method* [145], *boundary point method* [146] and *superposition method* [147]).

MFS-based approaches have gained increasing popularity throughout the last two decades [148]. Although most of the published work on the MFS seem to be for the Laplace's equation, recent applications on the solution of the Helmholtz equation include inhomogeneous and heterogeneous media [149, 150] and eigenvalue calculation problems [151].

More recently, Caruthers *et al.* [7, 152] proposed the use of point sources in a finite difference procedure. The method, called the Green Function Discretisation (GFD), was shown to have a dramatic computational advantage in comparison to conventional modelling methods [153–155].

The point sources were subsequently replaced by plane waves resulting in the Wave Expansion Discretisation (WED) method [156, 157]. An independent assessment on the WED method has been recently made by Ruiz and Rice [182], who also investigated the performance of a particular WED scheme for plate vibration analysis [158]. The WED method may be considered part of a relatively new and unknown group of wave-based methods. These approaches include meshless [159–162] and standard [163] FE models and boundary methods [164, 165].

2.4.3 Boundary Trefftz methods

There are two main approaches for the formulation of Trefftz boundary solution methods using T-complete functions: direct and indirect [127]. The conceptual difference between these techniques resides in the way one fits the boundary conditions of the problem.

To be more specific, consider for example, a steady-state acoustic problem where the pressure p is the field variable in a domain Ω_A with boundary Γ_A. Dirichlet conditions, $p = \overline{p}$, and Neumann conditions $q = \partial p/\partial n = \overline{q}$, are prescribed in Γ_D and Γ_N, respectively, where $\Gamma_A = \Gamma_D \cup \Gamma_N$.

To solve such a problem by a Trefftz method one has available[3] a T-complete set of solutions, say, $\{U_1, U_2, \ldots\}$. For 2D and 3D acoustic problems, these sets may be conveniently formulated in terms of Bessel, Hankel and Legendre functions (see e.g. reference [123]).

In the indirect Trefftz method, the pressure field distribution is approximated as a linear combination of the complete solutions

$$p \approx \tilde{p} = \sum_{i=1}^{N} a_i U_i = \mathbf{a}^T \mathbf{U}, \tag{2.22}$$

where the parameters a_i are unknown.

The approximation 2.22 satisfies the governing differential equation but, in general, do not satisfies the prescribed boundary conditions $\overline{p}$, $\overline{q}$ on Γ_D and Γ_N. In order to satisfy the boundary conditions, the unknown parameters a_i are determined so that the residuals

$$R_1 = \tilde{p} - \overline{p} = \mathbf{a}^T \mathbf{U} - \overline{p}, \ \mathbf{x} \in \Gamma_D, \tag{2.23}$$

$$R_2 = \tilde{q} - \overline{q} = \frac{\partial \tilde{p}}{\partial \mathbf{n}} - \overline{q}, \ \mathbf{x} \in \Gamma_N, \tag{2.24}$$

are minimised simultaneously, using a collocation (TCM), a Galerkin (TGM), a least-squares (TLSM) or other alternative scheme (see, e.g. references [127,167]). In practise, the choice of any particular approximation method has a critical influence on the convergence, accuracy and stability of the indirect Trefftz approach [126]. A rigorously investigation on cases of discontinuities in the boundary functions and boundary corner points has been recently carried out by Abou [168].

---

[3] When no solutions are already available, different procedures to find a T-complete set of functions have been proposed, including the use of "approximate" solutions [166].

The Trefftz direct method is similar to the boundary element method, in which the unknown variables are the physical quantities such as the pressure and its normal derivative over the boundary surface. The method is based on a weighted residual formulation of the governing differential equation, in which the T-complete function 2.22 is taken as the weighting function. Using integration by parts, and since the weighting function satisfies the governing equation, the problem reduces to find an approximate expression for the surface integral corresponding to the boundary conditions [127]. This is achieved discretising the boundary into a finite number of surface elements, and using a standard (polynomial) interpolation procedure as in the boundary element method.

The direct and indirect boundary Trefftz methods have been benchmarked against the exact solutions in plane elasticity [128] and exterior acoustic diffraction problems [129], showing a very similar performance.

2.4.4 The method of fundamental solutions

The single layer potential theory states that for a given volume Ω_A with no acoustic sources, the potential can be computed as the surface integral Γ_A (over the volume Ω_A) of a continuous function $\sigma(\mathbf{x})$ with the free-field Green's Function (see e.g. reference [119, chapter 1]):

$$\phi(\mathbf{x}) = \oint_{\Gamma_A} G(\mathbf{x}, \mathbf{x_q})\sigma(\mathbf{x}_q)dS, \;\; \mathbf{x} \in V, \;\; \mathbf{x}_q \in \Gamma_A \tag{2.25}$$

where $\mathbf{x}$ is a general field point in Ω_A, $\mathbf{x}_q$ is a source point in Γ_A and $\mathrm{G}(\mathbf{x}, \mathbf{x}_q)$ is the Green's kernel function (equations 2.13 and 2.14).

By enforcing the desired boundary conditions as $\mathbf{x} \to \mathbf{x}_q$ one obtains an integral equation for $\sigma(\mathbf{x}_q)$.

The Method of Fundamental Solutions (MFS) approximates $\sigma(\mathbf{x}_q)$ using a discrete number of singular point sources with unknown coefficients. The required regular condition of relationship 2.25, is obtained by locating the sources in an artificial boundary surrounding the physical domain. To find the solution two main approaches are usually followed: fixed and adaptive.

In the fixed formulation, the singularities are located *a priori* and remain fixed throughout the calculation process of the unknown parameters. The solution is obtained by collocating the boundary conditions at a discrete number of points in the physical domain. This leads to a square system of linear algebraic equations amenable to be solved directly [143,169]. As shown by Golberg and Chen [170], this MFS approach is nothing but a special case of the *discrete regular BEM* [122].

The MFS with moving singularities was first proposed by Mathon and Johnston [142]. In this approach, the locations of the singularities are determined along with the unknown coefficients. This is usually achieved by a least squares fit of the boundary data which leads to a non-linear maximisation problem. Kondapalli *et al.* [171] analysed the MFS with fixed and moving singularities for wave scattering in fluids and elastic regions.

The location of the singularities and collocation points in the fixed MFS has a critical influence in the convergence and stability of the method [172]. Bogomolny [143], showed that in the fixed MFS the approximation improves as point sources are moved away of the physical boundary. This completely contradicts the fact that the fixed MFS becomes highly ill-conditioned as this distance is increased. The ill-conditioning notwithstanding, the numerical solution is paradoxically largely unaffected [170].

Most of the research work on the fixed MFS has been devoted to resolve the ill-conditioning problems associated with this method (see e.g. references [173–175]). Despite this drawbacks, the fixed MFS has been applied to elastic waves, acoustic radiation and scattering [171,176] and inhomogeneous problems [149,150,177]. More recently, Karageorghis used a fixed MFS for the calculation of the eigenvalues of the Helmholtz equation [151] showing that the MFS leads to a much faster convergence than standard boundary integral methods.

2.4.5 T-element method

The basic idea of the T-element method is to divide the domain into subdomains or "elements". A non-conforming approximation of the field variable is independently performed in each element in terms of T-complete solutions of the homogeneous differential equation whose coefficients are undetermined. In addition, any particular solution of the governing equation may be also considered by adding the corresponding element value.

To enforce inter-element continuity and the external boundary conditions, two main strategies are generally adopted [178]: the use of an additional conforming element frame which leads to a hybrid formulation and a "frameless" approach using a least-squares procedure.

2.4.5.1 Hybrid Trefftz-element method (HT)

The concept of hybrid elements has been known for decades and used in conjunction with boundary integral formulations [131]. The idea of using T-complete functions seems to be due to Jirousek and Leon [179] and Jirousek [132].

In this approach, the unknown coefficients in the field variable expansion are related to the degrees of freedom (DOF) of the element via a conforming frame which is approximated in terms of the same DOF [178]. This approximation is done using conventional finite element polynomial interpolating functions defined in a local element coordinate system.

These interpolating functions may, as in classical finite elements, be of an arbitrary order [133]. For linear elements, for example, the frame functions are simply straight lines with a value 1 at the actual edge (corner) node and zero at the other one.

The most straightforward formulation is to relate the unknown coefficients with the nodal degrees of freedom by making stationary a suitable variational functional. This leads to a symmetric system of equations of the form $\mathbf{K}\mathbf{x} = \mathbf{b}$, where the integrations are carried out only along the boundaries of the element.

For elasticity problems, this relationship may be expressed in terms of the nodal displacement (HT-D) or by means of a traction frame (HT-T) [178]. The former is the best known and most applied [137].

An important aspect of the hybrid Trefftz method is that it may be readily combined with p-adaptive techniques [135], i.e., the possibility of including an arbitrary number of DOF associated to fictitious mid side nodes. This enables one to maintain both the mesh and the number of real nodes, thus circumventing the problems associated with the systematic remeshing procedures.

In comparison to conventional finite element p-adaptive models, the *HT p-elements* have the following principal advantages [180]:

(a) geometry flexibility associated with the FE method.

(b) the ability to provide T-elements with equal ease for C^0 and C^1 conformity problems.

(c) the possibility of accurately representing local effects without mesh adjustments.

(d) the capacity to handle various singularities or high gradient solutions without mesh refinement.

On the other hand, since the inter-element continuity is enforced by a polynomial interpolation, the actual accuracy of the method will be still limited to the accuracy of this functions to model the wave spatial (and possibly temporal) variation.

It should be noted also, that in order to implement non-reflective (radiating) boundary conditions in unbounded domains, this method suffers from the same drawbacks associated to classical FE models. That is, the infinite domain is truncated by an artificial boundary. A suitable boundary condition scheme (local, global or by infinite elements, see section 2.5) must then be implemented.

2.4.5.2 Least-squares frameless T-elements (LST)

As in the HT element approach, a set of homogeneous solutions of the governing equation is used to approximate the field variable in each subdomain. In the least square formulation, however, the vector of undetermined solution coefficients in each subdomain is independently used to conform the final linear system of equations [134]. That is, these coefficients represent the DOF in each subdomain.

It follows that an adaptive *h-p* approach is obtained simply by refining the mesh and/or increasing the number of solutions in the respective subdomain sets. The *p*-convergence in particular, has shown to be much faster than the conventional FE *p*-version [137].

The boundary conditions and the inter-element continuity are enforced in the least-squares sense [136]. This is performed by minimising a suitable functional in terms of the required values (potential, velocity, etc.) on all the subdomain interfaces.

Since the Sommerfeld radiation condition

$$\lim_{r \to \infty} r^{(d-1)/2} \left(\frac{\partial p}{\partial r} - ikp \right) = 0, \tag{2.26}$$

is assumed to be satisfied *a priori*, it is not included in the functional. This gives the LST element method an important advantage over the HT approach for external wave problems [138].

On the other hand, a rather complicate element mesh is required in order to perform a standard direct assembly process. This problem was circumvented by Monk and Wang [140], who investigated the use of Bessel functions and plane waves using an alternative least-square functional. The method suffers, however, from a large condition number (a drawback already pointed out in [138] in relation to the Bessel functions), rendering it less robust than standard finite elements.

2.4.6 Wave-based methods

Several methods in which the local basis are constructed using wave functions, have been recently proposed. Some of these schemes, as the GFD/WED method of

Caruthers *et al.* [7,152,156,157] and the Wave-based method (WBM) of Desmet *et al.* [164,165] are variants of the MFS and the boundary Trefftz methods, respectively. However, several techniques derived from the finite element formulation have also incorporated the use of wave functions in order to circumvent the approximation errors outlined in section 2.2.2.2. These include meshless methods [159–162] and "standard" Galerkin schemes [163].

The use of a conforming set of solutions in each element leads, as seen for the T-element methods, to a non-conforming global scheme. To enforce global conformity, a suitable alternative is to use a meshless approach, which can overcome the difficulties of the least-squares T-element method discussed in the previous section. The *Partition of Unity Finite Element Method* (PUFEM) of Melenk and Babuška [159,160] constructs a conforming basis from any function that have good local approximation properties [159,160]. Thus, for the solution of the Helmholtz equation, the use of plane waves have been proposed as a suitable option[4] [160]. This gives an important reduction in the number of degrees of freedom in comparison to the Galerkin, GLS and GFEM approaches for a similar accuracy.

More recently, Bouillard *et al.* [161,162] proposed an *Element-free Galerkin Method* (EFGM) for the Helmholtz equation, based on the formulation of Belytschko *et al.* [181]. The EFGM is as accurate as the Generalised Finite Element Method (GFEM) (see section 2.2.2.2) and can be applied equally well to non-uniform meshes. A comparison between the EFGM and the PUFEM has not yet been performed.

The use of plane waves used in combination to standard polynomial interpolation functions in a finite element formulation, has been recently investigated by Laghrouche and Bettess [163]. In the proposed approach, the potential at each node is expanded in terms of an arbitrary number of plane waves, i.e. each node has an arbitrary number of DOF. To enforce inter-element conformity, the wave functions are combined with standard piecewise polynomial functions.

---

[4] Hence, in this case the PUM may be regarded simply as a (MFS-type) variant of the frameless T-element method outlined above

The increase in the DOF per node has a negative effect on the dimension of the local element matrices and the quadrature integration rule. However, this drawbacks are apparently compensated by the displayed accuracy of the method. To implement the radiation boundary condition, Laghrouche and Bettess used a wave-envelope infinite element scheme, by enforcing the radiation condition on the plane wave functions at the boundary nodes.

The Green Function Discretisation Method (GFD) was first proposed by Caruthers *et al.* [7, 152], as a nearly bi-nodal optimal (2-3 points per wavelength) numerical tool for the solution of the Helmholtz equation. The GFD uses the minimum local energy combination of several point sources (Green's functions) in a finite difference procedure. That is, a solution at each discretisation point is sought in terms of the known values at the neighbouring nodes.

It is worth noting that the GFD may be regarded as a discrete field variant of the Method of Fundamental Solutions (MFS) outlined above. Indeed, the subdomain determined by each node and its neighbours may be regarded as a MFS domain in which the equation 2.25 can be applied. The source points are located outside the subdomain preventing any singular solution, whilst the collocation MFS points are the neighbouring points. This relationship between the GFD and the MFS was pointed out by French [153] and French *et al.* [154, 155], who showed the significant computational advantages of the GFD in comparison to conventional finite element methods.

The GFD was subsequently reformulated replacing the point sources with plane waves, resulting in the Wave Expansion Discretisation (WED) method [157]. The WED has been successfully applied to model a turbofan engine [156], and extended later to plate vibration analysis [158].

An assessment of the WED approach by Ruiz and Rice [182] showed that there are, however, some conditioning problems related to the implementation of the radiation boundary condition that need further investigation.

2.5 The exterior problem

The solution of problems involving propagating and evanescent waves in unbounded domains are related to a variety of physical phenomena, including acoustic, elastic and electromagnetic waves. In these cases, a constraint is required in the "infinite" domain to ensure that energy flux propagates in an outward direction. The Sommerfeld radiation condition [183] ensures that this is the case provided that

$$\lim_{r\to\infty} r^{(d-1)/2}\left(\frac{\partial p}{\partial r} - ikp\right) = 0, \tag{2.27}$$

where d is the dimension of the problem.

Numerical solutions to the wave equation in exterior domains have been sought primarily via techniques that are based on the Helmholtz integral equation, known as BEM [79]. These techniques have the benefit of *a priori* satisfaction of equation 2.27, and the (dubious) advantage of seeking solutions over a domain that is one-dimension lower than the original form of the problem.

The most straightforward BEM formulation (i.e. the direct BEM) gives non-unique solutions at discrete eigenfrequencies of an associated but physically unrelated Dirichlet interior problem. It can be modified, however, to produce unique solutions at the expense of adding auxiliary points in the interior region [82], or by the use of higher-order derivatives of the kernel functions [85] (see Section 2.3).

Alternatively, domain-based schemes such as finite differences or finite elements may be implemented over a truncated (finite) domain close to the radiating source or body [184]. Conditions must then be imposed on the boundary to ensure than the acoustic energy is absorbed, thus avoiding spurious reflections back into the finite domain.

Significant research efforts have been made in the last three decades in order to obtain accurate and efficient radiation conditions for both time-harmonic and transient problems (see e.g., references [185, 186]). These 'approximate' conditions can be classified into two broad categories: global and local.

The global boundary conditions [187–189], attempt to simulate the effect of the exterior in an exact sense and are fully coupled in space and time. Though this methods lead to a symmetric well-conditioned FE matrix, the artificial boundary must be of a geometrically simple shape. Furthermore, in some important cases, an exact external mapping condition may be not available or is impractical to implement.

Local boundary conditions on the other hand, are local in space and time, and can be used on generally shaped domains. Their efficiency is measured in the capacity to absorb waves impinging on the artificial boundary. The simplest implementation of these type of boundary conditions, is to use the specific acoustic impedance of freely propagating plane waves (PW damper) at the artificial boundary given by

$$p(\mathbf{x}) = \rho_0 c u_n(\mathbf{x}), \tag{2.28}$$

where p is the acoustic pressure, u_n is the normal particle velocity at the boundary, ρ_0 is the specific fluid density and c is the sound speed. For this condition to give accurate results, the artificial boundary must be sufficiently distant from the source of perturbation.

To circumvent this difficulty, higher-order boundary damping elements may be used. In the pioneering work of Engquist and Majda [190], an asymptotic set of non-reflecting conditions were formulated with the help of pseudo differential operators. Their use in conventional finite element and finite difference methods is, however, severely limited by the implementation of high-order derivatives occurring in the high-order boundary conditions. Moreover, in the simplest implementation form, they lead to a non-symmetric and ill-conditioned FE scheme.

Several other techniques have been devised based on the formulation of Engquist and Majda (see e.g., references [191–195]), and by the use of "localised" global conditions [196, 197]. Though the philosophy behind these schemes might be different, the major drawback associated to the Engquist and Majda conditions remains unsolved.

A number of different high-order NRBC methods without high-order derivatives have been recently reported in the literature. Guddati and Tassoulas [198] proposed a conditioning scheme by using a continued fraction expansion based on the original sequence of Engquist and Majda. More recently, Givoli and Patlashenko [199] proposed yet another NRBC scheme by means of an "optimal" local approximation of the exact non-local conditions. A thorough comparison of these techniques has not yet been reported.

The use of boundary integrals (BI) as a mesh termination scheme for finite elements methods has been also investigated. Muğen and Hulbert [200, 201] proposed an off-source FE/BI scheme based on the earlier work of Cunefare *et. al.* [202]. Since the system matrices retain the sparsity of the FE method, an important reduction in the computational storage cost results in comparison with the classical BEM.

A more radical approach to domain-based techniques is given by the infinite element concept [203]. In this method, the near field of the radiating source or body is modelled by using conventional finite element techniques *only*. A single layer of special elements, *infinite elements*, which stretch to infinity are then used to model the acoustic far field.

The infinite elements were originally formulated as a standard (finite element) shape functions multiplied by a decay function and an oscillatory wave function of the form e^{-ikr}. A local mapped (infinite) element was subsequently developed to obtain a more accurate representation of the radial wave decay.

In these infinite elements formulations, special numerical integration techniques have to be used in order to deal with the complex exponential integrand of the system matrices. The wave-envelope (WE) method [204] and more recently the mapped WE method [205, 206] circumvent this problem by utilising the complex conjugate of the shape function as the weighting function in a Petrov-Galerkin scheme, thus cancelling all oscillatory terms in the integrand.

Though the mapped WE method show a good radial accuracy, a loss in the resolution has been observed between the transverse and radial resolution for three dimensional problems as the frequency increases [207].

Chadwick *et.al.* [208] analysed an iterative infinite element method for short waves.

They modelled the wave envelope and phase rather than the velocity potential, using assumed radial and angle variations for the wave envelope and the phase. Even though more research still needs to be done on this technique, the results obtained for a typical two dimensional problem are promising.

The extension of the infinite element concept to elastodynamics applications has been proposed by several authors (see e.g. references [209, 210]). Most of these schemes are based on approximations of the displacement motion. Pinto and Coyette [211] proposed a conjugated infinite element scheme based on the nature of the elastic wave propagation, using the Stokes-Helmholtz decomposition of the governing equation in terms of dilatational and equivoluminal waves. Two interpolating functions are then used to model the wave amplitudes, the angular displacement and the phase variation. The results obtained for two dimensional examples show that the accuracy of this method is comparable to that of Givoli's DtN non-local boundary condition.

2.6 Discussion

In the BEM only the surface of the domain has to be modelled and discretized. Thus, the dimension of the problem is reduced by one. In addition, the Sommerfeld radiation condition is naturally satisfied by the fundamental Green's function. Based on these two properties, several authors refer to the BEM as the method of choice for wave modelling in exterior or unbounded domains [79, 89].

However, a more detailed analysis shows that less discretisation points does not necessarily means an overall computational advantage. Harari and Hughes [212] demonstrated that, in comparison with the FEM for interior and exterior acoustic problems, there is *no clear computational advantage* in the BEM approach.

On the other hand, it is widely known that the performance of the finite element approach severely deteriorates as the frequency increases. In a recent review of the FEM for short wave modelling problems, Zienkiewicz [3] pointed out that "Clearly, we can consider that this problem remains *unsolved* and a completely new method of approximation is needed to deal with the very short-wave solutions".

That is the idea behind the new alternative approaches, i.e. the use of (more physically related) basis functions that can accurately represent the wave behaviour for any frequency, thus reducing the number of discretisation points. In this sense, the GFD/WED method proposed by Caruthers *et al.* [7,152] is currently the most accurate method, with a nearly optimal (in the Nyquist sense [213]) bi-nodal resolution. The approach developed by Laghrouche and Bettess [163], though only applied to simple academic problems, shows also a good accuracy, of around four points per wavelength.

As seen with the boundary element method, however, there are several other important aspects in these formulations that have to be addressed:

- Is the method easily applicable?
- Does it give the same accuracy in 2D and 3D?
- Can it be applied to complex geometries?
- What are the completeness and convergence characteristics of the method?
- Are the matrices sparse and well conditioned?
- Can the method be made robust and stable?
- Can the radiation boundary condition be naturally satisfied?
- Can the method be generalised to other applications?

The best modelling approach will result from that which gives *the best possible combination* of these requirements, providing at the same time a high degree of accuracy.

It should be noted also that, giving the oscillating nature of the waves, the solution of large problems and/or sufficiently higher frequencies will require eventually (even for an 'ideal' method) an iterative (possible parallel) solution scheme as those discussed in Section 2.2.2.3. Hence, a last important feature of the 'ideal' method is that it can be implemented iteratively and in parallel platforms with relative facility.

2.7 Scope of the thesis

The major difficulty in the development of alternative numerical techniques, is to obtain not only an accurate approach, but also one that performs equally well in the other aspects of the implementation process. The overall performance will eventually determine the practical efficiency of a given method. In this framework, the wave expansion discretisation technique is, among the recently proposed methods, one of the most promising.

In order to determine whether the WED method may be considered as an efficient alternative technique, further research is required to assess not only the accuracy of the method but also the different aspects of the implementation process. This is the aim of the analysis presented in this thesis. Throughout the discussion of its methodology and its applications for two- and three-dimensional problems, it will become apparent that this technique provides an adequate way to comply with the challenge of extending the applicability of numerical modelling techniques towards higher frequencies.

Chapter 3

The Green's function discretisation and wave expansion discretisation methods in acoustic fields

3.1 Introduction

The Green's Function Discretisation (GFD) method was first proposed by Caruthers *et al.* [7, 152] as a discrete domain Green's function interpolation method with a minimum L^2 property and naturally applicable to non-uniform grids. For radiation problems, they obtained accurate solutions with less than three points per wavelength.

Plane waves were suggested in [152] as a viable alternative to the Green's functions, and used later for modelling inlet turbofan noise subjected to a Mach 0.4 flow [156]. The resulting approach was then called the Wave Expansion Discretisation (WED) method, showing a similar accuracy as the GFD [157].

The methodology of the GFD and WED schemes is detailed below. The fundamental formulation given in references [7, 152] is quite straightforward, and it is included here for completeness.

3.2 Physical and mathematical basis

3.2.1 Problem definition

The propagation of acoustic waves in homogeneous media without losses, is governed by the wave equation

$$\nabla^2 p = \frac{1}{c^2}\frac{\partial^2 p}{\partial t^2}, \tag{3.1}$$

where ∇^2 is the Laplace operator, $p(\mathbf{x}, t)$ is the acoustic pressure at a position vector $\mathbf{x}$ and time t, and c is the sonic speed.

Assuming a steady-state time harmonic excitation source $p = p(\mathbf{x}, \omega)$, where $\omega = 2\pi f$ is the circular frequency. Equation 3.1 then reduces to the Helmholtz equation

$$\nabla^2 p + k^2 p = 0, \tag{3.2}$$

where $k = \omega/c$ is the wave number.

Consider solving equation 3.2 in an acoustic domain Ω_A with boundary surface $\Gamma_A = \Gamma_D \cup \Gamma_N \cup \Gamma_R$, as shown in figure 3.1.

At the boundary, the following conditions are assumed to apply, namely

- imposed pressure (Dirichlet boundary condition)

$$p(\mathbf{x}_b) = \overline{p}, \ \mathbf{x}_b \in \Gamma_D \tag{3.3}$$

- imposed normal velocity (Neumann boundary condition)

$$\frac{\partial p(\mathbf{x}_b)}{\partial \mathbf{n}} = \overline{q}, \ \mathbf{x}_b \in \Gamma_N \tag{3.4}$$

- imposed impedance (radiation or mixed boundary condition)

$$\frac{\partial p(\mathbf{x}_b)}{\partial \mathbf{n}} = -\iota \frac{\rho_0 \omega}{Z} p(\mathbf{x}_b) = -\iota \rho_0 \omega \mathbf{v}_n, \ \mathbf{x}_b \in \Gamma_R \tag{3.5}$$

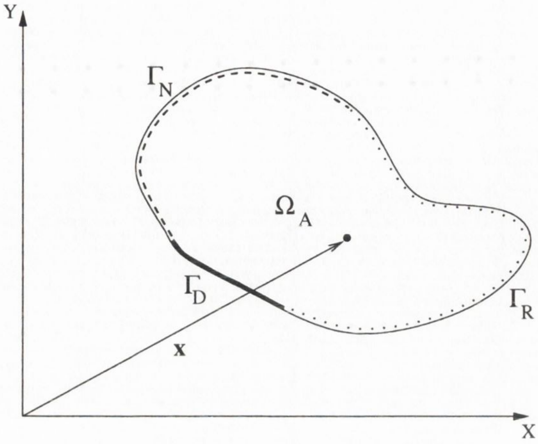

Figure 3.1: Illustration of the considered problem.

where $\mathbf{n}$ is the normal outward boundary, $\iota = \sqrt{-1}$, ρ_0 is the air density, and $\mathbf{v}_n$ and Z are the particle velocity and the specific acoustic impedance in the boundary outward normal direction, respectively.

We seek to solve the boundary value problem given by equations 3.2-3.5, by domain discretisation. That is, a finite number of points are selected, covering the domain. The value at each discrete point is obtained following a finite difference procedure, such that an approximation to the continuous solution surface is represented. Thus, the *unknown* field value at any point is determined in terms of the *known* values at the surrounding points in the domain. These values are approximated as a finite combination of fundamental solutions of the governing Helmholtz equation.

It will be shown in the subsequent sections, that such an interpolation procedure may be derived by a domain generalisation of the single layer potential integral equation [153]. Some authors [148], then refer to the GFD as a variant of the Method of Fundamental Solutions (MFS).

3.2.2 Discretisation of the single layer potential

Let $\hat{\Gamma}$ be an 'artificial' surface containing the physical domain Ω_A and surface Γ_A, as shown in figure 3.2. If there is no acoustic sources in Ω_A, the single layer potential

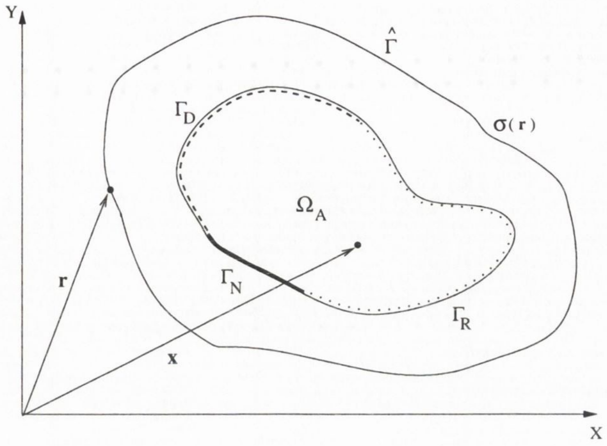

Figure 3.2: Original domain surrounded by an artificial surface $\hat{\Gamma}$.

theory states that the pressure at any interior point can be computed as the surface integral (over the volume) of the single layer potential with the free-field Green's function:

$$p(\mathbf{x}) = \int_{\hat{\Gamma}} G(\mathbf{x}, \mathbf{r})\sigma(\mathbf{r})\; d\Gamma_A,\;\; \mathbf{x} \in \Omega_A, \mathbf{r} \in \hat{\Gamma} \tag{3.6}$$

where $\sigma(\mathbf{r})$ is a continuous function defined over the surface $\hat{\Gamma}$, and

$$\begin{aligned} G(\mathbf{x}, \mathbf{r}) &= \frac{e^{-\iota k|\mathbf{x}-\mathbf{r}|}}{4\pi|\mathbf{x}-\mathbf{r}|},\;\; 3-D \\ &= \frac{\iota}{4} H_o^{(2)}(k|\mathbf{x}-\mathbf{r}|),\;\; 2-D \end{aligned} \tag{3.7}$$

is the Green's kernel function which relates the pressure at a domain point $\mathbf{x}$ produced by a unit monopole source located at the surface point $\mathbf{r}$ in $\hat{\Gamma}$.

Note that equation 3.6 is non-singular in the physical domain Ω_A. Thus, we may use a standard quadrature rule with nodes $\{\mathbf{r}_j\}_{j=1}^{n}$ and weights $\{w_j\}_{j=1}^{n}$ to approximate $p(\mathbf{x})$ giving

$$p(\mathbf{x}) = \int_{\hat{\Gamma}} G(\mathbf{x}, \mathbf{r})\sigma(\mathbf{r}) \simeq \tilde{p}_n(\mathbf{x}) = \sum_{j=1}^{n} [w_j \sigma(\mathbf{r}_j)] G(\mathbf{x}, \mathbf{r_j}). \tag{3.8}$$

Equation 3.8 may be written simply as

$$\tilde{p}_n(\mathbf{x}) = \sum_{j=1}^{n} c_j G(\mathbf{x}, \mathbf{r_j}). \tag{3.9}$$

In general, $\tilde{p}_n$ will not satisfy the boundary conditions, equations 3.3-3.5, imposed on Γ_A. Hence, the coefficients $\{c_j\}_{j=1}^{n}$ need to be chosen to satisfy the boundary condition in some sense. For any problem for which the Green's function $G(\mathbf{x}, \mathbf{r})$ is a fundamental solution, this procedure can be viewed as a discrete simple layer potential method. The representation 3.9 is usually referred to as the Method of Fundamental Solutions (MFS) [148].

In the MFS, the coefficients $\{c_j\}_1^n$ are usually obtained by a collocation procedure. That is, n points $\{\mathbf{x}_k\}_{k=1}^{n}$ are selected on Γ_A and set

$$\mathcal{G}(\mathbf{x}_k) = \begin{cases} p(\mathbf{x}_k)|_{\Gamma_D} = \overline{p}_k, & 1 \leq k \leq m, \\ \partial p(\mathbf{x}_k)/\partial \mathbf{n}|_{\Gamma_N} = \overline{q}_k, & m+1 \leq k \leq n-m, \\ \partial p(\mathbf{x}_k)/\partial \mathbf{n}|_{\Gamma_R} = -\iota \rho_0 \omega u(\mathbf{x}_k), & n-m+1 \leq k \leq n. \end{cases} \quad (3.10)$$

The geometry of the discretized model is shown in figure 3.3

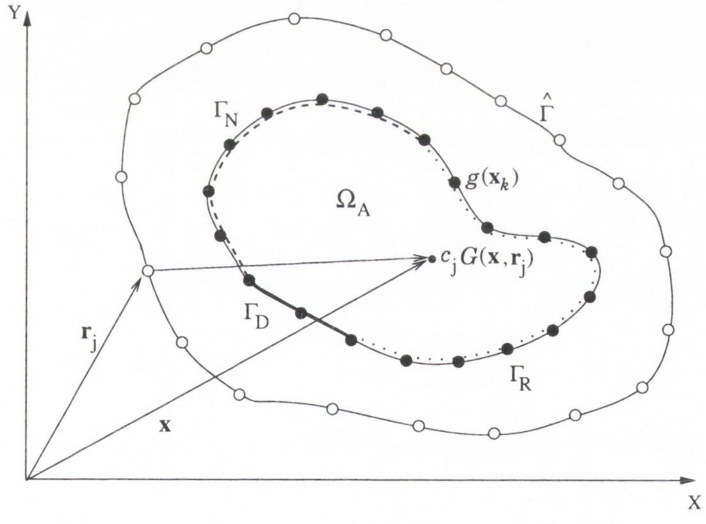

Figure 3.3: Illustration of the MFS concept.

Following this procedure, we obtain n equations

$$\sum_{j=1}^{n} c_j G(\mathbf{x}_k, \mathbf{r}_j) = \mathcal{G}(\mathbf{x}_k), \; 1 \leq k \leq n, \quad (3.11)$$

for the determination of the unknown coefficients. Once these coefficients have been determined, the approximated solution is obtained from equation 3.9.

3.2.3 Generalisation of the concept to the full domain

The fundamental concept of the MFS outlined in the precedent section, is to express the unknown field variable at any point in the domain, in terms of the known values of the field variable at discrete points in the surface of the continuum.

Consider a discretisation of Ω_A by a finite number of points which may not, in general, be uniformly distributed. A computational cell can then be determined considering each node and its neighbours, as shown in figure 3.4.

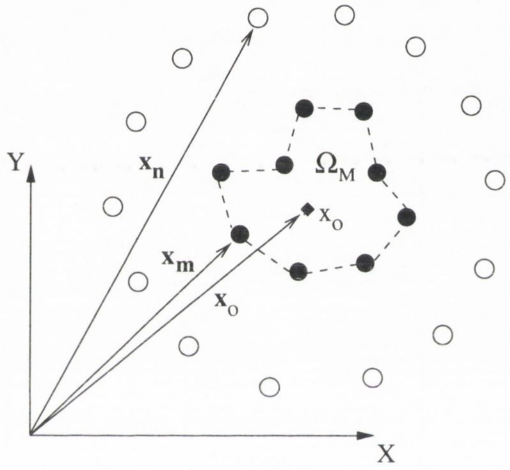

Figure 3.4: Computational molecule.

A similar procedure as described in the precedent section may be applied to the sub-domain Ω_M conformed by x_0 and its neighbouring points (see figure 3.4). That is, the value at x_0 may be approximated as the sum of N monopole sources located outside Ω_M as

$$p(\mathbf{x}_0) = \sum_{n=1}^{N} \gamma_n G(\mathbf{x}_0, \mathbf{x}_n), \tag{3.12}$$

where $G(\mathbf{x}_0, \mathbf{x}_n)$ is the Green's function given in equation 3.7, and $\{\gamma_n\}_{n=1}^{N}$ are the source strengths.

Following the same procedure at the other points in the cell, we obtain

$$p(\mathbf{x_m}) = \sum_{n=1}^{N} \gamma_n G(\mathbf{x}_m, \mathbf{x}_n), \; m = 1, \ldots, M. \tag{3.13}$$

Using matrix notation,

$$\mathbf{p} = \mathbf{G}\boldsymbol{\gamma} \tag{3.14}$$

where $\mathbf{p}$ and $\boldsymbol{\gamma}$ are $M \times 1$ and $N \times 1$ matrices, respectively, and $\mathbf{G} = G(\mathbf{x}_m, \mathbf{x}_n)$ is a $M \times N$ matrix. Solving equation 3.14 for the coefficients $\{\gamma_n\}_{n=1}^{N}$ we obtain the approximate pressure at $\mathbf{x}_0$ from equation 3.12.

3.2.3.1 Minimum norm solution

If the number of hypothetical point sources equals the number of surrounding points in the cell ($N = M$), then

$$\boldsymbol{\gamma} = \mathbf{G}^{-1}\mathbf{p} \tag{3.15}$$

gives the *only* solution for $\boldsymbol{\gamma}$ which match the M values at $\mathbf{r}_m$. However, $\mathbf{G}$ does not necessarily have to be a square matrix, and it may be beneficial to under-constrain the system, i.e. $N > M$. The rectangular system may have, in general, dependent rows and dependent columns which make the solution for $\boldsymbol{\gamma}$ not unique.

The matrix $\mathbf{G}$ can then be "pseudo-inverted" in order to obtain, among the infinite possible solutions for $\boldsymbol{\gamma}$, the (unique) *optimal* one for which $\sum_{n=1}^{N} \gamma_n^2$ is a minimum. It may be shown [214], that the optimal solution $\boldsymbol{\gamma}_{opt}$ has always M non-zero entries (i.e. it always lies in the row space of $\mathbf{G}$). The remaining $N - M$ components, called the "null space" are zero, thus rendering $\boldsymbol{\gamma}_{opt}$ the minimum vector length[1].

As pointed out by Caruthers [152], the pseudo-inverse operation imposes a smoothness condition on $\boldsymbol{\gamma}$, excluding those solutions with high amplitudes and irregular variations from source to source. Noting that the energy of a spherical acoustic wave is given by [1]

$$\Pi = \frac{4\pi R^2 \gamma^2}{2\rho_0 c}, \tag{3.16}$$

where R is the radial distance from the source, the pseudo-inversion then ensures that:

---

[1] For a more rigorous analysis on the algebraic properties of the generalised inverses, the reader is referred to references [215, 216].

- All the constraints are satisfied exactly.
- The least "energetic" solution otherwise results.

There are a number of different procedures which may be followed to obtain the minimal length solution to a rectangular system. The most popular approach is based on the Singular Value Decomposition (SVD) of the matrix **G** as

$$\mathbf{G} = \mathbf{Q_1 \Sigma Q_2^T}, \tag{3.17}$$

where $\mathbf{Q}_1$ and $\mathbf{Q}_2$ are any two orthogonal matrices of dimension $M \times M$ and the $\sigma_1, \ldots, \sigma_r$ (r = rank $\mathbf{G}$) nonnegative entries in the $M \times N$ diagonal matrix $\mathbf{\Sigma}$ are the singular values of **G**.

The pseudo-inverse of **G**, denoted by the '+' sign is then given by

$$\mathbf{G}^+ = \mathbf{Q_2 \Sigma^+ Q_1^T}, \tag{3.18}$$

where the pseudo-inverse $\mathbf{\Sigma}^+$ has components $1/\sigma_1, \ldots, 1/\sigma_r$.

The pseudo-inverse may be also calculated using a complete orthogonal factorisation of **G** followed by a least squares solution of $min\{||\mathbf{p} - \mathbf{G}\boldsymbol{\gamma}||\}$ [217]. The main advantage of these two approaches, resides in their robustness and applicability to badly conditioned systems. On the other hand, these processes require a fair level of computation time[2]. As shown in table 3.1, for a 4 times increase in the size of the matrix, the computation time of the pseudo-inverse using the SVD decomposition increases 12 times.

Once the pseudo-inverse has been calculated, the solution for the coefficients $\boldsymbol{\gamma}$ (equation 3.14) yields

$$\boldsymbol{\gamma} = \mathbf{G}^+\mathbf{p}. \tag{3.19}$$

---

[2] An alternative method based on an approach originally proposed by Greville has been recently assessed by Layton [218]. Despite the fact that the computation of the pseudo-inverse is much quicker in comparison to the SVD based approach, the method is not applicable to badly conditioned systems.

Size ($m \times n$)	CPU time (s)
8× 25	0.01
16× 25	0.02
27× 60	0.08
32× 60	0.12

Table 3.1: Typical computation time for rectangular matrices of different size, using SVD decomposition.

Letting $\mathbf{g}$ represent the column vector with elements $\mathbf{g}_n(\mathbf{x}) = G(\mathbf{x}_0, \mathbf{x}_n)$, then

$$p_0 = \mathbf{g}^T \mathbf{G}^+ \mathbf{p}, \tag{3.20}$$

where $p_0 = p(\mathbf{x}_0)$.

Expression 3.20 is referred to as the Green's Function Discretisation method (GFD) [152]. It relates the unknown pressure at a given point in the domain in terms of the known pressure values at a finite number of surrounding points.

Given the properties of the pseudo-inversion, boundary conditions may be implemented by augmenting the row count of the matrix $\mathbf{G}$ in equation 3.14, including the possibility of multiple restraints as will occur at mesh corners. Boundary conditions related to the normal derivatives of the pressure (i.e. Neumann or radiation) at cell points $\{p_k\}_{k=1}^{M}$ can be readily computed by taking the normal derivative of the constraint equation 3.14

$$\frac{\partial p_k}{\partial \mathbf{n}} = \frac{\partial \mathbf{G}_{kn}}{\partial \mathbf{n}} \gamma, \ 1 \leq k \leq m. \tag{3.21}$$

Equation 3.14 thus take the form

$$\left\{ \begin{array}{c} \mathbf{p} \\ \partial p_k / \partial \mathbf{n} \end{array} \right\} = \left\{ \begin{array}{c} \mathbf{G} \\ \partial \mathbf{G}_{kn} / \partial \mathbf{n} \end{array} \right\} \gamma = \mathbf{G}_{aug} \gamma. \tag{3.22}$$

Thus, the interpolating formula so obtained is not only an exact solution of the continuum equation at all neighbouring points, but *also* satisfies the boundary condition at up to $N - M$ discrete points along the boundary in the neighbourhood of the subject point.

After pseudo-inversion, the augmented matrix $\mathbf{G}_{aug}$ may be partitioned into $(\mathbf{G}^+_{aug})_L$ and $(\mathbf{G}^+_{aug})_R$. Then, a modified template (equation 3.20) with a forcing right hand side may be established as

$$p_0 - \mathbf{g}(\mathbf{G}^+_{aug})_L\mathbf{u} = \mathbf{g}(\mathbf{G}^+_{aug})_R \; \partial p_k/\partial \mathbf{n}. \tag{3.23}$$

In addition, Dirichlet constraints may be directly imposed on the appropriate degrees of freedom in the overall assembled stiffness matrix. Once the templates are formed, an overall sparse non-symmetric complex equation system

$$\mathbf{Kp} = \mathbf{f} \tag{3.24}$$

may be assembled with each template independently contributing a row.

3.2.3.2 The use of plane waves

In theory, any complete solution of the governing equation may be used to interpolate the desired field variable. A drawback associated to the use of Green's functions, is that a location for each monopole source has to be determined a priori. Furthermore, for acoustic problems in which the coefficients of the governing equation have a spatial dependency, as will occur in the propagation of acoustic waves within inhomogeneous flows, it is not possible to determine a single universally valid free space Green's function [156].

To circumvent some of these shortcomings, the infinite radial approximation of the Green's function, i.e. planes waves, may be used. The formulation is otherwise completely analogous to that outlined above for the GFD scheme. The pressure at the central point in the cell, may thus be approximated as a combination of plane waves

$$p(\mathbf{x}_0) = \sum_{n=1}^{N} \gamma_n e^{-\imath k \mathbf{d}_n \cdot \mathbf{x}_0}, \tag{3.25}$$

where $\mathbf{d}_n$ is the unit propagation direction vector of the n^{th} plane wave with complex amplitude γ_n. An illustration of the pressure field approximated by 8 plane waves is given in figure 3.5.

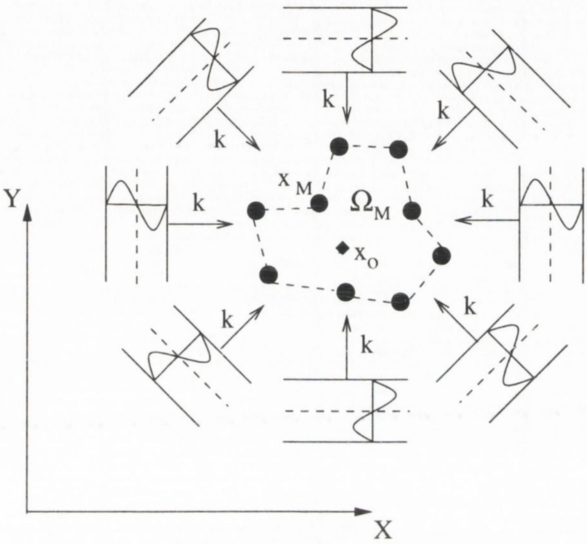

Figure 3.5: Sound field approximated by 8 plane waves.

Using matrix notation we may then write equation 3.25 as

$$p_0 = \mathbf{h}(\mathbf{x}_0)\boldsymbol{\gamma}, \tag{3.26}$$

where $p_0 = p(\mathbf{x}_0)$, $\mathbf{h}(\mathbf{x}_0)$ is a $1 \times N$ row vector of plane wave functions evaluated at $\mathbf{x}_0$ and $\boldsymbol{\gamma}$ is a column vector of the wave strengths. If we apply the same approximation to the other nodal positions in the cell we can write

$$\mathbf{p} = \mathbf{H}\boldsymbol{\gamma}, \tag{3.27}$$

where $\mathbf{p}$ is a $N \times 1$ vector of the pressures at each surrounding node $\{\mathbf{x}_m\}_{m=1}^{M}$, and

$$H_{mn} = e^{-\imath k \mathbf{d}_n \cdot \mathbf{x}_m}. \tag{3.28}$$

A computational template may then be formed by combining equation 3.26 and 3.27 to give

$$p_0 = \mathbf{h}\mathbf{H}^{+}\mathbf{p} \tag{3.29}$$

Equation 3.29 is referred to as the Wave Expansion Discretisation (WED) method [156].

3.3 Accuracy assessment

Following a similar procedure as described by Caruthers *et al.* [7,152] for the GFD approach, the convergence and conditioning of the wave expansion discretisation method for two- and three-dimensional acoustic problems is evaluated below.

3.3.1 Two dimensional interpolation

Consider a nine node square computational molecule of dimension $2h \times 2h$ immersed in a 2D acoustic domain as shown in figure 3.6. The acoustic field is produced by a monopole source located at radial distance $5h$ and 15^0 elevation angle from the central node in the cell. If $\mathbf{x}_S$ is the source position vector, the pressure at any field

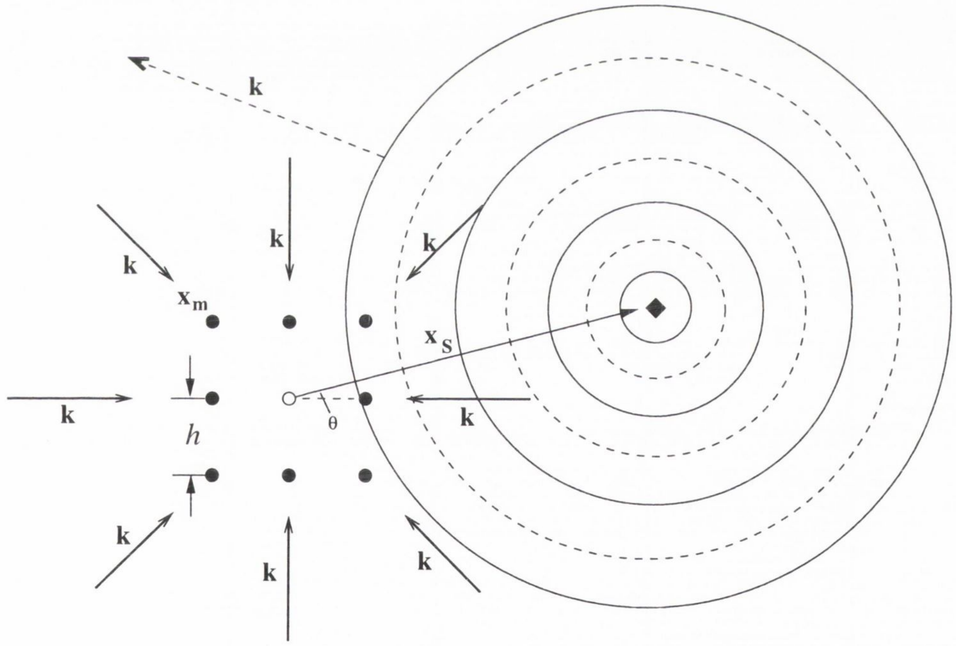

Figure 3.6: A 2D square molecule subjected to an acoustic monopole source field.

point $\mathbf{x} \neq \mathbf{x}_S$ is given by

$$P(\mathbf{x}) = \frac{\imath}{4} H_0^{(2)}(k|\mathbf{x} - \mathbf{x}_S|), \tag{3.30}$$

where $H_0^{(2)}$ is the zero-order Hankel function of the second kind. For convenience, consider the wave number normalised to the nodal spacing length h, that is $k = \omega h/c$.

The values at the $\mathbf{x}_m$ neighbouring points in the cell were fixed according to equation 3.30, whilst the pressure at the central point $p(\mathbf{x}_0)$ was determined using equation 3.29. The error at $\mathbf{x}_0$ was thus calculated according to

$$E = p(\mathbf{x}_0) - P(\mathbf{x}_0), \tag{3.31}$$

where $P(\mathbf{x}_0)$ was calculated from equation 3.30.

The pressure at the central point was approximated by a combination of 20 plane waves, evaluating two different cases: (a) the fundamental solutions are uniformly distributed around the cell and (b) the sources are located only in certain regions of the space.

Uniform source distribution

The amplitude error and phase error normalised by the point spacing h at the central point in the cell, are plotted in figure 3.7.

Despite the fact that the acoustic field is clearly not planar at the central point, the use of a plane wave interpolation scheme gives a very good result. The singularity observed occurs at the first eigenvalue, $k_{1,1} = \pi/\sqrt{2}$, of the Dirichlet problem within the computational cell ($2h \times 2h$), where (see, e.g. [1, chapter 9])

$$k_{l,m} = \left[\left(\frac{\pi}{2h}\right)^2 + \left(\frac{\pi}{2h}\right)^2\right]^{1/2}. \tag{3.32}$$

This frequency is that of a plane wave with a wavelength equal to the diagonal length of the cell. It corresponds to the bi-nodal wavelength limit, according to the Nyquist theory of digital signal processing (see e.g. [213]). In this sense, the wave expansion interpolation method (as observed for the GFD [152]), has an optimal accuracy and actually exceeds the Nyquist limit for rectangular cell arrangements [152].

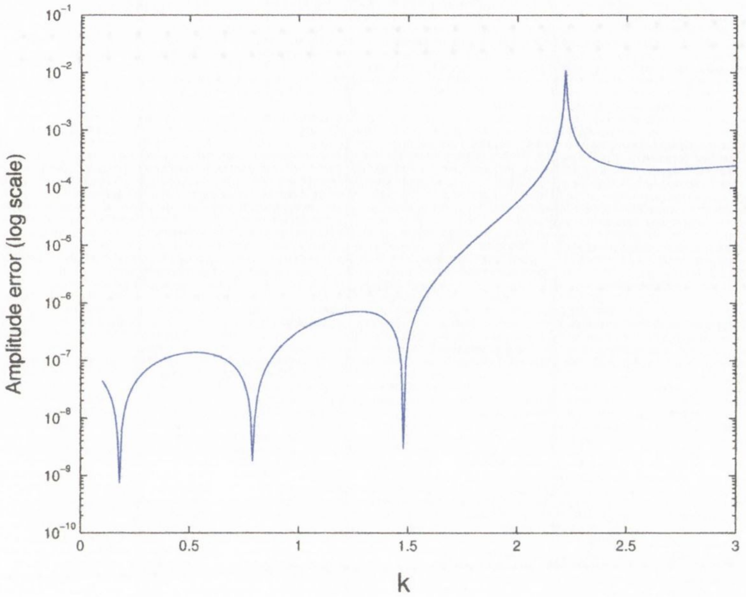

(a)

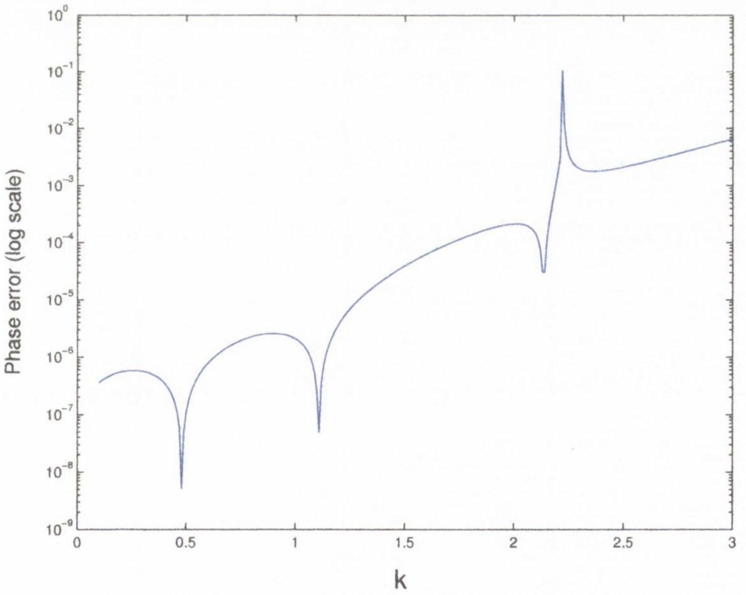

(b)

Figure 3.7: Error for the WED method at the central point. (a) Amplitude error. (b) Phase error.

For comparison purposes, the problem was solved with a standard Galerkin finite element scheme (an illustration of the formulation of the finite element in acoustics, is given in the Appendix A). In this method, the acoustic field inside the element is interpolated by a polynomial function, known as shape function. The order of the interpolating polynomial function may be arbitrary, and is determined by the number of nodes in the element. For this example, a higher-order quadratic Lagrangian element with 9 nodes was used.

The error obtained using the FE approach is depicted in figure 3.8. In comparison to the accuracy of the wave expansion interpolation, the error difference even for small values of k is very significant.

Non uniform source distribution

In principle, there is no a priori requirement in relation to the location of the sources. Since the pseudo-inversion process will select the optimal solution for any given set, restricting the location of the fundamental solutions to a particular region will exclude others which may have a lesser norm.

Consider the plane wave expansion approximation at the central point in the cell, equation 3.25. For two-dimensional problems, we may write

$$p(\mathbf{x}_0) = \sum_{n=1}^{N} \gamma_n e^{-\imath k \mathbf{d}_n \cdot \mathbf{x}_0} = \sum_{n=1}^{N} \gamma_n e^{-\imath k (x_0 \cos\theta_n + y_0 \sin\theta_n)},$$

where θ_n is the propagation angle of the n^{th} directional vector $\mathbf{d}_n$.

In order to investigate the effect of the spatial distribution of the plane waves on the accuracy of the method, three non-uniform vector distribution sets were used. Namely,

- Case 1: $0 \leq \theta_n \leq \pi,\ n = 1, \ldots, N.$
- Case 2: $\pi \leq \theta_n \leq 2\pi,\ n = 1, \ldots, N.$
- Case 3: $\begin{cases} 0 \leq \theta_n \leq \pi/4, & n = 1, \ldots, N/2 \\ 5\pi/4 \leq \theta_n \leq 3\pi/2 & n = N/2+1, \ldots, N. \end{cases}$

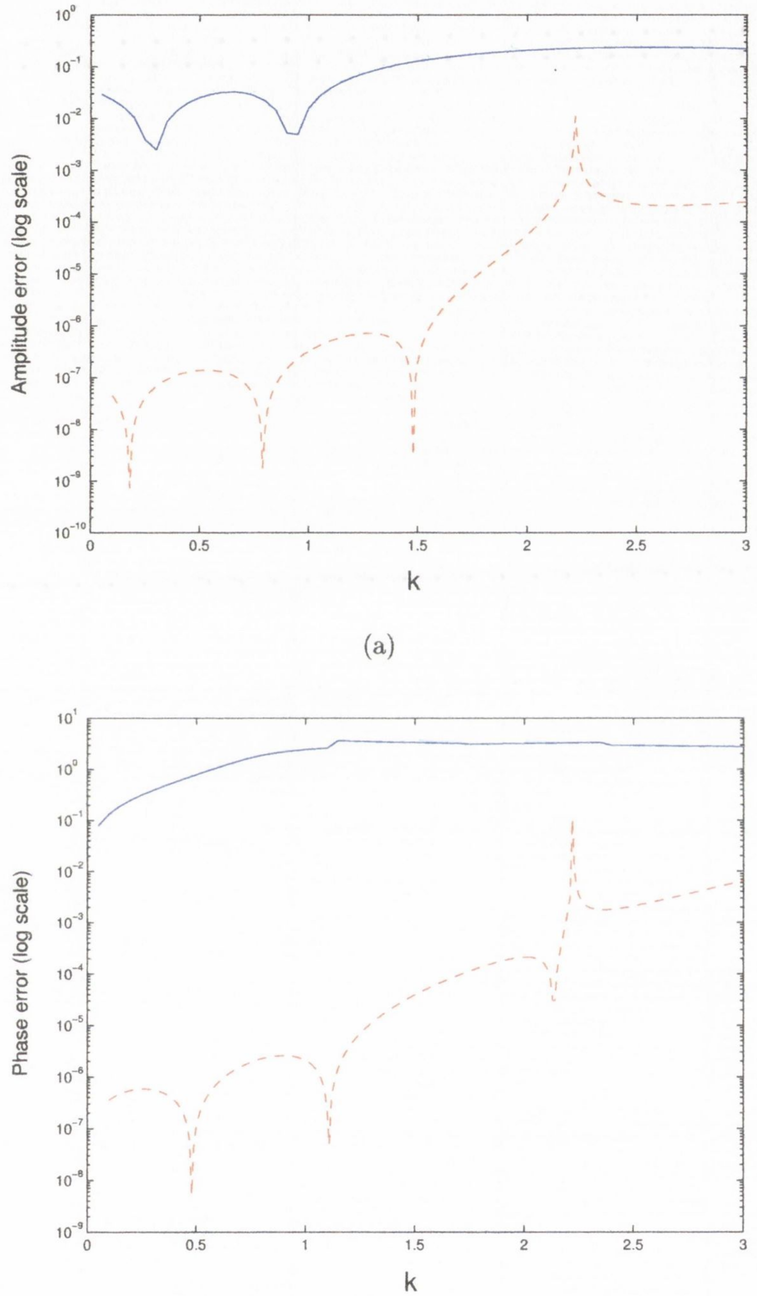

(a)

(b)

Figure 3.8: Error comparison for a nine noded Lagrangian FE method vs. the WED method at the central point in the cell. — FEM, − − − WED.(a) Amplitude error. (b) Phase error.

- Case 4: $0 \leq \theta_n \leq 2\pi$, $n = 1, \ldots, N$ (uniform source distribution used in figure 3.7).

For illustration, the vector directions for the Cases 1 - 3 are depicted in figure 3.9. As shown in the relative error plotted in figure 3.10, in comparison to the results obtained using a uniform distribution (Case 4) the accuracy of the WED approach deteriorates in the three non-uniform distribution cases tested. Note that, according the location of the source, the directions used in the Case 1 ($0 \leq \theta_n \leq \pi$) should give the best results. However, the minimum error is found using the second set ($\pi \leq \theta_n \leq 2\pi$) despite some of this directions are in the opposite direction as the propagating wave field.

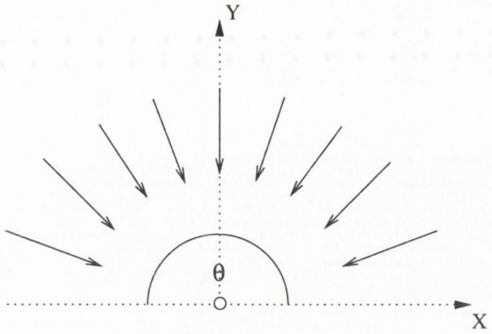

case 1

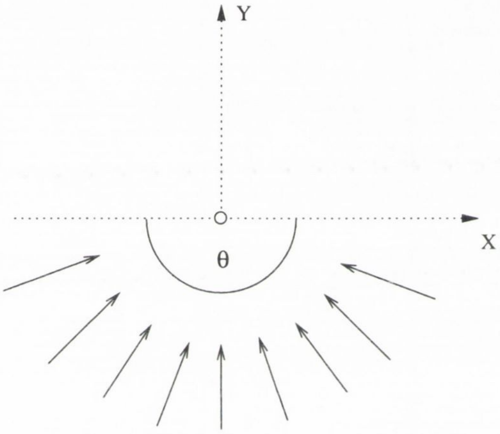

case 2

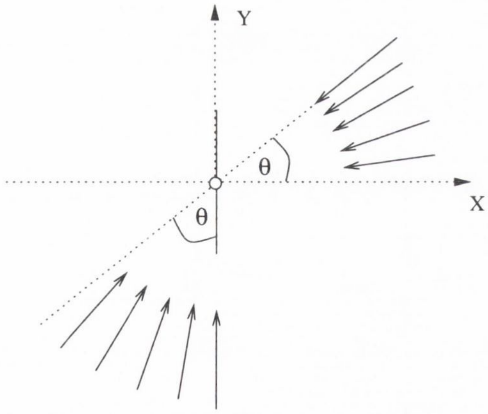

case 3

Figure 3.9: Illustration of the non-uniform directional sets.

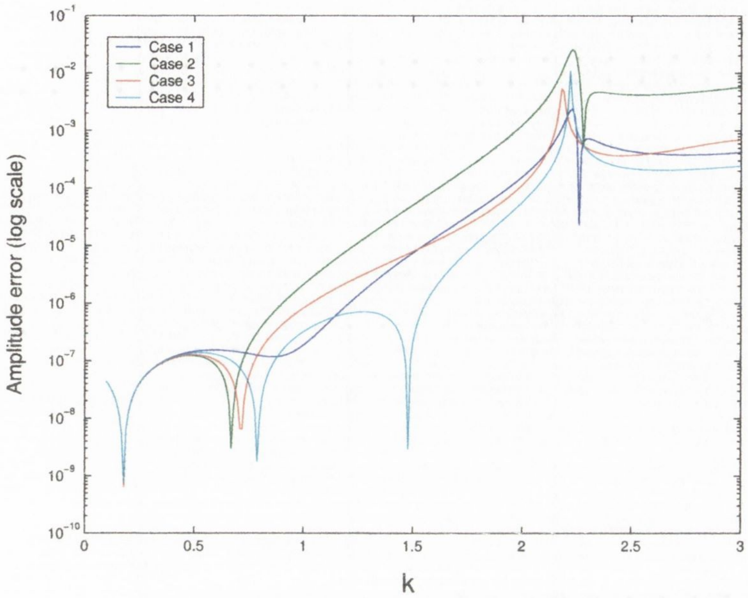

(a)

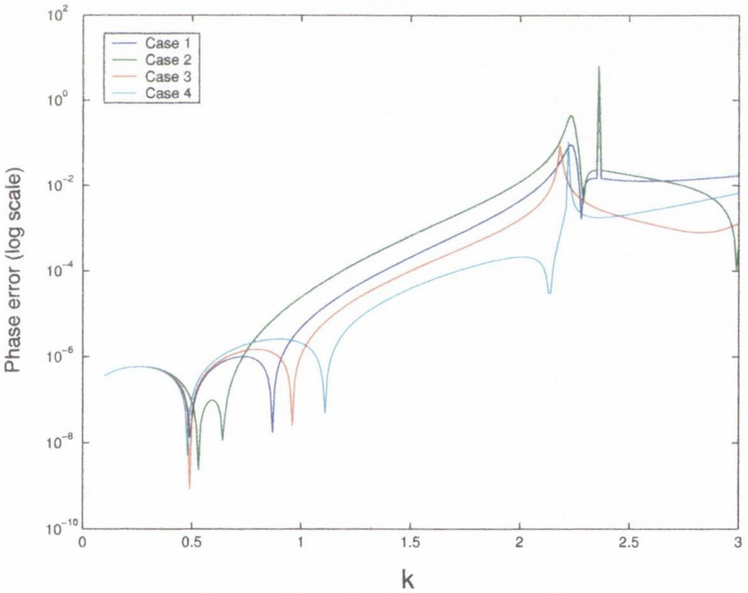

(b)

Figure 3.10: Error for the WED method at the central point for different plane wave distributions. (a) Amplitude error. (b) Phase error.

3.3.2 Three dimensional interpolation

The convergence properties of the plane wave interpolation in three dimensions, were evaluated considering a 27 node square computational cell, as shown in figure 3.11. The acoustic field was assumed to be produced by a monopole source located at radial distance $5h$ and 15^0 and 90^0 elevation and azimuthal angles, respectively.

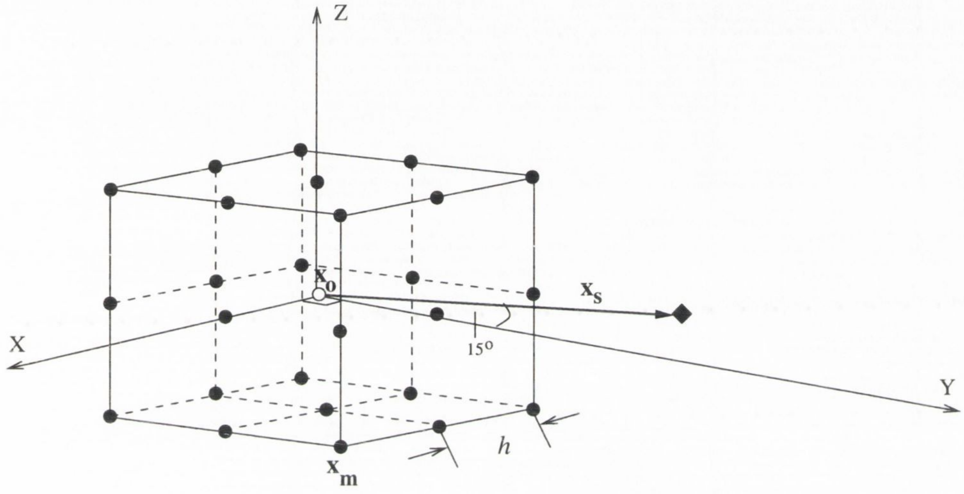

Figure 3.11: Three dimensional computational cell.

According to the results obtained for the two dimensional case, a combination of plane waves uniformly distributed around each cell point should be used in order to obtain the best approximation. However, whilst this restriction is easily achievable for two dimensional problems, a spherically symmetric distribution of plane waves is not possible for an arbitrary number of points [219, 220].

A best compromise to this problem is to use a direction set based on the Buckminster Fuller geodesic dome, as shown in figure 3.12. Thus 60 "evenly" spaced directions may be used (these directional vectors can be conveniently generated, for example, by using the ©Matlab function "bucky"). Following this approach, matrices **h** and **H** in equations 3.26 and 3.27, have dimensions 1×60 and 27×60, respectively.

The pressure values at the external points in the cell were fixed according to the

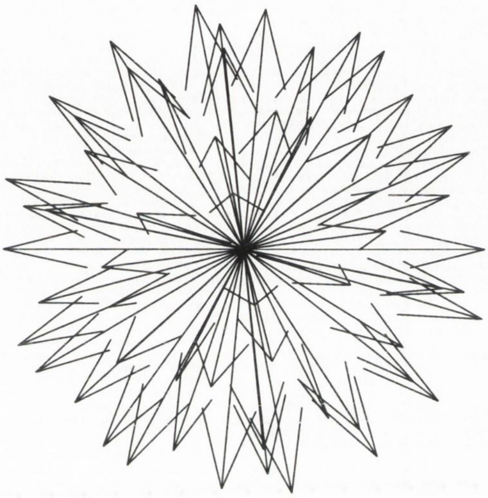

Figure 3.12: 3D wave direction system.

free field Green's function

$$P(\mathbf{x}) = \frac{e^{-\iota k(|\mathbf{x}-\mathbf{x}_S|)}}{|\mathbf{x}-\mathbf{x}_S|}. \tag{3.33}$$

The error at the central point $\mathbf{x}_0$ is thus given by

$$E = p(\mathbf{x}_0) - P(\mathbf{x}_0), \tag{3.34}$$

where $P(\mathbf{x}_0)$ is calculated from equation 3.33.

As shown in the relative amplitude error and the relative phase error, figure 3.13, a prominent singularity is now observed at $k = \sqrt{3}\pi/2$. According to the eigenvalue formula for a cubic cavity of dimension $(2h)^3$ (see, e.g., [1, chapter 9])

$$k_{l,m,n} = \left[\left(\frac{\pi}{2h}\right)^2 + \left(\frac{\pi}{2h}\right)^2 + \left(\frac{\pi}{2h}\right)^2\right]^{1/2}, \tag{3.35}$$

it follows that this frequency corresponds to that of the first eigenvalue, $k_{1,1,1}$, of the Dirichlet problem within the computational cell. As in the two-dimensional case, this frequency is that of a plane wave the wavelength of which equals the diagonal of the cell. Thus, the formulation gives also a nearly optimal (in the Nyquist sense)

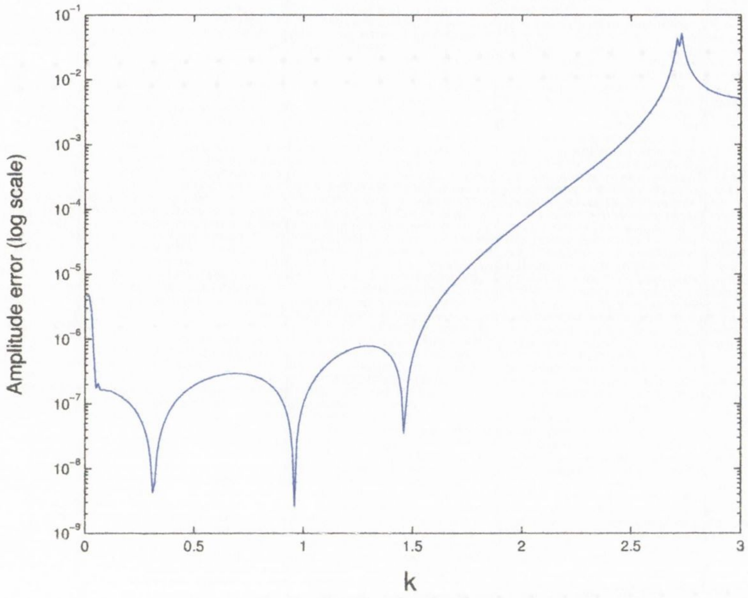

(a)

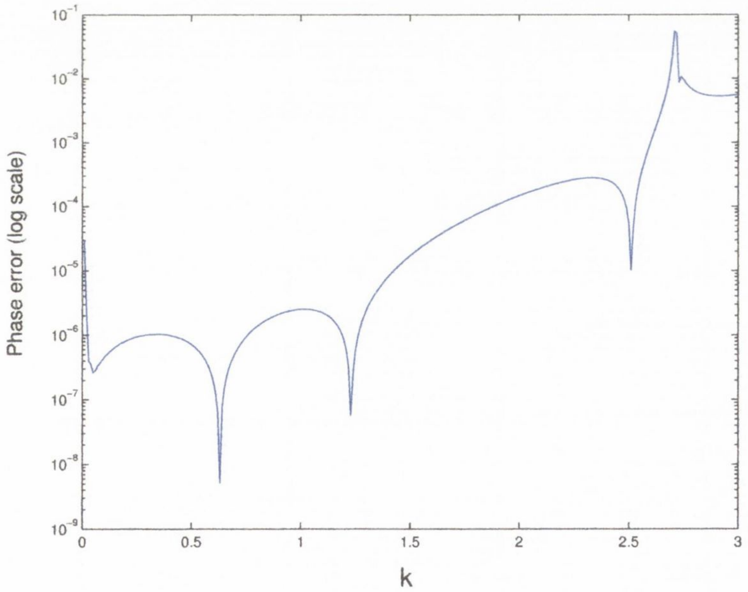

(b)

Figure 3.13: Error for the 3D wave expansion method at the central point. (a) Amplitude error. (b) Phase error.

accuracy in three dimensions. Finally, a deterioration of the interpolation accuracy near $k = 0$ is also observed. This behaviour, which is not yet completely understood, was also reported by Caruthers *et al.* [152] for the GFD approach in two dimensions.

3.4 Boundary condition implementation

Owing to the flexibility of the basic formulation, there will always be a choice of methods of imposing the boundary conditions. An assessment of the original formulation as proposed by Caruthers *et al.* [7], for a typical three dimensional problem is outlined below. The solutions proposed here were chosen because they provided stable solutions for a wide range of frequencies and they were the most easily implemented from a meshing viewpoint.

3.4.1 Dirichlet

These were implemented by simply constraining the appropriate degrees of freedom in the assembled matrix equation 3.24.

3.4.2 Neumann

According to the basic concept of the method, each discretisation point is approximated by a finite number of surrounding points. This leads to half/quarter/eight portions of the computational cell for face/edge/corners points. Consider, for example, the face shown in figure 3.14. At each node $\mathbf{x}_m^b$ on the face a normal velocity condition

$$\frac{\partial p(\mathbf{x}_m^b)}{\partial \mathbf{n}_m} = \bar{q}_m. \tag{3.36}$$

is applied to augment the constraint equation 3.27 (see equations 3.22-3.23) to

$$\begin{pmatrix} \mathbf{p} \\ \bar{q}_m \\ \vdots \end{pmatrix} = \begin{pmatrix} \mathbf{H} \\ \partial \mathbf{h}(\mathbf{x}_m^b)/\partial \mathbf{n}_m \\ \vdots \end{pmatrix} \gamma = \mathbf{H}_{aug}\gamma, \tag{3.37}$$

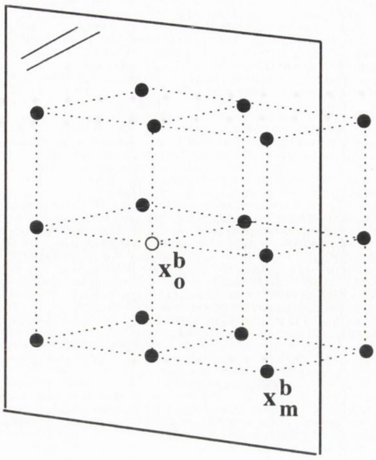

Figure 3.14: Face computational cell.

where $\mathbf{n}_m$ is the direction of the outward normal at the boundary point $\mathbf{x}_m^b$. The matrix $\mathbf{H}_{aug}$in equation 3.37 has now dimension $(17+9) \times N$.

A pseudo-inversion of equation 3.37 may be now performed giving

$$\gamma = \mathbf{H}_{aug}^{+} \begin{pmatrix} \mathbf{p} \\ \mathbf{q} \end{pmatrix}, \tag{3.38}$$

where $\mathbf{q}$ is a 9×1 column vector of the forcing nodal loads q_m. Substituting and left-right partitioning equation 3.38 into equation 3.26, yields

$$p_0 = \mathbf{h}(\mathbf{H}_{aug}^{+})_L \mathbf{p} + \mathbf{h}(\mathbf{H}_{aug}^{+})_R \mathbf{q}. \tag{3.39}$$

For a perfectly reflective surface surface $\mathbf{q} = 0$, and equation 3.39 yields

$$p_0 = \mathbf{h}(\mathbf{H}_{aug}^{+})_L \mathbf{p}. \tag{3.40}$$

Thus, a perfectly reflective condition must be always explicitly specified using a modified template 3.40, as this is not a "natural" boundary condition as would be the case in standard finite element methods.

3.4.3 Radiation

For problems related to very large or infinite physical domains, a non-reflective condition must be imposed on the boundaries of the hypothetical (truncated) numerical domain. Physically, this condition must ensure that all the acoustic energy is propagating outwardly, and no reflecting energy is being reflected back to the domain. This condition is given by the Sommerfeld radiation condition

$$\lim_{\mathbf{x}\to\infty} \mathbf{x}^{(\alpha-1)/2}\left(\frac{\partial p}{\partial \mathbf{x}} - ikp\right) = 0,$$

where α is the dimension of the problem.

It is of great interest that the radiation condition for arbitrary propagating waves can be satisfied exactly in order to reduce the numerical domain close to the excitation source, thus minimising the computational cost. At the same time, it is desirable that this condition can be achieved "naturally" in the formulation of the method.

Caruthers *et al.* [7], proposed to approximate the local near field at a point $\mathbf{x}^b$ laying in a radiating boundary, by selecting the directions of the fundamental solutions $\{e^{-\imath k \mathbf{d}_n \cdot \mathbf{x}^b}\}_{n=1}^{N}$ outside the domain determined by $\mathbf{x}^b$ and its neighbours, but inside the computational domain, as shown in figure 3.15.

A special "radiating" template equation 3.27 is then constructed including only outward propagating directions,

$$\mathbf{p} = \mathbf{H}_{rad}\boldsymbol{\gamma}. \tag{3.41}$$

The pressure at the subject radiating point, is then given by

$$p_0 = \mathbf{h}\mathbf{H}^{+}_{rad}\mathbf{p}. \tag{3.42}$$

Note that in this natural approach, no far field property of the radiating boundary is implied. For a two dimensional problem of a piston in an infinite wall [221], they obtained good results using this technique.

In principle, the directions of the plane waves may lie in the entire angle subtended by the physical domain ($-\pi/2, \pi/2$ in the figure 3.15), as they will be all radiating

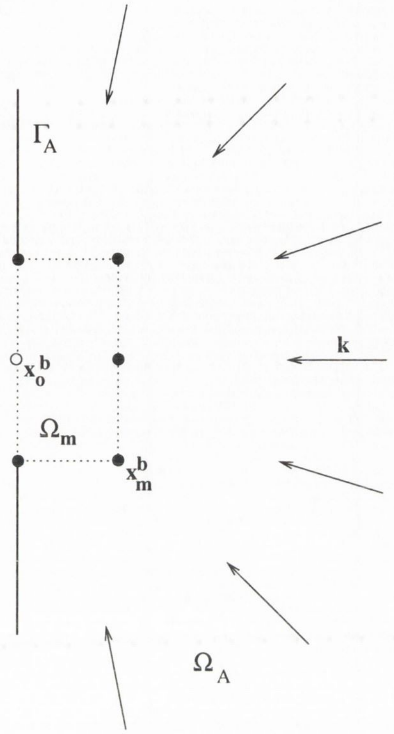

Figure 3.15: Illustration of the "natural" radiation boundary condition implementation.

outward from the boundary. It will be seen in the subsequent sections, however, that the overall convergence of the method is particularly sensitive to the way these directions are distributed.

An alternative, "non-natural" approach, is to use the specific acoustic impedance of freely propagating plane waves ("$\rho_0 c$" or "plane wave damper") defined as

$$\frac{\partial p(\mathbf{x}^b)}{\partial \mathbf{n}} = -\imath \frac{\rho_0 \omega}{Z} p(\mathbf{x}^b), \tag{3.43}$$

where $\mathbf{x}^b$ is any point laying on the radiating boundary, $\mathbf{n}$ is the normal outward boundary and ρ_0 is the air density. For a plane wave of the form $p = \gamma e^{-\imath k \mathbf{d} \cdot \mathbf{x}^b}$, with propagating direction $\mathbf{d}$, we have

$$\frac{\partial p}{\partial \mathbf{n}} = -\imath k (\mathbf{d} \cdot \mathbf{n}) p = -\imath k p \cos\theta, \tag{3.44}$$

where θ is the incidence angle of the plane wave at the boundary surface. The specific acoustic impedance Z in equation 3.43 then results [222]

$$Z = \frac{\rho_0 c}{\cos\theta}. \tag{3.45}$$

Since the angle of incidence θ in equation 3.45 is not generally known in advance, a normal incidence angle, i.e. $Z = \rho_0 c$, is usually assumed. This approximation, which is strictly valid only for plane waves propagating normal to the boundary, returns nonetheless a robust equation system which appears to generate stable solutions over the entire frequency range.

Furthermore, its implementation is straightforward and follows a similar procedure as described previously for the Neumann condition implementation. Thus, to implement relationship 3.43 at a face (figure 3.14), equation 3.27 is augmented for the half template to

$$\begin{pmatrix} \mathbf{p} \\ 0 \\ \vdots \end{pmatrix} = \begin{pmatrix} \mathbf{H} \\ \partial \mathbf{h}(\mathbf{x}_m^b)/\partial \mathbf{n}_m + \iota(\rho_0\omega/Z)\mathbf{h}(\mathbf{x}_m^b) \\ \vdots \end{pmatrix} \gamma = \mathbf{H}_{aug}\gamma, \tag{3.46}$$

where $\mathbf{n}_m$ is the direction of the outward normal at the boundary point $\mathbf{x}_m^b$.

After pseudo-inversion and partitioning, the template 3.46 then reduces to

$$p_0 = \mathbf{h}(\mathbf{H}_{aug}^{+})_L \mathbf{p} \tag{3.47}$$

The deviation from the normal incidence approximation, results in spurious waves reflected back to the domain. The magnitude of this error depends on the angle between the direction of the radiating wave $\mathbf{q}$ and the boundary normal $\mathbf{n}$

$$E_z = |1 - \cos^{-1}(\mathbf{n}\cdot\mathbf{d}/||\mathbf{n}||\cdot||\mathbf{d}||)|, \tag{3.48}$$

where $||\cdot||$ denotes vector norm.

Meshing can usually be formulated to ensure that the far field solution approximately propagates normal to the radiation boundary. In this case, the degree of error incurred will be slight. When this condition can not be satisfied, however, the error of the numerical solution can be significant.

To restore the accuracy of the solution, a simple iterative procedure is proposed here. Once the solution has been calculated using a normal incidence approximation (by augmenting $\mathbf{H}$ as in equation 3.46), we may find the amplitudes of the interpolating plane waves at any point in the domain as

$$\boldsymbol{\gamma} = \mathbf{H}^{+}\mathbf{p}, \tag{3.49}$$

where the components of the column vector $\mathbf{p}$ are the calculated pressure values of the neighbouring nodes. For boundary points, $\mathbf{p}$ has a dimension corresponding to half/quarter/eight portions of the computational cell for face/edge/corner. Note that $\boldsymbol{\gamma}$ has always the same dimension for any point in the domain.

The pseudo-inversion process selects the combination of interpolating plane waves that gives the least energetic solution. Thus, for points laying in a radiating boundary, the maximum component of the vector $\boldsymbol{\gamma}$ in equation 3.49 is given by the interpolating plane wave travelling at the minimum distance from the actual wave at the boundary, figure 3.16.

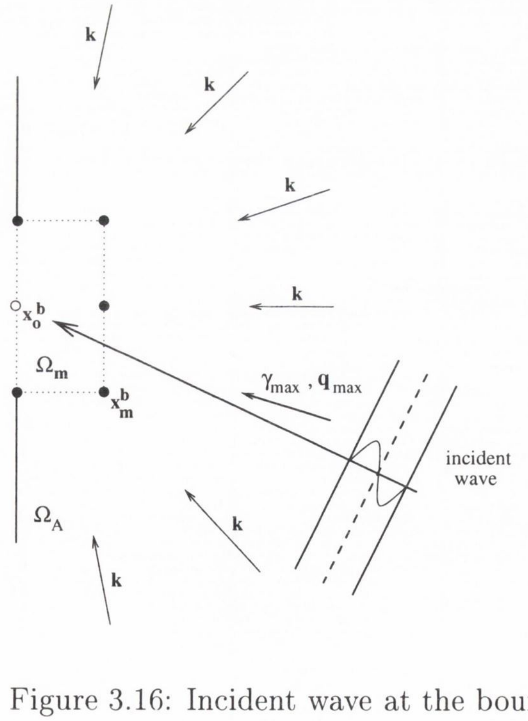

Figure 3.16: Incident wave at the boundary.

Denoting the maximum amplitude by γ_{max}, and $\mathbf{d}_{max}$ the propagation vector of the associated interpolating plane wave, the previously assumed normal incidence angle may be now changed according to $\cos^{-1}(\mathbf{n} \cdot \mathbf{d}_{max}/||\mathbf{n}|| \cdot ||\mathbf{d}_{max}||)$. The problem may then be solved again with the corrected incidence angles. Though this process may be repeated several times, one iteration gives in general satisfactory results, with little improvement observed for further iterations.

It should be noted that this iterative procedure, will not work in the case where there are two or more dominant wave directions propagating across the boundary.

3.4.4 Combination/corners

The Neumann and radiation boundary condition procedures outlined in the previous sections, can be readily combined should more than one restrain need to be imposed at the boundary points, such as may occur at corner points.

If a "$\rho_0 c$" approach is used for the radiation boundary condition, then equations 3.37 and 3.46 may be used in conjunction to augment the template matrix $\mathbf{H}$ according to the normal directions. For the natural radiation boundary approach, first a matrix radiating template $\mathbf{H}_{rad}$ is constructed from the correspondent outward directions *only*, and then augmented using relationship 3.37.

3.4.5 Numerical example

In order to demonstrate the boundary condition implementation, a three dimensional rectangular domain with an oblique ending, illustrated in figure 3.17, was modelled.

The mesh was set using 27 nodes in each cell with a maximum nodal spacing of 0.05m along the computational cell edges and 0.087m along the diagonals. Thus, the highest modelling frequency was placed in the range 1963-3400Hz, assuming a value of 340m/s for the sonic speed c.

Two excitation scenarios were considered, a propagating plane wave along the domain (duct problem) and a spherical wave propagating in free-field condition. To

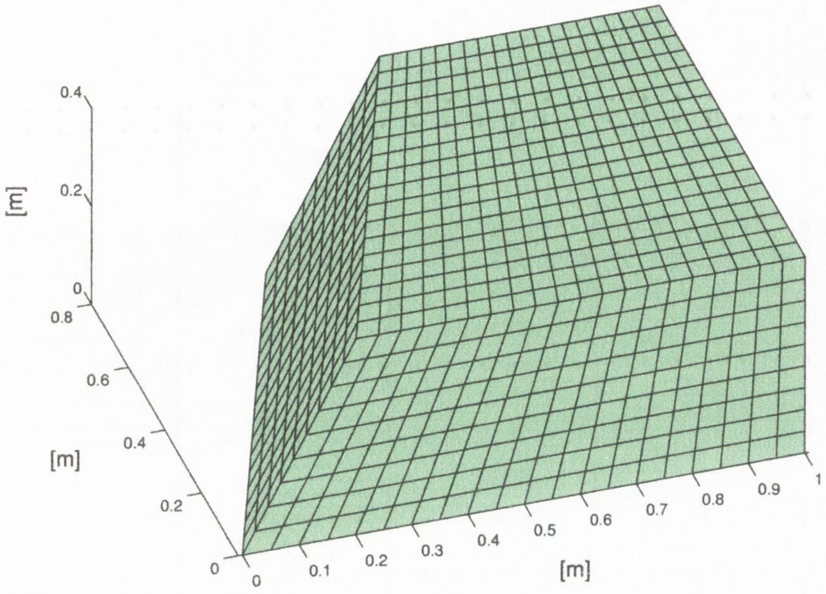

Figure 3.17: Test model.

implement the natural radiation boundary condition, as originally proposed by Caruthers *et al.* [7], a set of outward propagating directions for the radiating face(s) must be determined. In theory, any outward direction can be used. However, after experimenting with different outward vector direction arrangements, it was found that the distribution of these vectors has an important influence on the overall convergence of the wave expansion solution.

For illustration purposes, the performance of two different outward vector arrangements is shown below. The directions in the first set, denoted by SET1, were obtained from the outward directed vectors in the Fuller geodesic dome (figure 3.12). The second set, denoted by SET2, is given by 49 directions which fall within an optimised 82^0 cone normal to the radiating boundary, as shown in figure 3.18. Note that the directions are not uniformly distributed inside the cone, but grouped in three cones of 16 directions each with an angle difference of 3.75^0 between them. These directions were determined empirically, by modifying the angles of the cones until a good convergence was obtained for a wide range of frequencies.

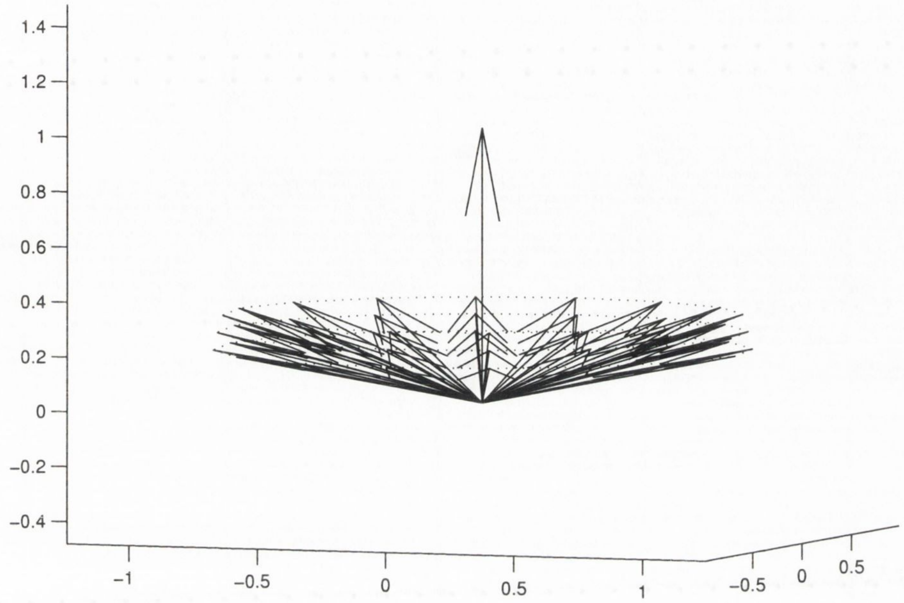

Figure 3.18: Optimised radiation vector cone.

Finally, a "$\rho_0 c$" non-natural approach was implemented and the obtained results were compared to those given by the natural method, by analysing the accuracy of the solution and conditioning of the system for the frequencies tested.

3.4.5.1 Plane wave: duct problem

An incoming plane wave (Dirichlet condition) was assumed at the flat end, Neumann ($\frac{\partial p}{\partial \mathbf{n}} = 0$) conditions were applied on the domain sides and free radiation condition applied to the oblique face. The maximum error was then calculated as

$$E_{max} = max\{p(\mathbf{x}) - P(\mathbf{x})\}, \tag{3.50}$$

where $p(\mathbf{x})$ is the wave expansion solution and $P(\mathbf{x}) = P(x) = e^{-jk(1-x)}$ is a plane wave of unit amplitude incoming at the flat end ($x = 1$ plane), and propagating towards the the oblique face.

As shown by the maximum amplitude error, plotted in figure 3.19(a), the natural approach using the optimised cone vector configuration (SET2) largely outperforms the SET1 given by the outward bucky ball vectors in the entire range of frequencies tested. A loss of stability is displayed at lower frequencies, as the number of nodal points per wavelength ratio (ppw) increases, figure 3.19(b). This ill-conditioning, which is similar for both outward configurations, seems to be inherent to the formulation itself without a major effect in the accuracy of the solution.

In comparison to the plane wave damper technique, the optimised natural approach (SET 2) is also more accurate particularly at mid-frequencies (see figure 3.20). However, despite the solution in the $\rho_0 c$ approach also becomes more ill-conditioned at lower frequencies, this method gives a significantly more stable solution in comparison to the natural scheme, with and without the iterative incidence angle correction. Note that, at lower frequencies, the error for the natural and the $\rho_0 c$ formulations becomes comparable. For illustration purposes, the real pressure distribution for $500Hz$ and $2500Hz$ using the optimised cone (SET2) and the $\rho_0 c$ approach with the iterative incidence angle correction procedure, is shown in figures 3.21 and 3.22, respectively.

Note that, despite the correction of the incidence angle improves the accuracy of the $\rho_0 c$ formulation, some spurious reflections from the oblique face still affect the pressure distribution, particularly at higher frequencies.

3.4.5.2 Point source

A Dirichlet point load was applied at one corner, Neumann conditions ($\frac{\partial p}{\partial \mathbf{n}} = 0$) were applied on the adjacent faces and free radiation conditions imposed on the remaining three faces. To apply the radiation boundary condition, the natural radiation formulation using the natural SET2 optimised cone distribution and the $\rho_0 c$ approach with 1 iteration for the correction of the incidence angle were implemented.

As shown in figure 3.23, and as previously observed for the duct problem (figure 3.20(b)), the $\rho_0 c$ and the natural (SET 2) radiation formulations become increasingly unstable at lower frequencies. Nonetheless, the numerical solution seems to be

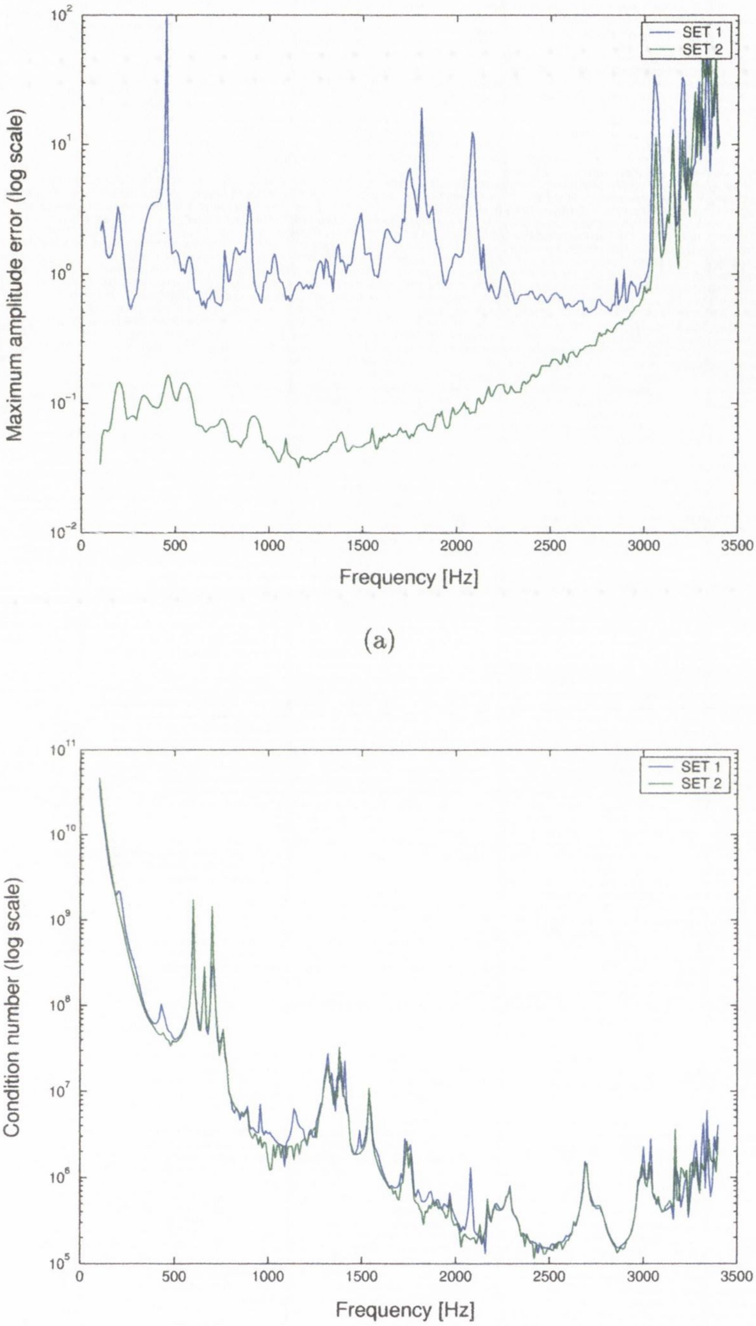

(a)

(b)

Figure 3.19: Performance of the "natural" solution approach. Duct problem. (a) Amplitude error. (b) Condition number.

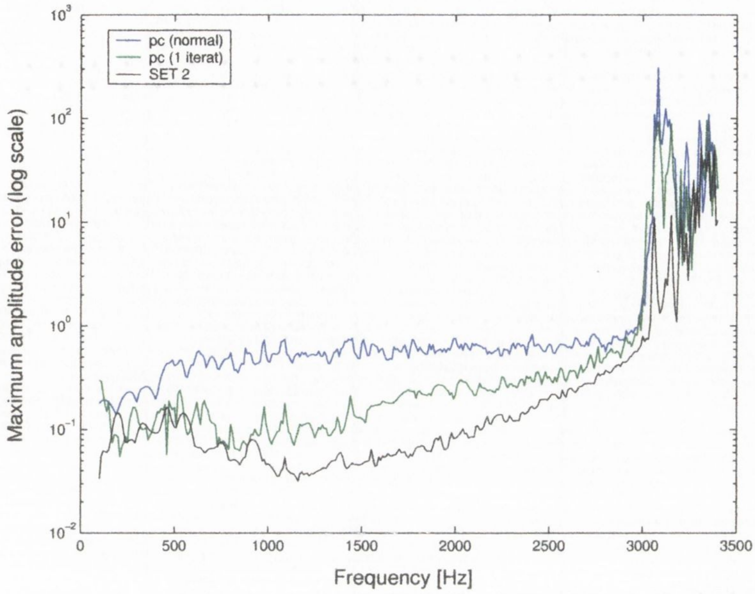

(a)

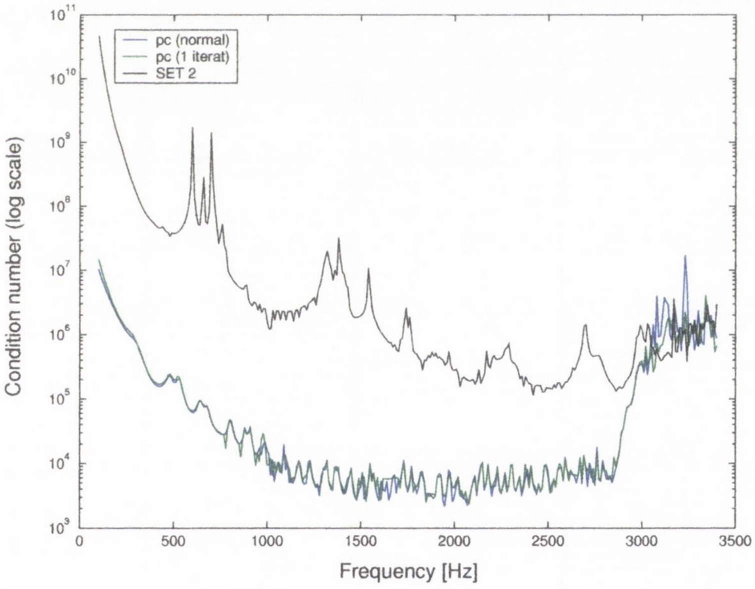

(b)

Figure 3.20: Performance of the "$\rho_0 c$" solution approach (the natural solution using the SET2 is also included for comparison). Duct problem. (a) Relative error. (b) Condition number.

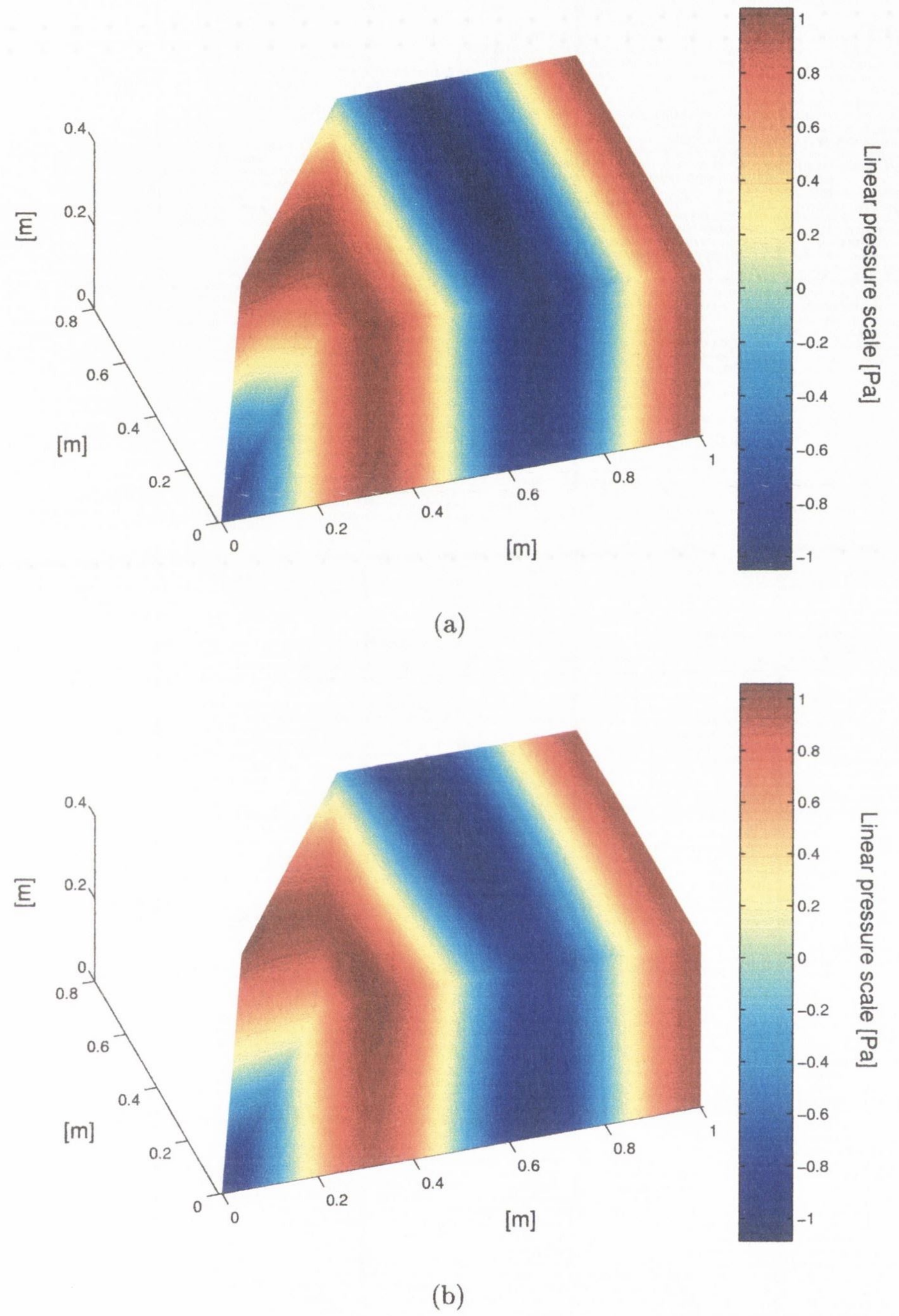

(a)

(b)

Figure 3.21: Duct problem, $500Hz$. (a) natural approach. (b) $\rho_0 c$ (iterative) approach.

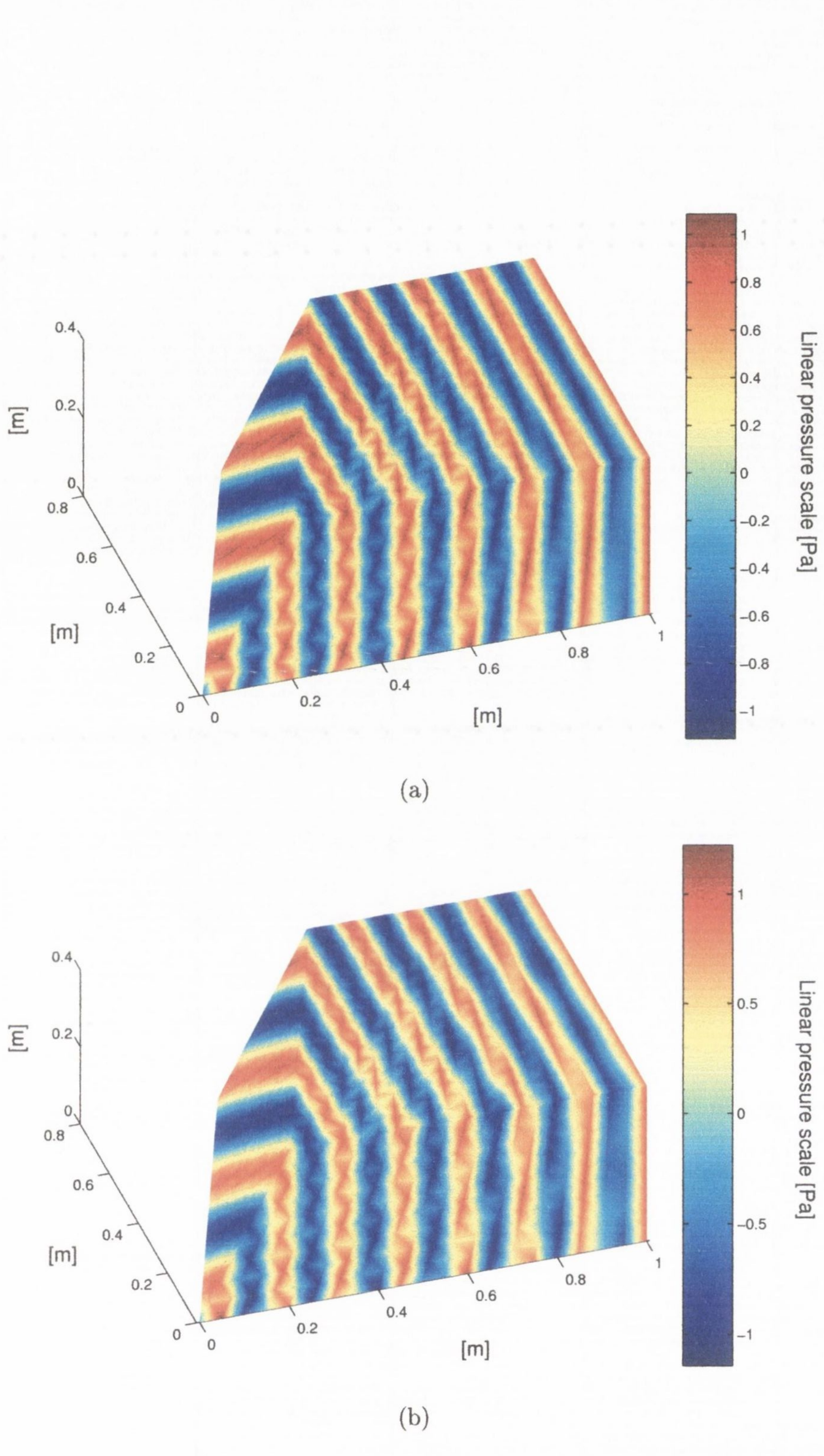

(a)

(b)

Figure 3.22: Duct problem, $2500Hz$. (a) natural approach (SET 2). (b) $\rho_0 c$ (iterative) approach.

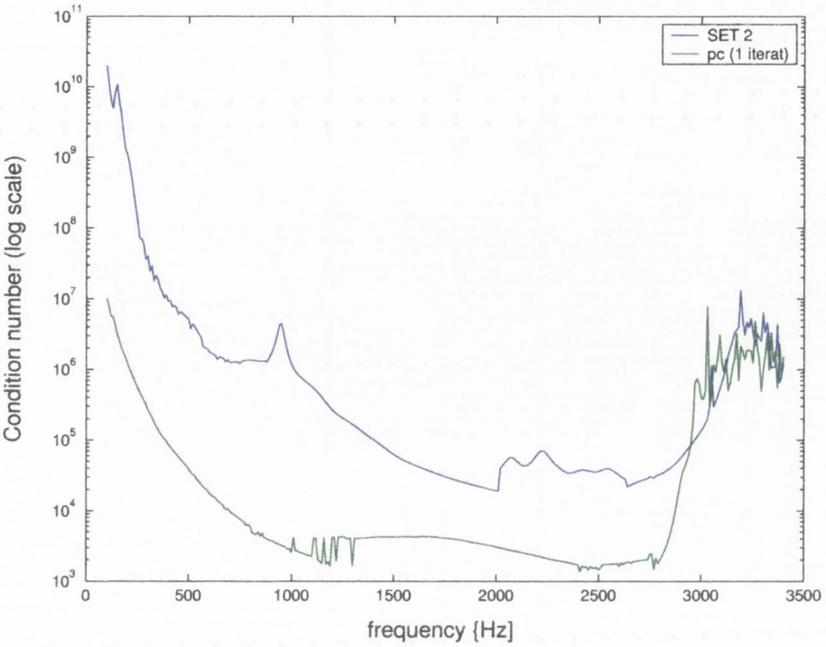

Figure 3.23: Condition number of the optimised (SET 2) natural approach vs the $\rho_0 c$ (1 iteration) for the point source problem.

indifferent to the ill-conditioning, as shown in figure 3.24 for the pressure distribution at $500Hz$.

Note that, since in this case the direction of propagation of the spherical wavefront is closer to the direction of the normal boundary vector at the radiating faces than in the duct example, the use of a $\rho_0 c$ radiating approach gives comparable results to that obtained with the natural method. This is further illustrated in figure 3.25, which shows also a good agreement in the pressure distribution for $2500Hz$ (2.8 edge points per wavelength for $h = 0.05m$ nodal spacing) for both methods.

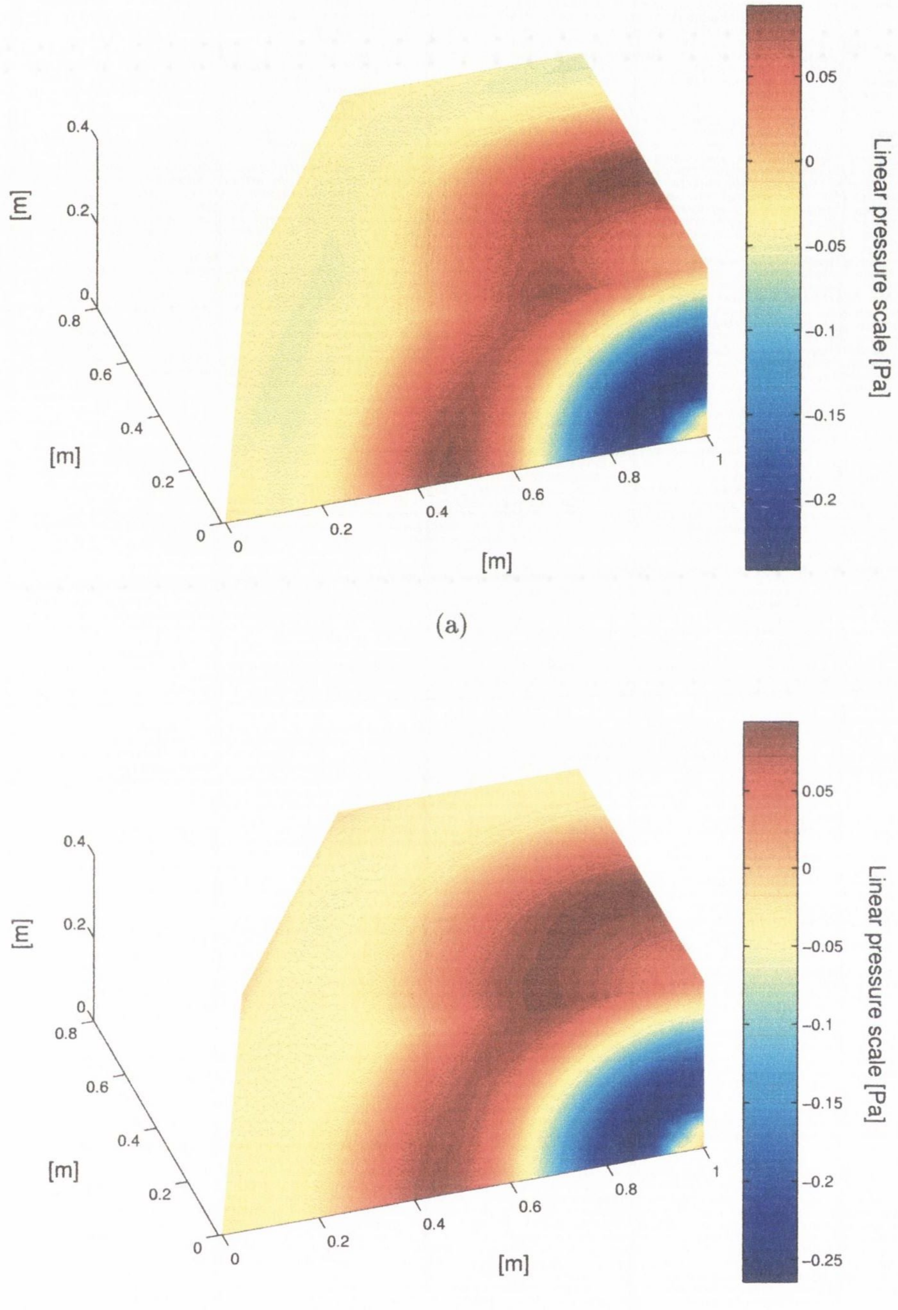

(a)

(b)

Figure 3.24: Point source problem, $500Hz$. (a) natural approach (SET 2). (b) $\rho_0 c$ approach (1 iter.).

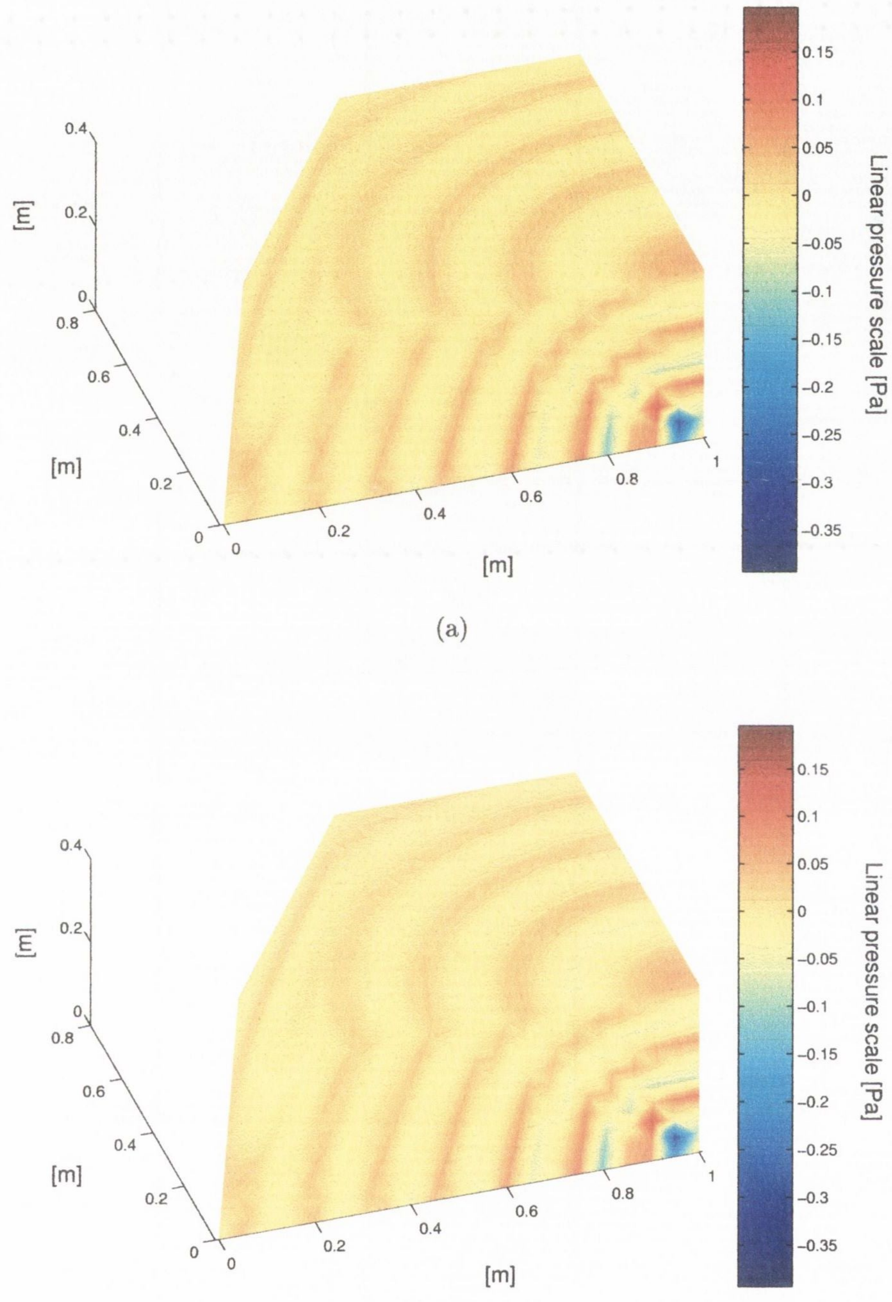

(a)

(b)

Figure 3.25: Point source problem, $2500Hz$. (a) natural approach. (b) $\rho_0 c$ approach.

3.5 Discussion

In this chapter, the interpolation properties of the GFD and WED methods are discussed. By using a simple example, the accuracy of the interpolation formulation in these approaches was observed close to the optimal in terms of the nodal points per wavelength theory of signal processing.

The plane wave expansion has some implementation advantages over the Green's function discretisation, since no radial source location needs to be determined beforehand further avoiding the use of singular sources. Moreover, no penalty is observed in the accuracy of the interpolation procedure. In comparison to a standard finite element scheme, these two approaches have an overwhelming superiority in the solution error, even for wave numbers that are well within the resolution of the finite element method.

Dirichlet and Neumann boundary conditions can be readily implemented within the formulation of the WED method. For the implementation of the radiation boundary condition, the original formulation as proposed by Caruthers *et al.* [7, 221], allows the use of outward plane waves without any far field approximation. This approach satisfies the radiation condition "naturally", within the formulation of the WED scheme.

It has been found, however, that these outward directions should not necessarily be evenly distributed. Following a trial-and-error procedure, an optimised cone of 49 directions that gives accurate results for a wide range of frequencies was determined. In addition, a non-natural $\rho_0 c$ plane wave damper approach, has also been proposed. For a plane wave propagating along a duct, the natural approach was shown to give a better performance in comparison to the $\rho_0 c$ formulation, in particular at higher frequencies. However, for a radiating spherical wave the error difference between these two approaches at higher frequencies becomes closer. Furthermore, the natural approach was shown to diverge in the point source example at very low frequencies, though convergence was restored after slightly modifying some of the directions in the optimised cone.

These formulations have associated an increasing ill-conditioned system as the nodal points per wavelength ratio increases. This effect is more significant in the natural (optimised cone) approach. Remarkably, the numerical solution remained largely unaffected by the bad conditioning of the system, giving accurate solutions even when the system may be regarded as unstable. This property is also found in the Trefftz-type boundary element formulations, i.e. direct and indirect Trefftz methods, the Method of Fundamental Solutions (MFS) and in the Wave Based Method proposed more recently by Desmet [164]. The ill-conditioning in these schemes is given by the fact that the plane wave functions set, used for the field variable expansions, consist of non-orthogonal functions, which are globally defined in the entire continuum domain [126].

However, for some "mildly" ill-conditioned problems, the numerical solution vector may still be accurate if the system satisfies the so-called Picard conditions [223]. Consider a singular value decomposition (equation 3.17) of the overall assembled stiffness matrix $\mathbf{K}$ with dimension $(n \times n)$, i.e.

$$\mathbf{K} = \mathbf{U\Sigma V}^H = \sum_{i=1}^{n} U_i \cdot \sigma_i \cdot V_i^H, \tag{3.51}$$

where $\mathbf{\Sigma}$ is a diagonal matrix of singular values σ_i, U_i and V_i are the i-th column vectors of the orthonormal matrices $\mathbf{U}$ and $\mathbf{V}$, and where the superscript ^{H} denotes Hermitian transpose.

The solution to the equation system (equation 3.24) $\mathbf{Kp} = \mathbf{f}$, may be thus written as

$$\mathbf{p} = \sum_{i=1}^{n} \frac{U_i^H \cdot \mathbf{f}}{\sigma_i} V_i = \sum_{i=1}^{n} \frac{\beta_i}{\sigma_i} V_i. \tag{3.52}$$

The Picard conditions state that accurate numerical solutions for ill-conditioned problems can only be obtained,

- if the difference between the amplitudes of two consecutive singular values $\sigma_i - \sigma_{i+1}$ sorted in descending order sequence, becomes only large at the end of the sequence,

- and if the coefficients $\beta_i = U_i \cdot \mathbf{f}$ are smaller or at least not very much larger than their associated singular values σ_i.

The first 1000 largest singular values for the WED solution of the duct and point source problems, using the optimised directional cone, are plotted in figure 3.26. The excitation frequency (freq=108Hz→k=0.1) corresponds to that which gave the worst conditioning of the system for the duct and point source examples. Since it is clear that the decay of the singular value curve is very smooth and since the coefficients β_i are much smaller than the associated singular values, the wave expansion model satisfies in general both Picard conditions.

Finally, it should be mentioned that the overall assembled system matrix $\mathbf{K}$ in the WED method is frequency dependent. Thus, the calculation of the undamped natural frequencies and mode shapes of acoustic systems (as well as elastic systems as will be shown in chapter 5) must be found computing the minimum determinant values of $\mathbf{K}$, and resolving the problem for the frequency range of interest. This may represent, in principle, a disadvantage in comparison to standard full domain discretisation methods, such as the FD and FEM, in which the final (undamped) system of equations is independent of the excitation frequency. The calculation of the natural frequencies then reduces to an eigenvalue analysis problem.

However, due to the poor accuracy of these approaches, the resulting final system at higher frequencies is very large, rendering the computation of the eigenvalues itself a very expensive process. The efficiency of the WED in comparison to standard methods will depend, ultimately, on the computational cost of solving the same problem several times with fewer nodes or only once for a significantly larger system with the associated cost of the eigenvalue analysis.

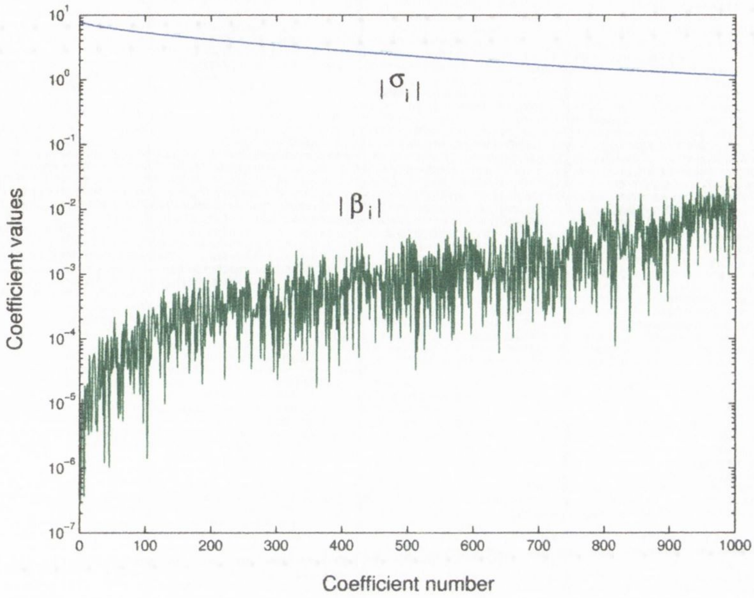

(a)

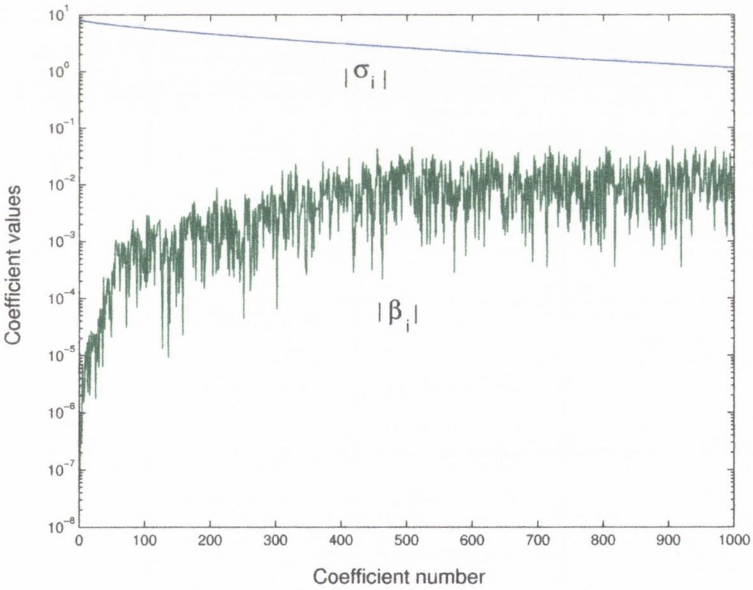

(b)

Figure 3.26: Picard analysis using the optimised directional cone, $108Hz$. (a) duct problem. (b) point source problem.

Chapter 4

Application of the wave expansion method in acoustic problems

4.1 Introduction

In this chapter, the wave expansion method, discussed in detail in the preceding sections, is applied to several steady-state acoustic problems in two and three dimensions. To illustrate the adaptability of the interpolation formulation, different conditions are applied not only at the boundaries, but also within the continuum domain.

A conceptual traffic noise problem is modelled in section 4.2.1. The performance of a parallel barrier interference system is briefly discussed. In section 4.2.2.1, the WED formulation is readily modified to include uniform and non-uniform flow conditions within the continuum domain. A monopole pressure field around a Joukowski aerofoil, subjected to a non-uniform flow is also investigated. Finally, in section 4.3, the use of 3D free tetrahedral meshes is explored. A schematic turbofan model subjected to a uniform Mach 0.3 flow is then modelled.

In order to demonstrate the accuracy of the technique, all the validation examples included here were solved using a nodal point per wavelength ratio between 2 and

3.5[1].

4.2 Two dimensional examples

4.2.1 Traffic noise barriers

Figure 4.1 shows the possible significant sound propagation paths over flat reflective ground radiating from a line or point source S to a receiver position R. In the absence of any obstacle the noise level at point R resulting from a traffic source at S is the sum of the contributions from the direct path SR and the reflected path SGR. To illustrate this effect, a monopole source radiating in free-field conditions over a flat reflective ground ($\partial p/\partial \mathbf{n} = 0$), was modelled (figure 4.2). The acoustic source was located at $1m$ from the bottom face. As shown in figure 4.3, the direct and reflected rays interfere over the free field, producing regions of higher and lower pressure level.

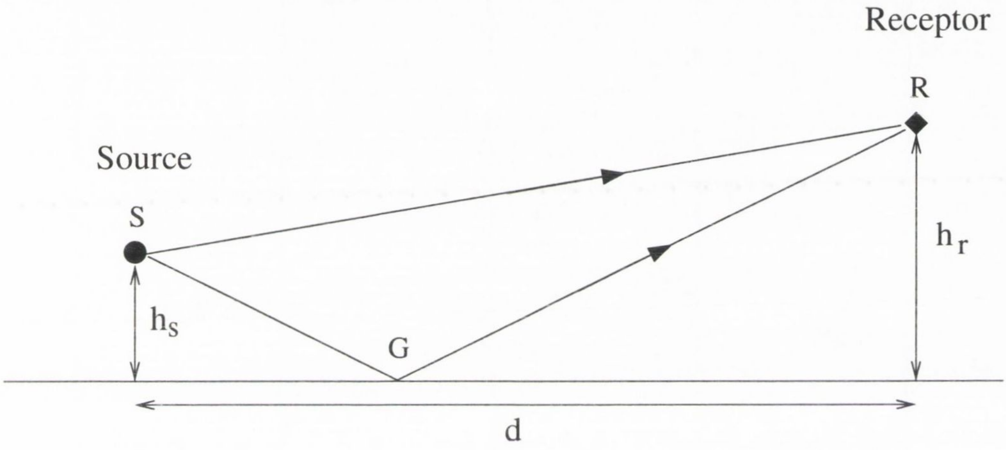

Figure 4.1: Direct and reflected rays over flat reflective ground.

When a barrier is placed between source and receiver, as shown in figure 4.4, the direct contribution is replaced by the diffracted paths over the top of the barrier,

---

[1] An illustration of the computational implementation of the method is given in the Appendix C

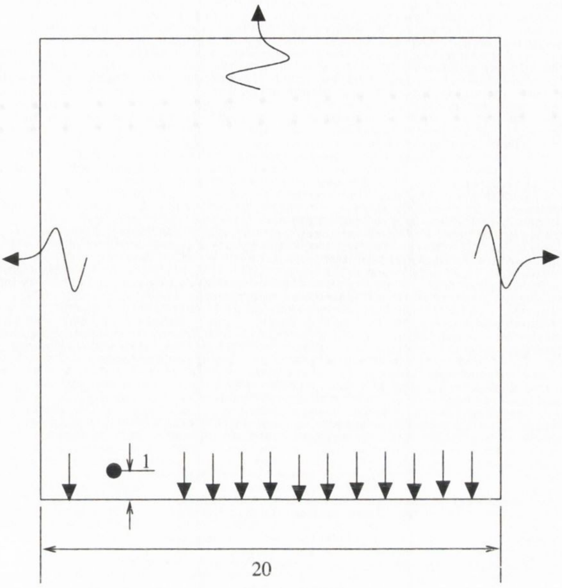

Figure 4.2: Schematic representation of the problem.

one of which involves a reflection from the ground plane. The interfering reflected path SGR, shown in figure 4.1, is prevented by the barrier.

The pressure field distribution for the point source previously depicted in figure 4.3, located at $3m$ from a perfectly reflective barrier of dimensions $3 \times 0.4m$, is shown in figure 4.5. At 1000Hz, the effectiveness of the barrier to produce a shadow zone shielding the receiver from the direct noise is increased. It should be noted that this may not be necessarily the case in all practical situations, as local resonant (interference) effects may affect the overall performance of a barrier.

A conceptual traffic noise problem was then modelled, in which a point source simulating a passing vehicle was located between two vertical, perfectly reflective barriers of $3 \times 0.4m$ erected on both sides of the road. An schematic of the problem is shown in figure 4.6.

The road, barriers, footpath and building were assumed perfectly reflective, whilst radiation conditions were imposed on the remaining boundaries. As shown in figure 4.7, the reflective condition of the barriers produce a local stationary wave effect, giving significant activity between the barriers. The pressure distribution at 800Hz,

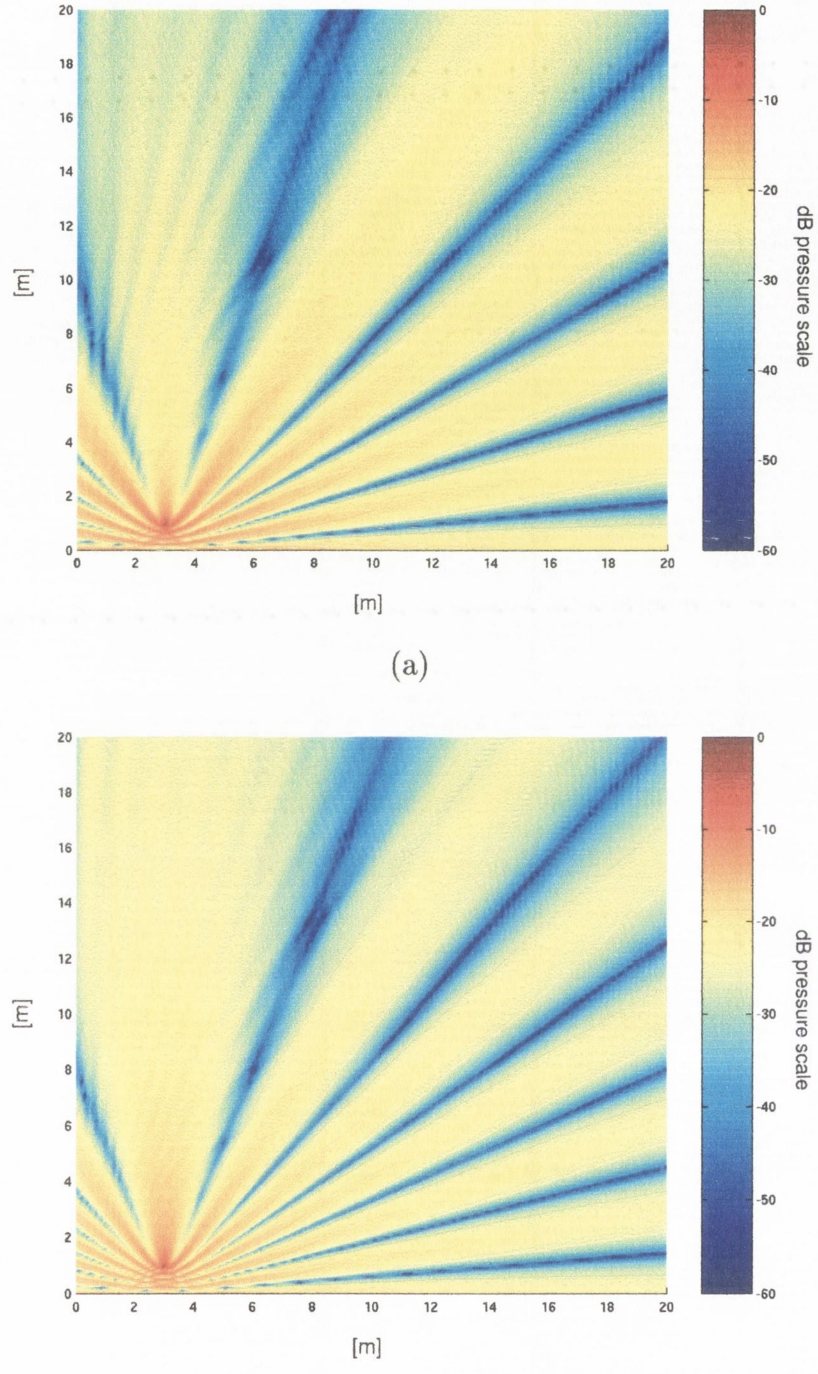

(a)

(b)

Figure 4.3: Pressure distribution in dB scale for a monopole source radiating in free field condition with reflective ground. (a) 800Hz. (b) 1000Hz.

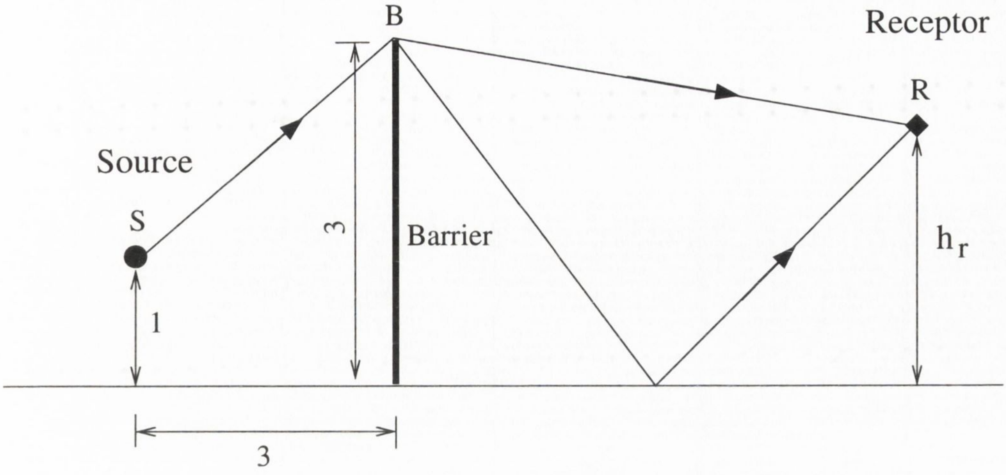

Figure 4.4: Direct, diffracted and reflected rays over a barrier.

figure 4.7(a), shows a similar standing wave effect between the second barrier (B) and the building. The reflections from the first barrier (A) reduce the effectiveness of the second barrier (B), making the shadow zone hardly noticeable. As the frequency increases, however, the effectiveness of the second barrier (B) improves, shielding the noise and producing a clear shadow zone between the barrier and the building, as shown in figure 4.7(b).

It should be noted that the boundary conditions can be readily modified to include absorbent material in the barrier. In addition, different (more efficient) barrier geometries could be also modelled [224], with the possibility of increasing the effectiveness of the barrier by considering active control solutions [225].

4.2.2 Radiation problems within inhomogeneous media

4.2.2.1 Homogeneous and inhomogeneous flow condition

By using interpolating plane waves with different velocity of propagation, the WED formulation may be efficiently used to model acoustic problems subjected to inhomogeneous flow conditions within the computational domain.

For an arbitrary directed flow of Mach vector $\mathbf{M}$, the pressure at a general field point

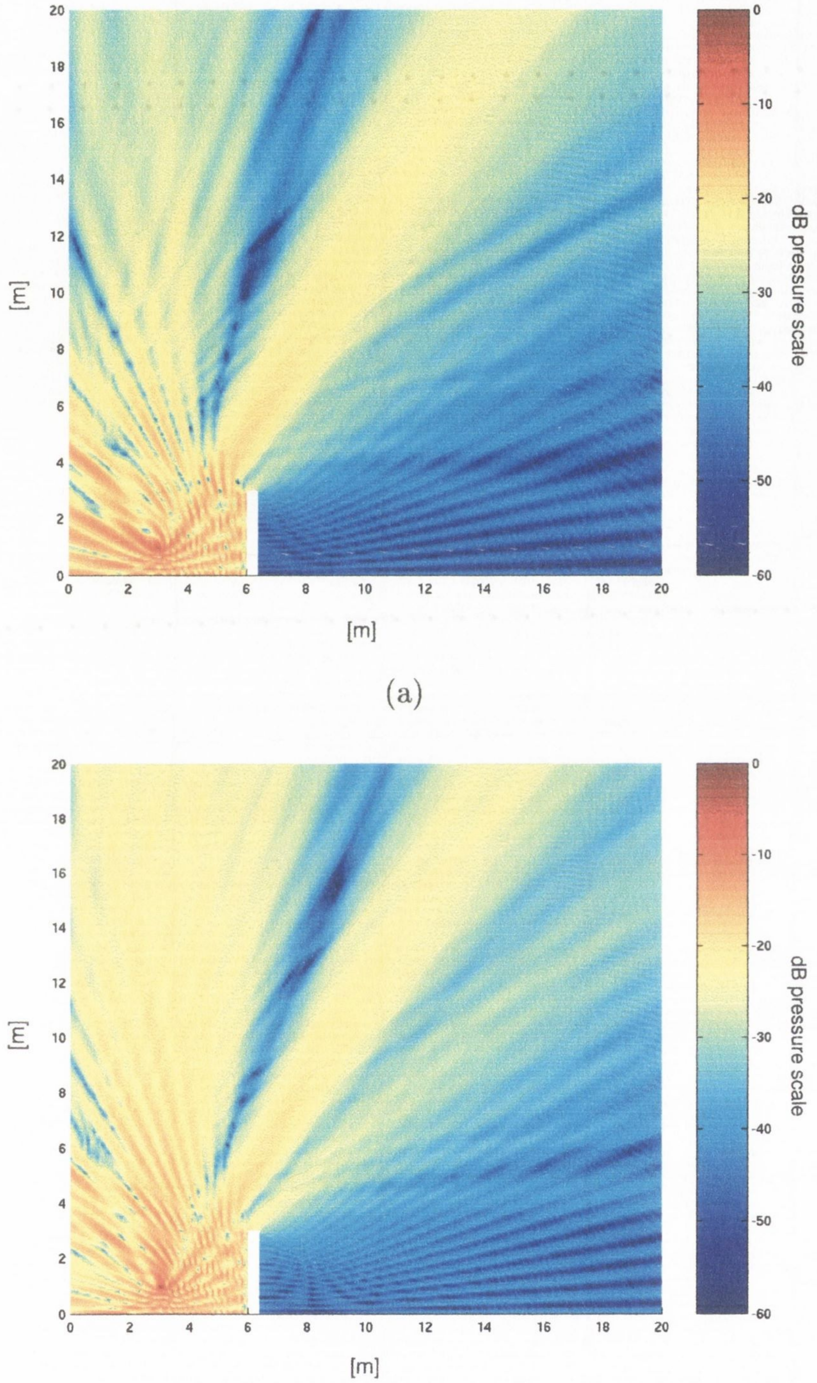

(a)

(b)

Figure 4.5: Pressure distribution in dB scale for a monopole source. (a) 800Hz. (b) 1000Hz.

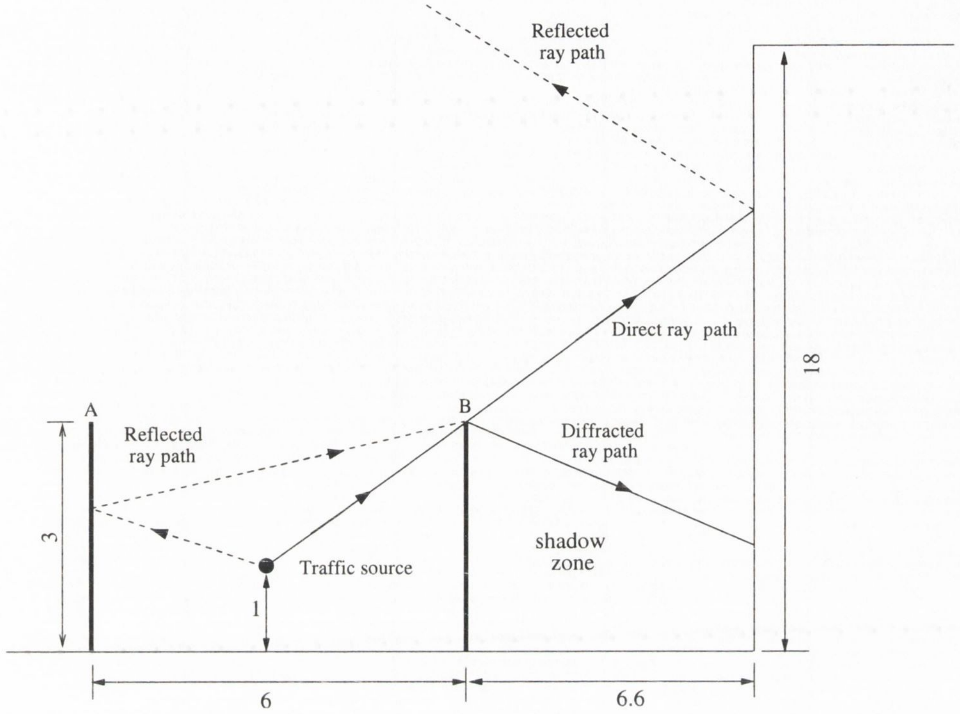

Figure 4.6: Illustration of a conceptual traffic problem. — direct and diffracted ray paths. - - - reflected ray paths.

$\mathbf{x}_0$ may be approximated by a combination of uniformly distributed plane waves

$$p_0 = \sum_{n=1}^{N} \gamma_n e^{\left(\frac{\iota k \mathbf{d}_n \cdot \mathbf{x}_0}{1-\mathbf{M}\cdot\mathbf{d}_n}\right)}, \tag{4.1}$$

where $\iota = \sqrt{-1}$, $\mathbf{d}_n$ is the directional vector of the n^{th} interpolating plane wave, and γ_n is the amplitude of the wave.

Consider a monopole source radiating in free field condition within a square domain of $20m$ edge length subjected to a uniform flow of $\mathbf{M} = \mathbf{M}_x = 0.5$, as shown in figure 4.8. The domain was uniformly meshed using nine noded square cells with a nodal distance of $0.1m$ along the edges and $0.14m$ along the diagonals.

Since the flow vector field has only one component, then

$$(1 - \mathbf{M}\cdot\mathbf{d}) = (1 - 0.5\cos\theta),$$

where θ is the plane wave propagating angle. Equation 4.1 may thus be re-written

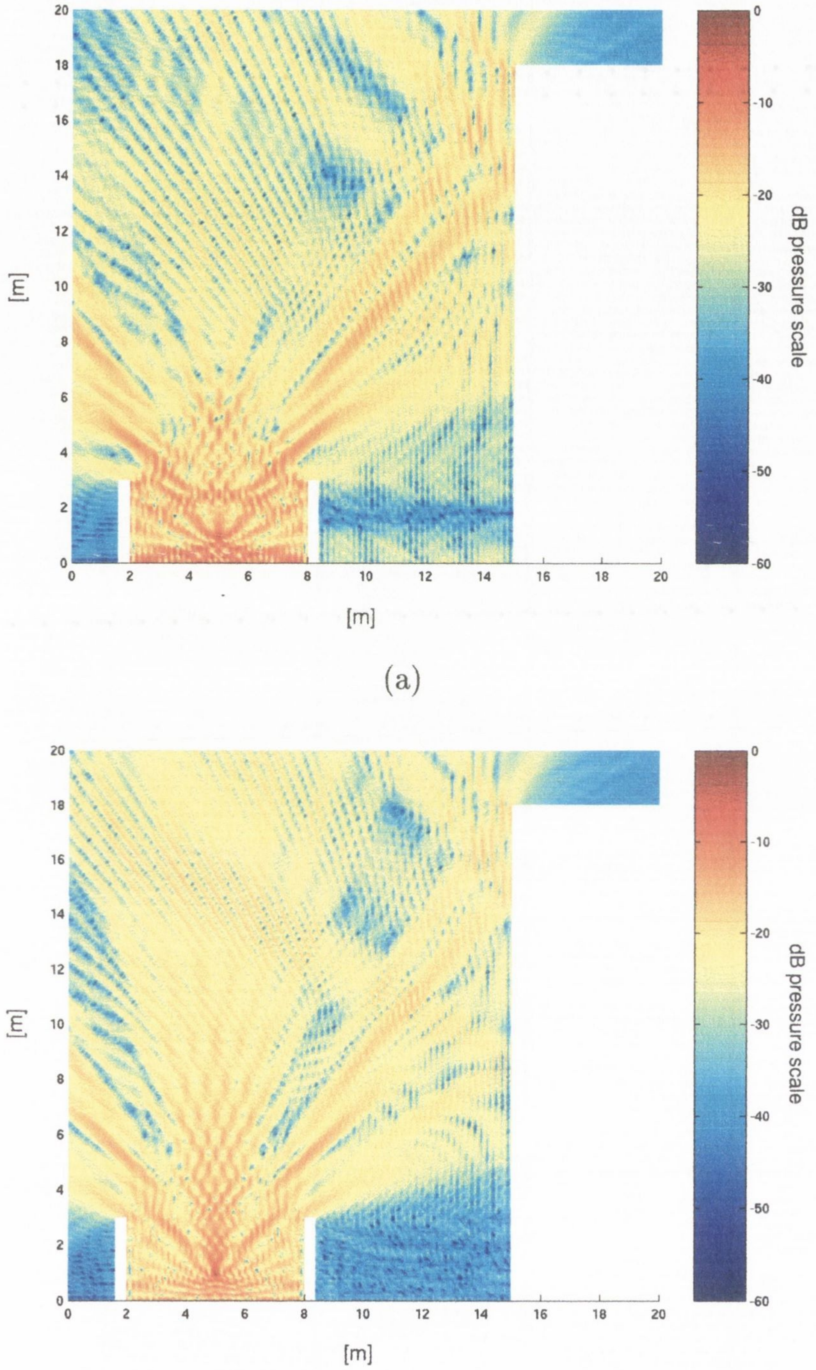

(a)

(b)

Figure 4.7: Pressure distribution in dB scale for conceptual traffic problem. (a) 800Hz. (b) 1000Hz.

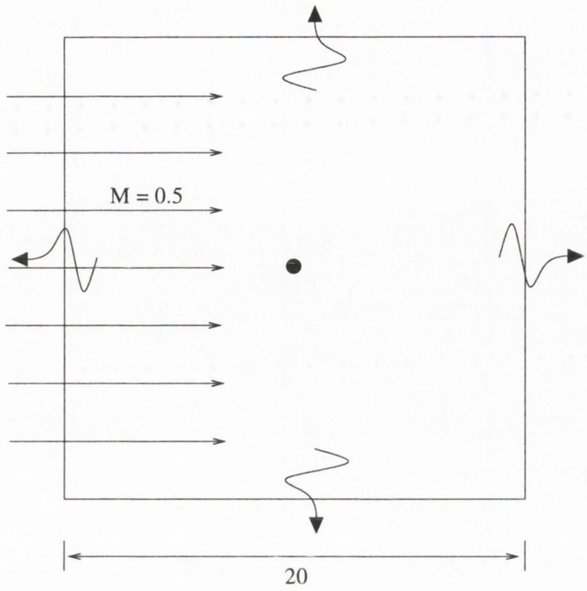

Figure 4.8: Point source in free field condition subjected to a $\mathbf{M}_x = 0.5$ flow.

as

$$p_0 = \sum_{n=1}^{N} \gamma_n e^{\left(\frac{\imath k \mathbf{d}_n \cdot \mathbf{x}_0}{1 - 0.5 \cos \theta_n}\right)}, \tag{4.2}$$

An illustration of the concept for two interpolating plane waves, is shown in figure 4.9. A computational template may then be formed by applying the same procedure

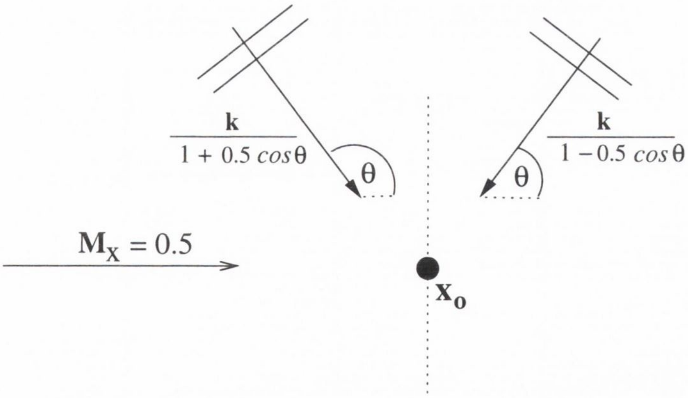

Figure 4.9: Illustration of the approximation used for a $\mathbf{M} = \mathbf{M}_x = 0.5$ flow.

to each neighbouring point, i.e.

$$p_0 = \mathbf{h}\mathbf{H}^{+}\mathbf{p}, \tag{4.3}$$

where

$$h_j = \sum_{j=1}^{N} e^{\left(\frac{\iota k \mathbf{d}_j \cdot \mathbf{x}_0}{1-0.5\cos\theta_j}\right)}, \tag{4.4}$$

and

$$H_{ij} = \sum_{i=1}^{S} \sum_{j=1}^{N} e^{\left(\frac{\iota k \mathbf{d}_j \cdot \mathbf{x}_i}{1-0.5\cos\theta_j}\right)}. \tag{4.5}$$

For this example, a $300Hz$ excitation frequency was assumed. In the static case, the point per wavelength ratio (ppw) would increase to 5.6 - 4 according to the nodal spacing. However, under the present flow condition, the frequency of an interpolating plane wave propagating at $\theta = 0$, yields

$$\frac{k}{(1-\mathbf{M})} = \frac{\omega}{c(1-0.5)} = \frac{\omega}{c/2} = 2\left(\frac{2\pi 300}{c}\right) = \frac{2\pi 600}{c}, \tag{4.6}$$

where ω is the circular frequency, and c is the sound speed. For this wave, the accuracy range of the wave expansion method considering the nodal edge and diagonal cell spacing is 2.8 - 2 points per wavelength. The numerical solution, depicted in figure 4.10, clearly shows the effect of the flow in the contraction and stretching of the wave fronts at the left and right hand sides of the source, respectively, known as the Doppler effect.

The approximation given in equation 4.1 may be readily applied for modelling radiation and scattering of acoustic waves within inhomogeneous flows [156]. For illustration purposes, consider a Joukowski aerofoil subjected to a flow of $75ms^{-1}$ with an incidence angle (equivalent elevation of the aerofoil) of 10^0, figure 4.11. A detailed view of the vector flow field at the front edge and trailing edge of the aerofoil is given in figure 4.12.

Using a quadratic (non-uniform) radial mesh as shown in figure 4.13, the acoustic pressure distribution produced by a monopole source radiating at $1000Hz$ was modelled. A radiation condition was applied on the external (artificial) computational

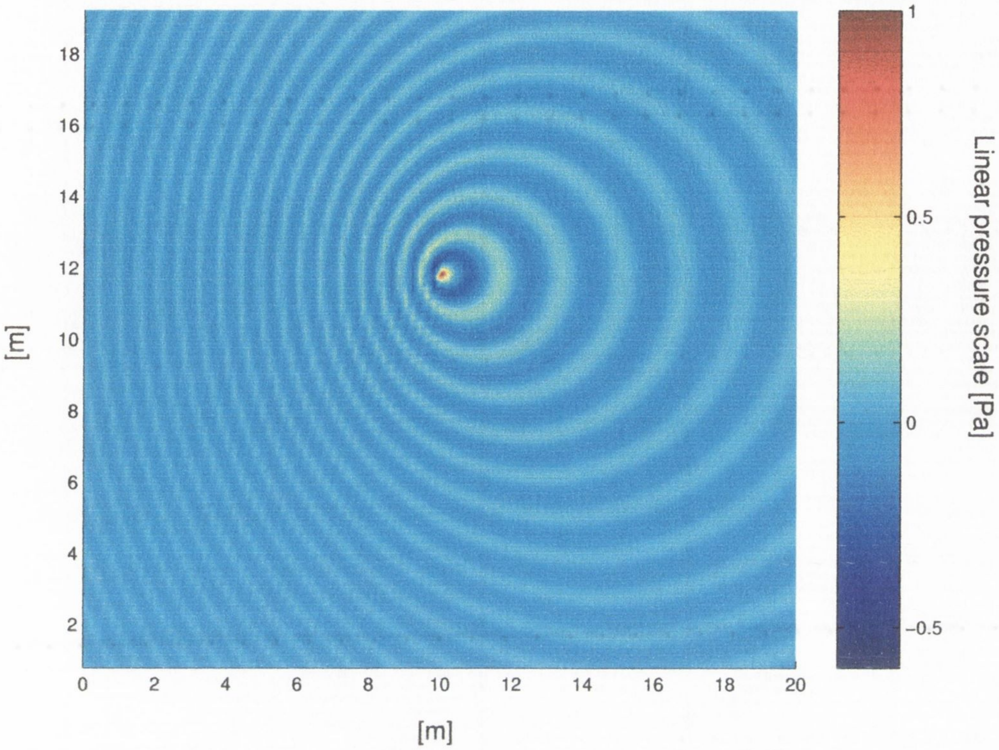

Figure 4.10: Point source subjected to a $\mathbf{M}_x = 0.5$ homogeneous flow. Linear pressure distribution at 300Hz.

boundary, whilst Neumann condition ($\frac{\partial p}{\partial \mathbf{n}} = 0$) was applied on the surface of the aerofoil. Note that, the boundary normal vector $\mathbf{n}$ is not uniquely defined at the trailing edge. Though there exist several possibilities to circumvent this drawback (as, e.g., truncating the geometry of the aerofoil at the trailing edge, in order to obtain a flat face with a well determined normal vector), for the present development, the direction of the normal was set according to the direction of the flow field at this point.

At each nodal point in the mesh we have a different Mach vector, either in direction and/or magnitude. Following the same procedure as applied for the homogeneous flow problem, the pressure value at the central point in the computational cell, may be then approximated in terms of the known pressure at the neighbouring points, equations 4.1-4.5, each one associated with a (possible different) Mach vector. That

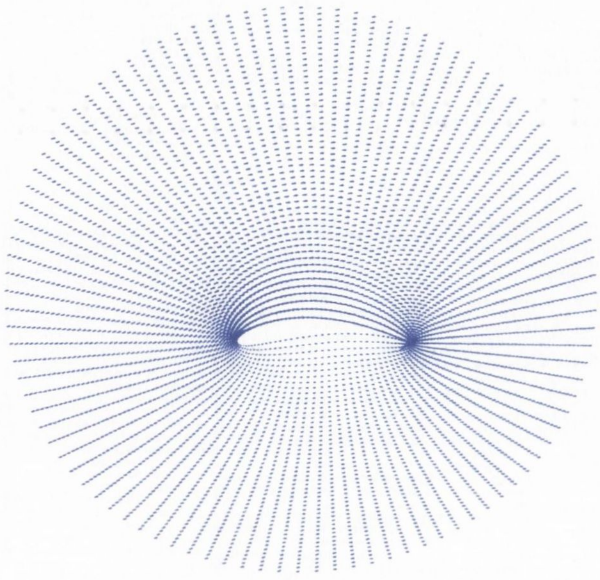

Figure 4.11: Flow around a Joukowski aerofoil. Full domain view.

is,

$$p_0 = \mathbf{h}\mathbf{H}^{+}\mathbf{p}, \tag{4.7}$$

where

$$h_j = \sum_{j=1}^{N} e^{\left(\frac{\iota k \mathbf{d}_j \cdot \mathbf{x}_0}{1 - \mathbf{M}_0 \cdot \mathbf{d}_j}\right)}, \tag{4.8}$$

and

$$H_{ij} = \sum_{i=1}^{S} \sum_{j=1}^{N} e^{\left(\frac{\iota k \mathbf{d}_j \cdot \mathbf{x}_i}{1 - \mathbf{M}_i \cdot \mathbf{d}_j}\right)}. \tag{4.9}$$

It was found, however, that the numerical solution does not converge to the desired value unless the Mach number in the surrounding points is assumed constant. The magnitude and direction of the Mach vector at the central node in the computational cell, $\mathbf{M}_0$, was then used to construct the template matrix $\mathbf{H}$, as

$$H_{ij} = \sum_{i=1}^{S} \sum_{j=1}^{N} e^{\left(\frac{\iota k \mathbf{d}_j \cdot \mathbf{x}_i}{1 - \mathbf{M}_0 \cdot \mathbf{d}_j}\right)}. \tag{4.10}$$

Thus, the maximum distance between the discretisation points, must be such that the variation of the flow remains relatively constant within the computational cell. This is easily achievable should the variation of the flow be sufficiently smooth. As

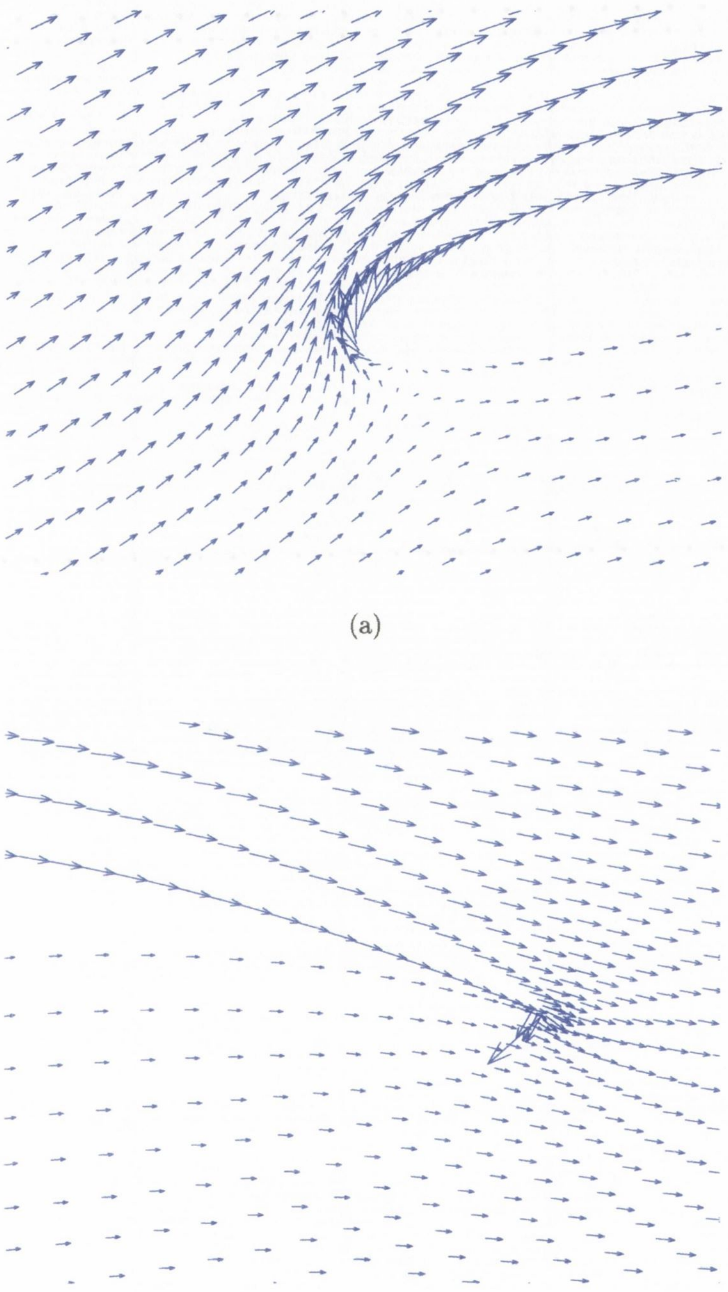

(a)

(b)

Figure 4.12: Flow around a Joukowski aerofoil. (a) Front edge. (b) Trailing edge.

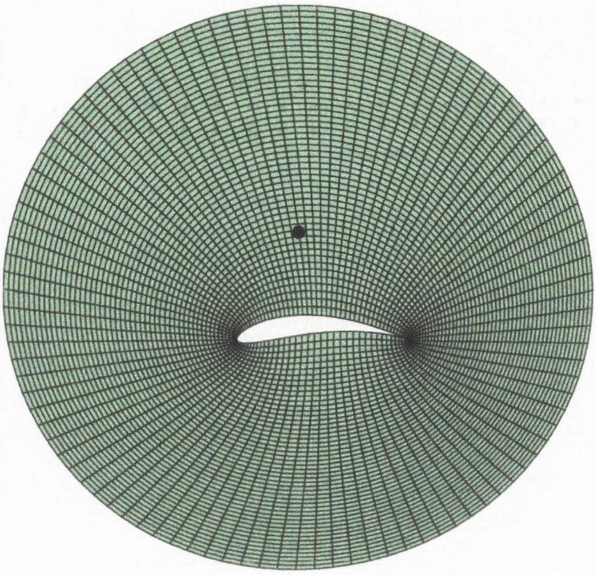

Figure 4.13: Mesh grid and point source location for a Joukowski aerofoil.

the inhomogeneities of the flow increase, the mesh must be refined accordingly. For highly inhomogeneous flow condition, this may result in a more stringent computational limitation than the one given by accuracy of the method, and gradients of the Mach vector should be incorporated into the formulation [156].

The numerical solution for the real linear pressure distribution at 1000Hz is shown in figure 4.14. Despite the Mach gradients in the flow vector field, the numerical solution was found to converge for a ratio of less than 3 points per wavelength.

The shielding effect of the aerofoil, even in the presence of the flow field, is better illustrated using a dB scale, as shown in figure 4.15. For comparison purposes, the homogeneous solution with $\mathbf{M} = 0$ is plotted in figure 4.16. Note that, due to the effect of the flow, the shadow region underneath the wing is reduced and displaced towards the trailing edge in comparison to the static solution.

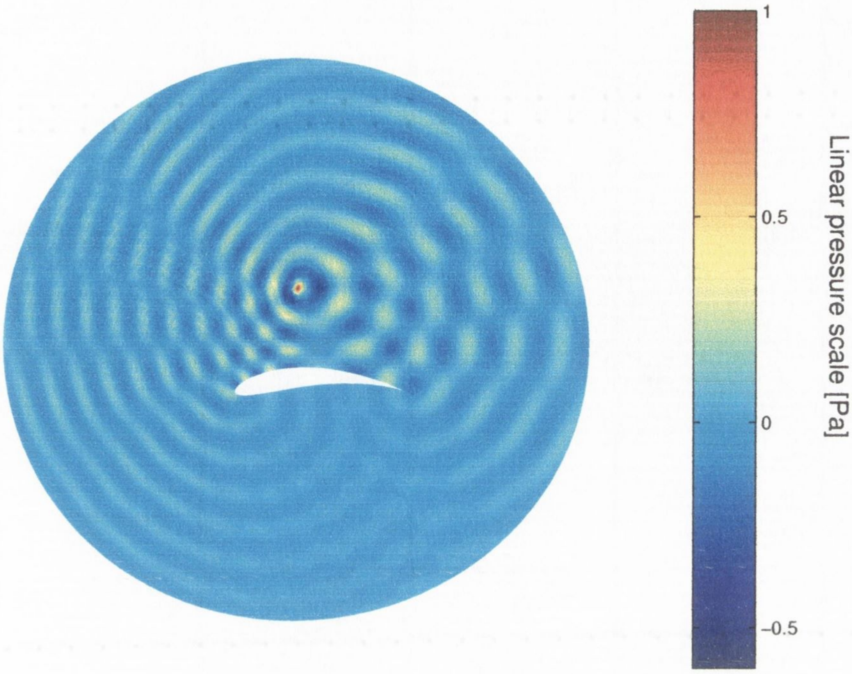

Figure 4.14: Real pressure distribution assuming a nonuniform flow condition.

4.3 Three dimensional examples

4.3.1 Tetrahedral meshes

In general, the geometry of the problem for most real life applications may have a complex shape including voids in the domain. Because of the limitations imposed by standard meshing tools, it is not always possible to perform a quadrilateral (2D) or hexahedral (3D) grid mesh in these cases.

For two dimensional problems, this drawback may be circumvented by conveniently dividing the original domain into more geometrically simple subdomains and meshing each subdomain separately. However, for three dimensional problems this process can be significantly more cumbersome. To circumvent this problem, a free tetrahedral mesh which may be applied to more general geometries, can be used. Since the formulation of the wave expansion method is not restricted to any particular meshing geometry, the use of tetrahedral computational molecules will then only

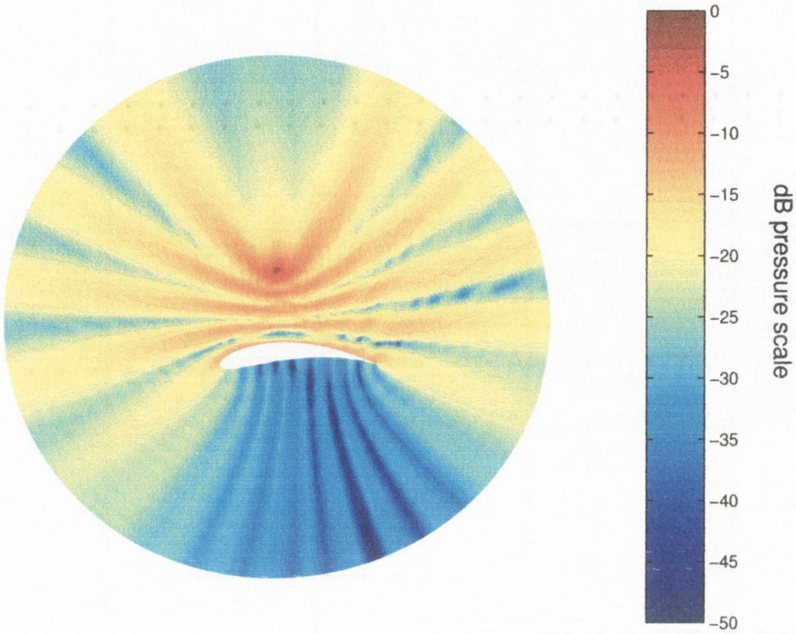

Figure 4.15: Logarithmic (dB) pressure distribution assuming a nonuniform flow condition.

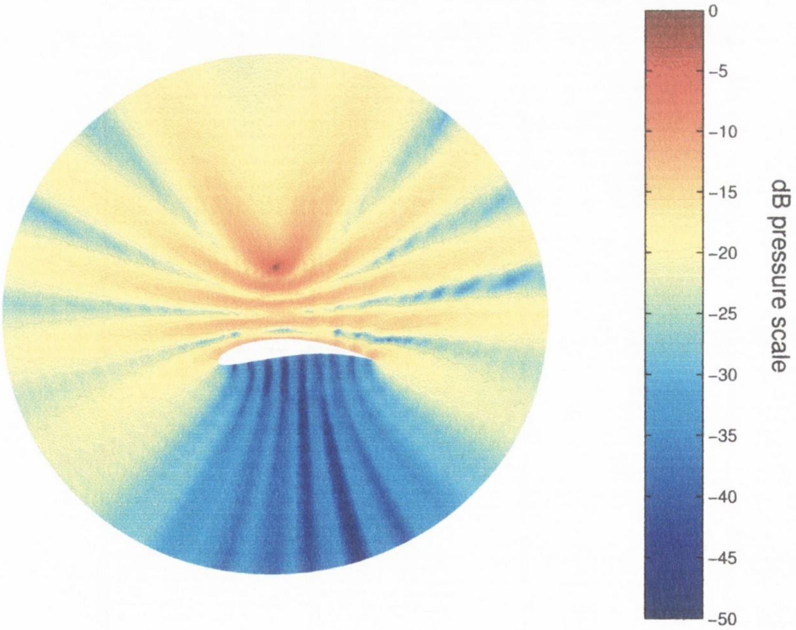

Figure 4.16: Logarithmic (dB) pressure distribution for the static (no flow) condition.

modify the number of surrounding points in the interpolation process. Furthermore, since the maximum number of surrounding points for free tetrahedral meshes does not usually exceed 18, a significant reduction in computation time, particularly in the pseudo-inversion process, may be additionally obtained.

Consider, for example, a discretisation of a conical horn of length $0.7m$ and radii $0.4m$ and $0.2m$, respectively, using tetrahedral elements with a maximum edge length of $0.05m$, as shown in figure 4.17.

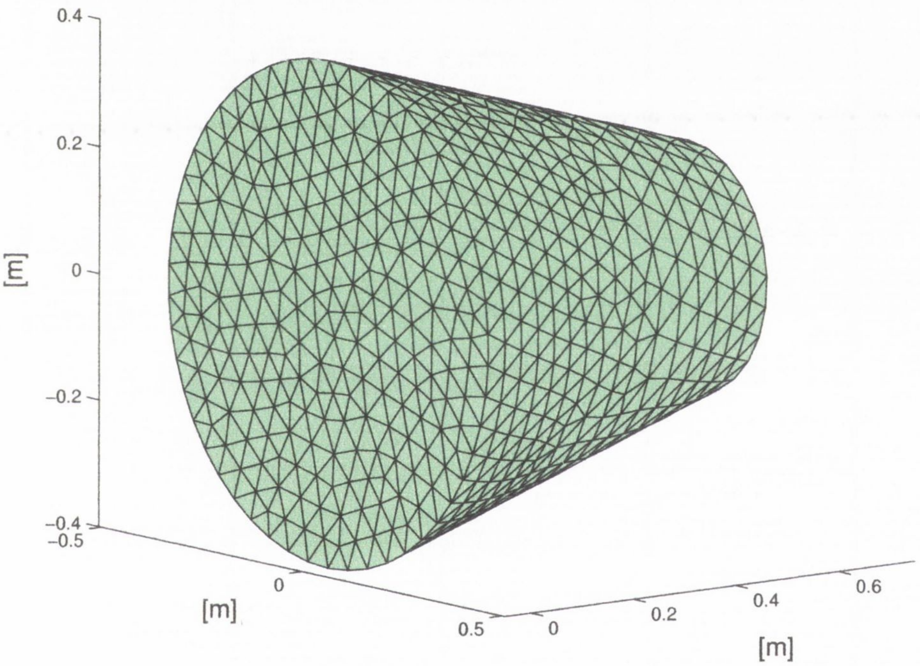

Figure 4.17: Tetrahedral mesh of a frustum.

An incoming plane wave of $1600Hz$ was assumed at one end (Dirichlet condition), whilst radiation and Neumann ($\frac{\partial p}{\partial \mathbf{n}} = 0$) conditions were applied at the other end and lateral face, respectively. The real pressure distribution is shown in figure 4.18.

Note that, since the fractional change in the cross sectional area of the horn becomes

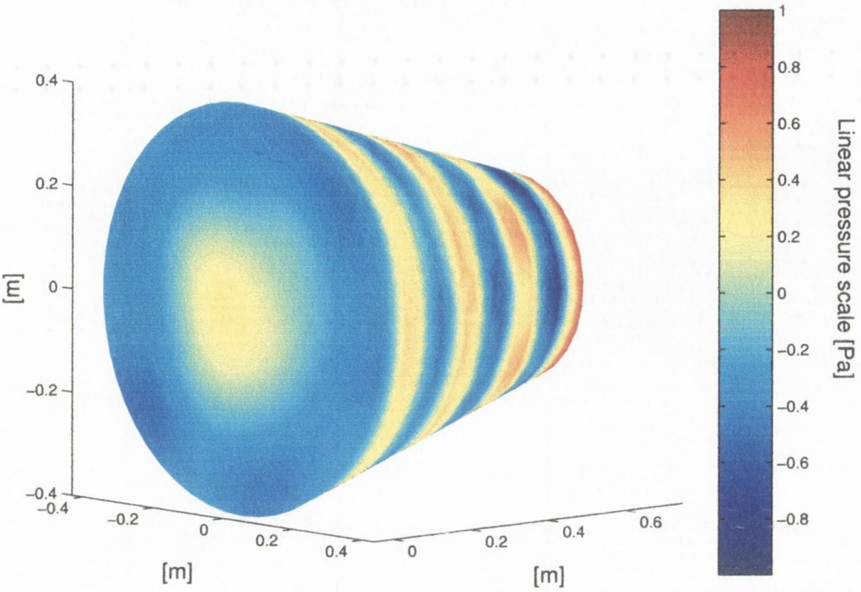

Figure 4.18: Real pressure distribution for a 1600Hz plane wave propagating along a linear horn.

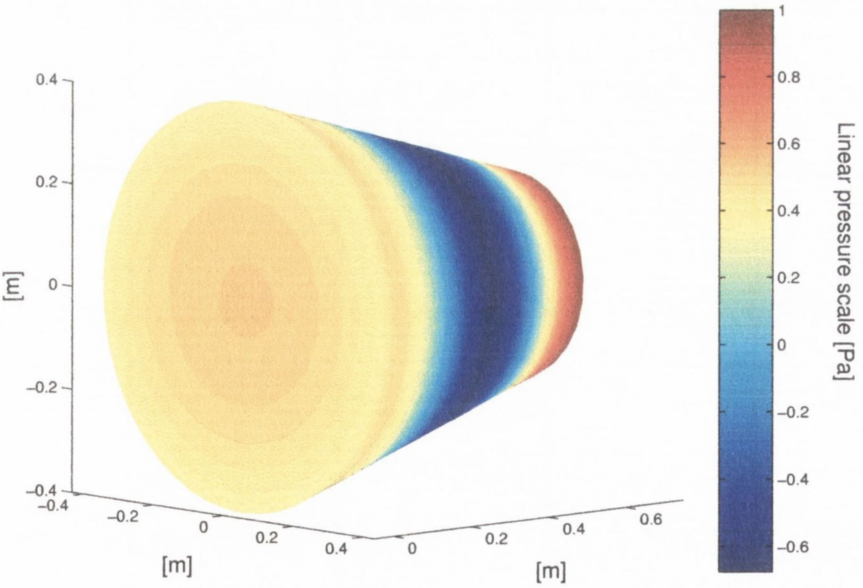

Figure 4.19: Real pressure distribution for a 500Hz plane wave propagating along a linear horn.

comparable to the wavelength, diffraction and reflection effects occur. A phase difference is observed between the axial propagation and an annular region closer to the cross sectional boundary face. The pressure distribution then becomes increasingly non-uniform as the wave propagates along the horn. For lower frequencies, the fractional change in the cross sectional area in relation to the wavelength becomes smaller, giving a more uniform wave across the horn, as illustrated in figure 4.19 for a $500Hz$ incoming plane wave.

4.3.2 Turbofan noise

The geometry used for the conical horn, was conveniently modified to represent a conceptual turbofan engine problem by dividing the original volume into an inlet volume and an exhaust volume, as shown in figure 4.20.

The noise produced by the fan was modelled as a Dirichlet condition, as illustrated. Neumann condition ($\partial p/\partial \mathbf{n} = 0$) was applied to the turbofan wall and the exhaust face. A computational domain was then determined embedding the turbofan in a cubic computational volume of $8m^3$, as shown in figure 4.21. The external boundaries of the domain were subjected to radiation condition.

The inlet duct and the exterior computational volume was meshed using free tetrahedral elements with a maximum edge spacing of $0.1m$ giving a total of 10,147 nodes and 52,076 elements. An illustration of the mesh at the axial plane of the turbofan is given in figure 4.22.

Two scenarios were considered, namely, a static solution with no flow and applying a uniform flow of Mach 0.3 at 0^0 incidence angle. In both cases, a 1000Hz excitation frequency was considered. The static solution is plotted in figure 4.23(a) and 4.23(b) for the linear and dB scaled pressure distribution, respectively.

Note that, in the static case, the turbofan acts like a horn transducer, redirecting the acoustic energy in the axial direction of the fan, where the maximum pressure levels are found. When the flow condition is applied, the frequency of the outgoing

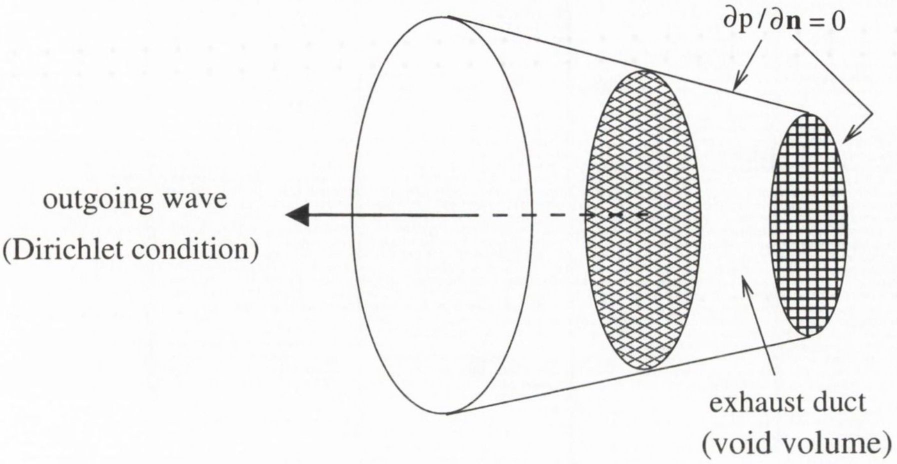

Figure 4.20: Schematic turbofan model.

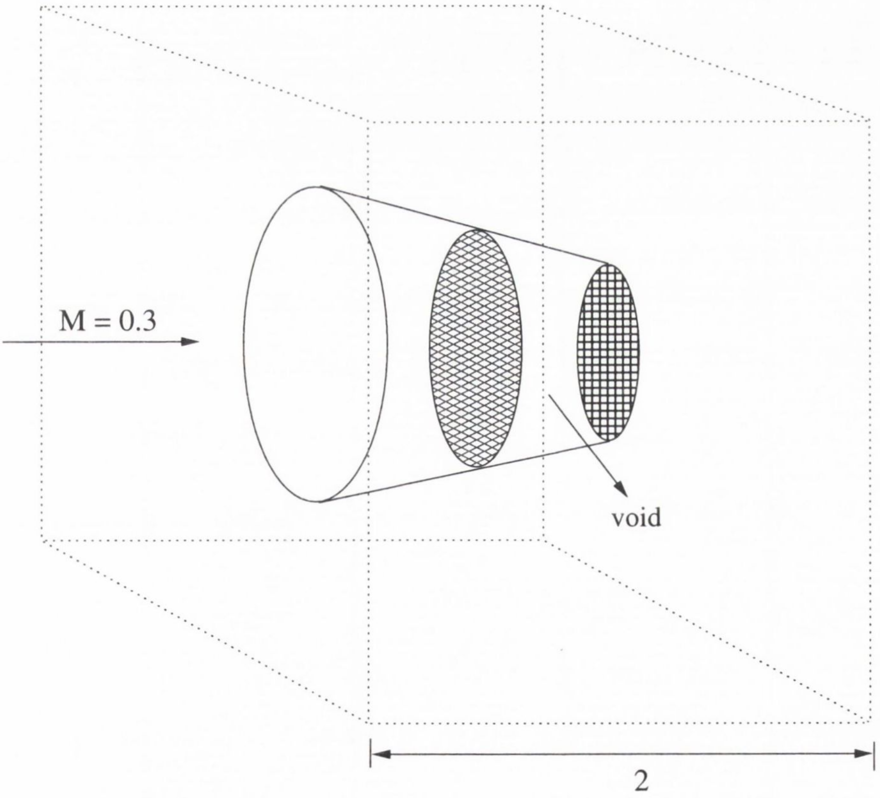

Figure 4.21: Computational domain.

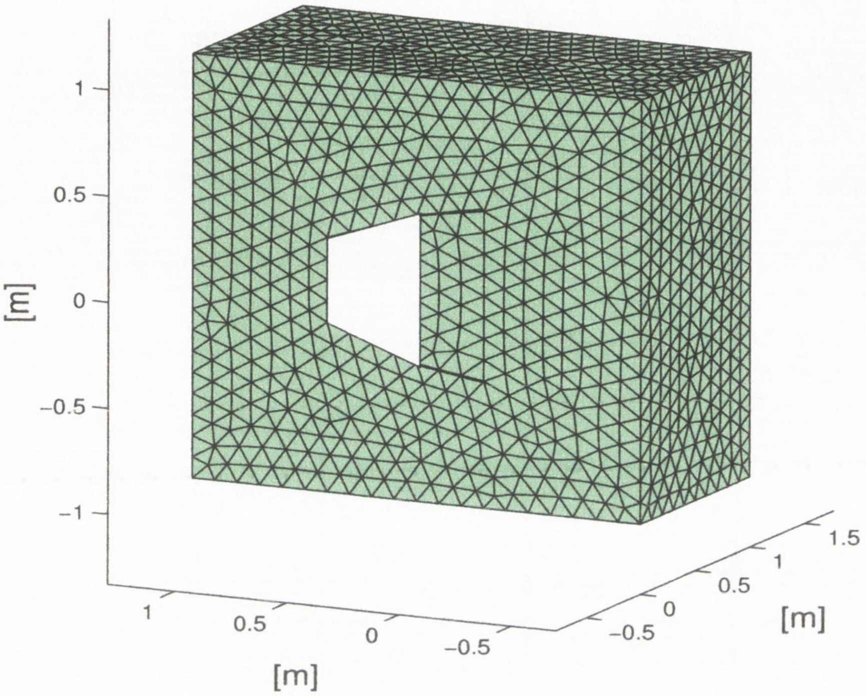

Figure 4.22: Domain discretisation (transversal slice view).

waves at the turbofan inlet is increased as expected. The horn-like radiation pattern of the turbofan in the static case is distorted by the flow, as shown in figure 4.24, with more activity in the regions above and below the turbofan.

An interesting effect of the flow in the pressure distribution is also found at the exhaust face of the turbofan, where some sort of constructive cancellation occurs. As a consequence the pressure level in this region is significantly higher than that obtained in the static case.

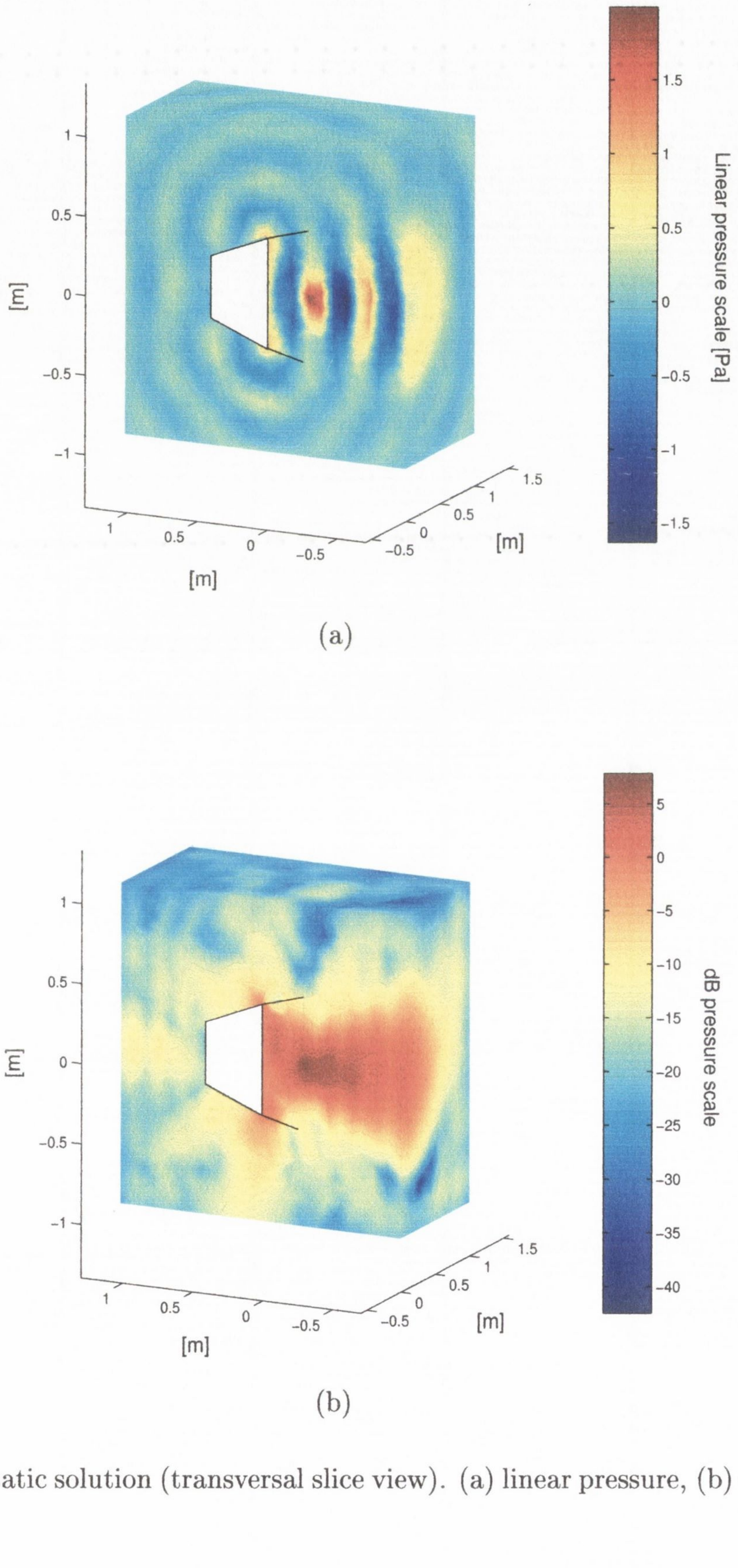

(a)

(b)

Figure 4.23: Static solution (transversal slice view). (a) linear pressure, (b) dB scale.

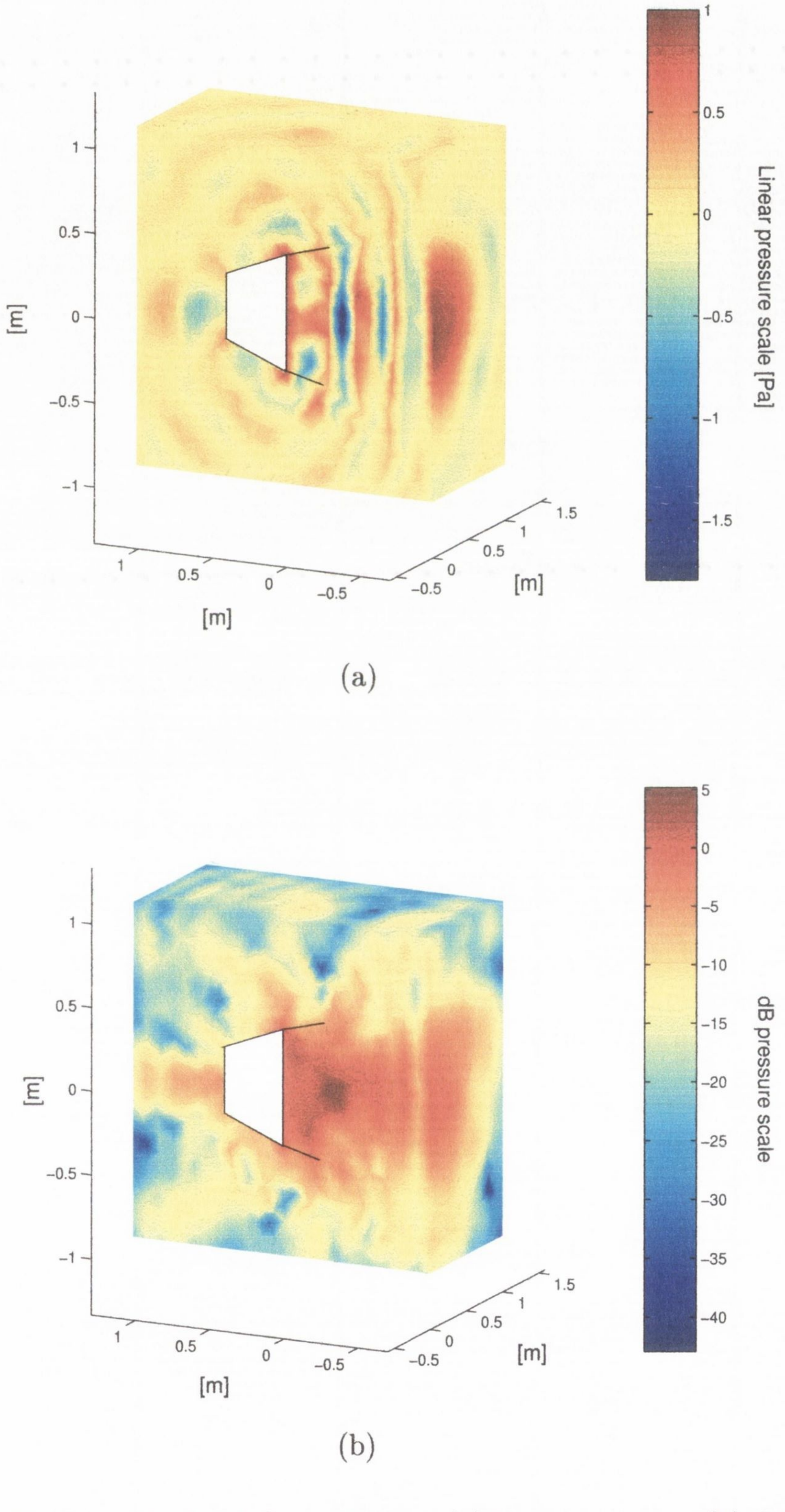

(a)

(b)

Figure 4.24: Uniform Mach 0.3 flow solution. (a) linear pressure, (b) dB scale.

4.4 Discussion

In this chapter, the flexibility of the wave expansion discretisation method (WED) to model linear homogeneous and inhomogeneous acoustic problems, was investigated with several applications in two and three dimensions. These problems included uniform and non-uniform flow field conditions within the continuum domain. In addition, non-uniform quadrilateral meshes in 2D and 3D and free tetrahedral meshes in 3D were also implemented.

The implementation of the WED method for these applications is not only remarkably simple, but also, no significant penalty was observed in the accuracy of the method. A point per wavelength ratio between 2 and 3.5 was used in all these examples.

The use of free tetrahedral meshes in 3D applications gives rise to the possibility of applying the WED approach to more general geometries. The formulation of the method need not be modified, as it is completely general to any nodal distribution. In addition, since for tetrahedral meshes the number of surrounding nodal points is in general less than that for hexahedral meshes, the computation of the pseudo-inverse is faster, reducing the overall computation time.

Chapter 5

The wave expansion method in elastodynamics

5.1 Introduction

The idea of using fundamental solutions of the governing differential equation as interpolating functions is not restricted exclusively to the acoustic case. Any problem in which the governing equations may be locally satisfied by a combination of plane waves (or any other suitable solution like, e.g. Green's functions) may, in principle, be solved using a similar approach.

Linear elastodynamics problems fall into this category. That is, the general displacement motion may be decomposed into two uncoupled wave equations, thus amenable to be solved by a WED scheme.

Elastic wave modelling represents, even to a greater extent than acoustic analogous, a major challenge to actual computational techniques. Several reasons for this could be mentioned, chief among them are the more intricate nature of the elastic wave propagation and the high computational cost required to solve even small problems. It is therefore of great interest to investigate the performance of the wave-based interpolation technique in the elastic case, as it is naturally well-posed to improve the accuracy of current available methods. This has been already demonstrated by Rice & Ruiz [158] in the analysis of a square plate vibration under clamped and simple supported boundary conditions, obtaining an average accuracy of 4 points per wavelength.

In the following section, a detailed description of the formulation of the wave expansion method applied to the simulation of isotropic elastic waves in two and three dimensions is given. Though the method follows the same basic principles described previously for the acoustic case, it is re-written here in the context of the elastic wave modelling. The details of the implementation for two and three dimensions (including the square plate analysis), validated with the corresponding test case examples, is then outlined. The results obtained are discussed in the final section.

5.2 General formulation of the WED method

In analogy with the formulation of the WED method outlined in the preceding sections, we seek to solve the governing differential equations by a finite difference discretisation. That is, to relate the unknowns at each discrete point in the domain to the values at a selected set of neighbouring points.

This interpolation process is based on fundamental solutions of the governing differential equations. Unlike the acoustic case, for elastodynamics and plate vibration analysis problems the generating functions are given as a combination of two types of plane waves. A detailed discussion on the implementation of the wave expansion method for two and three dimensional elastic problems, is given in the subsequent sections. The remaining details of the procedure which follows are otherwise similar as the acoustic WED, with the obvious exception of the boundary conditions.

Consider for simplicity, a two-dimensional isotropic homogeneous elastic domain Ω_E. A computational cell may be determined considering a general field point $\mathbf{x}_0$ and a finite number of surrounding points $\mathbf{x}_i$, as shown in figure 5.1.

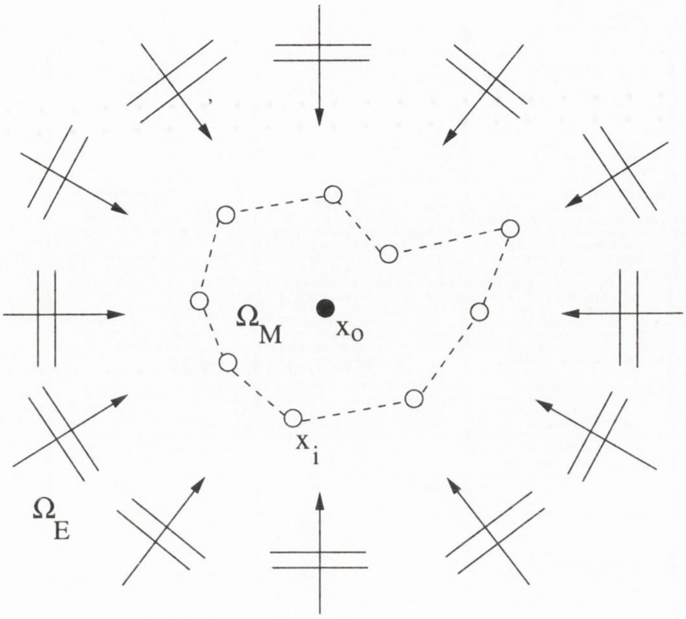

Figure 5.1: General computational molecule.

At each point $\mathbf{x} = (x, y)$, the displacement vector $\mathbf{u}$ has two degrees of freedom (dof)

$$\mathbf{u} = \left\{ \begin{array}{c} u_x \\ u_y \end{array} \right\}. \tag{5.1}$$

Provided that we have a set of functions that satisfy exactly the governing differential equations in Ω_M (see figure 5.1), we may relate the unknown displacement $\mathbf{u}_0$ at $\mathbf{x}_0$, in terms of the known displacement values $\mathbf{u}_i$ at the surrounding points $\mathbf{x}_i$ in the cell.

As discussed in the implementation of the WED for two- and three-dimensional elastic problems in the following sections, these functions may be conveniently expressed in terms of two types of uniformly distributed plane waves. Assuming that a number m of such plane waves are used, the displacement $\mathbf{u}_0$ at the point $\mathbf{x}_0$ may be expressed in vector notation as

$$\mathbf{u_0} = \mathbf{h}(\mathbf{x_0})\boldsymbol{\gamma}, \tag{5.2}$$

where, $\mathbf{h}$ is a $2 \times m$ matrix and $\boldsymbol{\gamma}$ is a $m \times 1$ column vector representing the strengths of each wave. If we apply the same approximation to the other n nodal positions in the cell, we obtain

$$\mathbf{u} = \mathbf{H}\boldsymbol{\gamma}, \tag{5.3}$$

where the $2n \times m$ matrix $\mathbf{H}$ is formed from individual matrices $\mathbf{h}$ evaluated at points $\mathbf{x_i}$.

Imposing the condition $m > n$ and then substituting equation 5.3 into 5.2 yields the computational template

$$\mathbf{u_o} - \mathbf{h}(\mathbf{x_o})\mathbf{H}^{+}\mathbf{u} = 0, \tag{5.4}$$

where superscript "+" denotes the Morse-Penrose pseudo-inverse operation. Thus, the locally least L^2-norm solution for γ is obtained whilst still ensuring that the expansion in equation 5.2 gives consistent results at all the other nodes in the template. Therefore, one or more boundary conditions may additionally be imposed by augmenting the row count of $\mathbf{H}$ prior to inversion.

After pseudo-inversion, the augmented matrix $\mathbf{H}_{aug}$ may be left-right partitioned into $(\mathbf{H}^{+}_{aug})_L$ and $(\mathbf{H}^{+}_{aug})_R$. Then, a modified template with a forcing right hand side may be established as

$$\mathbf{u_0} - \mathbf{h}(\mathbf{x_0})(\mathbf{H}^{+}_{\mathbf{aug}})_{\mathbf{L}}\mathbf{u} = \mathbf{h}(\mathbf{x_0})(\mathbf{H}^{+}_{\mathbf{aug}})_{\mathbf{R}}\mathbf{f}, \tag{5.5}$$

where $\mathbf{f}$ is a vector with the corresponding loading values (not necessarily restricted to the boundary points).

In addition, Dirichlet constraints may be directly imposed on the appropriate degrees of freedom in the overall assembled stiffness matrix. Once the templates have been formed, an overall sparse equation system

$$\mathbf{K}\mathbf{u} = \mathbf{f} \tag{5.6}$$

may be assembled with each template contributing two rows.

5.3 Application to linear elastic wave analysis

5.3.1 Description of the physical problem

Let us consider only elastodynamics problems in which body forces are absent and wave motions are generated by excitation of the external boundary of a body. In this case, the displacement equations of motion form a system of homogeneous partial differential equations, given by (see Appendix B)

$$\mu\nabla^2\mathbf{u} + (\lambda_e + \mu)\nabla\nabla\cdot\mathbf{u} = \rho\ddot{\mathbf{u}}, \tag{5.7}$$

where μ and λ_e are the Lame's elastic constants, $\mathbf{u}$ is the displacement vector and ρ is the material density.

It can be shown that equation 5.7 governs two fundamentally different types of displacement waves, given by [226]

$$\nabla^2\mathbf{u} = \ddot{\mathbf{u}}/c_L^2 \tag{5.8}$$

and

$$\nabla^2\mathbf{u} = \ddot{\mathbf{u}}/c_T^2, \tag{5.9}$$

where

$$c_L = \sqrt{\frac{\lambda_e + 2\mu}{\rho}} \tag{5.10}$$

and

$$c_T = \sqrt{\frac{\mu}{\rho}}, \tag{5.11}$$

are the corresponding speed of propagation.

Equation 5.8 is a wave equation for $\mathbf{u}$ governing waves in which deformation consists of volume change only, i.e. dilatational waves. On the other hand, equation 5.9 is a wave equation for $\mathbf{u}$ governing waves in which deformation consists of rotation only, i.e. equivoluminal waves (volume change is zero).

Thus, the nature of the displacement motion is the resulting combination of these two types of waves propagating at different speed. To illustrate the concept, consider a three dimensional plane wave propagating along the positive x_1 axis, figure 5.2.

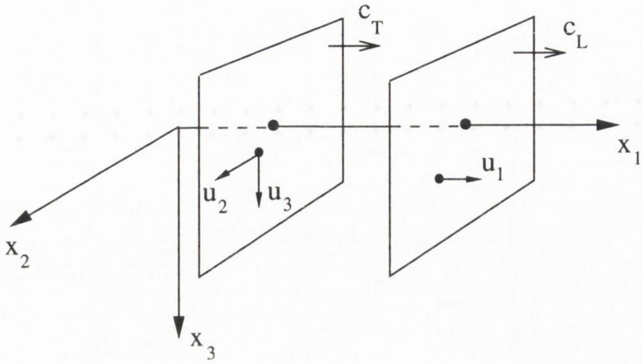

Figure 5.2: Plane dilatational and equivoluminal displacement waves

As shown, u_1 is a plane dilatational wave propagating with speed c_L, and is directed along the propagation direction, or normal to its plane. u_2 is a plane equivoluminal wave, travelling with speed c_T, and directed along the x_2 axis. Finally u_3 is also a plane equivoluminal wave, travelling with speed c_T, but directed along its plane in the x_3 direction.

It should be noted that the components of the displacement vector, form a system of waves that propagate in the x_1 direction, but are *independent* of each other[1]. These waves are only coupled at the boundaries of the continuum domain by the boundary conditions.

If we assume that only time harmonic displacement waves of the form

$$\mathbf{u}(\mathbf{x}, t) = \mathbf{u}(\mathbf{x})e^{(\iota\omega t)}$$

are present, where $\iota = \sqrt{-1}$ and $\omega = 2\pi f$ is the circular frequency, then equations 5.8 and 5.9 become the Helmholtz equations

$$\nabla^2\mathbf{u}(\mathbf{x}) + k_L^2\mathbf{u}(\mathbf{x}) = 0 \tag{5.12}$$

and

$$\nabla^2\mathbf{u}(\mathbf{x}) + k_T^2\mathbf{u}(\mathbf{x}) = 0, \tag{5.13}$$

---

[1] For plane X_1X_2 horizontally oriented, these waves may be identified as the *compressional* (P), *horizontal shear* (SH) and *vertical shear* (SV) seismic waves, respectively.

where $k_L = \omega/c_L$ and $k_T = \omega/c_T$ are the dilatational and equivoluminal wave numbers, respectively.

For the purpose of this study, a convenient solution to equations 5.12 and 5.13 is given by plane waves propagating at c_L and c_T (though other fundamental solutions are also possible as, e.g., Green's functions). We may therefore write

$$\mathbf{u}(\mathbf{x}) = \gamma\ e^{-\iota k_L \mathbf{x}\cdot\mathbf{q}} \tag{5.14}$$

and

$$\mathbf{u}(\mathbf{x}) = \gamma\ e^{-\iota k_T \mathbf{x}\cdot\mathbf{q}}, \tag{5.15}$$

where $\iota = \sqrt{-1}$, γ is the strength of the plane wave with directional vector $\mathbf{q}$ and $k_L = \omega/c_L$, $k_T = \omega/c_T$ are the dilatational and equivoluminal wave numbers, respectively.

Given an isotropic elastic domain Ω_E with boundary $\Gamma_E = \Gamma_C \cup \Gamma_F$, the displacement field governed by the dynamic equations 5.12 and 5.13 is uniquely defined, provided that one boundary condition is specified on Γ_E. In general, two boundary conditions are considered, namely

- Clamped condition

$$\mathbf{u}(\mathbf{x}_b) = 0,\ \ \mathbf{x}_b \in \Gamma_C, \tag{5.16}$$

- Free condition

$$\sigma_n = \tau_{ns_1} = \tau_{ns_2} = 0,\ \ \mathbf{x}_b \in \Gamma_F, \tag{5.17}$$

where σ_n and τ_{ns} are the normal and tangential edge stress components, respectively. By use of the stress-strain tensor relationship [227], conditions 5.17 may be conveniently expressed in terms of the displacement vector $\mathbf{u}$ as

$$\left.\begin{array}{c} (2\mu + \lambda_e)\partial u_n/\partial n + \lambda_e\ (\partial u_{ns_1}/\partial ns_1 + \partial u_{ns_2}/\partial ns_2) \\ \partial u_n/\partial ns_1 + \partial u_{ns_1}/\partial n \\ \partial u_n/\partial ns_2 + \partial u_{ns_2}/\partial n \end{array}\right\} = 0,\ \ \mathbf{x}_B \in \Gamma_F, \tag{5.18}$$

where the Lame's constants λ_e and μ, may be expressed in terms of the material properties ν (Poisson's compressibility ratio) and E (Young's modulus) as [227]

$$\mu = \frac{E}{(2+2\nu)} \tag{5.19}$$

and

$$\lambda_e = \frac{\nu E}{(1+\nu)(1-2\nu)}. \tag{5.20}$$

5.3.2 Two dimensional problems

5.3.2.1 Problem definition

We are interested here in the plain strain elastic solution (i.e, $u_z = 0$) of a two dimensional isotropic domain subjected to boundary conditions 5.16 and 5.17.

The resulting displacement motion is then a combination of dilatational and equivoluminal waves, propagating at c_L and c_T respectively int the x - y coordinate plane, figure 5.3.

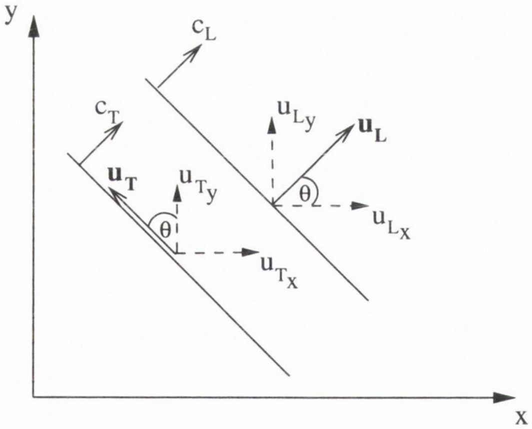

Figure 5.3: Two dimensional dilatational and equivoluminal waves.

The displacement vector $\mathbf{u_0}$ at a general field point $\mathbf{x}_0$

$$\mathbf{u_0} = \begin{pmatrix} u_x \\ u_y \end{pmatrix},$$

may thus be written as

$$\mathbf{u_0} = \begin{bmatrix} \cos\theta & -\sin\theta \\ \sin\theta & \cos\theta \end{bmatrix} \begin{pmatrix} e^{-\iota k_L \mathbf{x}_0\cdot\mathbf{q}} \\ e^{-\iota k_L \mathbf{x}_0\cdot\mathbf{q}} \end{pmatrix}, \tag{5.21}$$

where θ is the angle of the propagation direction of the plane wave displacement. It is useful for the subsequent sections, to define here the Cartesian components of $\mathbf{u}_L$ and $\mathbf{u}_T$ into separate vectors as

$$\mathbf{w_L} = \begin{pmatrix} \cos\theta \\ \sin\theta \end{pmatrix}, \ \mathbf{w_T} = \begin{pmatrix} -\sin\theta \\ \cos\theta \end{pmatrix} \tag{5.22}$$

5.3.2.2 Numerical implementation

Consider the nine noded computational molecule shown in figure 5.4, where each node has two degrees of freedom given by equation 5.21.

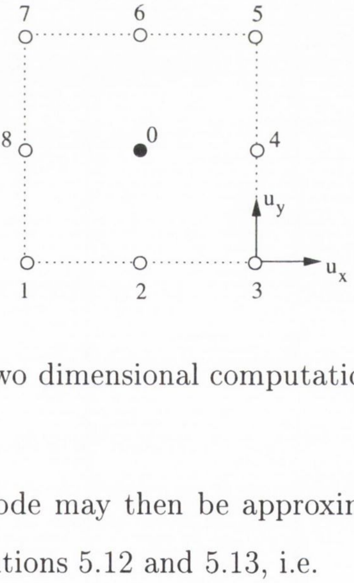

Figure 5.4: Two dimensional computational molecule.

The displacement at each node may then be approximated by a set of $\frac{m}{2}$ equally distributed fundamental solutions 5.12 and 5.13, i.e.

$$u_x^j(\mathbf{x}) = \left\{ \begin{array}{ll} \cos(\frac{4\pi j}{m})\ e^{-\iota k_L \mathbf{x}\cdot\mathbf{q}_j}; & j = 1,\ldots,\frac{m}{2} \\ -\sin(\frac{4\pi j}{m})\ e^{-\iota k_T \mathbf{x}\cdot\mathbf{q}_j}; & j = \frac{m}{2}+1,\ldots,m. \end{array} \right\}, \tag{5.23}$$

and

$$u_y^j(\mathbf{x}) = \left\{ \begin{array}{ll} \sin(\frac{4\pi j}{m})\ e^{-\iota k_L \mathbf{x}\cdot\mathbf{q}_j}; & j = 1,\ldots,\frac{m}{2} \\ \cos(\frac{4\pi j}{m})\ e^{-\iota k_T \mathbf{x}\cdot\mathbf{q}_j}; & j = \frac{m}{2}+1,\ldots,m. \end{array} \right\}, \tag{5.24}$$

where the propagation direction vectors $\mathbf{q}_j$ are given by

$$\mathbf{q}_j = \left(\cos\frac{4\pi j}{m},\ \sin\frac{4\pi j}{m}\right);\ j = 1, \ldots, m. \tag{5.25}$$

Equation 5.2 then results

$$\mathbf{u_o} = \mathbf{h}\boldsymbol{\gamma} \tag{5.26}$$

where

$$h_j = \begin{pmatrix} u_x^j(\mathbf{x}_0) \\ u_y^j(\mathbf{x}_0) \end{pmatrix},$$

is a matrix of dimension $2 \times m$, and $\boldsymbol{\gamma}$ is a vector of dimension $m \times 1$. Evaluating $\mathbf{h}$ at all the neighbouring points in the computational molecule, we obtain the constraint equation

$$\mathbf{u} = \mathbf{H}\boldsymbol{\gamma}, \tag{5.27}$$

where

$$H_{ij} = \begin{pmatrix} u_x^j(\mathbf{x}_i) \\ u_y^j(\mathbf{x}_i) \end{pmatrix}.$$

The number of entries on $\mathbf{H}$ depends on the number of surrounding points in the cell, each one contributing with two rows. For a 9-node two-dimensional cell, for example, $\mathbf{H}$ has dimension $16 \times m$.

Boundary conditions

To implement the free traction condition ($\sigma_n = \tau_{ns} = 0$), the matrix $\mathbf{H}$ was augmented using equation 5.18 before the pseudo-inversion operation. This requires evaluating the corresponding displacement components of $\mathbf{u_L}$ and $\mathbf{u_T}$ (see figure 5.3) along the normal and tangential directions at the boundary point $\mathbf{x}_B$.

Consider, for example, the normal and tangential vectors of edge Γ_2 in the validation model shown in figure 5.5 (section 5.3.3.1), expressed in matrix form as

$$\mathbf{N} = \begin{bmatrix} \cos\alpha & \sin\alpha \\ \cos(\alpha + \pi/2) & \sin(\alpha + \pi/2) \end{bmatrix}.$$

The dilatational and equivoluminal displacement along the normal and tangential vectors is then given by

$$\mathbf{u_L} = \mathbf{N} \cdot \mathbf{w_L}\ e^{-\iota k_L \mathbf{x}_b \cdot \mathbf{q}}, \tag{5.28}$$

and

$$\mathbf{u_T} = \mathbf{N} \cdot \mathbf{w_T}\ e^{-\iota k_T \mathbf{x}_b \cdot \mathbf{q}}, \tag{5.29}$$

where $\mathbf{w_L}$ and $\mathbf{w_T}$ are the Cartesian components of the displacement waves defined in relationship 5.22.

Deriving 5.28 and 5.29 with respect to $\mathbf{N}$ yields

$$\mathbf{du_L} = -\mathbf{u_L} \cdot \mathbf{w_L^T} \cdot \mathbf{N^T}\ \iota\ k_L \tag{5.30}$$

and

$$\mathbf{du_T} = -\mathbf{u_T} \cdot \mathbf{w_L^T} \cdot \mathbf{N^T}\ \iota\ k_T \tag{5.31}$$

where the resulting 2-by-m dimension matrices $\mathbf{du_L}$ and $\mathbf{du_T}$ are

$$\mathbf{du_L} = \begin{bmatrix} \partial u_n^L/\partial n & \partial u_n^L/\partial ns \\ \partial u_{ns}^L/\partial n & \partial u_{ns}^L/\partial ns \end{bmatrix} \tag{5.32}$$

and

$$\mathbf{du_T} = \begin{bmatrix} \partial u_n^T/\partial n & \partial u_n^T/\partial ns \\ \partial u_{ns}^T/\partial n & \partial u_{ns}^T/\partial ns \end{bmatrix}. \tag{5.33}$$

The constraint equation 5.27, may be then augmented as

$$\begin{pmatrix} \mathbf{u} \\ 0 \\ 0 \end{pmatrix} = \begin{pmatrix} \mathbf{H} \\ \sigma_n^L + \sigma_n^T \\ \tau_{ns}^L + \tau_{ns}^T \end{pmatrix} \gamma = \mathbf{H}_{aug}\gamma, \tag{5.34}$$

where the values of σ_n^L, σ_n^T, τ_{ns}^L and τ_{ns}^T are obtained substituting equations 5.32 and 5.33 into equation 5.18 for the dilatational and equivoluminal waves, respectively. Thus, equation 5.5 may be written simply as

$$\mathbf{u_0} = \mathbf{h}(\mathbf{H^+_{aug}})_\mathbf{L}\mathbf{u}. \tag{5.35}$$

In addition to implementing free boundary conditions by adding extra restraints as above, clamped conditions were directly imposed on the appropriate degrees of freedom in the overall assembled stiffness matrix.

For points with free and clamped restraints, **H** was augmented using 5.18 and then direct restraint was added to both degrees of freedom.

5.3.3 Two dimensional validation example

5.3.3.1 Modelling details

To illustrate the implementation of the proposed technique in two dimensional problems, an isotropic domain with material properties $E = 70GPa$, $\nu = 0.3$ and $\rho = 2770kg^{-3}$ was analysed. Thus, from equations 5.10 and 5.11, the speed of propagation of dilatational and longitudinal waves is $c_L = 5832ms^{-1}$ and $c_T = 3118ms^{-1}$, respectively.

As shown in figure 5.5, the geometry of the problem is given by a polygonal shape of side lengths $\Gamma_1 = 0.6m$, $\Gamma_2 = 0.45m$, $\Gamma_3 = 0.4m$ and $\Gamma_4 = 0.4m$, where Γ_2 is at $\alpha = 0.464rad$ from the vertical axis.

The problem was solved considering the following boundary conditions:

(i) *Clamped all round.*

$$\mathbf{u}(\mathbf{x_b}) = 0, \ \forall \ \mathbf{x_b} \in \Gamma_1 \cup \Gamma_2 \cup \Gamma_3 \cup \Gamma_4. \tag{5.36}$$

(ii) *Edge* Γ_2 *free.*

$$\mathbf{u}(\mathbf{x_b}) = 0, \ \mathbf{x_b} \in \Gamma_1, \Gamma_3, \Gamma_4. \tag{5.37}$$

$$\sigma_n = \tau_{ns} = 0, \ \mathbf{x_b} \in \Gamma_2. \tag{5.38}$$

(iii) *Edges* Γ_2 *and* Γ_3 *free.*

$$\mathbf{u}(\mathbf{x_b}) = 0, \ \mathbf{x_b} \in \Gamma_1, \Gamma_4. \tag{5.39}$$

$$\sigma_n = \tau_{ns} = 0, \ \mathbf{x_b} \in \Gamma_2, \Gamma_3. \tag{5.40}$$

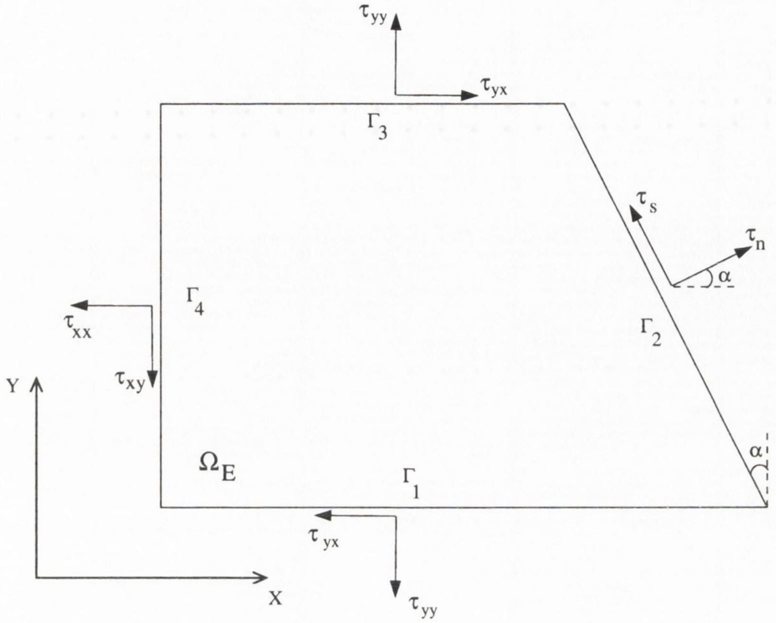

Figure 5.5: Two dimensional example.

To implement the free boundary condition, 5.38 and 5.40, two different formulations denoted here as partial edge implementation (FD_p) and full edge implementation (FD_f), were explored.

In the first test, FD_p, the computational molecule for each node was constructed considering strictly the surrounding points in the mesh. Hence, nine noded, six noded and four noded cells were formed for field, edge and corner points respectively. Consider for illustration purposes, a corner section of the mesh as shown in figure 5.6. To construct the local template matrix $\mathbf{H}$ at the upper right corner in the mesh, a molecule was formed considering surrounding points 13, 15 and 49. To implement a free boundary condition, $\mathbf{H}$ was augmented by adding the conditions

$$\begin{pmatrix} \sigma_n \\ \tau_{ns} \end{pmatrix} = \begin{pmatrix} (2\mu + \lambda_e)\partial u_n/\partial n + \lambda_e \, \partial u_{ns_1}/\partial ns_1 \\ \partial u_n/\partial ns_1 + \partial u_{ns_1}/\partial n \end{pmatrix} = 0 \tag{5.41}$$

for points 8, 13 and 15, according to the edge (or edges for point 8) normal and tangential directions. Once $\mathbf{H_{aug}}$ was formed, the template calculation was done according to equation 5.34.

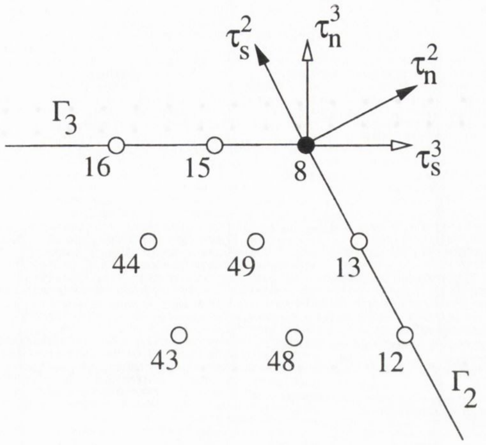

Figure 5.6: Boundary condition implementation.

In the second test, FD$_f$, the local template matrix **H** was constructed considering nine noded computational cells for every discretisation point in the mesh. Hence, for node 8 in figure 5.6 a template was formed using nodes 12, 13, 15, 16, 43, 44, 48, 49.

To implement the free boundary condition, the normal and tangential edge stress components at node 8 *only* were considered for augmenting **H**.

Unlike the acoustic case, for which and optimal meshing spacing in two dimensions was established by Caruthers *et al.* [152], for the elastic case the optimal meshing using the WED method has not yet been determined.

Thus, in each test case, the accuracy of the proposed FD schemes was assessed using three different mesh densities. The properties of the meshes along with the nodal spacing h along the edge Γ_1, is listed in table 5.1.

The results obtained with the wave expansion method, were compared with a similar finite element model using ANSYS with #PLANE82 quadratic elements. The FD and FE meshes corresponding to Table 5.1 are plotted in figure 5.7. The FD mesh is represented by unfilled + filled nodes, whilst the FEM mesh is represented by unfilled nodes only.

The resonance frequencies were found by searching for the minimum values of the

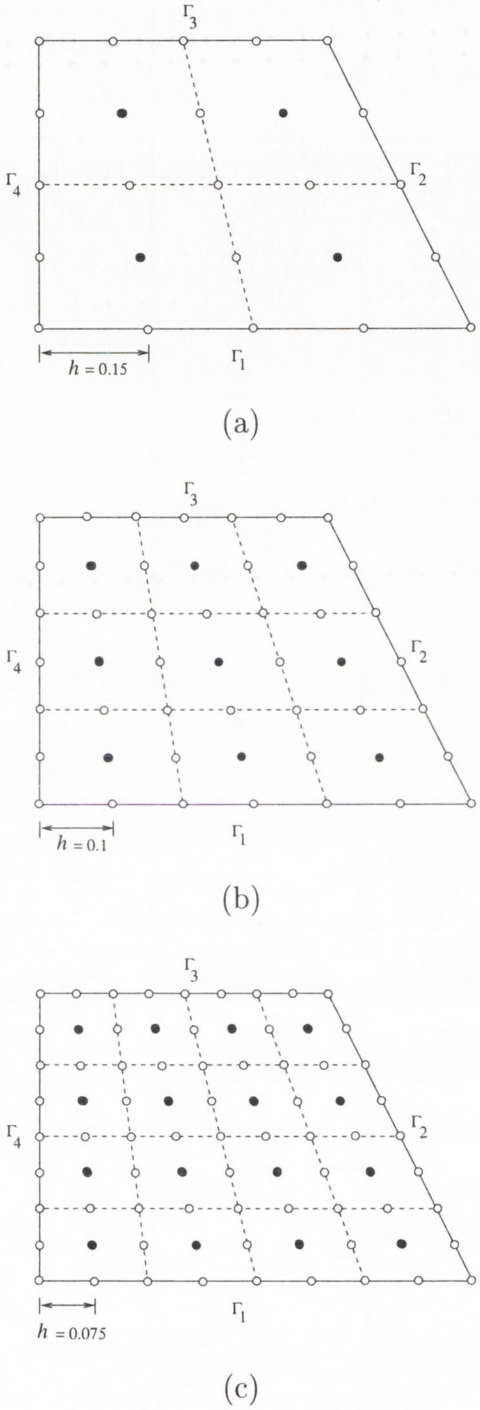

Figure 5.7: FD and FE meshes. (a) Mesh 1. (b) Mesh 2. (c) Mesh 3.

	FD		FE		h
	nodes	dof	nodes	dof	(Γ_1)
mesh 1	25	50	21	42	0.15
mesh 2	49	98	40	80	0.1
mesh 3	81	162	65	130	0.075

Table 5.1: Properties of FD and FE models

determinant of the stiffness matrix over a frequency range with a frequency step of 1Hz. The corresponding mode shape was then ascertained by enforcing a single point Dirichlet condition at a particular resonance frequency (an harmonic analysis), at one of the unrestrained field nodes.

As a benchmark for this study, each test case was modelled in ANSYS using a finer mesh of 32,821 nodes and 10,800 elements, figure 5.8.

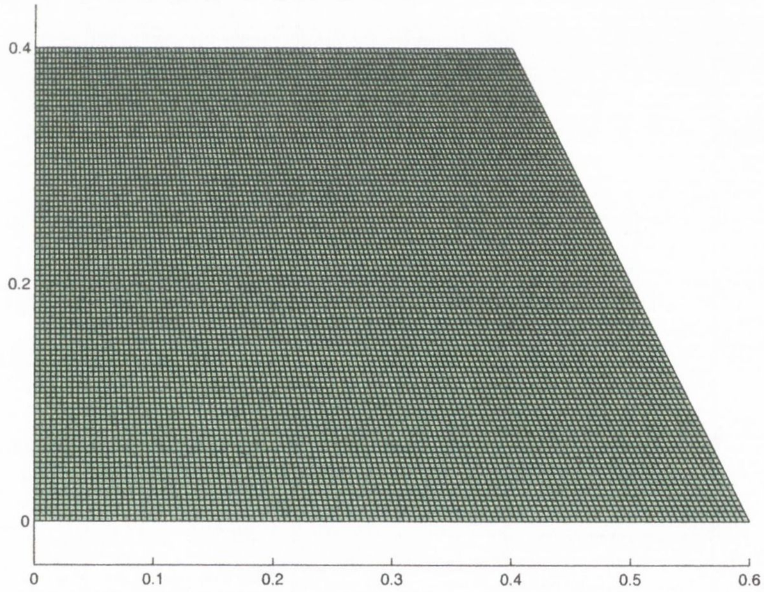

Figure 5.8: Reference mesh.

This gives a sufficient number of nodes per wavelength to consider it a good approximation of an exact solution. The error was then calculated as the percentage difference in Hz between the exact resonant frequencies and those obtained with the FE and FD$_p$ and FD$_f$ methods. That is,

$$E_{\%} = \frac{|f_n - F_n|}{100}, \tag{5.42}$$

where f_n are the natural frequencies calculated with the FD and FE methods, and F_n are the exact natural frequencies.

5.3.3.2 Results

The accuracy of the wave expansion method in the results obtained below, is assessed in terms of the nodal points per wavelength ratio (ppw) required to obtain the desired solution. In general, the ppw is defined as

$$ppw = \frac{c}{f \cdot h}, \tag{5.43}$$

where c is the velocity of propagation of the wave, f is the frequency and h is the maximum nodal spacing in the mesh. Since the displacement is produced by a combination of two types of waves, there are two possible values for the ppw, depending on whether c_L or c_T is used in equation 5.43. The minimum value for the ppw, used hereafter and referred to simply as ppw, is then obtained using the velocity of propagation of equivoluminal waves, $c_T = 3118ms^{-1}$, in equation 5.43.

Clamped all round

Since the basic difference between the two approaches resides in the implementation of the free boundary condition, no differentiation has been done between the partial or the full edge implementation (FD$_p$ or FD$_f$) in the resonant frequencies listed in table 5.2.

As shown, the wave expansion method is much more accurate than the finite element method for all natural frequencies in comparison to the "exact" solution. Note that, from the percentage error (equation 5.42), for the mesh 1 the solution for the FD is actually more accurate than that of the FE using the mesh 2, with nearly twice as many nodes, figure 5.9.

mesh 1		*mesh 2*		*mesh 3*		*FE reference*
FD	FE	FD	FE	FD	FE	*solution*
6797	6979	6794	6818	6791	6795	**6783**
7696	8255	7723	7830	7727	7758	**7722**
8314	9026	8260	8397	8236	8258	**8198**
10476	12003	10379	10667	10354	10441	**10312**
10809	13483	10755	11700	10727	10998	**10678**
11492	16848	11286	12134	11327	11586	**11352**
12780	17987	12141	13310	12126	12485	**12105**
13971	20013	13378	14364	13292	13616	**13206**
14298	29486	13523	15574	13495	14693	**13443**
-	-	14122	16097	14129	14780	**14092**

Table 5.2: Natural frequencies for the all round clamped case

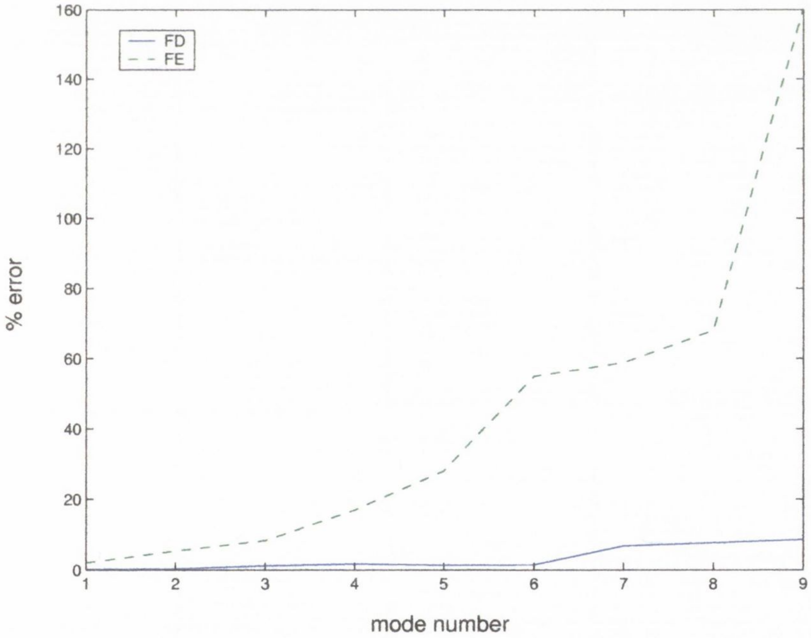

Figure 5.9: Error for mesh 1. All edges clamped.

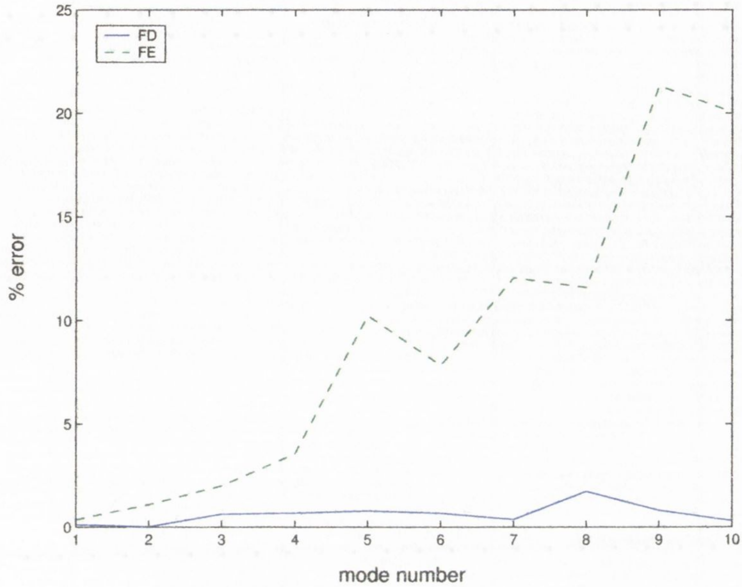

Figure 5.10: Error for mesh 2. All edges clamped.

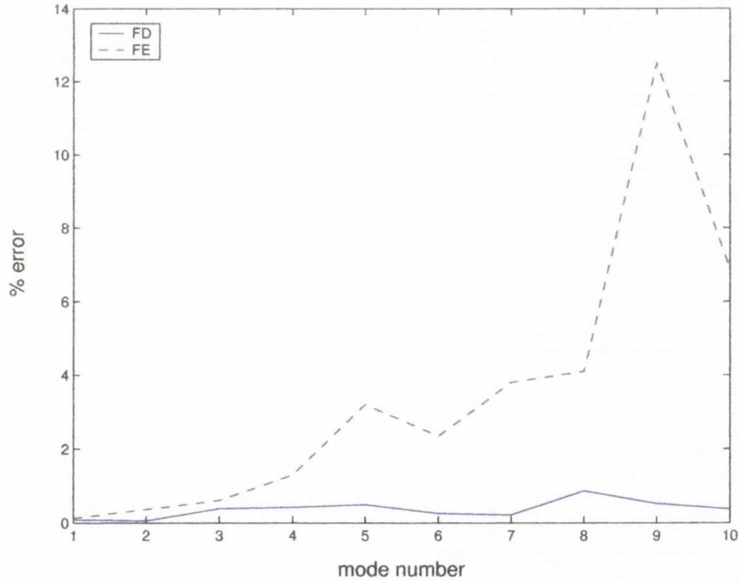

Figure 5.11: Error for mesh 3. All edges clamped.

The error for the FD and FE using mesh 2 and mesh 3 is shown in figures 5.10 and 5.11, respectively. As illustrated, as the mesh is refined the rate of convergence of the FE method to the exact natural frequencies is faster than that of the FD. For the mesh 3, the accuracy between the two methods becomes comparable.

One edge free

The resonant frequencies for the FE method and the FD$_p$ and FD$_f$ models are detailed in table 5.3.

mesh 1			*mesh 2*			*mesh 3*			*FE reference solution*
FD$_p$	FD$_f$	FE	FD$_p$	FD$_f$	FE	FD$_p$	FD$_f$	FE	
4596	*4665*	4730	4713	4614	4640	4785	4599	4608	**4568**
6500	6841	6990	6627	6755	6815	6826	6714	6740	**6650**
7167	7076	7906	*6943*	*7003*	7112	7109	6981	7010	**6937**
8473	8640	9255	8530	8587	8727	8554	8560	8610	**8529**
8956	8954	10156	9036	9088	9451	9084	9099	9195	**9102**
9324	9360	11896	9237	9269	9546	*9212*	*9227*	9300	**9170**
10477	10735	14235	10691	10890	12287	10608	10785	11131	**10619**
11397	12014	15756	11936	11981	12606	11715	11834	12151	**11755**
12283	12212	16281	12045	12106	13115	11965	11980	12446	**11955**
12999	13052	19194	12861	12878	13875	12006	12057	12514	**11976**

Table 5.3: Resonant frequencies for edge Γ_2 free.

As shown, the process of refining the mesh (i.e. increasing the ppw) does not systematically improve the accuracy in the FD$_p$ scheme for the entire range of frequencies. A loss of convergence is observed at higher frequencies, with increasing error whenever the ppw ≥ 4.5. (For clarity, the frequencies for which the ppw $= 4.5$ in each mesh, are emphasised).

The FD$_f$ model, on the other hand, has a similar performance behaviour as the FE model. That is, it converges monotonically to the exact solution as the number of nodal points per wavelength increases. However, the FD$_p$ approach is more accurate than the FD$_f$ for ppw's ≤ 4.5. As shown in figures 5.12-5.14, in comparison to

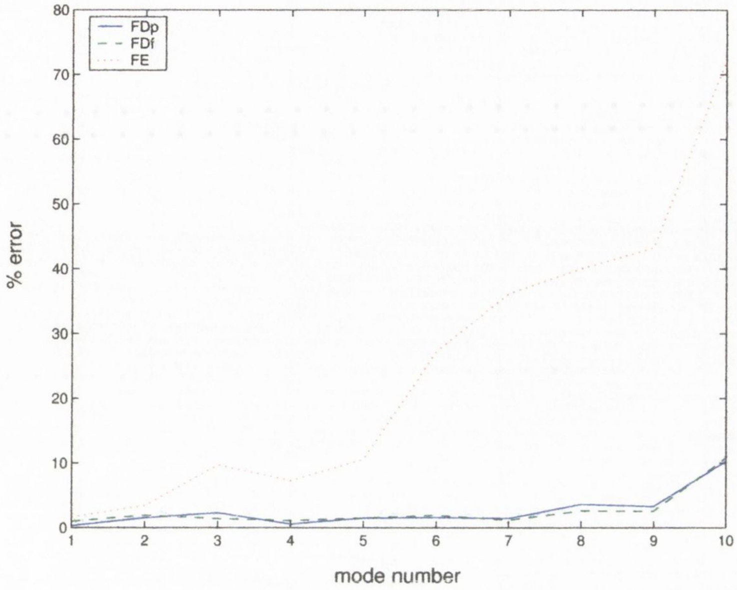

Figure 5.12: Error comparison for mesh 1. One edge free.

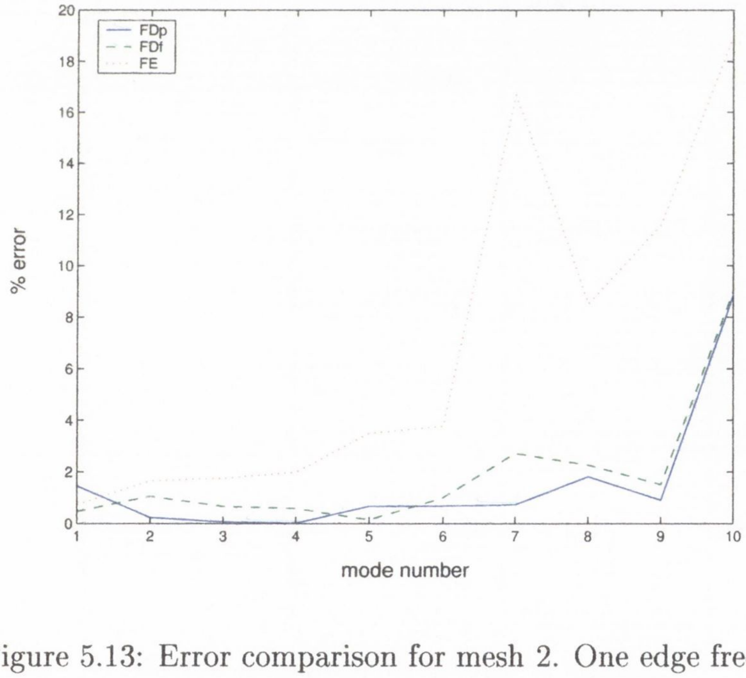

Figure 5.13: Error comparison for mesh 2. One edge free.

the FE model, both FD schemes give overall better results, particularly at higher frequencies.

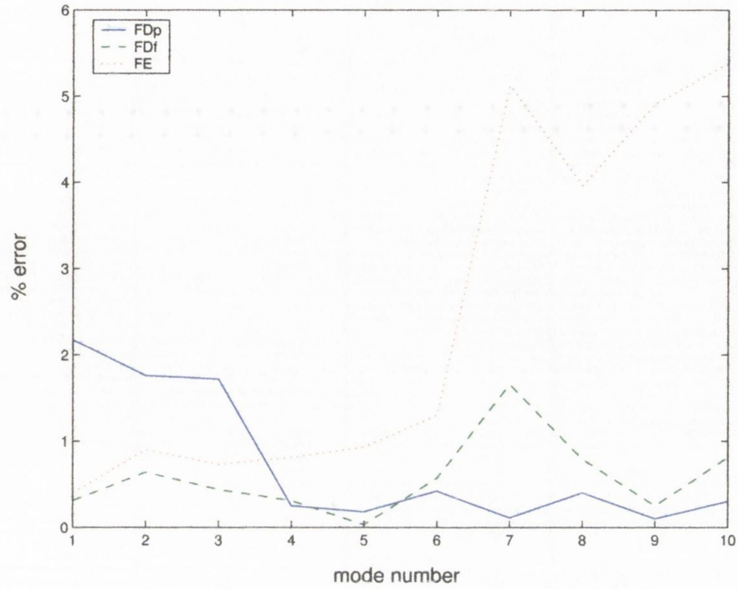

Figure 5.14: Error comparison for mesh 3. One edge free.

In order to evaluate whether the different behaviour between the FD_p and the FD_f is related to the conditioning of the final system (equation 5.6), the condition number of the overall assembled stiffness matrix $\mathbf{K}$ was calculated for each natural frequency. As shown in figure 5.15 for the mesh 1, above the third resonant frequency the conditioning of the system for the FD_p formulation is significantly higher than that obtained with the FD_f approach.

For meshes 2 and 3, however, the difference in the conditioning of the final system between the FD_p and the FD_f schemes is reduced, figures 5.16 and 5.17.

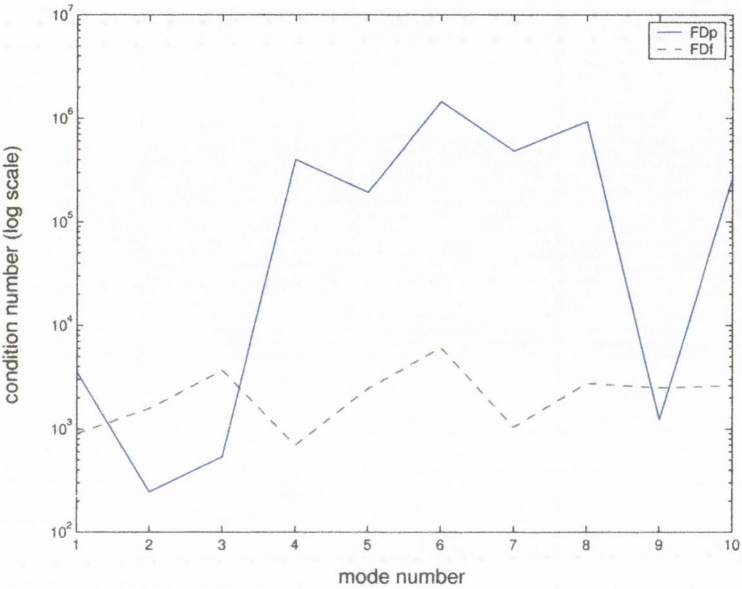

Figure 5.15: Condition number for FD_p and FD_f. Mesh 1. One edge free.

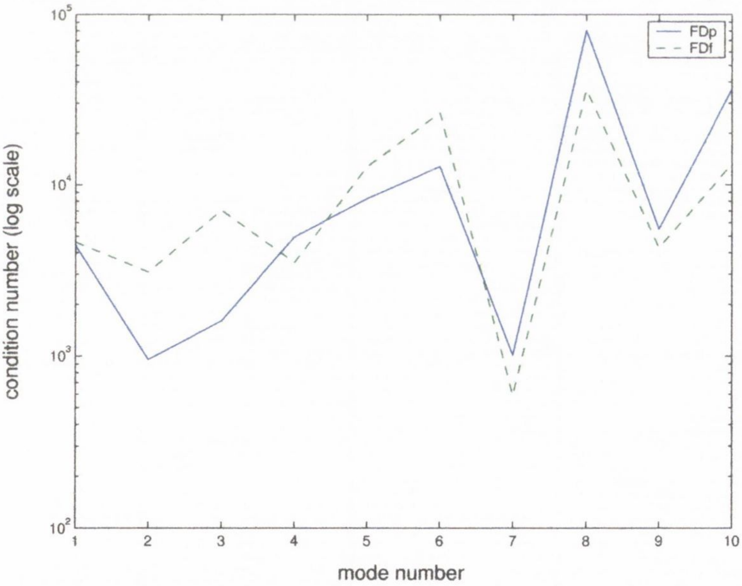

Figure 5.16: Condition number for FD_p and FD_f. Mesh 2. One edge free.

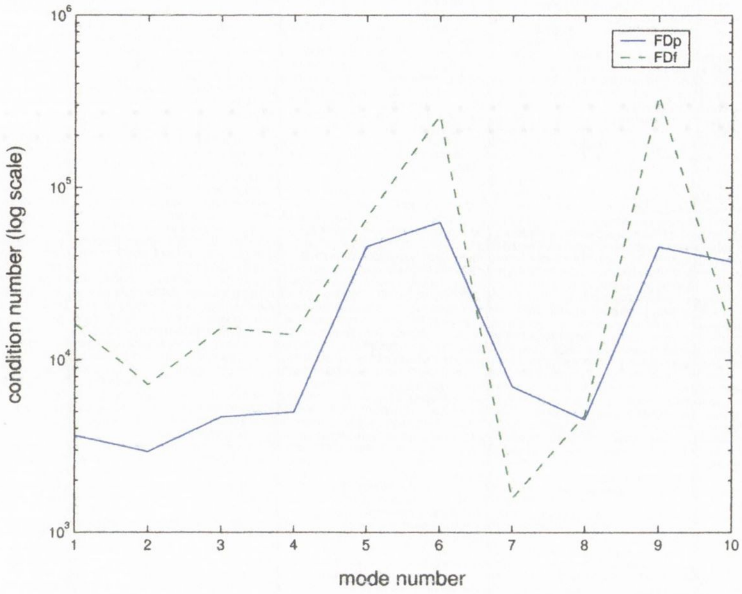

Figure 5.17: Condition number for FD_p and FD_f. Mesh 3. One edge free.

Two edges free

The 10 lowest resonant frequencies, assuming a free boundary condition in edges Γ_2 and Γ_3 for the FD_p, FD_f and FE methods, are summarised in table 5.4.

In this case, the FD_f formulation shows a better performance in comparison to the FD_p for most resonant frequencies. The similar behaviour observed for the FD_p in the one edge free case is exhibit here, i.e., the method fails to converge whenever the number of nodal points per wavelength increase above certain value. Unlike the one edge free case, however, this value is not clearly defined.

The FD_f method, on the other hand, converges monotonically to the exact solution as the mesh is refined. Despite the fact that the rate of convergence is not as fast as that shown by the FE, the FD_f approach gives overall a more accurate solution, in particular for the mesh 1. For comparison, the error for the three methods is plotted in figures 5.18-5.20.

In order to explore the stability of the wave expansion approaches and to compare against that shown by these methods for the one edge free case, the condition number

mesh 1			*mesh 2*			*mesh 3*			*FE reference*
FD$_p$	FD$_f$	FE	FD$_p$	FD$_f$	FE	FD$_p$	FD$_f$	FE	*solution*
3480	3488	3491	3499	3485	3483	3504	3484	3481	**3476**
4043	4210	4215	4222	4182	4176	4251	4175	4169	**4165**
4938	4997	5073	4953	4956	4941	5007	4922	4915	**4900**
6524	6906	7319	6693	6772	6865	6845	6743	6778	**6722**
7948	8082	8916	8103	8027	8307	8039	7996	8079	**7961**
8279	8290	10095	8292	8361	8583	8334	8351	8416	**8330**
8966	9124	10575	8929	9040	9456	8978	9012	9158	**9017**
10006	10043	11487	10050	9878	10066	9745	9833	9888	**9794**
11305	10515	12478	10790	10471	11263	10270	10343	10591	**10257**
12501	10877	14211	11230	10847	11616	10787	10837	11022	**10799**

Table 5.4: Resonant frequencies for edges Γ_2 and Γ_3 free.

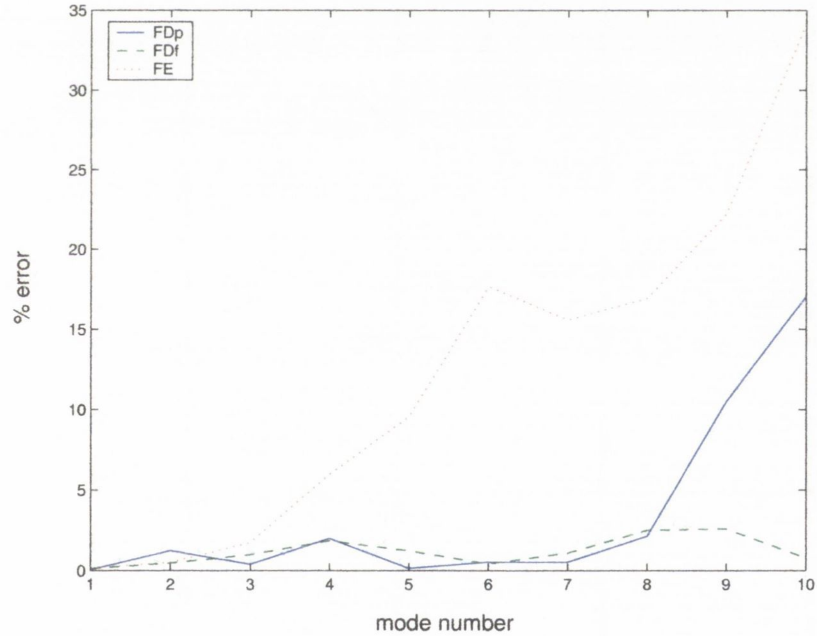

Figure 5.18: Error comparison for mesh 1. Two edges free.

for the FD$_p$ and FD$_f$ schemes was calculated for all the resonant frequencies using the three mesh densities. The results are plotted in figures 5.21-5.23.

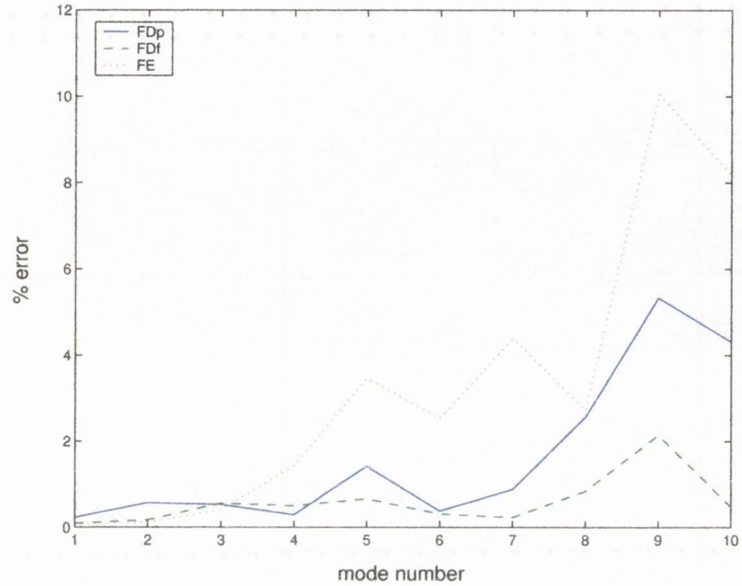

Figure 5.19: Error comparison for mesh 2. Two edges free.

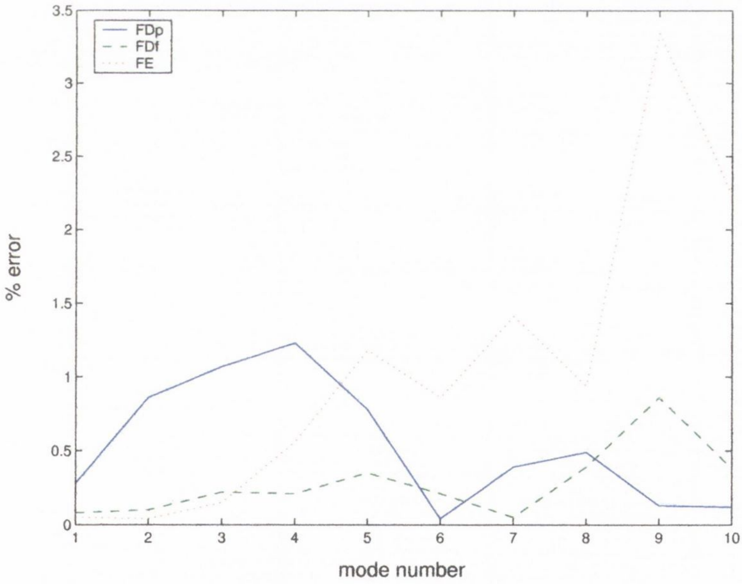

Figure 5.20: Error comparison for mesh 3. Two edges free.

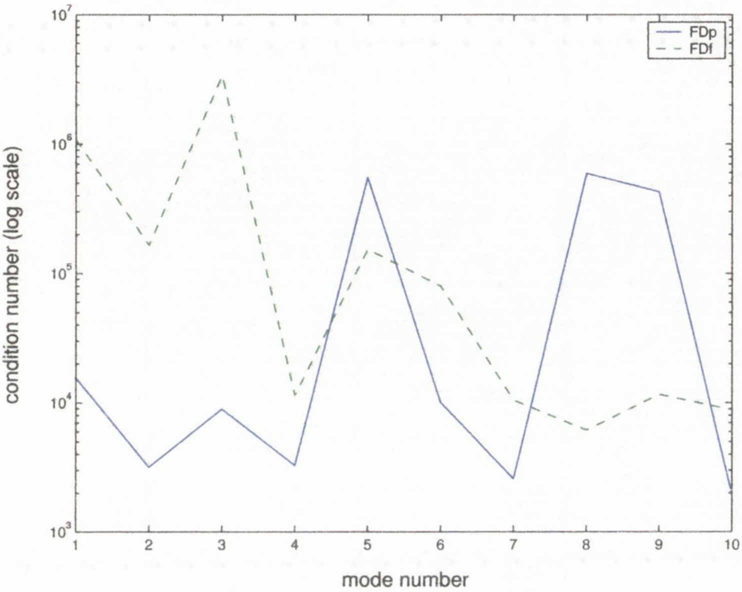

Figure 5.21: Condition number for FD_p and FD_f. Mesh 1. Two edges free.

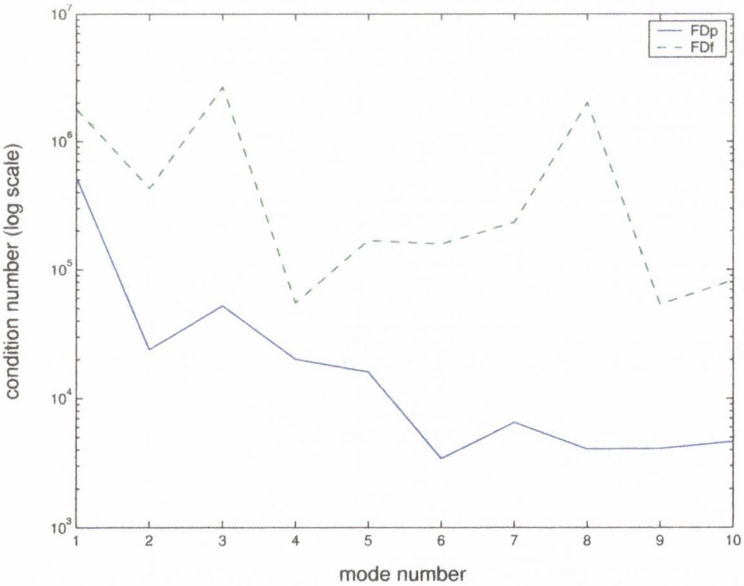

Figure 5.22: Condition number for FD_p and FD_f. Mesh 2. Two edges free.

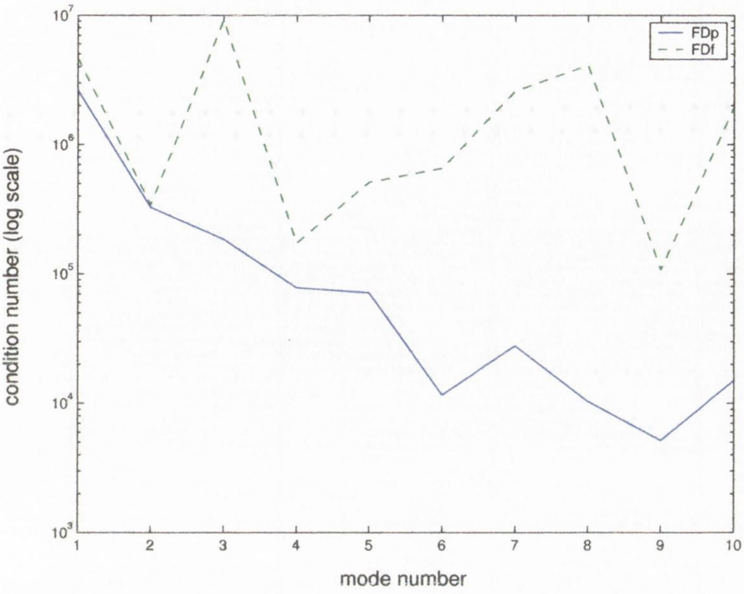

Figure 5.23: Condition number for FD_p and FD_f. Mesh 3. Two edges free.

Despite the good convergent behaviour of the FD_f formulation in comparison to the FD_p, the conditioning of the final system is higher for meshes 2 and 3. As in the one edge free case, the accuracy of the FD methods seems to be only partially related to the conditioning of the final system. In addition, the condition number shows no established pattern behaviour, as in the acoustic case, increasing and decreasing rather randomly.

5.3.4 Three dimensional problems

5.3.4.1 Problem definition

In section 5.3.1, the three dimensional displacement motion was described as a combination of one dilatational and two equivoluminal waves, moving orthogonally of each other with speed of motion c_L and c_T, respectively. The Cartesian components of each wave are completely defined in terms of the propagating angles θ and ϕ (known as Euler angles), as shown in figure 5.24 (see e.g. Meriam [228]). Using matrix notation, we may write

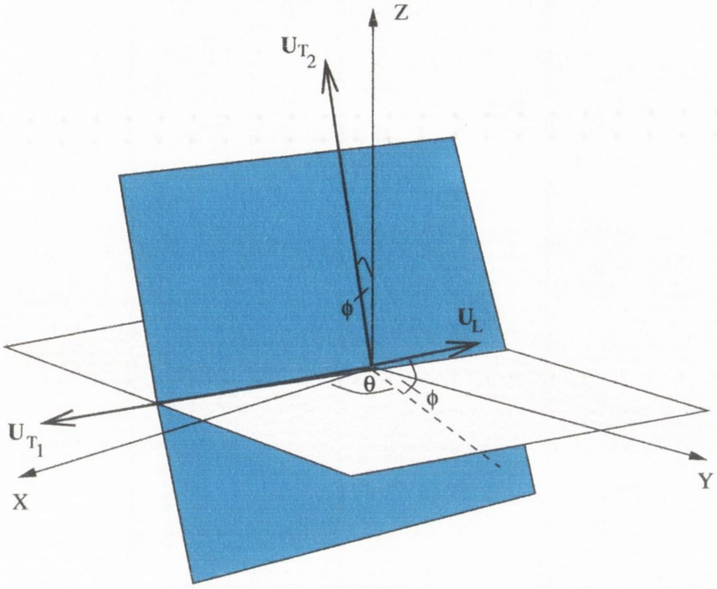

Figure 5.24: 3D elastic displacement.

$$\mathbf{u} = \begin{pmatrix} u_x \\ u_y \\ u_z \end{pmatrix} = \begin{bmatrix} \cos\phi\cos\theta & -\sin\theta & -\sin\phi\cos\theta \\ \cos\phi\sin\theta & \cos\theta & -\sin\phi\sin\theta \\ \sin\phi & 0 & \cos\phi \end{bmatrix} \begin{pmatrix} e^{-\iota k_L \mathbf{x}\cdot\mathbf{q}} \\ e^{-\iota k_L \mathbf{x}\cdot\mathbf{q}} \\ e^{-\iota k_L \mathbf{x}\cdot\mathbf{q}} \end{pmatrix}. \qquad (5.44)$$

For convenience, let us define here the Cartesian components of each displacement wave separately. That is,

$$\mathbf{w_L} = \begin{pmatrix} \cos\phi\cos\theta \\ \cos\phi\sin\theta \\ \sin\phi \end{pmatrix}, \ \mathbf{w_{T_1}} = \begin{pmatrix} -\sin\theta \\ \cos\theta \\ 0 \end{pmatrix}, \ \mathbf{w_{T_2}} = \begin{pmatrix} -\sin\phi\cos\theta \\ -\sin\phi\sin\theta \\ \cos\phi \end{pmatrix} \qquad (5.45)$$

5.3.4.2 Numerical implementation

Consider a 27 noded computational cell as shown in figure 5.25, where each node has three degrees of freedom given by the displacement vector 5.44.

We seek to relate the unknown displacement at point $\mathbf{x_0}$ to the known displacement at the 26 surrounding points in the computational cell. This values are approximated by a finite combination of m fundamental solutions (plane waves) uniformly

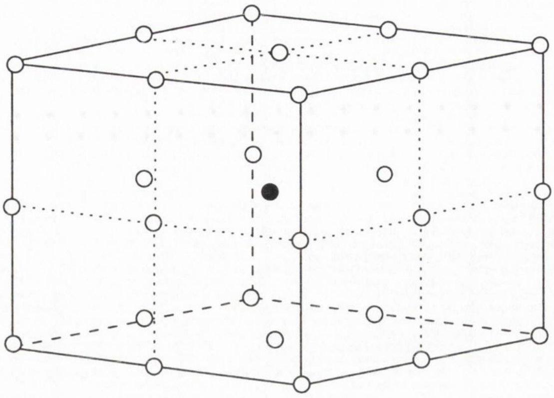

Figure 5.25: 3D computational molecule.

distributed in the three dimensional space.

However, a serious problem in the implementation of these concepts now arises in this case. Since the elastic wave motion comprises one dilatational and two equivoluminal orthogonal waves, three sets (with a total number of at least 78 directions) of *non-repeated, evenly distributed and orthogonal* directional vectors are effectively required to generate a satisfactory template.

The first drawback is related to the symmetry of the vectors in the three dimensional space as previously discussed in section 3.3.2 for the acoustic case. However, even in the ideal case scenario of having an arbitrary number of equidistant, non-repeated set of vectors it may still not be possible to construct two other sets with the same characteristics and, in addition, mutually orthogonal.

Note that, since there is no certainty that any particular wave system will give good results beforehand, the best distribution must be found by investigating its performance with a test case example. Following a trial-and-error procedure, a best compromise to this problem was obtained by constructing the orthogonal vector sets based on the Buckminster Fuller geodesic dome ("bucky ball'). Excluding the repeated directions, three sets of 58 non-repeated orthogonal vectors were obtained (thus, 78×174 templates result for the cell shown in figure 5.25). For illustration purposes, the wave direction systems are plotted in figures 5.26 and 5.27.

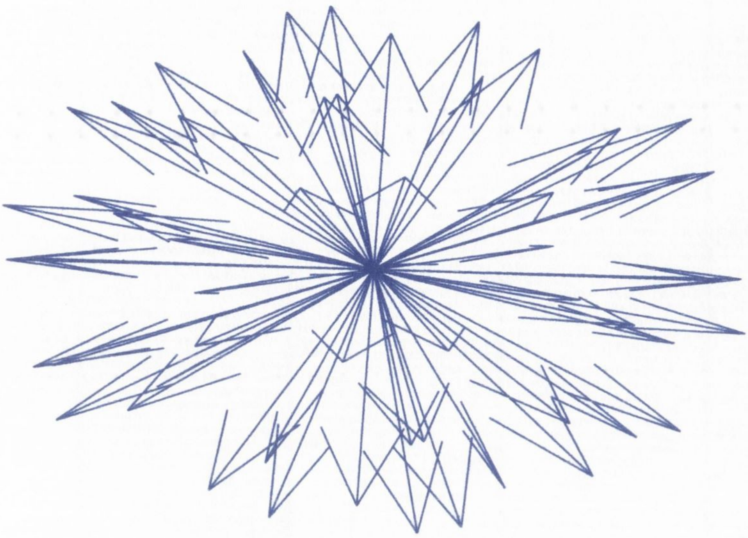

Figure 5.26: Dilatational wave vector system (bucky ball).

As illustrated, though the orthogonality and non-repeatability conditions are satisfied, the resulting directions are not uniformly distributed. Thus, as previously discussed in section 3.3.1 for the two-dimensional acoustic case, the interpolation method is only expected to give accurate solutions whenever the physical displacement may be efficiently approximated by these wave systems. Nonetheless, it will be shown in the subsequent section that assuming certain boundary conditions these wave systems may still give accurate solutions.

Once the dilatational and equivoluminal vector directions have been determined, the generating functions may be formulated following a similar procedure as in the two-dimensional elastic case. That is,

$$u_x(\mathbf{x}) = \left\{ \begin{array}{l} \cos\theta_j \cos\phi_j \; e^{-\iota k_L \cdot \mathbf{x} \cdot \mathbf{q}_j}, \; j = 1, \ldots, \frac{m}{3} \\ -\sin\theta_j \; e^{-\iota k_T \cdot \mathbf{x} \cdot \mathbf{q}_j}, \; j = \frac{m}{3} + 1, \ldots, \frac{2m}{3} \\ -\cos\theta_j \sin\phi_j \; e^{-\iota k_T \cdot \mathbf{x} \cdot \mathbf{q}_j}; \; j = \frac{2m}{3} + 1, \ldots, m \end{array} \right\}, \tag{5.46}$$

$$u_y(\mathbf{x}) = \left\{ \begin{array}{l} \cos\phi_j \sin\theta_j \; e^{-\iota k_L \cdot \mathbf{x} \cdot \mathbf{q}_j}, \; j = 1, \ldots, \frac{m}{3} \\ +\cos\theta_j \; e^{-\iota k_T \cdot \mathbf{x} \cdot \mathbf{q}_j}, \; j = \frac{m}{3} + 1, \ldots, \frac{2m}{3} \\ -\sin\phi_j \sin\theta \; e^{-\iota k_T \cdot \mathbf{x} \cdot \mathbf{q}_j}; \; j = \frac{2m}{3} + 1, \ldots, m \end{array} \right\}, \tag{5.47}$$

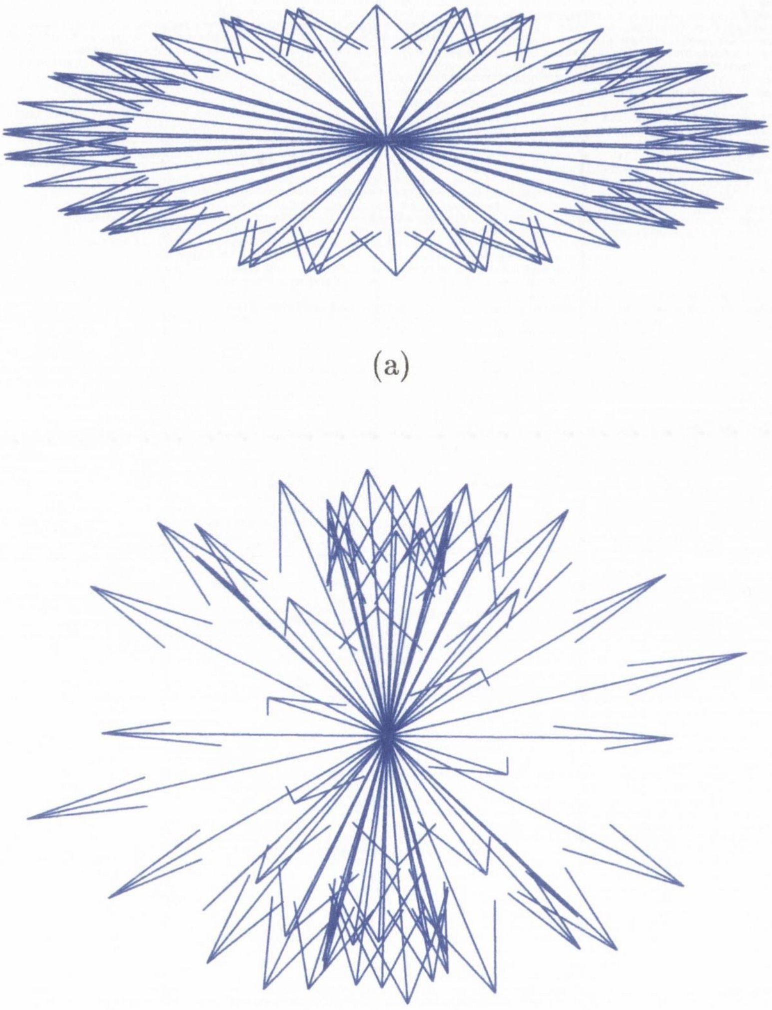

Figure 5.27: Equivoluminal wave vector systems.

and

$$u_z(\mathbf{x}) = \left\{ \begin{array}{l} \sin\phi_j \; e^{-\iota k_L \cdot \mathbf{x} \cdot \mathbf{q}_j}, \; j = 1, \ldots, \frac{m}{3} \\ + \, 0, \; j = \frac{m}{3} + 1, \ldots, \frac{2m}{3} \\ + \cos\phi_j \; e^{-\iota k_T \cdot \mathbf{x} \cdot \mathbf{q}_j}; \; j = \frac{2m}{3} + 1, \ldots, m \end{array} \right\}, \tag{5.48}$$

where the angles θ and ϕ are obtained from the directions given by each vector configuration. The propagating vectors $\mathbf{q}_j$ are then defined as

$$\mathbf{q}_j = \left(\cos\phi_j \cos\theta_j, \; \cos\phi_j \sin\theta_j, \; \sin\phi_j\right), \; j = 1, \ldots, m. \tag{5.49}$$

Equation 5.44 may then be written as

$$\mathbf{u} = \mathbf{h}(\mathbf{x_0})\boldsymbol{\gamma} = \begin{pmatrix} u_x(\mathbf{x_0}) \\ u_y(\mathbf{x_0}) \\ u_z(\mathbf{x_0}) \end{pmatrix} \boldsymbol{\gamma}. \tag{5.50}$$

Upon evaluating matrix $\mathbf{h}$ at all the surrounding molecule nodes, we obtain the constraint equation

$$\mathbf{u} = \mathbf{H}\boldsymbol{\gamma}, \tag{5.51}$$

where the $78 \times m$ matrix $\mathbf{H}$ is formed from individual $3 \times m$ sub-matrices $\mathbf{h}$ evaluated at neighbouring nodes.

The implementation of the free boundary conditions is completely analogous to that outlined for two dimensional problems in section 5.3.2.2. Thus, we need to evaluate the components of the derivatives of the displacement along the normal and tangential vectors at the boundary.

Let us consider a boundary face with normal and tangential vectors given by

$$\mathbf{N} = \begin{pmatrix} n \\ ns_1 \\ ns_2 \end{pmatrix} = \begin{bmatrix} 0 & 1 & 0 \\ 1 & 0 & 0 \\ 0 & 0 & 1 \end{bmatrix}.$$

By employing equation 5.45, we may write the displacements in matrix notation as

$$\mathbf{u_L} = \mathbf{N} \cdot \mathbf{w_L} \; e^{-\iota k_L \mathbf{x}_b \cdot \mathbf{q}}, \tag{5.52}$$

for the dilatational wave, and

$$\mathbf{u_{T_1}} = \mathbf{N} \cdot \mathbf{w_{T_1}} \; e^{-\iota k_T \mathbf{x} \cdot \mathbf{q}} \tag{5.53}$$

and

$$\mathbf{u_{T_2}} = \mathbf{N} \cdot \mathbf{w_{T_2}} \; e^{-\iota k_T \mathbf{x} \cdot \mathbf{q}}, \tag{5.54}$$

for the equivoluminal waves. The derivatives of the above equations with respect to $\mathbf{N}$ yields

$$\mathbf{du_L} = -\mathbf{u_L} \cdot \mathbf{w_L^T} \cdot \mathbf{N^T} \iota \; k_L, \tag{5.55}$$

and

$$\mathbf{du_{T_1}} = -\mathbf{u_{T_1}} \cdot \mathbf{w_{T_1}^T} \cdot \mathbf{N^T} \iota \; k_T, \tag{5.56}$$

$$\mathbf{du_{T_2}} = -\mathbf{u_{T_2}} \cdot \mathbf{w_{T_2}^T} \cdot \mathbf{N^T} \iota \; k_T, \tag{5.57}$$

where the 3-by-m dimension matrices $\mathbf{du_L}$, $\mathbf{du_{T_1}}$ and $\mathbf{du_{T_2}}$ are given as

$$\mathbf{du_L} = \begin{bmatrix} \partial u_n^L/\partial n & \partial u_n^L/\partial ns_1 & \partial u_n^L/\partial ns_2 \\ \partial u_{ns_1}^L/\partial n & \partial u_{ns_1}^L/\partial s_1 & \partial u_{ns_1}^L/\partial s_1 \\ \partial u_{ns_2}^L/\partial n & \partial u_{ns_2}^L/\partial s_1 & \partial u_{ns_2}^L/\partial ns_2 \end{bmatrix}, \tag{5.58}$$

$$\mathbf{du_{T_1}} = \begin{bmatrix} \partial u_n^{T_1}/\partial n & \partial u_n^{T_1}/\partial ns_1 & \partial u_n^{T_1}/\partial ns_2 \\ \partial u_{ns_1}^{T_1}/\partial n & \partial u_{ns_1}^{T_1}/\partial ns_1 & \partial u_{ns_1}^{T_1}/\partial ns_1 \\ \partial u_{ns_2}^{T_1}/\partial n & \partial u_{ns_2}^{T_1}/\partial ns_1 & \partial u_{ns_2}^{T_1}/\partial ns_2 \end{bmatrix}, \tag{5.59}$$

and

$$\mathbf{du_{T_2}} = \begin{bmatrix} \partial u_n^{T_2}/\partial n & \partial u_n^{T_2}/\partial ns_1 & \partial u_n^{T_2}/\partial ns_2 \\ \partial u_{ns_1}^{T_2}/\partial n & \partial u_{ns_1}^{T_2}/\partial ns_1 & \partial u_{ns_1}^{T_2}/\partial ns_1 \\ \partial u_{ns_2}^{T_2}/\partial n & \partial u_{ns_2}^{T_2}/\partial ns_1 & \partial u_{ns_2}^{T_2}/\partial ns_2 \end{bmatrix}. \tag{5.60}$$

The augmented template $\mathbf{H}$, then takes the form

$$\begin{pmatrix} \mathbf{u} \\ 0 \\ 0 \\ 0 \end{pmatrix} = \begin{pmatrix} \mathbf{H} \\ \sigma_n^L + \sigma_n^{T_1} + \sigma_n^{T_2} \\ \tau_{ns_1}^L + \tau_{ns_1}^{T_1} + \tau_{ns_1}^{T_2} \\ \tau_{ns_2}^L + \tau_{ns_2}^{T_1} + \tau_{ns_2}^{T_2} \end{pmatrix} \boldsymbol{\gamma} = \mathbf{H}_{aug} \boldsymbol{\gamma}, \tag{5.61}$$

where the values of σ and τ correspond to those of equation 5.18 for the dilatational and equivoluminal waves, respectively. Thus, equation 5.5 may be written as

$$\mathbf{u_0} = \mathbf{h}(\mathbf{x_0})(\mathbf{H}^{+}_{\mathbf{aug}})_{\mathbf{L}}\mathbf{u}. \tag{5.62}$$

5.3.5 Three dimensional validation example

5.3.5.1 Modelling details

Consider an isotropic bar of dimensions $0.6 \times 0.15 \times 0.1m$ and material properties $E = 70GPa$, $\nu = 0.3$ and $\rho = 2770kg^{-3}$, as schematically plotted in figure 5.28.

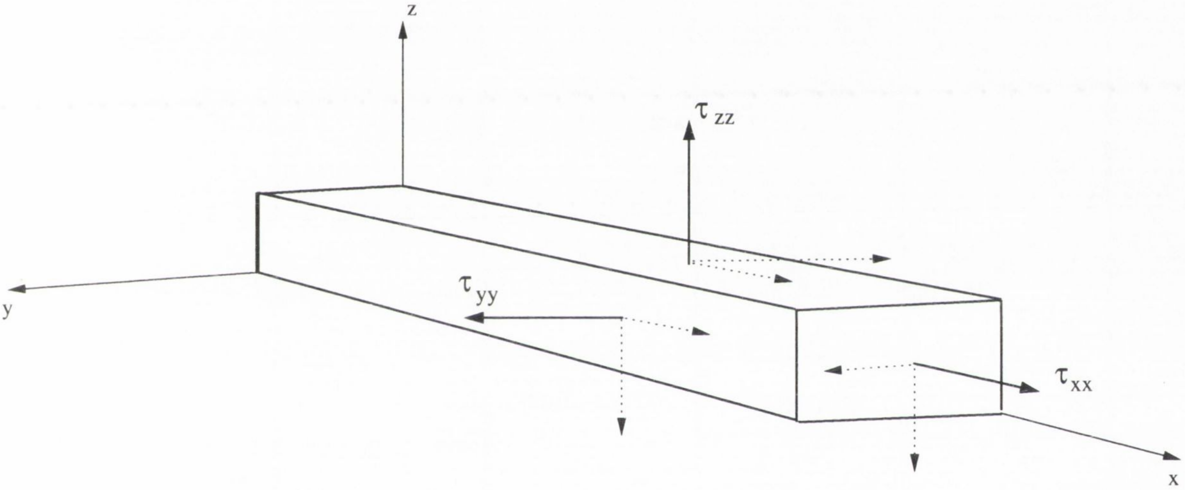

Figure 5.28: 3D validation problem.

The bar was uniformly meshed using 27 nodes in each cell with a maximum nodal spacing of $0,025m$ along the computational cell edges and $0.043m$ along the diagonals, respectively (see figure 5.29). The problem was solved considering the following boundary conditions:

(i) Clamped all round

$$\mathbf{u}(\mathbf{x}_b) = 0, \ \forall \ \mathbf{x}_b \in \Gamma_E, \tag{5.63}$$

where Γ_E is the boundary surface.

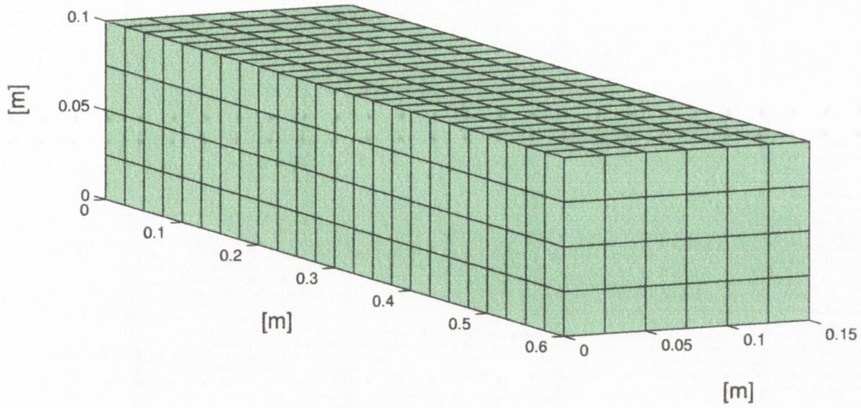

Figure 5.29: Illustration of the mesh.

(ii) Clamped at the end faces

$$\mathbf{u}(\mathbf{x}_b) = 0 \ \forall \ \mathbf{x}_b \in \Gamma_C, \tag{5.64}$$

$$\sigma_n = \tau_{ns} = 0 \ \forall \ \mathbf{x}_b \in \Gamma_F, \tag{5.65}$$

where Γ_C and Γ_F are the clamped ($x = 0$ and $x = 0.6$) and free ($y = 0$, $y = 0.15$, $z = 0$, $z = 0.1$) faces, respectively.

Though the all clamped condition represents only a fictitious problem, it allows one to investigate the performance of the interpolation formulation, as no errors are produced by the approximation of the derivatives of the displacement along free surfaces. Note that only 78×174 templates will then result as no row count is added to matrix **H**, thus simplifying also the implementation.

In all cases, the resonant frequencies were initially calculated by performing a modal analysis using ANSYS "SOLID#95" quadratic elements. These frequencies were then compared against those obtained with the wave expansion method, by forcing the system at a particular point over a frequency range, and searching for peaks in the ensuing frequency response function. The properties of the FE and FD models are summarised in table 5.5.

	nodes	dof
FE	3165	6330
FD	875	2625

Table 5.5: properties of the FE and FD models used

5.3.5.2 Results

All clamped condition

To illustrate the performance of the proposed FD approach, the displacement distribution for two excitation frequencies, $19246Hz$ and $22864Hz$, is shown below. These frequencies correspond to the first and third resonant modes for the all round clamped bar.

According to the edge and diagonal nodal distances in the FD model, the nodal point per wavelength ratios (equation 5.43) are 3.8-6.5 and 3.1-5.4 for the first and third resonant frequencies, respectively.

The FE reference solution for the first mode shape, is shown in figures 5.30 and 5.31 for the u_x and u_y displacement components, respectively.

The FD solution, illustrated in figures 5.32 and 5.33, shows a good agreement with the finite element solution.

As shown in figures 5.34-5.37, a good agreement is also observed between the FD and the reference solution for the third resonant frequency.

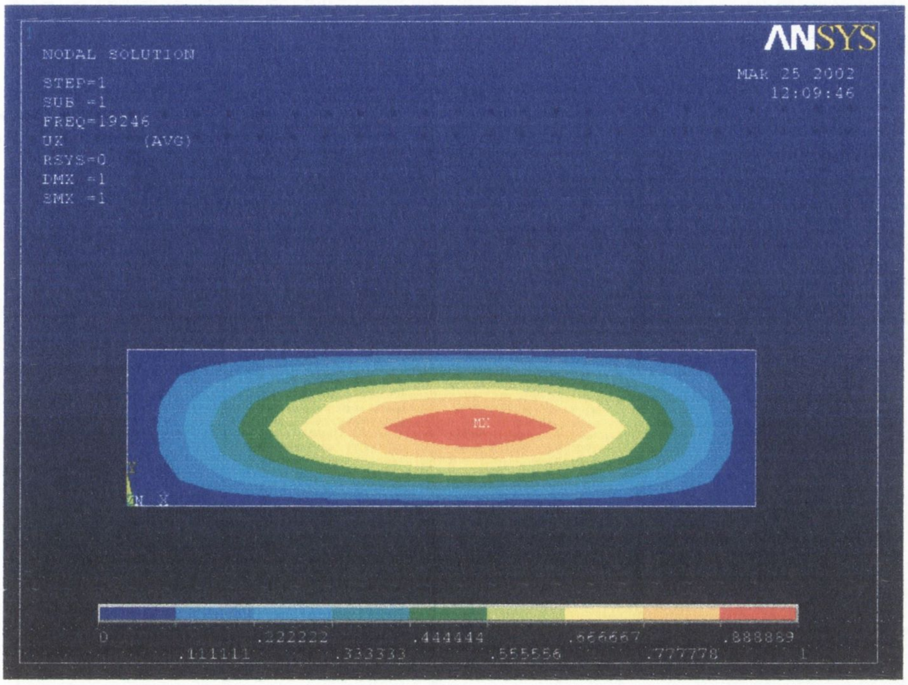

Figure 5.30: FE solution for the u_x displacement. All clamped condition; 19,246Hz.

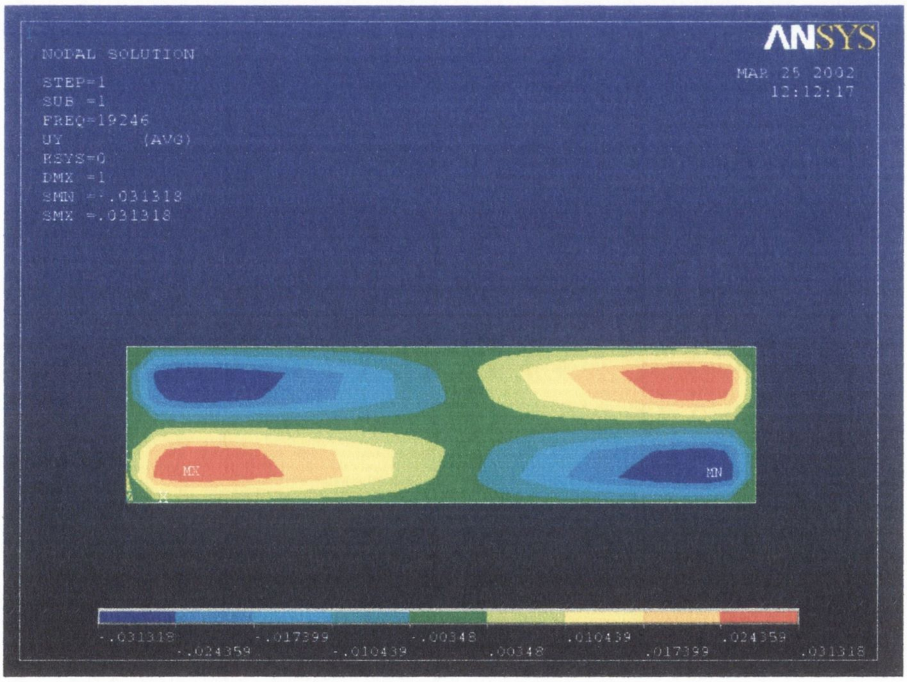

Figure 5.31: FE solution for the u_y displacement. All clamped condition; 19,246Hz.

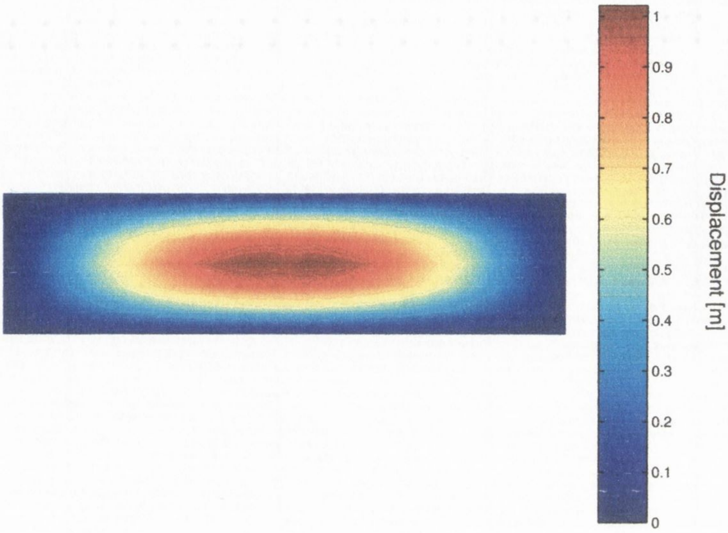

Figure 5.32: FD solution for the u_x displacement component. All clamped condition; 19,246Hz.

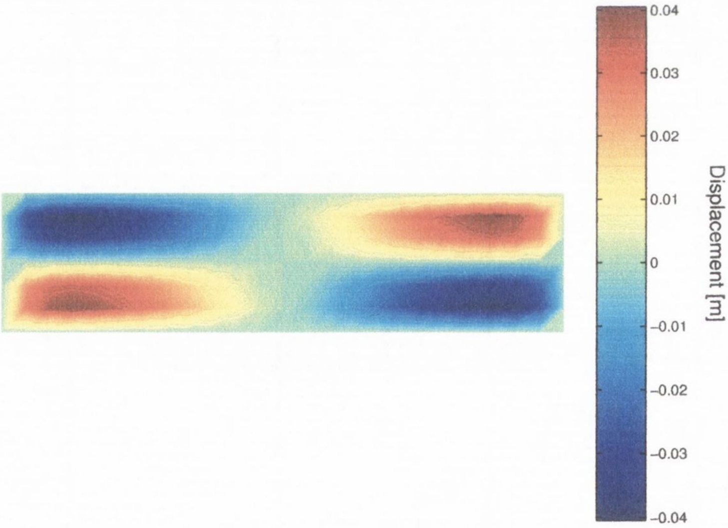

Figure 5.33: FD solution for the u_y displacement component. All clamped condition; 19,246Hz.

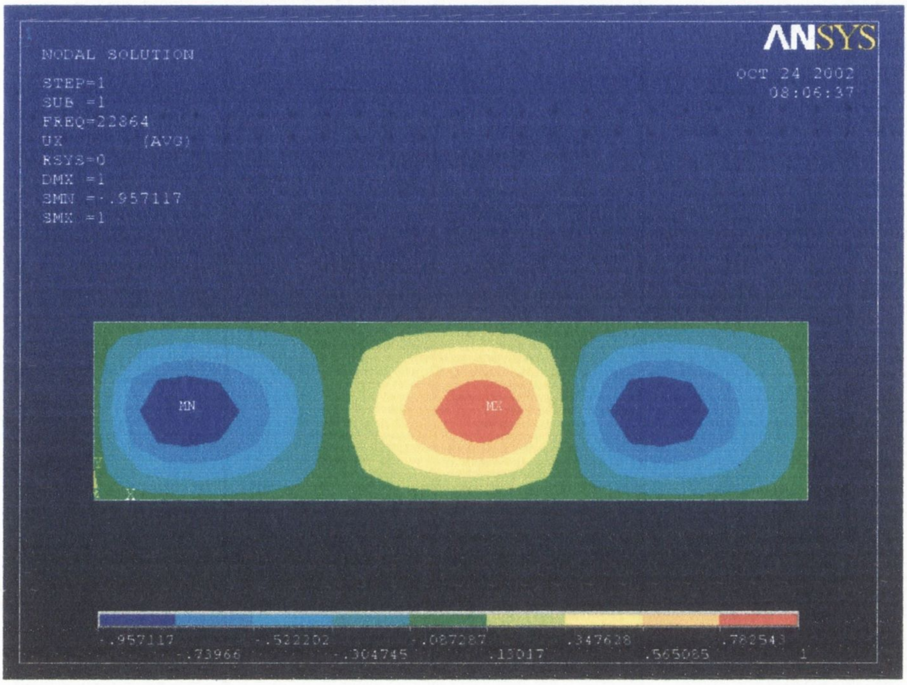

Figure 5.34: FE solution for the u_x displacement. All clamped condition; 22,864Hz.

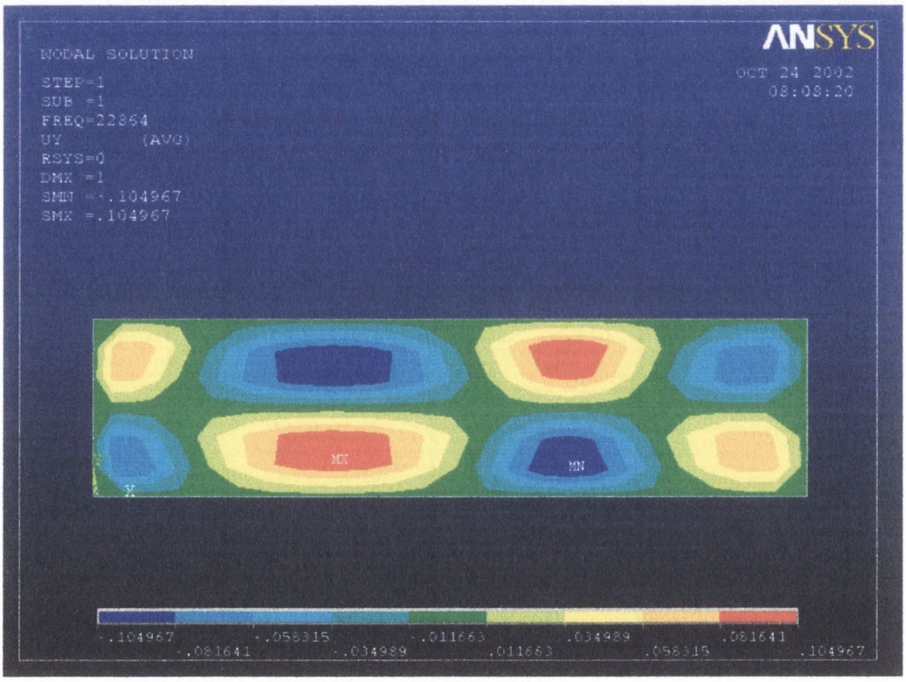

Figure 5.35: FE solution for the u_y displacement. All clamped condition; 22,864Hz.

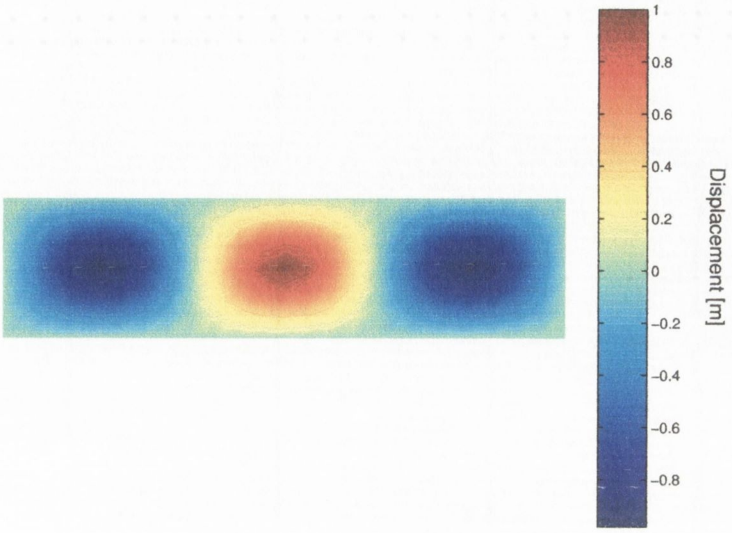

Figure 5.36: FD solution for the u_x displacement component. All clamped condition; 22,864Hz.

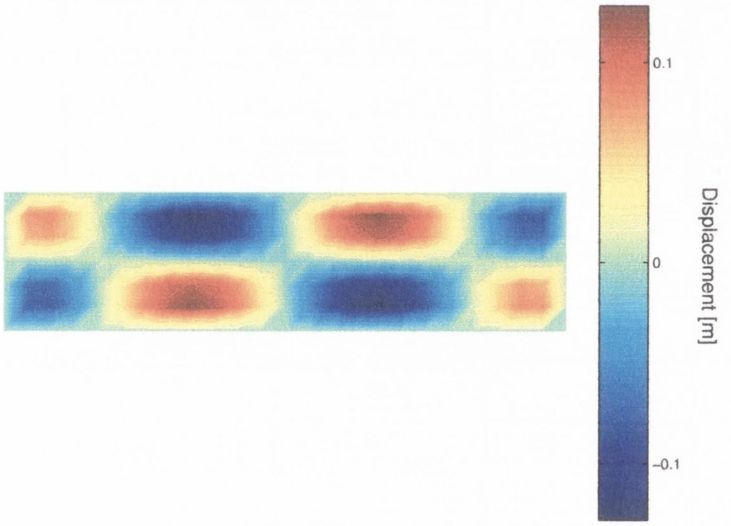

Figure 5.37: FD solution for the u_y displacement component. All clamped condition; 22,864Hz.

Clamped at the end faces

In this case, the resonant frequencies obtained with the FD method, were not in good agreement with those given by the FE model. By driving the bar at the resonant frequencies, discrepancies were also found in the displacement distribution of the associated mode shapes.

This was particularly remarkable for those natural frequencies associated to torsional modes. These frequencies could not be found by searching for minimum values of the determinant of the overall stiffness matrix, nor the actual mode shape modelled using a harmonic analysis (the actual frequency and displacement distribution for these modes was known beforehand from the FE solution).

5.4 Plate vibration analysis

Despite the drawbacks associated to the implementation of the proposed FD scheme for three dimensional elastic problems, the method may be implemented more easily in the modelling of plate vibration.

Whenever the thickness of the plate is negligible in comparison to all the other dimensions of the plate, the approximation of the desired field variables may be obtained using a uniform distribution of bi-dimensional plane waves. The application of the wave expansion method to plate vibration problems was recently proposed by Rice and Ruiz [158]. For a homogeneous, simple supported square plate, they obtained accurate solutions with four points per wavelength, which represents an important improvement over standard finite element approaches.

The formulation of the proposed scheme is outlined below. Though the method follows a similar procedure as already discussed for two dimensional elastic problems, it is re-written here for completeness.

5.4.1 Description of the physical problem

The dynamic equation which governs the bending motion in a thin, flat (homogeneous) plate, is given by the biharmonic equation [229]

$$\nabla^2 \nabla^2 \mathbf{u} - \beta^4 \mathbf{u} = 0 \tag{5.66}$$

where $\mathbf{u}(\mathbf{x})$ is the complex transverse deflection at frequency ω and position $\mathbf{x}$. The parameter β is related to the plate properties and driving frequency according to

$$\beta^4 = \frac{12(1-\nu^2)\omega^2}{Et^2} \tag{5.67}$$

where E is the Young's modulus, ν is the Poisson's ratio, ρ is the density and t is the thickness.

Since the dynamic equation 5.66 is a fourth-order equation, the displacement field is uniquely defined, should two boundary conditions are specified at each boundary point. Consider a plate Ω_E with boundary $\Gamma_E = \Gamma_S \cup \Gamma_C \cup \Gamma_F$. Denoting by s and n the coordinates in the tangential and normal directions, the following conditions are usually considered [230]:

- Simply supported edge (mixed condition)

  $$\mathbf{u} = \overline{u} \quad \text{on } \Gamma_S, \tag{5.68}$$

  $$M_n = \overline{m}_n \quad \text{on } \Gamma_S, \tag{5.69}$$

  where $\overline{u}$ is a prescribed transversal displacement, and

  $$M_n = D\left(\frac{\partial^2 \mathbf{u}}{\partial \mathbf{n}^2} + \nu \frac{\partial^2 \mathbf{u}}{\partial \mathbf{s}^2}\right) \tag{5.70}$$

  is the normal bending moment per unit length of a plate with flexural rigidity D and $\overline{m}_n$ is a prescribed bending function.

- Clamped edge (kinematic condition)

  $$\mathbf{u} = \overline{u} \quad \text{on } \Gamma_C, \tag{5.71}$$

  $$\frac{\partial \mathbf{u}}{\partial n} = -\overline{\theta}_n \quad \text{on } \Gamma_C, \tag{5.72}$$

  where $\overline{\theta_n}$ is a prescribed rotation function.

- Free edge (mechanical condition)

$$M_n = \overline{m}_n \quad \text{on } \Gamma_F, \tag{5.73}$$

$$Q_n = -\frac{\partial \overline{m}_{ns}}{\partial s} = \overline{q}_n \quad \text{on } \Gamma_F, \tag{5.74}$$

  where Q_n is the shearing force per unit length, $\overline{q}_n$ is a prescribed shear force function and $\overline{m}_{ns}$ is the twisting moment per unit length about the direction n.

Noting that equation 5.66 may be written as

$$[\nabla^2 + \beta^2][\nabla^2 + (\iota\beta)^2]\mathbf{u} = 0, \tag{5.75}$$

it follows that a convenient set of fundamental solutions of equation 5.66 is given by propagating and evanescent waves defined by

$$\gamma e^{-\iota\beta\mathbf{x}\cdot\mathbf{q}}; \ \gamma e^{-\beta\mathbf{x}\cdot\mathbf{q}} \tag{5.76}$$

where $\mathbf{q}$ is an arbitrary unit vector oriented in the direction of propagation of the plane wave and γ is a complex constant representing the strength of the wave.

5.4.2 Numerical implementation

Consider the nine noded computational template shown in figure 5.38, where each node has three degrees of freedom given by the displacement vector $\mathbf{u_i}$ as

$$\mathbf{u_i} = \begin{pmatrix} u_i \\ \partial u/\partial x_i \\ \partial u/\partial y_i. \end{pmatrix} \tag{5.77}$$

Following the same basic interpolation approach used for two-dimensional elastic problems, we may then approximate the displacement $\mathbf{a_0}$ at $\mathbf{x_0}$ by $\frac{m}{2}$ equally distributed fundamental solutions 5.76 as

$$g_j(\mathbf{x}) = \left\{ \begin{array}{c} e^{-\iota\beta\mathbf{x}\cdot\mathbf{q_j}}; \ j = 1 : m/2 \\ e^{-\beta\mathbf{x}\cdot\mathbf{q_j}}; \ j = m/2 + 1 : m \end{array} \right\} \tag{5.78}$$

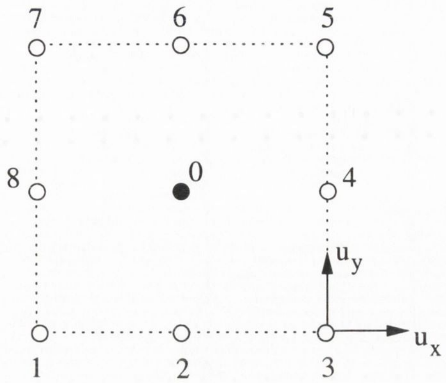

Figure 5.38: 2D computational molecule.

with propagation vectors given by

$$\mathbf{q_j} = \left(\cos\frac{4\pi j}{m},\ \sin\frac{4\pi j}{m}\right);\ j = 1 : m \tag{5.79}$$

The transverse displacement (equation 5.77) may then be written as

$$\mathbf{u_0} = \begin{pmatrix} \mathbf{g}(\mathbf{x_0}) \\ \partial\mathbf{g}/\partial x(\mathbf{x_0}) \\ \partial\mathbf{g}/\partial y(\mathbf{x_0}) \end{pmatrix} = \mathbf{h}(\mathbf{x_0})\gamma, \tag{5.80}$$

where $\mathbf{h}(\mathbf{x_0})$ is a $3 \times m$ matrix of generating functions and their derivatives, and γ is a column vector of dimension $m \times 1$ representing the strengths of the individual functions. Evaluating $\mathbf{h}$ at all the surrounding points in the computational molecule, we obtain the computational template

$$\mathbf{u_o} - \mathbf{h}(\mathbf{x_0})\mathbf{H}^{+}\mathbf{u} = 0, \tag{5.81}$$

where '+' denotes pseudo-inverse operation.

5.4.2.1 Boundary conditions

The pseudo-inverse operation, which requires that $m \geq 24$, ensures that the least "energetic" combination of generating functions is used to approximate the response locally whilst still ensuring that the expansion in equation 5.80 gives consistent results at all the boundary nodes in the template. Thus, one or more boundary conditions may additionally be satisfied by augmenting **H** prior to inversion.

To implement a simple supported edge boundary condition, equations 5.68 and 5.69, the matrix **H** may be augmented by the corresponding derivatives of the generating functions with respect to the edge normal and tangential directions. That is,

$$\begin{pmatrix} \mathbf{u} \\ \dfrac{M_{nn}}{D} \end{pmatrix} = \begin{bmatrix} \mathbf{H} \\ \left(\dfrac{\partial^2 \mathbf{g}}{\partial \mathbf{n}^2} + \nu \dfrac{\partial^2 \mathbf{g}}{\partial \mathbf{s}^2} \right) (\mathbf{x}_b) \end{bmatrix} \gamma = \mathbf{H}_{aug} \gamma \tag{5.82}$$

where

$$\frac{\partial^2 g_j}{\partial \mathbf{n}^2} = \begin{cases} \beta^2 (\mathbf{n} \cdot \mathbf{q}_j)^2 \; g_j(\mathbf{x}_b) & j = 1 : m/2 \\ \beta^2 (\mathbf{n} \cdot \mathbf{q}_j)^2 \; g_j(\mathbf{x}_b) & j = m/2 + 1 : m. \end{cases} \tag{5.83}$$

The second order derivative along the tangential direction vector **s**, may be obtained by simply replacing the corresponding direction vector in equation 5.83. Once the template calculation is performed according to equation 5.81, direct restraint may be applied to the first degree of freedom of the boundary node $\mathbf{x}_b$.

To apply clamped boundary conditions, the appropriate degrees of freedom in the overall assembled stiffness matrix may be directly restrained.

5.4.3 Test case description and modelling details

Two numerical test were performed on a square plate of side length $1m$ and properties $E = 70GPa$, $\nu = 0.3$, $t = 0.001m$ and $\rho = 2770kg^{-3}$. In each case, only nine noded computational cells as shown in figure 5.38 were considered.

In the first test the plate was clamped all round, whilst in the second test it was clamped along one edge and simply supported on the other three. Thus the results from the first case could be compared against the exact solution for a mode p, k given by [231]

$$\omega_{pk}^2 = \frac{D\rho}{t} \pi^4 (p^2 + k^2)^2 \tag{5.84}$$

The plate was discretized using 121 equally spaced nodes. In all cases, 30×2 equidirectional generating functions 5.78 were used to formulate the computational templates. To implement the boundary conditions, a full edge discretisation (FD_f) procedure, as previously discussed in section 5.3.3.1 for two dimensional problems, was applied.

For illustration purposes, consider the lower left corner of the plate as shown in figure 5.39. A full template was formed around node 1 using all the other nodes depicted. Clamping was then implemented by directly restraining all three degrees of freedom of node 1 in the overall assembled stiffness matrix **K**. To change this to simple support, the local template matrix **H** was augmented using relationship 5.82, before the pseudo-inversion. It should be noted that for edges points, only rotational restraint to one of the axis is required.

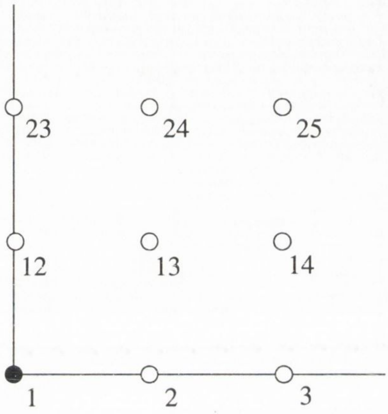

Figure 5.39: boundary condition implementation.

The results for the simply supported cases were compared against two finite element models using ANSYS Element #93 quadratic elements (the formulation of the finite element method applied to plate vibration analysis is briefly discussed in Appendix). The properties of the three models are detailed in table 5.6.

The mesh for the plate is shown in figure 5.40 together with the FE I mesh superimposed. As shown in table 5.6, the FE I model will have a similar memory and computational loading as the present finite difference technique.

FD		FE I		FE II	
nodes	dof	nodes	dof	nodes	dof
121	383	96	280	343	1023

Table 5.6: properties of FD and FE models

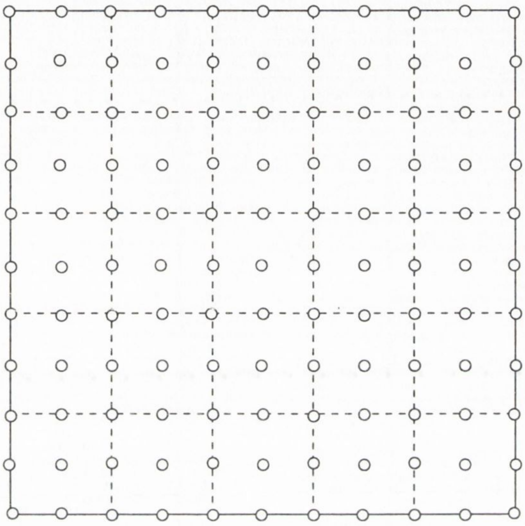

Figure 5.40: Plate FD and FE (coarse) meshes.

5.4.4 Results

5.4.4.1 Simply supported square plate

The symmetric modes over the complete coherent analysis range is included in table, where the results are compared to the finite element estimates from the coarse (FE I) and fine (FE II) models.

The performance of the finite difference is excellent and outperforms the finite element model which uses twice as many nodes per wavelength.

5.4.4.2 One clamped edge and three edges simply supported

To illustrate the performance of the proposed wave expansion scheme in a system with non-symmetric modes, an analysis of the same plate with one side clamped

Mode	FD	Exact	FE I	FE II
(1,1)	4.753	4.753	4.696	4.734
(2,2)	19.01	19.01	10.02	18.93
(3,3)	42.77	42.78	45.39	42.57
(4,4)	76.48	76.05	89.21	76.54
(5,5)	119.9	118.8	128.1	124.2

Table 5.7: five resonant frequencies for a simply supported plate

and the other three simply supported was verified.

For comparison purposes, the problem was solved with the finite element model FE II, using the fine mesh. As a benchmark for this study, the results obtained were compared against a finite element model with 7,701 nodes and 23,103 degrees of freedom, as shown in figure 5.41.

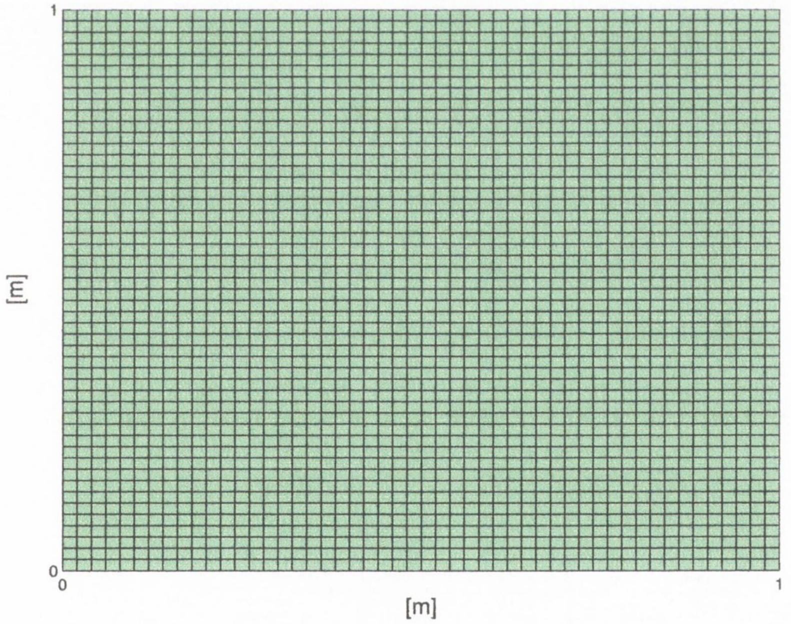

Figure 5.41: Reference finite element model.

The results obtained are listed in table 5.8. As illustrated, in comparison to the

Mode	FD	FE II	Reference (FE)
(1,1)	5.694	5.678	**5.722**
(1,2)	12.443	12.416	**12.505**
(2,1)	14.123	14.090	**14.194**
(2,2)	20.735	20.675	**20.841**
(1,3)	24.144	24.103	**24.269**
(2,3)	32.205	32.124	**32.373**

Table 5.8: lowest resonant frequencies of ss plate with one side clamped.

reference finite element solution, the results obtained with the FD model are more accurate than those of the FE II with less than half the number of nodes.

5.5 Discussion

In the present chapter, the performance of the wave base expansion technique applied to the numerical solution of elastic wave propagation in two and three dimensions and bending plate vibration has been investigated. For two-dimensional problems, a plain strain condition was assumed throughout the analysis.

Two different implementations of the free boundary condition were evaluated for the two dimensional elastic case: a partial edge discretisation, denoted as FD_p and a full edge discretisation denoted as FD_f (it should be noted that other schemes are also possible, for example, to use a FD_p method but considering only the restraints of the actual boundary node as in the FD_f approach, or vice versa).

A different behaviour was observed between these two boundary implementation formulations. Whilst the FD_f technique was very stable and converged monotonically to the exact solution for all frequencies tested, the accuracy of the FD_p approach deteriorated in general at lower frequencies. Unlike the acoustic case, where a loss of stability was observed at lower frequencies, the conditioning of the system in the elastic case shows a more random behaviour. As the mesh was refined, however, the conditioning of the system given by the FD_p or the FD_f formulations became more similar.

It should be noted that the accuracy (and ultimately the convergence to the desired solution) in the wave expansion method, resides entirely in the possibility of obtaining a best combination of solutions from a given set. This task is performed by the pseudo-inverse operation. However, if all the interpolating functions give a very accurate approximation to the local solution, it may not be possible to clearly identify which one, or which combination of them, gives the best result.

In all the validation tests performed, the FD method outperformed the FE method using the same number of nodes, and even twice as many nodes for the "all round clamped" test. Furthermore, no penalty in the accuracy was observed by imposing mixed restraints at the boundary points.

Under the present formulation, the implementation of the FD method in 3D problems, however, faces a serious limitation imposed by the requirement to have three sets of at least 78 uniform, non repeated and orthogonal vectors. Though for an all round clamped bar, the use of a 58 "bucky ball" vector configuration was shown to give accurate results, the method did not converge to the desired solution when free boundary conditions were applied. Further work is required in order to investigate whether this problem is related to the non-uniform distribution of the interpolating waves or the actual formulation of the free boundary conditions.

One possible way to circumvent this problem, is to approximate the displacement field by using Green's functions instead of plane waves. Thus, only one set of uniformly distributed points is required. However, since the location of the monopole sources must be defined beforehand, some additional parameters are involved in the formulation.

Though the 3D implementation appears to be inviable under the present formulation, an important number of other problems (besides the 2D elastic) may still be accurately solved. The analysis of a plate vibration shows that the FD method is also more accurate than FE techniques for this type of problems, using comparable computational resources. The application of boundary conditions is extremely flexible, particularly in the modelling of corners, where multiple restraints may be imposed.

Since the formulation of the wave expansion method directly uses wave models, its implementation is very direct and physical in nature. Thus, it is also possible, in principle, to extend the method to other applications, like shell vibration analysis, Rayleigh surface waves and the use of complex wave numbers for modelling porous materials.

Chapter 6

Conclusions and future work

6.1 Conclusions

6.1.1 The WED in acoustics

From the results obtained, it is concluded that:

- The wave-based interpolation technique gives a nearly optimal accuracy in two and three dimensions. That is, the interpolation formally breaks down at the Nyquist frequency (two nodal points per wavelength) limit. This conclusion is consistent with the results in two dimensions obtained by Caruthers *et al.* [152].

- An increasing instability is associated with the WED method at lower frequencies. However, despite the ill-conditioning the accuracy of the wave expansion interpolation remains remarkably unaffected. This property is also characteristic of the method of fundamental solutions (from which the WED is derived) and other Trefftz methods [164]. Thus, in the strict sense[1] the method is not stable at these frequencies, but it is sufficiently robust to give accurate results.

---

[1] Some authors have suggested the use of a different conditioning test in order to assess this methods considering the nature of the interpolation formulation and the structure of the resulting system of equations [170].

- Dirichlet and Neumann boundary conditions may be readily incorporated within the formulation of the method. The use of a 'natural' radiation condition formulation based on outward radiating plane waves, as originally proposed by Caruthers *et al.* [7], was found to be only viable using a more limited range of outward directions. Nonetheless, using these directions the resulting formulation was shown to be accurate and robust for a wide range of frequencies.

  Alternatively, a ('non-natural') $\rho_0 c$ plane wave approach that iteratively recalculates the incidence angle was also proposed. This method gave an extremely stable solution over all frequencies tested, though at the expense of iteratively resolving the problem. The accuracy of this formulation was demonstrated to be comparable to that obtained with the 'natural' approach, whenever the incidence angle of the wave field at the boundary was relatively close to the angle of the outward boundary normal.

- Since the formulation of the WED is completely general to any nodal distribution, the use of non-regular meshes and/or different element geometries is straightforward.

- The interpolation formulation is extremely flexible, giving the opportunity to easily include, for example, a flow condition within the computational domain, without any penalty in the accuracy of the method.

6.1.2 The WED in elastodynamics

From the analysis and results obtained for the wave expansion method applied to elastic wave modelling, the following conclusion may be drawn:

- Given the natural physical concept of the wave expansion method, the formulation as originally derived for the acoustic case, need to be only slightly modified in order to include the physical characteristics of the wave propagation in elastic media. The resulting approach is straightforward to implement, and gives the possibility of including multiple restraints, as will occur at boundary corners.

- Under the present formulation, however, the method does not appear to be viable for general three-dimensional elastic problems with free boundaries. Further research is required in order to assess whether this limitation is related to the formulation of the free boundary condition or the non-uniform distribution of the interpolating plane waves.

- For two-dimensional (plane strain) problems, the accuracy and convergence of the method was shown to depend strongly on the formulation used to implement the (traction) free boundary condition. According to the problem, the most stable formulation was not necessarily the most accurate over the entire range of frequencies. Unlike the acoustic case, the conditioning of the resulting system of equations is not directly related to the frequency, showing a more random behaviour.

- In comparison to a standard finite element method using similar computational resources, the wave expansion method is much more accurate, resulting in a significant reduction in the number of nodal points required to obtain the desired solution.

- The method was demonstrated to be also highly accurate and robust for modelling plate vibration under different boundary conditions. The performance of the method was not affected by the inclusion of multiple restraints at corner points, giving significantly more accurate results than a comparable finite element model.

- The method naturally lends itself to efficient calculation of harmonic responses at higher frequencies where non-modal approaches are appropriate.

6.1.3 Final conclusions

Throughout this study, it has been pointed out that the overall effectiveness of a given numerical method is not only related to the accuracy of the interpolation procedure, but to several aspects related to the numerical solution process.

Since the wave expansion method is a discrete domain technique, the matrix system resulting from the interpolation procedure is very sparse though not symmetric. Despite this, the final system is substantially smaller in comparison to that given by standard numerical methods. The ultimate effectiveness of the wave expansion method for large domain applications will depend on whether the (non-symmetric) system may be efficiently solved using iterative solution techniques.

6.2 Future work

In order to obtain a versatile and generally applicable modelling technique, the next steps in the development of the wave expansion discretisation technique might focus on the following aspects:

1. properties and applicability of the method
    - the formulation of the radiation boundary condition needs further investigation, assessing alternative formulations in terms of the stability and convergence of the resulting solution,
    - address the convergence and conditioning resulting from the use of triangular/tetrahedral meshes in a wide range of frequencies,
    - solution of three-dimensional problems subjected to non-uniform flow conditions,
    - use of non-overlapping meshes, following a finite element procedure,
    - alternative formulation for three-dimensional elastic problems, using point sources instead of plane waves.

- extension of the WED formulation for modelling Rayleigh surface waves.

2. computational efficiency

    - alternative techniques for the computation of the pseudo-inverse,
    - performance of iterative solution techniques and the use of parallel platforms,
    - domain-decomposition techniques for large domains.

Publications and presentations associated with this thesis

Rice H. and Ruiz G. A finite difference analysis of plate vibration using a wave expansion technique. In *ISMA25*, pages 1477-1482, 2000.

Ruiz G. and Rice H. An implementation of wave-based finite difference scheme for a 3D acoustic problem. *J. Sound Vib.*, 256(2):373-381, 2002.

Ruiz G. Efficient modelling of acoustic waves. Poster presentation at the Bernard Crossland Symposium, Belfast, 2002.

Ruiz G. Modelling waves with waves. Seminar at the Dept. of Mech. and Manuf. Eng., Trinity College Dublin, 2001.

Bibliography

[1] Kinsler L.E. Frey A.R. Coppens A.B. and Sanders J.V. *Fundamentals of Acoustics.* John Wiley & Sons, Inc., 4th edition, 2000.

[2] Oppenheim A.V. and Schafer R.W. *Digital Signal Processing.* Prentice-Hall, 1975.

[3] Zienkiewicz O.C. Achievements and some unsolved problems of the finite element method. *Int. J. Numer. Meth. Engng.*, 47:9–28, 2000.

[4] Davis J.L. *Finite Difference Methods in Dynamics of Continuous Media.* Macmillan; Collier-Macmillan, 1986.

[5] Zienkiewicz O.C. *The Finite Element Method*, volume 1. McGraw-Hill, London, 4 edition, 1989.

[6] Ciskowski R.D. and Brebbia C.A., editors. *Boundary Element Method in Acoustics.* Elsevier Applied Science, 1991.

[7] Caruthers J.E. French J.C. and Ravinprakash G.K. Recent developments concerning a new discretization method for the Helmholtz equation. In *1st AIAA/CEAS Aeroacoustic Conference, CEAS/AIAA-95-117*, pages 819–826, Munich Germany, May 1995.

[8] Baumeister K.J. and Kreider K.L. Finite difference time marching in the frequency domain: A parabolic formulation for aircraft acoustic nacelle design. In *International Mechanical Engineering Congress and Exposition: The Winter*

Annual Meeting, San Francisco, California, November 1995. American Society of Mechanical Engineers.

[9] Botteldooren D. Finite-difference time-domain simulation of low-frequency room acoustic problems. *J. Acoust. Soc. Am.*, 98(6):3302–3308, December 1995.

[10] De Poorter J. and Botteldooren D. Acoustical finite-difference time-domain simulations of subwavelength geometries. *J. Acoust. Soc. Am.*, 104(3, Pt. 1):1171–1177, September 1998.

[11] Hastings F.D. Schneider J.B. and Broschat S.L. A finite-difference time-domain solution to scattering from a rough pressure-release surface. *J. Acoust. Soc. Am.*, 102(6):3394–3400, December 1997.

[12] Hestholm S. and Ruud B. 3D finite-difference elastic wave modeling including surface topography. *Geophysics*, 63(2):613–622, March-April 1998.

[13] Saenger E.H. Gold N. and Shapiro S.A. Modeling the propagation of elastic waves using a modified finite-difference grid. *Wave Motion*, 31:77–92, 2000.

[14] Kunz K. and Luebers R.J. *Finite Difference Time Domain Method for Electromagnetics.* CRC Press, 1993.

[15] Tal-Ezar H. Kosloff D. and Koren Z. An accurate scheme for seismic forward modeling. *Geophysical Prospecting*, 35:479–490, 1987.

[16] Gaitonde D. and Shang J.S. Optimized compact-difference-based finite-volume schemes for linear wave phenomena. *J. Comput. Physics*, 138:617–643, 1997.

[17] Allen M.B. Herrera I. and Pinder G.F. *Numerical Modeling in Science and Engineering.* John Wiley & Sons, 1988.

[18] Bamberger A. Guillot J.C. and Joly P. Numerical diffraction by a uniform grid. *SIAM J. Numer. Anal.*, 25(4):753–783, August 1988.

[19] Hildebrand F.B. *Finite-Difference Equations and Simulations.* Prentice-Hall, Inc., 1968.

[20] Min D-J. Shin C. Kwon B-D. and Cheung S. Improved frequency-domain elastic wave modeling using weighted-averaging difference operators. *Geophysics*, 65(3):884–895, May-June 2000.

[21] Singer I. and Turkel E. High-order finite difference methods for the Helmholtz equation. *Comput. Methods Appl. Mech. Engrg.*, 163:343–358, 1998.

[22] Holland R. The finite difference solution of Maxwell's equations in generalized nonorthogonal coordinates. *IEEE Trans. Nucl. Sci.*, NS-30(6), Dec. 1983.

[23] Lee J-F. Palandech R. and Mittra R. Modeling three-dimensional discontinuities in waveguides using nonorthogonal FDTD algorithm. *IEEE Trans. Microwave Theory Tech.*, MTT-40:346–352, 1992.

[24] Botteldooren D. Acoustical finite-difference time-domain simulation in a quasi-Cartesian grid. *J. Acoust. Soc. Am.*, 95(5, Pt. 1):2313–2319, May 1994.

[25] Gaitonde D.V. Shang J.S. and Young J.L. Practical aspects of higher-order numerical schemes for wave propagation phenomena. *Int. J. Numer. Meth. Engng.*, 45:1849–1869, 1999.

[26] Hughes T.J.R. *The Finite Element Method: Linear Static and Dynamic Finite Element Analysis.* Prentice Hall, Englewood Cliffs, New Jersey, 1987.

[27] Bathe K-J. *Finite Element Procedures in Engineering Analysis.* Prentice-Hall, Englewood Cliffs, New Jersey, 1982.

[28] Ihlenburg F. and Babuška I. Dispersion analysis and error estimation of Galerkin finite element methods for the Helmholtz equation. *Int. J. Numer. Meth. Engng.*, 38:3745–3774, 1995.

[29] Ihlenburg F. Babuška I. and Sauter S. Reliability of finite element methods for the numerical computation of waves. *Advances in Engineering Software*, 28:417–424, 1997.

[30] Semblat J.F. and Brioist J.J. Efficiency of higher order finite elements for the analysis of seismic wave propagation. *J. Sound Vib.*, 231(2):460–467, 2000.

[31] Stewart J.R. and Hughes T.J.R. A tutorial in elementary finite element error analysis: A systematic presentation of a priori and a posteriori error estimates. *Comput. Methods Appl. Mech. Engrg.*, 158:1–22, 1998.

[32] Ihlenburg F. and Babuška I. Finite element solution of the Helmholtz equation with high wave number. part 1: the *h*-version of the FEM. *Comput. Math. Applic.*, 38(9):9–37, 1995.

[33] Ihlenburg F. and Babuška I. Finite element solution of the Helmholtz equation with high wave number. part 2: the *hp*-version of the FEM. *SIAM Numer. Anal.*, 34(1):315–358, 1997.

[34] Gerdes K. and Ihlenburg F. On the pollution effect in FE solutions of the 3D-Helmholtz equation. *Comput. Methods Appl. Mech. Engrg.*, 170:155–172, 1999.

[35] Bouillard Ph. Allard J-F. and Warzée. Superconvergent patch recovery technique for the finite element method in acoustics. *Comm. Appl. Numer. Methods*, 12:581–594, 1996.

[36] Bouillard Ph. Influence of the pollution on the admissible field error estimation for FE solutions of the Helmholtz equation. *Int. J. Numer. Meth. Engng.*, 45:783–800, 1999.

[37] Bouillard Ph. and Ihlenburg F. Error estimation and adaptivity for the finite element method in acoustics: 2D and 3D applications. *Comput. Methods Appl. Mech. Engrg.*, 176:147–163, 1999.

[38] Irimie S. and Bouillard Ph. A residual a posteriori error estimator for the finite element solution of the Helmholtz equation. *Comput. Methods Appl. Mech. Engrg.*, 190:2027–2042, 2001.

[39] Harari I. and Hughes T.J.R. Galerkin/least-squares finite element methods for the reduced wave equation with non-reflecting boundary conditions in unbounded domains. *Comput. Methods Appl. Mech. Engrg.*, 98:411–454, 1992.

[40] Thompson L.L. and Pinsky P.M. A Galerkin least-squares finite element method for the two dimensional Helmholtz equation. *Int. J. Numer. Meth. Engng.*, 38:371–397, 1995.

[41] Franca L.P. and Dutra do Carno E.G. The Galerkin gradient least-squares method. *Comput. Methods Appl. Mech. Engrg.*, 74:41–54, 1989.

[42] Harari I. and Haham S. Improved finite element methods for elastic waves. *Comput. Methods Appl. Mech. Engrg.*, 166:143–164, 1998.

[43] Babuška I. Ihlenburg F. Paik E.T. and Sauter S.A. A generalized finite element method for solving the Helmholtz equation in two dimensions with minimal pollution. *Comput. Methods Appl. Mech Engrg.*, 128:325–359, 1995.

[44] Oberai A.A and Pinsky P.M. A multiscale finite element method for the Helmholtz equation. *Comput. Methods Appl. Mech. Engrg.*, 154:281–297, 1998.

[45] Hughes T.J.R. Multiscale phenomena: Green's functions, the Dirichlet-to-Neumann formulation, subgrid scale models, bubbles and the origins of stabilized methods. *Comput. Methods Appl. Mech. Engrg.*, 127:387–401, 1995.

[46] Oberai A.A. and Pinski P.M. A residual-based finite element method for the Helmholtz equation. *Int. J. Numer. Meth. Engng.*, 49:399–419, 2000.

[47] Patera A.T. A spectral element method for fluid dynamics: Laminar flow in a channel expansion. *J. Comput. Physics.*, 54:533–549, 1984.

[48] Seriani G. and Priolo E. High-order spectral element method for acoustic wave modelling. In *Proceedings 61st Annual International SEG Meeting*, pages 1561–1564, Houston, 1991.

[49] Seriani G. Priolo E. Carcione E. and Padovani E. High-order spectral element method for elastic wave modelling. In *Proceedings 62nd Annual International SEG Meeting*, pages 1285–1288, New Orleans, 1992.

[50] Seriani G. and Priolo E. Spectral element method for acoustic wave simulation in heterogeneous media. *Finite Elements in Analysis and Design*, 16:337–348, 1994.

[51] Zampieri E. and Tagliani A. Numerical approximation of elastic wave equations by implicit spectral methods. *Comput. Methods Mech. Engrg.*, 144:33–50, 1997.

[52] Komatitsch D. Vilotte J-P. Vai R. Castillo-Covarrubias J.M. and Sánchez-Sesma F.J. The spectral element method for elastic wave equations - application to 2D and 3D seismic problems. *Int. J. Numer. Meth. Engng.*, 45:1139–1164, 1999.

[53] Dauksher W. and Emery A.F. Accuracy in modelling the acoustic wave equation with Chebyshev spectral finite elements. *Finite Elements in Analysis and Design*, 26:115–128, 1997.

[54] Dauksher W. and Emery A.F. The solution of elastostatic and elastodynamics problems with Chebyshev spectral finite elements. *Comput. Methods Appl. Mech. Engrg.*, 188:217–233, 2000.

[55] Finnveden S. Exact spectral finite element analysis of stationary vibrations in a railway car structure. *Acta Acustica*, 2:461–482, 1994.

[56] Langley R.S. Analysis of power flow in beams and frameworks using the direct-dynamic stiffness method. *J. Sound Vib.*, 81:439–452, 1990.

[57] Finnveden S. Spectral finite element analysis of the vibration of straight fluid-filled pipes with flanges. *J. Sound. Vib.*, 199:125–154, 1997.

[58] Bilodeau B.A. and Doyle J.F. Spectral elements for acoustic wave propagation through thin-walled complex structures. In Ferguson N.S. Wolfe H.F. and Mei C., editors, *Proceedings of the 6th International Conference on Recent Advances in Structural Dynamics*, pages 279–293, Southampton, 1997.

[59] Finnveden S. Spectral finite element analysis of stationary vibrations in a beam-plate structure. *Acustica - Acta Acustica*, 82:478–497, 1996.

[60] Lee U. and Lee J. Dynamic analysis of one and two dimensional structures using spectral finite element method. In Ferguson N.S. Wolfe H.F. and Mei C., editors, *Proceedings of the 6th International Conference on Recent Advances in Structural Dynamics*, pages 263–277, Southampton, 1997.

[61] Nour-Omid B. Solving large linearized systems in mechanics. In Papadrakakis M., editor, *Solving Large-Scale Problems in Mechanics*, chapter 2, pages 39–64. John Wiley & Sons Ltd., 1993.

[62] Van der Vorst H.A. Krylov subspace iteration. *Computing in Science and Engineering*, pages 32–37, January/February 2000.

[63] Saad Y. and Zhang J. Enhanced multi-level block ILU preconditioning strategies for general sparse linear systems. *Journal of Computational and Applied Mathematics*, 130:99–118, 2001.

[64] Wesseling P. *An Introduction to Multigrid Methods.* Wiley, Chichester, 1992.

[65] Hess R. and Joppich W. A comparison of parallel multigrid and a Fast Fourier Transform algorithm for the solution of the Helmholtz equation in numerical weather prediction. *Parallel Computing*, 22:1503–1512, 1997.

[66] Shapira Y. Multigrid methods for 3D definite and indefinite problems. *Applied Numerical Mathematics*, 26:377–398, 1998.

[67] Piacentini A. and Rosa N. An improved domain decomposition method for the 3D Helmholtz equation. *Comput. Methods Appl. Mech. Engrg.*, 162:113–124, 1998.

[68] Farhat C. Macedo A. Lesoine M. Roux F-X. Magoulès F. and de La Bourdonnaie A. Two-level domain decomposition methods with Lagrange multipliers for the fast iterative solution of acoustic scattering problems. *Comput. Methods Appl. Mech. Engrg.*, 184:213–239, 2000.

[69] Susan-Resiga R.F. and Atassi H.M. Domain-decomposition method for time-harmonic aeroacoustic problems. *AIAA Journal*, 39(5):802–809, 2001.

[70] Adeli H. High-performance computing for large-scale analysis optimization and control. *Journal of Aerospace Engineering*, 13(1):1–10, January 2000.

[71] Bayliss A. Goldstein C. I. and Turkel E. An iterative method for the Helmholtz equation. *J. Comput. Physics*, 49:443–457, 1983.

[72] Nour-Omid B. and Parlett B.N. Element preconditioning using splitting techniques. *SIAM J. Sci. Stat. Comput.*, 6(3):761–770, 1985.

[73] Baumeister K.J. and Kreider K.L. Preconditioning the Helmholtz equation. *J. Sound Vib.*, 209(1):77–97, 1998.

[74] Benamou J-D. and Desprès B. A domain decomposition method for the Helmholtz equation and related optimal control problems. *J. Comput. Physics*, 136:68–82, 1997.

[75] Chevalier P. and Nataf F. An optimized order 2 (002) method for the Helmholtz equation. *C. R. Acad. Sci. Paris, Analyse numérique/ Numerical Analysis*, 326(1):769–774, 1998.

[76] Shaw R.P. A brief history of boundary integral/element methods in acoustics. In Ciskowski R.D. and Brebbia C.A., editors, *Boundary Element Methods in Acoustics*, chapter 1. Computational Mechanics Publications, Southampton, 1991.

[77] Bonnet M. *Boundary Integral Equation Methods for Solids and Fluids.* John Wiley & Sons Ltd., 1995.

[78] Brebbia C.A. *The Boundary Element Method for Engineers.* Pentech Press, London, 1978.

[79] Wu T.W. and Seybert A.F. Acoustic radiation and scattering. In Ciscowski R.D. and Brebbia C.A., editors, *Boundary Element Methods in Acoustics*, chapter 3, pages 61–76. Computational Mechanics Publications & Elsevier Applied Science, Southampton, 1991.

[80] Wu T.W. Two-dimensional problems and three-dimensional problems. In Wu T.W., editor, *Boundary Element Acoustics: Fundamental and Computer Codes*, chapter 2-3, pages 29–68. WIT Press, 2000.

[81] Provatidis C. and Zafiropoulos N. On the 'interior Helmholtz integral equation formulation' in sound radiation problems. *Engineering Analysis with Boundary Elements*, 26:29–40, 2002.

[82] Schenk H.A. Improved integral formulation for acoustic radiation problems. *J. Acoust. Soc. Am.*, 44:41–58, 1968.

[83] Seybert A.F. and Rengarajan T.K. The use of CHIEF to obtain unique solution for acoustic radiation using boundary integral equations. *J. Acoust. Soc. Am.*, 81:1299–1306, 1987.

[84] Hwang W.S. A boundary integral method for acoustic radiation and scattering. *J. Acoust. Soc. Am.*, 101(6):3330–3335, June 1997.

[85] Burton A.J. and Miller G.F. The application of integral equation methods to the solution of some boundary-value problems. *Proc. R. Soc. London*, 323:201–210, 1971.

[86] Chien C.C. Rajiyah J. and Atluri S.N. An effective method for solving the hypersingular integral equations in 3D acoustics. *J. Acoust. Soc. Am.*, 88(2):918–937, August 1990.

[87] Wu T.W. and Wan G.C. Numerical modeling of acoustic radiation and scattering from thin bodies using a cauchy principal integral equation. *J. Acoust. Soc. Am.*, 92:271–287, 1992.

[88] Liu Y. and Rizzo F.J. A weakly singular form of the hypersingular boundary integral equation applied to 3D acoustic wave problems. *Comput. Methods Appl. Mech. Engrg.*, 96:271–287, 1992.

[89] Lin T.C. The numerical solution of Helmholtz's equation in three dimensions. *SIAM J. Num. Anal.*, 22:670–686, 1985.

[90] Filippi P.J.T. Layer potentials and acoustic diffraction. *J. Sound Vib.*, 54:473–500, 1977.

[91] Vai R. Castillo-Covarrubias J.M. Sánchez-Sesma F.J. Komatitsch D. and Vilotte J-P. Elastic wave propagation in an irregularly layered medium. *Soil Dynamics and Earthquake Engineering*, 18:11–18, 1999.

[92] Koopman G.H. and Benner H. Method for computing the sound power of machines based on the Helmholtz integral. *J. Acoust. Soc. Am.*, 71(1):77–89, 1982.

[93] Bernhard R.J. Gardner B.K. and Mollo C.G. Prediction of sound fields in cavities using boundary element methods. *AIAA*, 25:1176–1183, 1987.

[94] Raavendra S.T. Vlahopoulos N. and Glaves A. An indirect boundary element formulation for multi-valued impedance simulation in structural acoustics. *Applied Mathematical Modelling*, 22:379–393, 1998.

[95] Vlahopoulos N. Indirect variational boundary element method in acoustics. In Wu T.W., editor, *Boundary Element Acoustics: Fundamentals and Computer Codes*, chapter 6, pages 83–116. WIT Press, 2000.

[96] Raavendra S.T. An efficient indirect boundary element technique for multi-frequency acoustic analysis. *Int. Jnl. Numer. Meth. Engng.*, 44:59–76, 1999.

[97] Tadeu A.J. and Santos P. Performance of higher order elements in the analysis of a two dimensional acoustic medium. In Brebbia C.A. and Power H., editors, *Boundary Elements XXI*, volume 6 of *International Series on Advances in Boundary Elements*, pages 497–512, Worcester College, Oxford University, August 1999. Wessex Institute of Technology, UK, WIT Press.

[98] Tadeu A.J. and Santos P. Performance of the BEM solution in 3D acoustic wave scattering. *Advances in Engineering Software*, 32:629–639, 2001.

[99] Feistauer M. Hsiao G.C. and Kleinman R.E. Asymptotic and a posteriori error estimates for boundary element solutions of hypersingular integral equations. *SIAM J. Numer. Anal.*, 33(2):666–685, April 1996.

[100] Kita E. and Kamiya N. Recent studies on adaptive boundary element methods. *Adv. Engng. Software*, 19(1):21–32, 1994.

[101] Kita E. and Kamiya N. Error estimation and adaptive mesh refinement in boundary element method, an overview. *Engineering Analysis with Boundary Elements*, 25:479–495, 2001.

[102] Charafi A. Neves C. and Wrobel L.C. *h*-hierarchical adaptive boundary element method using local reanalysis. *Int. J. Numer. Meth. Engng.*, 38:2185–2207, 1995.

[103] Rodríguez J.J. and Power H. *h*-adaptive mesh refinement strategy for the boundary element method based on local error analysis. *Engineering Analysis with Boundary Elements*, 25:565–579, 2001.

[104] Chen J.T. Chen K.H. and Chen C.T. Adaptive boundary element method of time-harmonic exterior acoustics problems in two dimensions. Comput. Methods Appl. Mech. Engrg., to appear, 2002.

[105] Yokoyama M. and Zhan J. A *p*-adaptive 3D BEM for acquiring the desired accuracy. *Advances in Engineering Software*, 28:395–401, 1997.

[106] Tomioka S. Nisiyama S. Itagaki M. and Enoto T. Internal field error reduction in boundary element analysis for Helmholtz equation. *Engineering Analysis with Boundary Elements*, 23:211–222, 1999.

[107] Brebbia C.A. Telles J.C. and Wrobel L.C. *Boundary Element Techniques*. Berlin: Springer, 1984.

[108] Pierce A.D. and Wu X-F. Variational method for prediction of acoustic radiation from vibrating bodies. *J. Acoust. Soc. Am.*, 74(Suppl. 1, S107), 1983.

[109] Ademoyero A.A. Bartholomew-Biggs M.C. and Davies A.J. Computational linear algebra issues in the Galerkin boundary element method. *Computers and Mathematics with Applications*, 42:1267–1283, 2001.

[110] Valente F.P. and Pina H.L. Iterative techniques for 3D boundary element method systems of equations. *Engineering Analysis with Boundary Elements*, 25:423–429, 2001.

[111] Saad Y. and Schultz M.H. GMRES: A generalized minimal residual algorithm for solving nonsymmetric linear systems. *SIAM J. Sci. Stat. Comput.*, 7(3):856–869, July 1986.

[112] Van der Vorst H.A. Bi-CGStab: A fast and smoothly converging variant of Bi-CG for the solution nonsymmetric linear systems. *SIAM J. Sci. Stat. Comput.*, 13(2):631–644, 1992.

[113] Chen K. and Harris P.J. Efficient preconditioners for iterative solution of the boundary element equations for three-dimensional Helmholtz equation. *Applied Numerical Mathematics*, 36:475–489, 2001.

[114] Davey K. Bounds S. Rosindale I. and Alonso Rasgado M.T. A coarse preconditioner for multi-domain boundary element equations. *Computers and Structures*, 80:643–658, 2002.

[115] Makarov S.N. and Ochmann M. An iterative solver of the Helmholtz integral equation for high-frequency acoustic scattering. *J. Acoust. Soc. Am.*, 103(2):742–750, February 1998.

[116] Chen S. and Liu Y. A unified boundary element method for the analysis of sound and shell-like structure interactions. II. Efficient solution techniques. *J. Acoust. Soc. Am.*, 108(6):2738–2745, December 2000.

[117] Araújo F.C. Martins C.J. and Mansur W.J. An efficient BE iterative-solver-based substructuring algorithm for 3D time-harmonic problems in elastodynamics. *Engineering Analysis with Boundary Elements*, 25:795–803, 2001.

[118] Tricomi F. *Integral Equations.* Interscience, New York, 1957.

[119] Golberg M.A. and Chen C.S. *Discrete Projection Methods for Integral Equations.* Computational Mechanics Publications, 1997.

[120] Trefftz E. Ein Gegenstück zum Ritzschen Verfahren. In *2nd Int. Cong. Appl. Mech.*, pages 131–137, Zürich, 1926.

[121] Kupradze V.D. A method for the approximate solution of limiting problems in mathematical physics. *Comput. Math. Math. Phys.*, 4:199–205, 1964.

[122] Wearing J.L. and Sheikh M.A. The development of the Trefftzian methodology for engineering design analysis. *Advances in Engineering Software*, 24:117–131, 1995.

[123] Herrera I. and Sabina F.J. Connectivity as an alternative to boundary integral equations: Construction of bases. *Proc. Natl. Acad. Sci. USA*, 75(5):2059–2063, May 1978.

[124] Herrera I. Boundary methods: A criterion for completeness. *Proc. Natl. Acad. Sci. USA*, 77(8):4395–4398, August 1980.

[125] Herrera I. Trefftz-Herrera domain decomposition. *Advances in Engineering Software*, 24:43–56, 1995.

[126] Zieliński A.P. and Herrera I. Trefftz method: Fitting boundary conditions. *Int. Jnl. Numer. Meth. Engng.*, 24:871–891, 1987.

[127] Kita E. and Kamiya N. Trefftz method: an overview. *Advances in Engineering Software*, 24:3–12, 1995.

[128] Jin W.G. Cheung K. and Zienkiewicz O.C. Application of the Trefftz method in plane elasticity problems. *Int. J. Numer. Meth. Engng.*, 30:1147–1161, 1990.

[129] Cheung Y.K. Jin W.G. and Zienkiewicz O.C. Solution of the Helmholtz equation by Trefftz method. *Int. J. Numer. Meth. Engng.*, 32:63–78, 1991.

[130] Jin W.G. and Cheung K. Trefftz direct method. *Advances in Engineering Software*, 24:65–69, 1995.

[131] Zienkiwicz O.C Kelly D.W. and Bettess P. Marriage à la mode - the best of both worlds (finite elements and boundary elements). In Glowinski R. Rodin E.Y. and Zienkiewicz O.C., editors, *Energy Methods in Finite Element Analysis*, chapter 5, pages 81–107. John Wiley and Sons Ltd., 1979.

[132] Jirousek J. Basis for development of large finite elements locally satisfying all field conditions. *Comput. Methods Appl. Mech. Engrg.*, 14:65–92, 1978.

[133] Jirousek J. and Teodorescu P. Large finite elements method for the solution of problems in the theory of elasticity. *Computers and Structures*, 15(5):575–587, 1982.

[134] Zieliński A.P. and Zienkiewicz O.C. Generalized finite element analysis with T-complete boundary solution functions. *Int. J. Numer. Meth. Engng.*, 21:509–528, 1985.

[135] Jirousek J. The Hybrid-Trefftz model - a finite element model with special suitability to adaptive solutions and local effect calculations. In Hughes T.J.R., editor, *Finite Element Methods for Plate and Shell Structures*, volume 1:Element Technology, chapter 9, pages 219–243. Pineridge Press Limited, 1986.

[136] Jirousek J. and Stojek M. Numerical assessment of a new T-element approach. *Computers and Structures*, 57(3):367–378, 1995.

[137] Jirousek J. and Zieliński A.P. Survey of Trefftz-type element formulations. *Computers and Structures*, 63(2):225–242, 1997.

[138] Stojek M. Least-squares Trefftz-type elements for the Helmholtz equation. *Int. J. Numer. Meth. Engng.*, 41:831–849, 1998.

[139] Texeira de Freitas J.A. Hybrid finite element formulations for elastodynamic analysis in the frequency domain. *Int. Journal of Solids and Structures*, 36:1883–1923, 1999.

[140] Monk P. and Wang D-Q. A least-squares method for the Helmholtz equation. *Comput. Methods Appl. Mech. Engrg.*, 175:121–136, 1999.

[141] Hsiao G.C. Schnack E. and Wendland W.L. Hybrid coupled finite-boundary element methods for elliptic systems of second order. *Comput. Methods Appl. Mech. Engrg.*, 190:431–485, 2000.

[142] Mathon R. and Johnston R.L. The approximate solution of elliptic boundary-value problems by fundamental solutions. *SIAM J. Numer. Anal.*, 14(4):638–650, September 1977.

[143] Bogomolny A. Fundamental solutions method for elliptical boundary value problems. *SIAM J. Numer. Anal.*, 22(4):644–699, August 1985.

[144] Johnston R.L. and Fairweather G. The method of fundamental solutions for problems in potential flow. *Appl. Math. Modelling*, 8:265–270, 1984.

[145] de Mey G. Integral equations for potential problems with the source function not located on the boundary. *Computer and Structures*, 8:113–115, 1978.

[146] Johnston D. Plate bending by a boundary point method. *Computer and Structures*, 26:673–680, 1987.

[147] Bugess G. and Mahajerin E. A comparison of the the boundary element and superposition methods. *Computers and Structures*, 19(5/6):697–705, 1984.

[148] Fairweather G. and Karageorghis A. The method of fundamental solutions for elliptic boundary value problems. *Advances in Computational Mathematics*, 9:69–95, 1998.

[149] Manolis G.D. and Shaw R.P. Fundamental solutions to Helmholtz's equation for inhomogeneous media by a first-order differential equation system. *Soil Dynamics and Earthquake Engineering*, 16:81–94, 1997.

[150] Shaw R.P. and Manolis G.D. A generalized Helmholtz equation fundamental solution using a conformal mapping and dependent variable transformation. *Engineering Analysis with Boundary Elements*, 24:177–188, 2000.

[151] Karageorghis A. The method of fundamental solutions for the calculation of the eigenvalues of the Helmholtz equation. *Applied Mathematical Letters*, 14:837–842, 2001.

[152] Caruthers J.E. French J.C. and Ravinprakash G.K. Green function discretization for numerical solution of the Helmholtz equation. *J. Sound Vib.*, 187(4):553–568, 1995.

[153] French J.C. Three dimensional combustion stability modeling for solid rocket motors. In *34^{th} AIAA/ASMA/SAE/ASEE Joint Propulsion Conference*, AIAA paper 98-3702, Cleveland, OH, July 1998.

[154] French J.C. and Dang A.L. Analytic combustion stability analysis of a non-axis-symmetric motor cavity, including non-axial acoustic modes: A status report. In *JANNAF Propulsion Conference*, Tucson, AZ, December 1998.

[155] French J.C and Coats D.E. Automated 3D solid rocket combustion stability analysis. In *AIAA-99-2797*, 1999.

[156] Caruthers J.E. Engels R.C. and Ravinprakash G.K. A wave expansion computational method for discrete frequency acoustics within inhomogeneous flows. In *2nd AIAA/CEAS Aeroacoustic Conference, CEAS/AIAA-96-1684*, pages 1–11, State College, PA, May 1996.

[157] Caruthers J.E. Steinhoff J.S. and Engels R.C. An optimal finite difference representation for a class of linear PDE's with application to the Helmholtz equation. *Journal of Computational Acoustics*, 7(4):245–252, 1999.

[158] Rice H. and Ruiz G. A finite difference analysis of plate vibration using a wave expansion technique. In *ISMA25*, pages 1477–1482, 2000.

[159] Melenk J.M. and Babuška I. The partition of unity finite element method: basic theory and applications. *Comput. Methods Appl. Mech. Engrg.*, 139:289–314, 1996.

[160] Babuška I. and Melenk J.M. The partition of unity method. *Int. J. Numer. Meth. Engng.*, 40:727–758, 1997.

[161] Bouillard Ph. and Suleau S. Element-free Galerkin solutions for Helmholtz problems: Formulation and numerical assessment of the pollution effect. *Comput. Methods Appl. Mech. Engrg.*, 162:317–335, 1998.

[162] Suleau S. Deramaeker A. and Bouillard Ph. Dispersion and pollution of meshless solutions for the Helmholtz equation. *Comput. Methods Appl. Mech. Engrg.*, 190:639–657, 2000.

[163] Laghrouche O. and Bettess P. Short wave modelling using special finite elements. *Journal of Computational Acoustics*, 8(1):189–210, 2000.

[164] Desmet W. *A Wave Based Prediction Technique for Coupled Vibro-Acoustic Analysis.* PhD thesis, Katholieke Universiteit Leuven, Heverlee(Leuven), Belgium, 1998.

[165] van Hal B. Desmet W. Vandepetite D. and Sas P. Application of the efficient wave based prediction technique for the steady-state dynamic analysis of flat plates. In Sas P and Moens D., editors, *ISMA25*, pages 607–614, Leuven, Belgium, September 2000.

[166] Reutskiy S. A boundary method of Trefftz type with approximate trial functions. *Engineering Analysis with Boundary Elements*, 26:341–353, 2002.

[167] Piltner R. Recent developments in the Trefftz method for finite element and boundary element applications. *Advances in Engineering Software*, 24:107–115, 1995.

[168] Abou-Dina M.S. Implementation of Trefftz method for the solution of some elliptic boundary value problems. *Applied Mathematics and Computation*, 127:125–147, 2002.

[169] Katsurada M. and Okamoto H. The collocation points of the fundamental solution method for the potential problem. *Computers Math. Applic.*, 31(1):123–137, 1996.

[170] Golberg M.A. and Chen C.S. The method of fundamental solutions for potential, Helmholtz and diffusion problems. In Golberg M.A., editor, *Boundary Integral Methods: Numerical and Mathematical Aspects*, chapter 4, pages 103–176. Computational Mechanics Publications/WIT Press, 1999.

[171] Kondapalli P.S. Shippy D.J. and Fairweather G. Analysis of acoustic scattering in fluids and solids by the method of fundamental solutions. *J. Acoust. Soc. Am.*, 91(4):1844–1854, April 1992.

[172] Zieliński A.P. On trial functions applied in the generalized Trefftz method. *Advances in Engineering Software*, 24:147–155, 1995.

[173] Kitagawa T. Asymptotic analysis of the fundamental solution method. *Jnl. Comput. Appl. Math.*, 38:263–269, 1991.

[174] Christiansen S. and Saranen J. The conditioning of some numerical methods for first kind boundary integral equations. *Journal of Computational and Applied Mathematics*, 67:43–58, 1996.

[175] Ochmann M. The full-field equations for acoustic radiation and scattering. *J. Acoust. Soc. Am.*, 105:2574–2584, May 1999.

[176] Song L. Koopmann H. and Fahnline J.B. Numerical errors associated with the method of superposition for computing acoustic fields. *J. Acoust. Soc. Am.*, 89(6):2625–2633, June 1991.

[177] Chen C.S. Golberg M.A. and Hon Y.C. Numerical justification of fundamental solutions and the quasi-Monte Carlo method for Poisson-type equations. *Engineering Analysis with Boundary Elements*, 22:61–69, 1998.

[178] Qin Q-H. *The Trefftz Finite Element & Boundary Element Method.* WIT Press, 2001.

[179] Jirousek J. and Leon N. A powerful finite element for plate bending. *Comput. Methods Appl. Mech. Engrg.*, 12:77–96, 1977.

[180] Jirousek J. Venkatesh A. Zieliński and Rabemantantsoa H. Comparative study of p-extensions based on conventional assumed displacement and Hybrid-Trefftz FE models. *Computers and Structures*, 46:261–278, 1993.

[181] Belytschko T. Lu Y.Y. and Gu L. Element-free Galerkin methods. *Int. J. Numer. Meth. Engng.*, 37:229–256, 1994.

[182] Ruiz G. and Rice H. An implementation of a wave-based finite difference scheme for a 3D acoustic problem. *J. Sound Vib.*, 256(2):373–381, 2002.

[183] Sommerfeld A. *Partial Differential Equations in Physics.* Academic Press, New York, 1949.

[184] Harari I. Barbone P.E. and Montgomery J.M. Finite element formulations for exterior problems: Application to hybrid methods, non-reflecting boundary conditions, and infinite elements. *Int. Jnl. Numer. Meth. Engng.*, 40:1791–2805, 1997.

[185] Tsynkov S.V. Numerical solution problems in unbounded domains: A review. *Applied Numerical Mathematics*, 27:465, 1998.

[186] Astley R.J. FE mode-matching schemes for the exterior Helmholtz problem and their relationship to the FE-DtN approach. *Commun. Num. Meth. Engng.*, 12:257–267, 1996.

[187] Givoli D. and Keller J.B. A finite element method for large domains. *Comput. Methods Appl. Mech. Engrg.*, 76:41–66, 1989.

[188] Harari I. Barbone P.E. and Montgomery J.M. Studies of domain-based formulations for computing exterior problems of acoustics. *Int. J. Numer. Meth. Engng.*, 37:2935–2950, 1994.

[189] Oberai A.A Malhotra M. and Pinsky P.M. On the implementation of the Dirichlet-to-Neumann radiation condition for iterative solution of the Helmholtz equation. *Applied Numerical Mathematics*, 27:443–464, 1998.

[190] Engquist B. and Madja A. Radiation boundary conditions for acoustic and elastic waves. *Commun. Pure Appl. Math.*, 32:313–357, 1979.

[191] Bayliss A. and Turkel E. Radiation boundary conditions for wave-like equations. *Commun. Pure Appl. Math.*, 33:707–725, 1980.

[192] Bayliss A. Gunzburger M. and Turkel E. Boundary conditions for the numerical solution of elliptic equations in exterior regions. *SIAM Journal Appl. Math.*, 42(2):707–725, April 1982.

[193] Bossut R. and Decarpigny J-N. Finite element modeling of radiating structures using dipolar damping elements. *J. Acoust. Soc. Am*, 86(4):1234–1244, October 1989.

[194] Assaad J. Decarpigny J-N. Bruneel C. Bossut R. and Hamonic B. Application of the finite element method to two-dimensional radiation problems. *J. Acoust. Soc. Am.*, 94(1):562–573, July 1993.

[195] Quarteroni A. Tagliani A. and Zampieri E. Generalized Galerkin approximations of elastic waves with absorbing boundary conditions. *Comput. Methods Appl. Mech. Engrg.*, 163:323–341, 1998.

[196] Pinsky P.M. Thompson L.L. and Abboud N.N. Local high-order radiation boundary conditions for the two-dimensional time-dependent structural acoustics problem. *J. Acoust. Soc. Am.*, 91(3):1320–1335, March 1992.

[197] Givoli D. Patlashenko I. and Keller J.B. High-order boundary conditions and finite elements for infinite domains. *Comput. Methods Appl. Mech. Engng.*, 143:13–39, 1997.

[198] Guddati M.N. and Tassoulas J.L. Continued-fraction absorbing boundary conditions for the wave equation. *Journal of Computational Acoustics*, 8(1):139–156, 2000.

[199] Givoli D. and Patlashenko I. An optimal high-order non-reflecting finite element scheme for wave scattering problems. *Int. J. Numer. Meth. Engng.*, 53:2389–2411, 2002.

[200] Muğan A. and Hulbert G. Nonreflecting boundary conditions in acoustics for finite element methods based upon off-source boundary integral equations. *Comput. Methods Appl. Mech. Engrg.*, 188:289–306, 2000.

[201] Muğan A. and Hulbert G. Nonreflecting boundary conditions in elastodynamics for finite element methods based upon off-source boundary integral equations. *Comput. Methods Appl. Mech. Engrg.*, 190:1289–1307, 2000.

[202] Cunefare K.A. Koopmann G. and Brod K. A boundary element method for acoustic radiation valid for all wavenumbers. *J. Acoust. Soc. Am.*, 85(1):39–48, January 1989.

[203] Bettess P. *Infinite Elements.* Penshaw Press: Sunderland, 1992.

[204] Cremers L. Fyfe K.R. and Coyette J.P. A variable order infinite acoustic wave envelope element. *J. Sound Vib.*, 171(4):483–508, 1994.

[205] Astley R.J. Macaulay G.J. and Coyette J.P. Mapped wave envelope elements for acoustical radiation and scattering. *J. Sound Vib.*, 170(1):97–118, 1994.

[206] Astley R.J. Macaulay G.J. Coyette J.P. and Cremers L. Three-dimensional wave-envelope elements of variable order for acoustic radiation and scattering.

Part I. Formulation in the frequency domain. *J. Acoust. Soc. Am.*, 103:49–63, 1998.

[207] Astley R.J. Mapped spheroidal wave-envelope elements for unbounded wave problems. *Int. J. Numer. Meth. Engng.*, 41:1235–1254, 1998.

[208] Chadwick E. Bettess P. and Laghrouche O. Diffraction of short waves modelled using new mapped wave envelope finite and infinite elements. *Int. J. Numer. Meth. Engng.*, 45:335–354, 1999.

[209] Chow Y.K. and Smith I.M. Static and periodic infinite elements. *Int. J. Numer. Meth. Engng.*, 17:503–526, 1981.

[210] Medina F. and Taylor R.L. Finite element techniques for problems of unbounded domains. *Int. J. Numer. Meth. Engng.*, 19:1209–1226, 1983.

[211] Pinto T. and Coyette J.P. Conjugated infinite elements for two-dimensional time-harmonic elastodynamics. *Journal of Computational Acoustics*, 8(3):473–493, 2000.

[212] Harari I. and Hughes T.R.J. A cost comparison of boundary element and finite element methods for problems of time-harmonic acoustics. *Comput. Methods Appl. Mech. Engrg.*, 97:77–102, 1992.

[213] Oppenheim A.V. and Schafer R.W. *Discrete-Time Signal Processing.* Signal Processing. Prentice-Hall, 1985.

[214] Strang G. *Linear Algebra and its Applications.* Harcourt College Publishers, third edition, 1988.

[215] Nashed M.Z. and Votruba G.F. A unified operator theory of generalized inverses. In Nashed M.Z., editor, *Generalized Inverses and Applications*, pages 111–124, The University of Wisconsin, Madison, October, 8-10 1976. Mathematics Research Center, Academic Press.

[216] Kalman R.E. Algebraic aspects of the generalized inverse of a rectangular matrix. In Nashed M.Z., editor, *Generalized Inverses and Applications*, pages 111–124, The University of Wisconsin, Madison, October, 8-10 1976. Mathematics Research Center, Academic Press.

[217] Ben-Israel A. and Greville T.N.E. *Generalized Inverses: theory and applications.* Texts, Monographs & Tracts. Wiley-Interscience, John Wiley & Sons, 1974.

[218] Layton J.B. Efficient direct computation of the pseudo-inverse and its gradient. *Int. J. Numer. Meth. Engng.*, 40:4211–4223, 1997.

[219] Rusin D. Topics on sphere distributions. http://www.math.niu.edu/ rusin/known-math/95/sphere.faq.

[220] Berezin A.A. Electrostatic stability and instability of n equal charges in a circle. *Chemical Physics Letters*, 123:62–64, 1986.

[221] ICASE/LaRC Workshop on Benchmark Problems in Computational Aeroacoustics. *A Numerical Solution Method for Axisymmetric Bodies*, Hampton, Virginia, 1994.

[222] Pierce A.D. *Acoustics: An Introduction to its Physical Principles and Applications.* in mechanical engineering. McGraw-Hill, 1981.

[223] Varah J.M. A practical examination of some numerical methods for linear discrete ill-posed problems. *SIAM Review*, 21(1):100–111, January 1979.

[224] Watts G.R. Acoustic performance of an interference-type noise-barrier profile. *Applied Acoustics*, 49(1):1–16, 1996.

[225] Duhamel D. Sergent P. Hua C. and Cintra D. Measurement of active noise control efficiency around noise barriers. *Applied Acoustics*, 55(3):217–241, 1998.

[226] Timoshenko S.P. and Goodier J.N. *Theory of Elasticity.* Engineering Societies Monographs. McGraw-Hill, third edition, 1984.

[227] Landau L.D. Lifshits E.M. Kosevich A.M. and Pitaevski L.P. *Theory of Elasticity.* Course of theoretical physics. Oxford: Pergamon, 3rd edition, 1986.

[228] Meriam J.L. *Dynamics, SI-version.* John Wiley & Sons, Inc., second edition, 1975.

[229] Fahy F. *Sound and Structural Vibration: radiation, transmission and response.* Academic Press, 1985.

[230] Gatti P.L. and Ferrari V. *Applied Structural and Mechanical Vibrations: theory, methods and measuring instrumentation.* E & FN Spon, 1999.

[231] Blevins R.D. *Formulas for Natural Frequencies and Mode Shape.* Krieger Publishing Company, 1979.

[232] Lee N-S. and Bathe K-J. Effects of elements distortions on the performance of isoparametric elements. *Int. J. Numer. Meth. Engng.*, 36:3553–3576, 1993.

[233] Achenbach J.D. Gautesen A.K. and McMaken H. *Ray Methods for Waves in Elastic Solids.* Pitman Books Ltd., 1882.

[234] Miklowitz J. *The Theory of Elastic Waves and Waveguides.* North-Holland Publishing Co., 1978.

[235] Washizu K. *Variational Methods in Elasticity and Plasticity.* Pergamon Press, third edition, 1982.

[236] Dhatt G. Touzot G. and Cantin G. *The Finite Element Method Displayed.* John Willey & Sons, 1984.

[237] Duff I.S. Erisman A.M. and Reid J.K. *Direct Methods for Sparse Matrices.* Oxford: Clarendon, 1986.

[238] Schendel U. *Sparse Matrices: Numerical Aspects with Applications for Scientists and Engineers.* Ellis Horwood, 1989.

[239] Cohoon J.P. and Davidson J.W. *C++ Program Design: An Introduction to Programming and Object Oriented Design.* Chicago; London: Irwin, 1997.

[240] Kundert K.S. Sparse matrix techniques. In Albert Ruehli, editor, *Circuit Analysis.* North-Holland, 1986.

[241] Balay S. Buschelman K. Gropp W.D. Kaushik D. Curfman L. McInnes L.C. and Smith B.F. PETSc home page. http://www.mcs.anl.gov/petsc, 2001.

[242] Balay S. Gropp W.D. McInnes L.C. and Smith B.F. PETSc users manual. Technical report, ANL-95/11 - Revision 2.1.3, 2002.

[243] Balay S. Buschelman K. Gropp W.D. Kaushik D. Curfman L. McInnes L.C. and Smith B.F. Efficient management of parallelism in object oriented numerical software libraries. In Arge E. Bruaset A.M. and Langtangen H.P., editors, *Modern Software Tools in Scientific Computing*, pages 163–202. Birkhauser Press, 1997.

[244] Axelsson O. *Iterative Solution Methods.* Cambridge University Press, 1994.

[245] Faber V. and Manteuffel T. Necessary and sufficient conditions for the existence of a conjugate gradient method. *SIAM J. Numer. Anal.*, 21(2):352–362, April 1984.

Appendix A

Finite element method for acoustic problems

A.1 Helmholtz equation

Acoustic responses in a fluid are usually regarded as small perturbations to an ambient reference state. For a fluid, the ambient state is characterised by those values (p_0, ρ_0, $\mathbf{v}_0$) which the pressure, density, and fluid velocity have when the perturbation is absent.

The total pressure p, mass density ρ and velocity vector $\mathbf{v}$ at any time t and any position vector $\mathbf{x}$ in the fluid may then be expressed as

$$p(\mathbf{x}, t) = p_0(\mathbf{x}, t) + p'(\mathbf{x}, t) \tag{A.1}$$

$$\rho(\mathbf{x}) = \rho_0(\mathbf{x}, t) + \rho'(\mathbf{x}, t) \tag{A.2}$$

$$\mathbf{v}(\mathbf{x}, t) = \mathbf{v}_0(\mathbf{x}, t) + \mathbf{v}'(\mathbf{x}, t), \tag{A.3}$$

where p', ρ' and $\mathbf{v}'$ represent the acoustic contributions to the overall pressure and density fields.

For the derivation of the dynamic equations that govern the acoustic perturbation fields, the conservation of mass, conservation of momentum and the pressure-density relation are applied to an infinitesimal fluid volume $dV = dx\ dy\ dz$.

Consider a small rectangular volume element dV, as shown in figure A.1, which is fixed in space and through which elements of the fluid travel. Referring to figure A.1, we see that the net influx of mass into this fixed infinitesimal volume resulting from flow in the x direction is

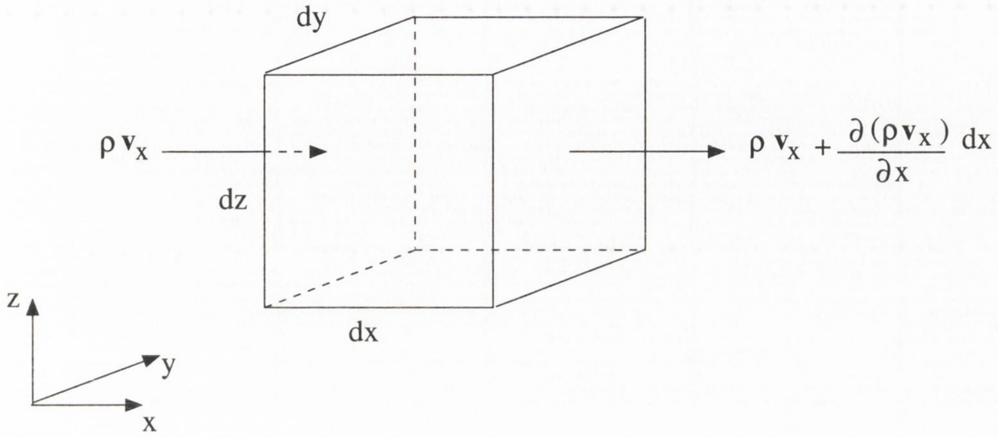

Figure A.1: Mass flow in the x direction for an infinitesimal fluid volume dv. A similar diagram can be drawn for fluid flowing in the y and z directions.

$$\left[\rho\mathbf{v}_x - \left(\rho\mathbf{v}_x + \frac{\partial(\rho\mathbf{v}_x)}{\partial x}dx\right)\right] dy\ dz = -\frac{\partial(\rho\mathbf{v}_x)}{\partial x}\ dV \tag{A.4}$$

Using similar expressions for the net influx for the y and z directions, the total influx is given by

$$-\left(\frac{\partial(\rho\mathbf{v}_x)}{\partial x} + \frac{\partial(\rho\mathbf{v}_y)}{\partial y} + \frac{\partial(\rho\mathbf{v}_z)}{\partial z}\right)\ dV = -\nabla\cdot(\rho\mathbf{v})\ dV \tag{A.5}$$

Since the increase per unit time of the mass of the fluid volume dV must equal the net mass entering the volume, we obtain the continuity equation

$$\frac{\partial(\rho_0 + \rho')}{\partial t} + \nabla\cdot((\rho_0 + \rho')\mathbf{v}') = 0. \tag{A.6}$$

The conservation of momentum requires a dynamic force balance in the orthogonal directions x, y and z. Assuming an inviscid fluid, the dynamic forces acting on dV are depicted in figure A.2.

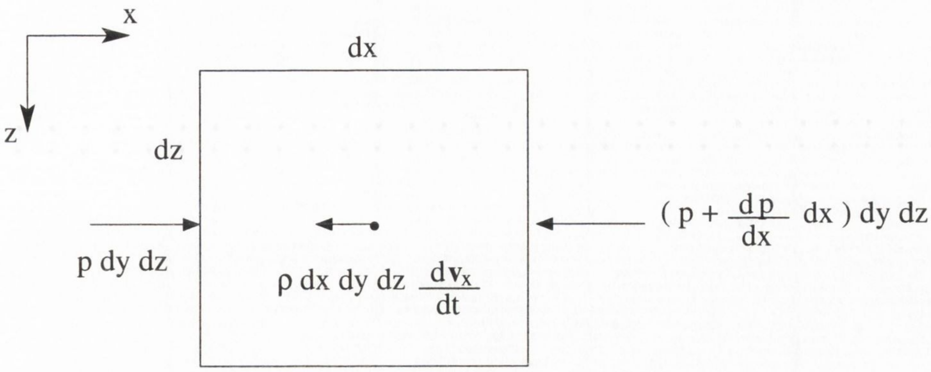

Figure A.2: Dynamic forces acting in the x-direction.

The conservation of momentum in the x-direction then becomes

$$\rho\ dx\ dy\ dz\ \frac{d\mathbf{v}_x}{dt} = -\frac{\partial p}{\partial x}\ dx\ dy\ dz, \tag{A.7}$$

where the total time derivative of the x-component of the fluid velocity vector is given by

$$\frac{d\mathbf{v}_x}{dt} = \frac{\partial \mathbf{v}_x}{\partial t} + \frac{\partial \mathbf{v}_x}{\partial x}\ \mathbf{v}_x + \frac{\partial \mathbf{v}_x}{\partial y}\ \mathbf{v}_y + \frac{\partial \mathbf{v}_x}{\partial z}\ \mathbf{v}_z = \left(\frac{\partial}{\partial t} + \mathbf{v}\cdot\nabla\right)\ \mathbf{v}_x. \tag{A.8}$$

Together with similar expressions for the dynamic force balances in the y and z-direction, the conservation of momentum may be expressed as a vector equation

$$(\rho_0 + \rho')\left(\frac{\partial}{\partial t} + \mathbf{v}'\cdot\nabla\right)\ \mathbf{v}' = -\nabla\,(p_0 + p') \tag{A.9}$$

For a gas, e.g. air, with constant specific (per unit mass) heat coefficients c_p and c_v at constant temperature and volume, respectively, and for which the pressure p is proportional to the density ρ at constant temperature, sound propagation occurs with negligible internal heat flow. That is, it is an adiabatic process. This principle leads to a pressure-density relation of the form

$$p = \mathcal{F}(\rho) = K\rho^{\gamma}, \tag{A.10}$$

where $\gamma = c_p/c_v$ is the specific-heat ratio ($\gamma = 1.4$ for air).

Equation A.10, may be also be expressed as a Taylor expansion,

$$p = \mathcal{F}|_{\rho=\rho_0} + \frac{d\mathcal{F}}{d\rho}(\rho - \rho_0) + \frac{1}{2}\frac{d^2\mathcal{F}}{d\rho^2}|_{\rho=\rho_0}(\rho - \rho_0)^2 + \dots \tag{A.11}$$

Using equations A.1 and A.2 in equation A.12 yields

$$p' = \frac{\gamma_0}{\rho_0}\,\rho' + \frac{\gamma(\gamma-1)}{2\rho_0^2}\,(\rho')^2 + \dots \tag{A.12}$$

The linear approximation (often referred to as the *acoustic approximation*) neglects second- and higher-order terms, so the linear equations take the form

$$\frac{\partial \rho'}{\partial t} + \rho_0 \nabla \cdot \mathbf{v}' = 0 \tag{A.13}$$

$$\rho_0 \frac{\partial \mathbf{v}'}{\partial t} = -\nabla p' \tag{A.14}$$

$$p' = \frac{\gamma p_0}{\rho_0}\,\rho' \tag{A.15}$$

The wave equation results from the linear wave equations given above if one uses equation A.15 to eliminate ρ' from the mass-conservation equation and then takes the time derivative of the resulting equation. This sequence of steps yields

$$\nabla^2 p' - \frac{1}{c^2}\frac{\partial^2 p'}{\partial t^2} = 0, \tag{A.16}$$

where c denotes the phase speed of an acoustic wave in a fluid,

$$c = \sqrt{\frac{\gamma p_0}{\rho_0}}. \tag{A.17}$$

Assuming a time-harmonic excitation of the form

$$p'(\mathbf{x}, t) = p'(\mathbf{x})e^{\iota\omega t}, \tag{A.18}$$

the wave equation A.16 transforms into the linear Helmholtz equation[1]

$$\nabla^2 p' + k^2 p' = 0, \tag{A.19}$$

---

[1] also referred to as the *reduced wave equation*.

where $k = \omega/c$ is the acoustic wavenumber, and $\iota = \sqrt{-1}$. The transformation of the momentum equation A.14 yields the relation between the steady-state fluid velocity vector field and the steady-state pressure field,

$$\mathbf{v}' = \frac{\iota}{\rho_0 \omega} \nabla p' \tag{A.20}$$

The primes on the acoustic variables in equations A.19 and A.20 are usually omitted, when there is little possibility of confusing the total field variables with their acoustic perturbations.

A.2 Weighted residual formulation

Consider a domain Ω_A with boundary Γ_A, in which the propagation of waves is governed by the Helmholtz equation A.19. Since for each point in Ω_A equation A.19 applies, then

$$\int_{\Omega_A} \tilde{w}(\nabla^2 p + k^2 p)\; d\Omega_A = 0 \tag{A.21}$$

is satisfied for any weighting function $\tilde{w}$, that is bounded and uniquely defined in Ω_A and on its boundary surface Γ_A.

We seek to approximate the pressure field p in equation A.21, by a known given function, N say. In order to reduce the continuity order required by the approximating function, a 'weak form' of equation A.21 may be obtained using integration by parts and the divergence theorem. That is,

$$\int_{\Omega_A} \left[\frac{\partial}{\partial x}\left(\tilde{w}\frac{\partial}{\partial x}\right) + \frac{\partial}{\partial y}\left(\tilde{w}\frac{\partial}{\partial y}\right) + \frac{\partial}{\partial z}\left(\tilde{w}\frac{\partial}{\partial z}\right) \right] d\Omega_A \\ - \int_{\Omega_A} \left(\frac{\partial \tilde{w}}{\partial x}\frac{\partial p}{\partial x} + \frac{\partial \tilde{w}}{\partial y}\frac{\partial p}{\partial y} + \frac{\partial \tilde{w}}{\partial z}\frac{\partial p}{\partial z} \right) d\Omega_A + \int_{\Omega_A} k^2 \tilde{w} p \; d\Omega_A = 0 \tag{A.22}$$

Applying the divergence theorem to the first integral term in equation A.22, yields the 'weak form' of the weighted residual formulation of the linear Helmholtz equation

$$\int_{\Omega_A} (\nabla \tilde{w} \cdot \nabla p)\; d\Omega_A - \omega^2 \int_{\Omega_A} \left(\frac{1}{c^2} \tilde{w} p \right) d\Omega_A = - \int_{\Gamma_A} (\iota \rho_0 \omega \tilde{w} \mathbf{v} \cdot \mathbf{n})\; d\Gamma_A, \tag{A.23}$$

where $\mathbf{n}$ is the unit normal vector with positive orientation away from the volume Ω.

A.3 Implementation of the FEM

For any domain Ω_E in which the propagation of acoustic waves is governed by the Helmholtz equation A.19, a unique pressure distribution is obtained, provided that one boundary condition is specified at each point on the boundary $\Gamma_A = \Gamma_D \cup \Gamma_N \cup \Gamma_R$. In general, three types of boundary conditions are applied:

$$p = \overline{p}, \text{ on } \Gamma_A \tag{A.24}$$

$$\mathbf{v} \cdot \mathbf{n} = \overline{v} \text{ on } \Gamma_N \tag{A.25}$$

$$\mathbf{v} \cdot \mathbf{n} = \frac{p}{\overline{Z}} \text{ on } \Gamma_R, \tag{A.26}$$

where $\overline{p}$, $\overline{v}$ and $\overline{Z}$ are prescribed pressure, normal velocity and normal impedance functions, respectively.

A.3.1 Definition of the shape functions and parametric mapping

The finite element method performs an independent approximation of the exact solution in smaller sub-domains $\Omega_e \in \Omega_A$, called *elements*. A number of nodes, say n_e, are defined at some particular locations in each element. The distribution of the pressure is interpolated within each element using a set of prescribed *shape functions* N_i^e, only defined within the considered element domain Ω_e,

$$p(\mathbf{x}) \approx \hat{p} = \sum_{i=1}^{n_p} N_i^e(\mathbf{x}) \hat{p}_i, \ \mathbf{x} \in \Omega_e \tag{A.27}$$

Each shape function N_i^e is defined such that it has a value of unity at node i of the element and that it is zero at all other element nodes. In general, two basic interpolation techniques are used: *serendipity* and *Lagrangian.* These techniques are developed considering local element coordinates (ξ, η) in 2D and (ξ, η, ζ) in 3D, called *normalised coordinates*, as shown in figure A.3.

In the serendipity interpolation technique, the physical conditions are assumed constant throughout the element. The shape function is then dependent only on nodes

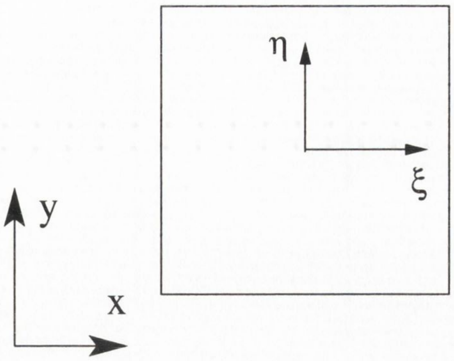

Figure A.3: Normalised local coordinates.

values located along the boundary (fourth-order serendipity elements have an interior node only to have a complete fourth-order polynomial interpolation function). An illustration of the first four order quadrilateral serendipity elements is shown in figure A.4.

The shape functions for two-dimensional quadrilateral serendipity elements are defined as follows:

- linear element

$$N_i^e = \frac{1}{4}(1+\xi_i\xi)(1+\eta_i\eta) \tag{A.28}$$

- quadratic element

  vertex nodes

$$N_i^e = \frac{1}{4}(1+\xi_i\xi)(1+\eta_i\eta)(\xi_i\xi+\eta_i\eta-1), \tag{A.29}$$

  edge nodes

$$\xi_i = 0,\ N_i^e = \frac{1}{2}(1-\xi^2)(1+\eta_i\eta),$$

$$\eta_i = 0,\ N_i^e = \frac{1}{2}(1+\xi_i\xi)(1-\eta^2)$$

- cubic element

  vertex nodes

$$N_i^e + \frac{1}{32}(1+\xi_i\xi)(1+\eta_i\eta)[-10+9(\xi^2+\eta^2)], \tag{A.30}$$

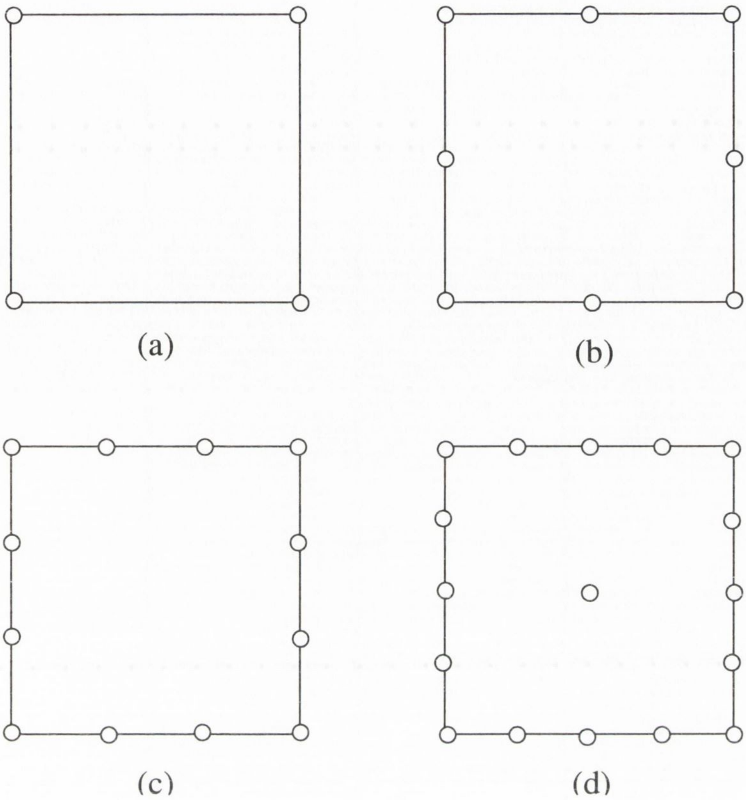

Figure A.4: Serendipity elements: (a) lineal, (b) quadratic, (c) cubic, (d) fourth-order.

edge nodes

$$\xi_i = \pm 1, \; \eta_i = \pm\frac{1}{3},$$

$$N_i^e = \frac{9}{32}(1+\xi_i\xi)(1-\eta^2)(1+9\eta_i\eta)$$

Triangular serendipity elements are defined following an analogous procedure (see, e.g. [5]).

Whenever a given (serendipity) element discretisation fails to give an accurate solution, a non-constant physical condition is present in some or all the elements. The size of the elements is then reduced in size (mesh refinement) until a constant physical condition is (approximately) reached.

In the Lagrangian elements, shown schematically in figure A.5, the boundaries as well as the interior of the element are discretized. Hence, this interpolation technique is often referred to as 'high-order interpolation' technique. In the Lagrangian interpolation approach, the physical conditions are assumed to vary in the interior of the element. Thus, a refinement of the mesh is, in principle, not necessary should the interpolation order and element size used give an inaccurate solution. In this case, a higher order function is used, maintaining the same size of the element.

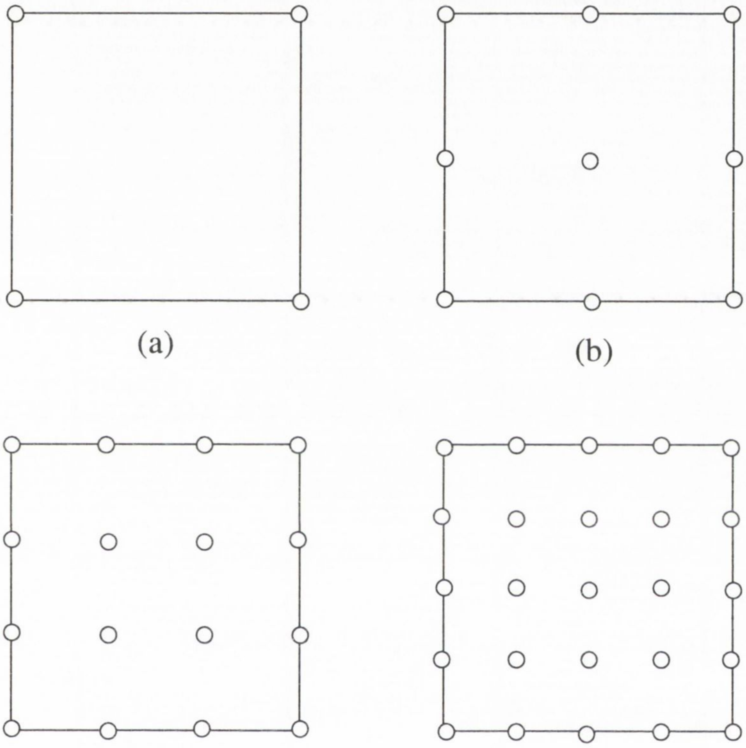

(a) (b)

(c) (d)

Figure A.5: Lagrangian elements: (a) lineal, (b) quadratic, (c) cubic, (d) fourth-order.

For any arbitrary variable α, the Lagrangian functions are defined as

$$l_k^n(\alpha) = \frac{(\alpha-\alpha_2)(\alpha-\alpha_2)\ldots(\alpha-\alpha_{i-1})(\alpha-\alpha_{i+1})\ldots(\alpha-\alpha_n)}{(\alpha_k-\alpha_1)(\alpha_k-\alpha_2)\ldots(\alpha_k-\alpha_{k-1})(\alpha-\alpha_{k+1})\ldots(\alpha_k-\alpha_n)}, \tag{A.31}$$

giving a unit value at α_k and zero at n points. That is, the total number of nodes along the α coordinate is $n+1$. For two-dimensional quadrilateral elements, as those shown in figure A.5, we have

$$N_i^e = N_{IJ} = l_I^n(\xi) l_J^m(\eta), \tag{A.32}$$

where I, J denote the row and column position of each node in the element and n, m the number of subdivisions in the ξ and η directions, respectively.

Based on the element shape functions N_i^e, some global shape functions N_i defined in the entire domain may be constructed. For each element domain Ω_e, to which node i belongs, we have

$$N_i = \begin{cases} N_j^e, & \text{if } i = j, \\ 0, & \text{otherwise.} \end{cases} \tag{A.33}$$

Using this notation, a global pressure expansion may then be expressed as

$$\hat{p} = \sum_{i=1}^{n_f} N_i^e(\mathbf{x}) \hat{p}_i = \mathbf{N}\hat{\mathbf{p}}, \;\; \mathbf{x} \in \Omega_A. \tag{A.34}$$

where n_f is the total number of nodes in the discretisation, $\mathbf{N}$ is a $1 \times n_f$ vector of global shape functions and $\hat{\mathbf{p}}$ is a $n_f \times 1$ vector of unknown nodal pressure values. Whether serendipity or Lagrangian elements (linear or of higher order) are used in the expansion formulation, an isoparametric mapping procedure is usually performed in order to define the geometry of the elements[2]. That is, a one-to-one correspondence is defined between a point in the parent element (in the local coordinate system) and a point in the mapped element (in the global coordinate system). This relation is expressed as an expansion in terms of the same shape function. The contributions of each shape function to the expansion are the desired global coordi-

---

[2] Lagrangian elements have been shown to give better results than serendipity elements for curved-edge and angular element distortions, see e.g. [232].

nates of the element nodes, i.e.,

$$x = \sum_{i=1}^{n_e} N_i^e(\xi, \eta, \zeta)\; x_i = \mathbf{N}^e \mathbf{x}_i$$

$$y = \sum_{i=1}^{n_e} N_i^e(\xi, \eta, \zeta)\; y_i = \mathbf{N}^e \mathbf{y}_i \tag{A.35}$$

$$z = \sum_{i=1}^{n_e} N_i^e(\xi, \eta, \zeta)\; z_i = \mathbf{N}^e \mathbf{z}_i \tag{A.36}$$

According to the chain rule of partial differentiation, the derivatives of the shape functions N_i^e with respect to the local coordinates (ξ, η, ζ) may be expressed in terms of the global coordinates (x, y, z) by means of the Jacobian matrix $\mathbf{J}$ as

$$\begin{pmatrix} \frac{\partial N_i^e}{\partial \xi} \\ \\ \frac{\partial N_i^e}{\partial \eta} \\ \\ \frac{\partial N_i^e}{\partial \zeta} \end{pmatrix} = \begin{bmatrix} \frac{\partial x}{\partial \xi}, & \frac{\partial y}{\partial \xi}, & \frac{\partial z}{\partial \xi} \\ \\ \frac{\partial x}{\partial \eta}, & \frac{\partial y}{\partial \eta}, & \frac{\partial z}{\partial \eta} \\ \\ \frac{\partial x}{\partial \zeta}, & \frac{\partial y}{\partial \zeta}, & \frac{\partial z}{\partial \zeta} \end{bmatrix} \begin{pmatrix} \frac{\partial N_i^e}{\partial x} \\ \\ \frac{\partial N_i^e}{\partial y} \\ \\ \frac{\partial N_i^e}{\partial z} \end{pmatrix} = \mathbf{J} \begin{pmatrix} \frac{\partial N_i^e}{\partial x} \\ \\ \frac{\partial N_i^e}{\partial y} \\ \\ \frac{\partial N_i^e}{\partial z} \end{pmatrix}.$$

Each element in the Jacobian matrix $\mathbf{J}$ is a function in the local coordinates (ξ, η, ζ), which is obtained from the mapping relationship A.35. A volume element $d\Omega_A$, for example, is mapped as $d\Omega_A = dx\; dy\; dz = \det(\mathbf{J}) d\xi\; d\eta\; d\zeta$.

A.3.2 Galerkin finite element

In a Galerkin weighted residual approach, the weighting function $\tilde{w}$ is expanded in terms of the same shape functions as used for the pressure expansion. Equation A.23 then takes the form

$$\int_{\Omega_A} \left(\nabla \mathbf{N}^T \cdot \nabla \mathbf{N}\right)\; d\Omega_A\, \hat{p} - \omega^2 \int_{\Omega_A} \left(\mathbf{N}^T \frac{1}{c^2} \mathbf{N}\right)\; d\Omega_A\, \hat{p} = \\ - \imath\omega \int_{\Gamma_N} \mathbf{N}^T \rho_0\;\; d\Gamma_N\, \overline{v} - \imath\omega \int_{\Gamma_R} \left(\mathbf{N}^T \frac{\rho_0}{Z} \mathbf{N}\right)\; d\Gamma_R\, \hat{p}, \tag{A.37}$$

Using matrix notation, equation A.37 may be expressed as

$$\left[\mathbf{K} - \omega^2\mathbf{M} + \imath\omega\mathbf{C}\right]\hat{\mathbf{p}} = -\imath\omega\mathbf{S}\overline{\mathbf{v}}. \tag{A.38}$$

where **K** is the $(n_f \times n_f)$ acoustic *stiffness* matrix, with components

$$\begin{aligned} K_{ij} &= \int_{\Omega_A} \left(\frac{\partial N_i}{\partial x}\frac{\partial N_j}{\partial x} + \frac{\partial N_i}{\partial y}\frac{\partial N_j}{\partial y} + \frac{\partial N_i}{\partial z}\frac{\partial N_j}{\partial z} \right) d\Omega_A \\ &= \sum_{e=1}^{m_{ij}} \left\{ \int_{\Omega_e} \left(\frac{\partial N_i^e}{\partial x}\frac{\partial N_j^e}{\partial x} + \frac{\partial N_i^e}{\partial y}\frac{\partial N_j^e}{\partial y} + \frac{\partial N_i^e}{\partial z}\frac{\partial N_j^e}{\partial z} \right) d\Omega_A \right\}, \end{aligned} \tag{A.39}$$

where m_{ij} is the number of elements, to which both node i and node j belong. Similarly, the $(n_f \times n_f)$ mass and damping matrices are defined as

$$M_{ij} = \int_{\Omega_A} \left(\frac{1}{c^2} N_i N_j \right) d\Omega_A = \sum_{e=1}^{m_{ij}} \left\{ \int_{\Omega_e} \left(\frac{1}{c^2} N_i^e N_j^e \right) d\Omega_A \right\}. \tag{A.40}$$

$$C_{ij} = \int_{\Gamma_R} \left(\rho_0 \frac{1}{\overline{Z}} N_i N_j \right) d\Gamma_R = \sum_{f=1}^{m_{c_{ij}}} \left\{ \int_{\Gamma_e^f} \left(\rho_0 \frac{1}{\overline{Z}} N_i^e N_j^e \right) d\Gamma_A \right\}, \tag{A.41}$$

where $m_{c_{ij}}$ is the number of elements faces Γ_e^f, on which both node i and node j are located and that are part of the boundary surface Γ_R. The specification of the prescribed normal impedance is usually restricted to a constant value per element in Γ_R.

Since each node belongs to common elements with only a few, adjacent nodes, only a few matrix elements in the stiffness, mass and damping matrices are non-zero. Thus, **K**, **M** and **C** are sparsely populated.

Finally, the $(n_f \times 1)$ vector **S** is defined as

$$S_{ni} = \int_{\Gamma_N} \left(N_i \rho_0 \overline{v} \right) d\Gamma_A = \sum_{e=1}^{m_{vi}} \sum_{f=1}^{f_{vi}^e} \left\{ \int_{\Gamma_e^f} \left(N_i^e \rho_0 \overline{v} \right) d\Gamma_A \right\}, \tag{A.42}$$

where m_{vi} is the number of elements, for which node i is located on their f_{vi}^e element faces Γ_e^f, that are part of the boundary surface Γ_N.

A.3.3 Properties of the acoustic finite element model

From the element expressions, the following properties of the stiffness, mass and damping matrices may be derived:

- The approximation results in system of equations that is sparse, due to the local character of the shape functions.
- The matrices are symmetrical. Moreover, the stiffness and mass matrices are also real (though not definite for acoustic problems).
- Since the expansion in each element is performed regardless the excitation frequency, the stiffness and mass matrices $\mathbf{K}$ and $\mathbf{M}$ are frequency independent.

Appendix B

Finite element method in elastodynamics

B.1 Wave motion equations for linear isotropic solids

B.1.1 The strain tensor

In discussing the deformation of an elastic body it will be assumed that there are enough constraints to prevent the body from moving as a rigid body so that no displacements of particles of the body are possible without a deformation of it.

As a direct implication of the notion of continuum, the deformation of the medium can be expressed in terms of the gradients of the displacement vector

$$\mathbf{u} = \left\{ \begin{array}{c} u_1 \\ u_2 \\ u_3 \end{array} \right\}. \tag{B.1}$$

Within the restrictions of the linearised theory[1] the deformation is described in a

---

[1] The spatial gradients of the displacement components are assumed to be much smaller than unity.

very simple manner by the small strain tensor ε, with components

$$\varepsilon_{ij} = \frac{1}{2}\left(\frac{\partial u_i}{\partial x_j} + \frac{\partial u_j}{\partial x_i}\right), \tag{B.2}$$

where x_i denotes a general coordinate system.

It follows that $\varepsilon_{ij} = \varepsilon_{ji}$, i.e., ε is a symmetric tensor of rank two. The usual convention notation is to express the normal strain tensor components as ε and the tangential strain components as γ, i.e.

$$\varepsilon_i = \frac{\partial u_j}{\partial x_i} \tag{B.3}$$

$$\gamma_{ij} = \frac{1}{2}\left(\frac{\partial u_i}{\partial x_j} + \frac{\partial u_j}{\partial x_i}\right) \tag{B.4}$$

B.1.2 The stress tensor and the general equation of motion

Let us consider a section from an elastic body in the form of a tetrahedron as shown in figure B.1. The surface Γ_E of the section is subjected to the traction $\mathbf{t}(\mathbf{x},\mathrm{t})$. In addition, the body of volume Ω_E, may be subjected to a body force per unit volume, $\mathbf{f}(\mathbf{x},\mathrm{t})$. Since in equilibrium the sum of the forces acting on the body must vanish, we have

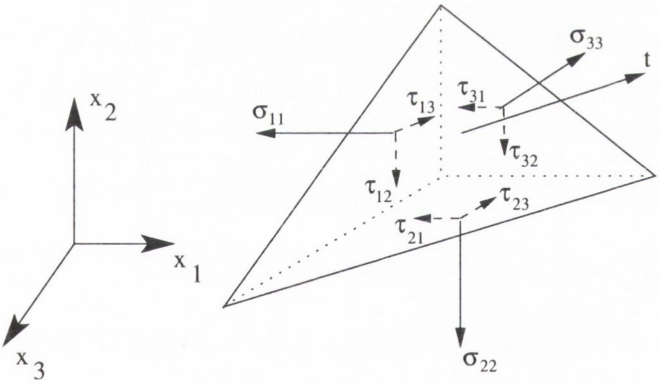

Figure B.1: Stress components and the stress vector T on a tetrahedron.

$$\int_{\Gamma_E} \mathbf{t}\; d\Gamma_E + \int_{\Omega_E} \mathbf{f}\; d\Omega_E = \int_{\Omega_E} \rho\ddot{\mathbf{u}}\; d\Omega_E, \tag{B.5}$$

where ρ is the mass density of the elastic medium, and $\ddot{\mathbf{u}} = \partial^2 \mathbf{u}(\mathbf{x}, t)/\partial t^2$. Hence, the instantaneous rate of change of the linear momentum of the body is equal to the resultant external force acting on it at the particular instant of time.

In the limit $\Omega_E \to 0$, we obtain the Cauchy's stress formula

$$t_i = \tau_{ji} n_j, \tag{B.6}$$

where τ_{ji} are the stresses on the surface with unit normal $\mathbf{i}_j$, as shown in figure B.1. Substitution of equation B.6 into B.5 yields

$$\int_{\Gamma_E} \tau_{ij} n_j \; d\Gamma_E + \int_{\Omega_E} f_i \; d\Omega_E = \int_{\Omega_E} \rho \ddot{u}_i \; d\Omega_E. \tag{B.7}$$

The surface integral can be transformed into a volume integral by Gauss's theorem, leading to the *Cauchy's first law of motion*

$$\int_{\Omega_E} \left(\frac{\partial \tau_{ji}}{\partial x_j} + f_i - \rho \ddot{u}_i \right) \; d\Omega_E = 0. \tag{B.8}$$

Equation B.8 is the general equation of motion, from which the elastic wave equations are derived.

In general, σ is used to represent the normal stresses, whilst τ is used to represent the shear stresses, i.e.

$$t_i = \sigma_i n_j, \;\; i = j \tag{B.9}$$

$$t_i = \tau_{ij} n_j, \;\; i \neq j. \tag{B.10}$$

It may be demonstrated (see e.g. reference [233, pp. 14-15]) that the stress tensor is also symmetric. Hence,

$$\tau_{km} = \tau_{mk} \tag{B.11}$$

B.1.3 Hooke's law

In general form, the linear relation between the components of the stress tensor and the components of the strain tensor (Hooke's law) is

$$\tau_{ij} = C_{ijkl} \varepsilon_{kl} \tag{B.12}$$

where

$$C_{ijkl} = C_{jikl} = C_{klij} = C_{ijlk}.$$

The solid is homogeneous if the coefficients C_{ijkl} are constants. It is isotropic when there are no preferred directions. It can be shown that in this case, the constants C_{ijkl} may be expressed as

$$C_{ijkl} = \lambda\delta_{ij}\delta_{kl} + \mu(\delta_{ik}\delta_{jl} + \delta_{il}\delta_{jk}), \tag{B.13}$$

where δ_{ij} is the Kronecker delta ($\delta_{ij} = 0$, if $i \neq j$), and λ and μ are known as Lamé's elastic constants, which can be written in terms of the readily measurable constants, the modulus of elasticity E, and Poisson's ratio ν as

$$\mu = \frac{E}{2(1+\nu)}, \; \lambda = \frac{\nu E}{(1+\nu)(1-2\nu)}. \tag{B.14}$$

Equation B.12 then assumes the form

$$\tau_{ij} = \lambda\varepsilon_{kk}\delta_{ij} + 2\mu\varepsilon_{ij}. \tag{B.15}$$

For three-dimensional Cartesian coordinates (x, y, z), equation B.15 yields

$$\sigma_x = \lambda\left(\frac{\partial u_y}{\partial y} + \frac{\partial u_z}{\partial z}\right) + \mu\left(\frac{\partial u_x}{\partial x}\right) \tag{B.16}$$

$$\tau_{xy} = \mu\left(\frac{\partial u_x}{\partial y} + \frac{\partial u_y}{\partial x}\right). \tag{B.17}$$

The equations for the stress-strain relationship in the y and z coordinates are completely analogous.

B.1.4 Displacement equations of motion

If the strain-displacement relations B.2 are substituted into Hooke's law equation B.15, we obtain

$$\tau_{ij} = \lambda u_k\delta_{ij} + \mu\left(\frac{\partial u_i}{\partial x_j} + \frac{\partial u_j}{\partial u_i}\right). \tag{B.18}$$

Substituting equation B.18 in the stress-equation of motion B.8, yields the displacement equations of motion

$$\mu \frac{\partial^2 u_i}{\partial x_j^2} + (\lambda + \mu) \frac{\partial^2 u_j}{\partial x_j \partial x_i} + \rho f_i = \rho \ddot{u}_i. \tag{B.19}$$

Equation B.19 along with the strain-displacement relations, Hooke's law and the stress-equations must be satisfied at every interior point of the undeformed elastic body Ω_E.

For any elastic domain Ω_E in which the propagation of elastic waves is governed by the displacement equation of motion B.19, a unique solution at Ω_E is ensured, provided that one boundary condition is defined at each point in the boundary surface $\Gamma_E = \Gamma_C \cup \Gamma_F$. The following conditions may be applied:

- *Displacement boundary conditions*: some or all components u_i are prescribed on the boundary.

- *Traction boundary conditions*: some or all components τ_{ij} are prescribed on the boundary.

- A combination of the above two, where displacements are defined on part Γ_C of the boundary and traction boundary conditions are defined on the remaining part Γ_F.

Boundary conditions must be complemented with initial conditions. In Ω_E at time t = 0, we have

$$u_i(\mathbf{x}, 0) = \tilde{u}_i(\mathbf{x})$$

$$\dot{u}_i(\mathbf{x}, 0^+) = \tilde{v}_i(\mathbf{x}).$$

B.2 Waves of dilatation and waves of distortion

In the absence of body forces ($\mathbf{f} = 0$), we can express equationB.19 in vector notation as

$$\mu \nabla^2 \mathbf{u} + (\lambda + \mu) \nabla \nabla \cdot \mathbf{u} = \rho \ddot{\mathbf{u}}, \tag{B.20}$$

where ∇^2 is the Laplace operator

$$\nabla^2 = \frac{\partial^2}{\partial x_1^2} + \frac{\partial^2}{\partial x_2^2} + \frac{\partial^2}{\partial x_3^2}.$$

The first term on the right hand side of equation B.20 represents a zero volume expansion deformation, i.e. distortion and rotation only, while the second term is related to the irrotational deformation. Consider a decomposition of the displacement vector of the form [234]

$$\mathbf{u} = \nabla\varphi + \nabla \times \boldsymbol{\psi}, \tag{B.21}$$

where φ and $\boldsymbol{\psi}$ are a scalar and vector potentials, respectively. Substituting equation B.21 into equation B.20 yields

$$\mu\nabla^2[\nabla\varphi + \nabla \times \boldsymbol{\psi}] + (\lambda + \mu)\nabla\nabla \cdot [\nabla\varphi + \nabla \times \boldsymbol{\psi}] = \rho\frac{\partial^2}{\partial t^2}[\nabla\varphi + \nabla \times \boldsymbol{\psi}]. \tag{B.22}$$

Since $\nabla \cdot \nabla\varphi = \nabla^2\varphi$ and $\nabla \cdot \nabla \times \boldsymbol{\psi} = 0$, we obtain

$$\nabla[(\lambda + 2\mu)\nabla^2\varphi - \rho\ddot{\varphi}] + \nabla \times [\mu\nabla^2\boldsymbol{\psi} - \rho\ddot{\boldsymbol{\psi}}] = 0. \tag{B.23}$$

Equation B.21 satisfies the equation of motion if

$$\nabla^2\varphi = \frac{1}{c_L^2}\ddot{\varphi} \tag{B.24}$$

and

$$\nabla^2\boldsymbol{\psi} = \frac{1}{c_T^2}\ddot{\boldsymbol{\psi}}. \tag{B.25}$$

These are uncoupled equations for *dilatational* and *equivoluminal* waves respectively, where c_L and c_T are the wave velocities given by

$$c_L^2 = \frac{\lambda + 2\mu}{\rho} \tag{B.26}$$

and

$$c_T^2 = \frac{\mu}{\rho}. \tag{B.27}$$

When solutions are found to equations B.24 and B.25, **u** can be obtained from relationship B.21. Noting that the Cartesian form of equation B.21 is

$$u_i = \varphi_{,i} + c_{ijk}\psi_{k,j}, \tag{B.28}$$

it follows from this equation that planes waves of u_i will have the character of the planes waves of φ and $\psi_{k,j}$, i.e., it will be composed in general of planes waves that propagate with c_L and c_T.

Assuming a steady-state harmonic excitation of the form

$$\mathbf{u}(\mathbf{x}, t) = \mathbf{u}(\mathbf{x}, \omega)e^{-j\omega t}, \tag{B.29}$$

and substituting into equation B.23, yields the Helmholtz equations

$$\nabla^2\varphi + k_L^2\varphi = 0 \tag{B.30}$$

and

$$\nabla^2\boldsymbol{\psi} + k_T^2\boldsymbol{\psi} = 0, \tag{B.31}$$

where $\omega = 2\pi f$ is the circular frequency, and $k_L = \omega/c_L$ and $k_T = \omega/c_T$ are the dilatational and equivoluminal wavenumbers, respectively.

B.3 Weighted residual formulation

The weighted residual finite element formulation in a continuum elastic domain Ω_E with boundary surface Γ_E, is derived from the general stress-equation of motion B.8. Using vector notation, we have

$$\int_{\Omega_E} \left(\mathbf{L}^T\boldsymbol{\sigma} + \mathbf{f} - \rho\ddot{\mathbf{u}}\right)\, d\Omega_E = 0, \tag{B.32}$$

where (using Cartesian coordinates)

$$\boldsymbol{\sigma} = \begin{pmatrix} \sigma_x \\ \sigma_y \\ \sigma_z \\ \tau_{xy} \\ \tau_{xz} \\ \tau_{yz} \end{pmatrix}, \tag{B.33}$$

is the stress tensor, and $\mathbf{L}$ is a differential operator defined as

$$\mathbf{L} = \begin{bmatrix} \frac{\partial}{\partial x} & 0 & 0 \\ 0 & \frac{\partial}{\partial y} & 0 \\ 0 & 0 & \frac{\partial}{\partial z} \\ \frac{\partial}{\partial y} & \frac{\partial}{\partial x} & 0 \\ \frac{\partial}{\partial z} & 0 & \frac{\partial}{\partial x} \\ 0 & \frac{\partial}{\partial z} & \frac{\partial}{\partial y} \end{bmatrix}, \tag{B.34}$$

If a steady-state harmonic excitation (equation B.29) is assumed, equation B.32 may be re-written as

$$\int_{\Omega_E} \left(\mathbf{L}^T \boldsymbol{\sigma} + f_i + \omega^2 \rho \mathbf{u}\right) \, d\Omega_E = 0. \tag{B.35}$$

Since for each point in Ω_E, equation B.35 applies, then

$$\int_{\Omega_E} \tilde{w} \left(\mathbf{L}^T \boldsymbol{\sigma} + f_i + \omega^2 \rho \mathbf{u}\right) \, d\Omega_E = 0, \tag{B.36}$$

is satisfied for any arbitrary weighting function $\tilde{w}$, that is bounded and uniquely defined in Ω_E and on its boundary surface Ω_E. Equation B.36 may be conveniently expressed in terms of the displacement vector $\mathbf{u}$, by means of the stress-strain relationship B.15. Using vector notation, the stress tensor components can be expressed as

$$\boldsymbol{\sigma} = \mathbf{D}\boldsymbol{\epsilon} = \mathbf{D}\mathbf{L}\mathbf{u}, \tag{B.37}$$

where $\mathbf{D}$ is the elasticity matrix, and $\boldsymbol{\epsilon}$ is the stress tensor defined as (using equations B.3 and B.4)

$$\boldsymbol{\epsilon} = \begin{pmatrix} \varepsilon_x \\ \varepsilon_y \\ \varepsilon_z \\ \gamma_{xy} \\ \gamma_{xz} \\ \gamma_{yz} \end{pmatrix} = \mathbf{L} \begin{pmatrix} u_x \\ u_y \\ u_z \end{pmatrix} = \mathbf{Lu}. \tag{B.38}$$

The definition of the elasticity matrix $\mathbf{D}$ varies for two-dimensional problems, depending on whether the stress-strain relationship is defined in terms of a plain stress or a plain strain condition (see, e.g. [5]). For three-dimensional problems, the components of the matrix $\mathbf{D}$ are defined as

$$\mathbf{D} = \frac{E(1-\nu)}{(1+\nu)(1-2\nu)} \times \begin{bmatrix} 1 & \frac{\nu}{(1-\nu)} & \frac{\nu}{(1-\nu)} & 0 & 0 & 0 \\ & 1 & \frac{\nu}{(1-\nu)} & 0 & 0 & 0 \\ & & 1 & 0 & 0 & 0 \\ & & & \frac{(1-2\nu)}{2(1-\nu)} & 0 & 0 \\ & & & & \frac{(1-2\nu)}{2(1-\nu)} & 0 \\ & & & & & \frac{(1-2\nu)}{2(1-\nu)} \end{bmatrix} \tag{B.39}$$

Substituting equation B.37 into equation B.36 yields

$$\int_{\Omega_E} \tilde{w} \left(\mathbf{L}^T \mathbf{D} \mathbf{L} + f_i + \omega^2 \rho \right) \mathbf{u} \; d\Omega_E = 0. \tag{B.40}$$

Applying integration by parts and the divergence theorem [235], we obtain the 'weak form' of the weighted residual equation for elastic problems

$$\int_{\Omega_E} (\mathbf{L}^T \tilde{w} \mathbf{D} \mathbf{L}) \mathbf{u} \; d\Omega_E - \omega^2 \int_{\Omega_E} (\rho \tilde{w} \mathbf{u}) \; d\Omega_E + \int_{\Omega_E} \tilde{w} \mathbf{f} \; d\Omega_E = -\int_{\Gamma_E} \tilde{w} \boldsymbol{\sigma} \cdot \mathbf{n} \; d\Gamma_E, \tag{B.41}$$

where $\mathbf{n}$ is the unit normal vector with positive orientation away from the volume Ω_E.

B.4 Implementation of the FEM

Consider a three dimensional elastic, isotropic domain Ω_E with boundary $\Gamma_E = \Gamma_C \cup \Gamma_F$, in which the propagation of elastic waves is governed by the displacement (and general) equations of motion B.19. The resulting displacement distribution produced by an exterior force, is uniquely defined should one condition is defined at each point on the boundary surface. In general, two types of boundary condition are applied:

$$\mathbf{u} = \overline{\mathbf{u}}, \text{ on } \Gamma_C, \tag{B.42}$$

$$\boldsymbol{\sigma} = \overline{\boldsymbol{\sigma}}, \text{ on } \Gamma_F. \tag{B.43}$$

Note that the boundary conditions outlined above, allow the possibility of restraining only some of the displacement and/or the stress components, as will occur, for example, in simple supported conditions.

The implementation of the finite element in elastodynamics follows a similar procedure as previously outlined for acoustic waves in the Appendix A. That is, the volume Ω_E and its boundary surface Γ_E are discretized into a finite number of subdomains Ω_e, called 'elements', and a number of nodes are defined at some particular locations in each element.

The displacement $\mathbf{u}$ within each element, is expanded in terms of a prescribed set of shape functions N_i^e, defined in each element (the formulation and properties of the shape functions commonly used in the standard finite element method are briefly outlined in the Appendix A (for a more detailed discussion, the reader is referred to [236]). That is,

$$\mathbf{u}(\mathbf{x}) \approx \hat{u} = \sum_{i=1}^{n_p} N_i^e(\mathbf{x})\hat{u}_i, \ \mathbf{x} \in \Omega_e \tag{B.44}$$

where n_p is the number of shape functions used in the interpolation process.

A global interpolation expression may thus be written as

$$\hat{u} = \sum_{i=1}^{n_f} N_i(\mathbf{x})\hat{u}_i = \mathbf{N}\hat{\mathbf{u}}, \ \mathbf{x} \in \Omega_E, \tag{B.45}$$

where n_f is the total number of nodes in the discretisation, $\hat{\mathbf{p}}$ is a $(n_f \times 1)$ vector of unknown nodal pressure values, and $\mathbf{N}$ is a $(1 \times n_f)$ vector of global shape functions, defined such that $N_i = N_i^e$ in the subdomain Ω_e to which node i belongs, and zero in all the others.

Substituting the approximate displacement $\hat{u}$ in the weighted residual equation B.41, yields

$$\int_{\Omega_E} (\mathbf{L}^T \tilde{w} \mathbf{D} \mathbf{L} \mathbf{N}) \hat{u} \; d\Omega_E - \omega^2 \int_{\Omega_E} (\rho \tilde{w} \mathbf{N}) \hat{u} \; d\Omega_E + \int_{\Omega_E} \tilde{w} \mathbf{f} \; d\Omega_E = - \int_{\Gamma_F} \tilde{w} \overline{\boldsymbol{\sigma}} \cdot \mathbf{n} \; d\Gamma_E. \tag{B.46}$$

B.4.1 Galerkin finite element method

In the Galerkin finite element approach, the shape functions $\mathbf{N}$ are used as weighting function in equation B.46. That is,

$$\int_{\Omega_E} (\mathbf{L}^T \mathbf{N}^T \mathbf{D} \mathbf{L} \mathbf{N}) \hat{u} \; d\Omega_E - \omega^2 \int_{\Omega_E} (\rho \mathbf{N}^T \mathbf{N}) \hat{u} \; d\Omega_E + \int_{\Omega_E} \mathbf{N}^T \mathbf{f} \; d\Omega_E = - \int_{\Gamma_E} \mathbf{N}^T \overline{\boldsymbol{\sigma}} \cdot \mathbf{n} \; d\Gamma_F. \tag{B.47}$$

Defining

$$\mathbf{B} = \mathbf{L}\mathbf{N} = \begin{bmatrix} \frac{\partial N_i}{\partial x} & 0 & 0 \\ 0 & \frac{\partial N_i}{\partial y} & 0 \\ 0 & 0 & \frac{\partial N_i}{\partial z} \\ \frac{\partial N_i}{\partial y} & \frac{\partial N_i}{\partial x} & 0 \\ 0 & \frac{\partial N_i}{\partial z} & \frac{\partial N_i}{\partial y} \\ \frac{\partial N_i}{\partial z} & 0 & \frac{\partial N_i}{\partial x} \end{bmatrix}, \tag{B.48}$$

and substituting into equation B.47, yields

$$\int_{\Omega_E} (\mathbf{B}^T \mathbf{D} \mathbf{B}) \hat{u} \; d\Omega_E - \omega^2 \int_{\Omega_E} (\rho \mathbf{N}^T \mathbf{N}) \hat{u} \; d\Omega_E + \int_{\Omega_E} \mathbf{N}^T \mathbf{f} \; d\Omega_E = - \int_{\Gamma_F} \mathbf{N}^T \overline{\boldsymbol{\sigma}} \cdot \mathbf{n} \; d\Gamma_F. \tag{B.49}$$

Using matrix notation, equation B.49 may be expressed as

$$[\mathbf{K} - \omega^{\mathbf{2}} \mathbf{M}] \hat{u} = \mathbf{b}, \tag{B.50}$$

where the $(n_f \times n_f)$ stiffness matrix $\mathbf{K}$ and the $(n_f \times n_f)$ mass matrix $\mathbf{M}$ are defined as

$$\mathbf{K} = \int_{\Omega_E} \mathbf{B}^T \mathbf{D} \mathbf{B} \; d\Omega_E \tag{B.51}$$

$$\mathbf{M} = \int_{\Omega_E} \mathbf{N}^T \rho \mathbf{N} \; d\Omega_E. \tag{B.52}$$

The $(n_f \times 1)$ force vector $\mathbf{b}$ is defined as

$$\mathbf{b} = -\int_{\Omega_E} \mathbf{N}^T \mathbf{f} \; d\Omega_E + \int_{\Gamma_F} \mathbf{N}^T \overline{\boldsymbol{\sigma}} \; d\Gamma_F, \tag{B.53}$$

If the body forces (like gravity) are negligible, $\mathbf{f} = 0$, and the first term in equation B.53 vanishes. Note also that, for a free boundary condition $\boldsymbol{\sigma} = 0$, and $\mathbf{b} = 0$. Thus, the free boundary condition is 'naturally' satisfied within the formulation of the finite element formulation, if no constraints are defined at the boundary points.

B.4.2 Properties of the elastic finite element method

The properties outlined for the acoustic finite element method in the Appendix A are completely general and applicable for the elastic case. That is,

- The approximation results in system of equations that is sparse, due to the local character of the shape functions.
- The matrices are symmetrical. Moreover, the stiffness and mass matrices are also real.
- Since the expansion in each element is performed regardless of the excitation frequency, the stiffness and mass matrices $\mathbf{K}$ and $\mathbf{M}$ are frequency independent. Thus, the calculation of the modal frequencies and mode shapes may be performed using standard eigenvalue solvers.

Appendix C

Programming the wave expansion method

The computational implementation of the WED method, as used throughout this thesis, is based in a general program structure that was conveniently changed according to the different applications, as outlined in chapter 4.

According to the formulation of the WED for acoustic problems, for each discretisation point we need to calculate two template matrices, namely, **h** and **H**, defined as

$$h_i = \sum_{i=1}^{N} e^{k(\mathbf{x}_0 \cdot \mathbf{q}_i)}, \tag{C.1}$$

where **h** is a vector of dimension $(1 \times N)$ which approximates the pressure value at the central point in the computational cell, and

$$H_{ij} = \sum_{j=1}^{M} \sum_{i=1}^{N} e^{k(\mathbf{x}_j \cdot \mathbf{q}_i)}, \tag{C.2}$$

where **H** is a matrix of dimension $(M \times N)$, which approximates the pressure values at a discrete number M of neighbouring points in the cell. The pressure at the central point in the cell, p_0, is then given as

$$p_0 = \mathbf{h}\mathbf{H}^{+}\mathbf{p}, \tag{C.3}$$

where $\mathbf{p}$ is a $(M \times 1)$ vector of pressure values at the neighbouring nodes, and the superscript '+' denotes pseudo-inverse operation.

In order to compute the matrices $\mathbf{h}$ and $\mathbf{H}$, it is necessary to know the coordinates of the nodal points in the computational molecule and their numbering order, generally referred to as the 'connectivities' of the central node.

The next step is the computation of the pseudo-inverse of the matrix $\mathbf{H}$. This procedure gives the best possible approximation among all the plane wave solutions in equation C.2, provided that $N > M$. For nine-noded two-dimensional molecules $(M = 8)$, accurate results were obtained for $N = 20$, with negligible improvement for larger values.

For boundary nodes, Neumann and/or radiation conditions can be imposed by augmenting the template matrix $\mathbf{H}_{aug}$ prior to the pseudo-inversion operation. This procedure involves the computation of the derivatives of the equation C.2 along the direction normal to the boundary. Once $\mathbf{H}^{+}$ (or $\mathbf{H}^{+}_{aug}$) has been calculated, the resulting matrix is used to fill the overall stiffness matrix (and the right hand side force vector if the matrix was augmented).

The procedure outlined above, is repeated for each discretisation point in the mesh. Once the overall stiffness matrix has been fully assembled, Dirichlet constraints can be directly applied in the appropriate degrees of freedom of the stiffness matrix. A flow diagram, detailing the structure of the program, is shown in figure C.1.

For illustration purposes, a ©MATLAB program, based on the flow diagram shown in figure C.1 for two-dimensional acoustic applications, is shown below.

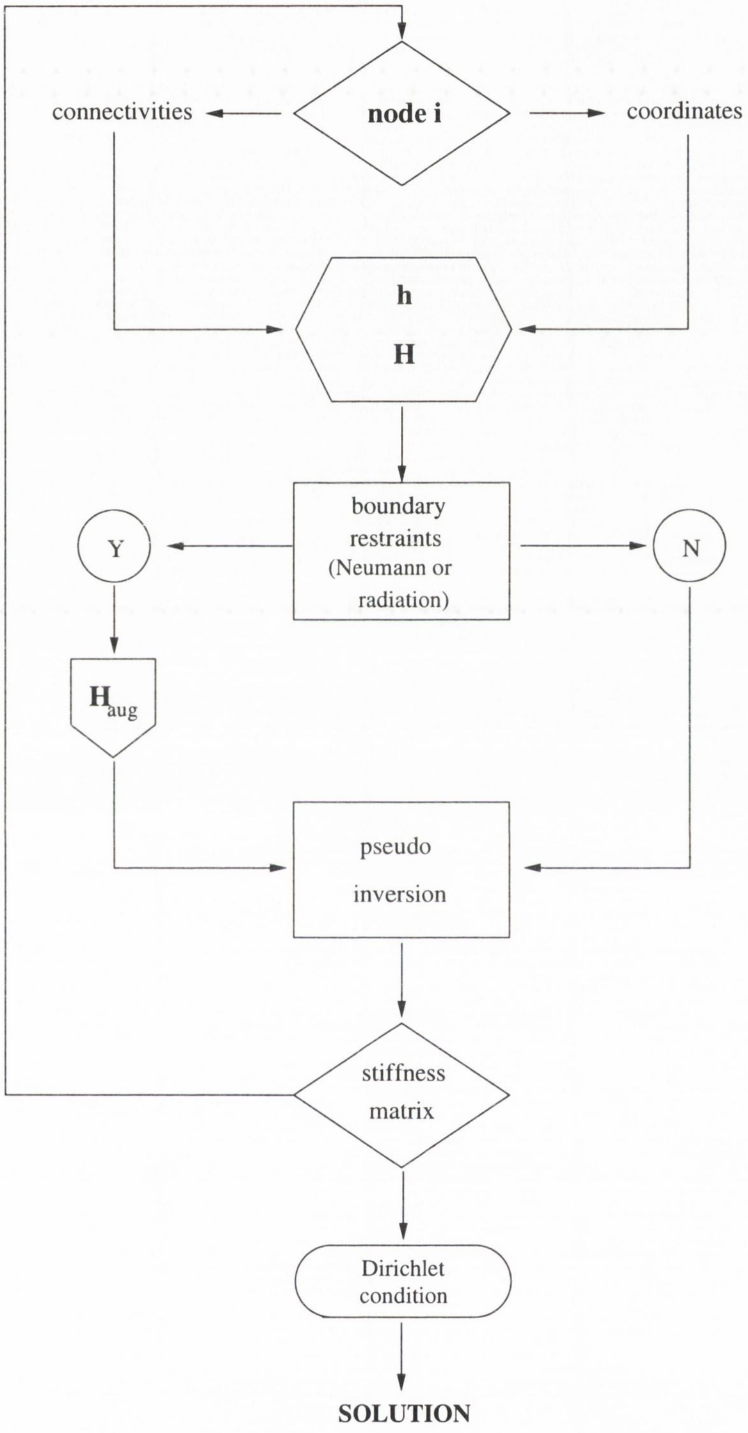

Figure C.1: General structure of the wave expansion program.

```
% MATLAB script to implement the WED method in 2D acoustic problems
% author: Gabriel Ruiz, Trinity College Dublin, 2002.

% Input information:

%  conn -> connectivity data
%  nodes -> nodal coordinates
%  Boundary matrices:
%  neucs = [node_number normal_angle value flag] -> Neumann/radiation
%  dircs = [node_number value] -> Dirichlet
%  rest -> restraint information

% Program variables and matrix allocation
npts = size((nodes),1);
conn = size((conn),1);
nneucs = size((neucs),1);
ndircs = size((dircs),1);
ndir = 20; % number of directional plane waves
w = 2*pi*freq;
k = w/340;
stiff = sparse(npts,npts);
force = sparse(npts,1);
% Assembling
for i = 1:npts
  % construct template matrix H
  tnodes = conn(i,find(conn(i,:)));
  tlen = length(tnodes);
  H = gplane(nodes(tnodes,:),k,ndir); % H is (MxN)
  % augment H if necessary
  if rest(i,1)
     bnodes = rest(i,find(rest(i,:)));
     blen = length(bnodes);
     dHdn = dgplane(nodes(neucs(bnodes,1),:),k,ndir,neucs(bnodes,2));
     H = [H;dHdn];
  end
  % central node approximation
  h = gplane(nodes(i,:),k,ndir); % h is (1xN)
  % pseudo-inversion
  Hplus = pinv(H);
  % fill the stiffness matrix according to po-h*Hplus*p=0
  stiff(i,i) = 1;
  stiff(i,tnodes) = -(h * Hplus(:,1:tlen));
  % apply Neumann and/or radiation boundary conditions
  if rest(i,1)
    tmp = h * Hplus(:,tlen+1:blen);
    for ig = 1:blen
```

```
        if neucs(bnodes(ig),4) == 1
          % Neumann
          force(i,1) = force(i,1) + tmp(ig) * neucs(bnodes(ig),3);
        else
          % radiation
          stiff(i,neucs(bnodes(ig),1)) = stiff(i,neucs(bnodes(ig),1)) + \
                                             j * k * tmp * neucs(bnodes(ig),3);
        end
      end
    end
  end
% Apply Dirichlet condition
if isempty(dircs) == 0
  for i = 1:ndircs
    stiff(dircs(i,1),:) = 0;
    stiff(dircs(i,1),dircs(i,1)) = 1;
    force(dircs(i,1)) = dircs(i,2);
  end
end
% Solve the system
p = stiff\force;

% Plane wave generating function
function g = gplane(nodes,k,ndir)
dt = 2*pi/ndir;
theta = dt:dt:2*pi;
g = exp(-j*k*(nodes(:,1)*cos(theta) + nodes(:,2)*sin(theta)));

% Derivatives along boundary normal direction
function dgdn = dgplane(nodes,k,ndir,normal)
dt = 2*pi/ndir;
theta = dt:dt:2*pi;
dn = -j*k*(cos(norm)*cos(theta) + sin(norm)*sin(theta));
dgdn = dn .* gplane(nodes,k,ndir);
```

As illustrated, the input information is given by five matrices: nodal coordinates (nodes), connectivities for each node (conn), Neumann and radiation conditions (neucs) and Dirichlet condition (dircs). The matrix 'rest' is used to implement the Neumann and radiation boundary conditions as outlined in section 3.4, augmenting the row count in the template matrix **H**.

Each discretisation point (whether it is a Neumann/radiation boundary point or not) has associated one row in the 'rest' matrix, which is initially zero. For Neumann and/or radiation boundary points, the corresponding (non-zero) row in the 'rest' matrix has the location of these points in the 'neucs' matrix, and that of the (Neumann/radiation) neighbouring points in the cell that need also to be restrained. For illustration, consider for example, a corner region in an 2D acoustic domain Ω_A with boundary Γ_A, along which a radiation condition is imposed. An schematic illustration is given in figure C.2.

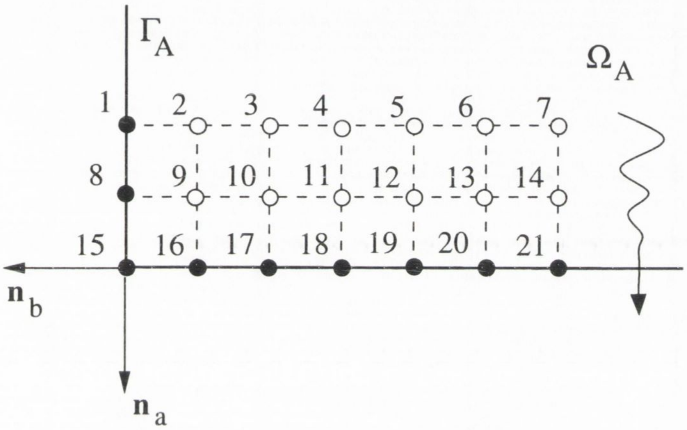

Figure C.2: Illustration of a radiation condition implementation.

Referring to the figure, the connectivities for the nodes $15-20$ in the matrix 'conn', are given as

$$
\text{conn} = \left(\begin{array}{lcccccccc}
 & & & & \vdots & & & & \\
\text{row } 15 \rightarrow & 8 & 9 & 16 & 0 & 0 & 0 & 0 & 0 \\
 & 8 & 9 & 10 & 15 & 17 & 0 & 0 & 0 \\
 & 9 & 10 & 11 & 16 & 18 & 0 & 0 & 0 \\
 & 10 & 11 & 12 & 17 & 19 & 0 & 0 & 0 \\
 & 11 & 12 & 13 & 18 & 20 & 0 & 0 & 0 \\
\text{row } 20 \rightarrow & 12 & 13 & 14 & 19 & 21 & 0 & 0 & 0 \\
 & & & \vdots & & & & &
\end{array}\right)
$$

Since one boundary point may have more than one normal angle, type of boundary condition and boundary value associated, it may occur that a given nodal point is repeated in the 'neucs' matrix. For nodes 15 – 20, the 'neucs' matrix is constructed as

$$\text{neucs} = \left(\begin{array}{lcccc} & & & \vdots & \\ \text{row } 15 \rightarrow & 15 & \theta_{n_a} & 1 & 2 \\ & 15 & \theta_{n_b} & 1 & 2 \\ & 16 & \theta_{n_a} & 1 & 2 \\ & 17 & \theta_{n_a} & 1 & 2 \\ & 18 & \theta_{n_a} & 1 & 2 \\ & 19 & \theta_{n_a} & 1 & 2 \\ \text{row } 21 \rightarrow & 20 & \theta_{n_a} & 1 & 2 \\ & & \vdots & & \end{array}\right),$$

where θ_{n_a} and θ_{n_b} are the angles associated to normals $\mathbf{n_a}$ and $\mathbf{n_b}$, respectively. From the neucs matrix, the restraint matrix is then constructed as

$$\text{rest} = \left(\begin{array}{lccccc} & & & \vdots & & \\ \text{row } 15 \rightarrow & 15 & 16 & 8 & 17 & 0 \\ & 17 & 15 & 16 & 8 & 18 \\ & 18 & 17 & 19 & 0 & 0 \\ & 19 & 18 & 20 & 0 & 0 \\ & 20 & 19 & 21 & 0 & 0 \\ \text{row } 20 \rightarrow & 21 & 20 & 22 & 0 & 0 \\ & & \vdots & & & \end{array}\right).$$

Assuming that a prescribed pressure $\overline{p} = 1$ is directly imposed on nodes 15 – 20, a

Dirichlet matrix ‘dircs’ is determined as

$$\text{dircs} = \begin{pmatrix} \text{row } 15 \rightarrow & 15 & 1 \\ & 16 & 1 \\ & 17 & 1 \\ & 18 & 1 \\ & 19 & 1 \\ \text{row } 20 \rightarrow & 20 & 1 \end{pmatrix}.$$

Also note that the matrices described above, can be automatically constructed from standard finite element meshing programs, using the nodal coordinates and the (finite element) meshing connectivity information.

C.1 C++ implementation

For large domain applications, with a large number of discretisation points, a high performance programming language is necessary in order to minimise the computation time. The use of a high-level programming language, like C or Fortran, has the disadvantage that no in-built functions are provided to store and operate sparse matrices. To circumvent this drawback, a number of different storage methods have been devised (see e.g. [237, 238]).

Alternatively, an object-oriented language, like C++, may be used [239]. The allocation and algebraic manipulation of sparse matrices may be efficiently performed through the use of an array of ordered-linked-lists[1]. An illustration of the concept is shown in figure C.3.

As illustrated, each linked-list has a ‘head’, initialised to zero, and linked to the first element in the list. Since each linked list is allocated at one position in the array, the search for the heads in the array is performed very efficiently. Each entry in the list has assigned a location value, an actual value and a link to the next entry

---

[1] this type of structure may be also used in C [240], though it is not as straightforward to implement as in C++.

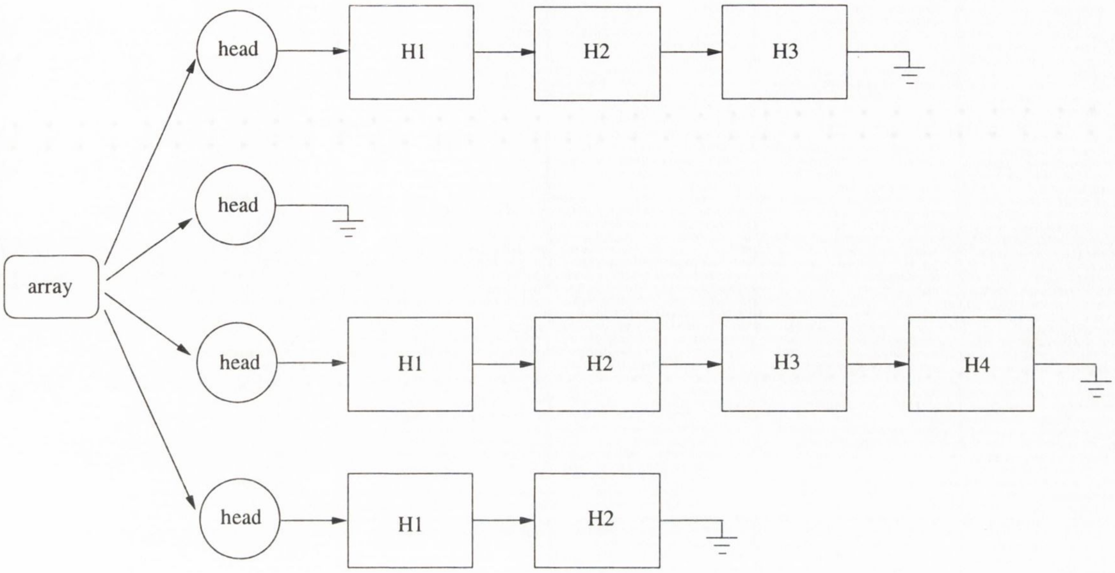

Figure C.3: An array of linked-lists.

(zero by default). The search along the list is finished whenever a zero link is found. Below is an example of a C++ template class 'node', which defines the functions required by each link in the list.

```
// Node template class
// author: Gabriel Ruiz, Trinity College Dublin, 2002.

// It creates a new entry in a linked list in position ‘index’
// with a general type (char, float, double or complex) value.

template <class T>
class Node {

 // public funtions
 public:

    Node(Node<T>* p = 0, int i = 0, T val = 0){ // constructor
        link = p;
        index = i;
        data = val;
    };

    ~Node(){ // destructor
        delete link;
     };

    Node<T>* link; // link to next node in the list

    void addafter(int, T){ // tag on a node after this one
        link = new Node<T>( link, i, value );
    };


    // accessor functions

    int get_index(){return index;}; // returns node index
    T& get_data(){return data;};   // returns node data
    Node* get_link(){return link;}; // returns link to following node
                                    // in the list

 private:

   int index;
    T data;

};
```

Note that the link to the next node in the list is a pointer to a node. Thus, by assigning the memory address of the next node to the variable link in the class function 'node' above, the nodes in the list are connected. In order to allocate a new entry in an ordered fashion, the preceding node in the list is 're-linked' to the new entry, whilst the new entry is linked to the following node in the list. Using such a procedure, the allocation and filling process of the overall stiffness matrix may be efficiently performed.

Once the stiffness matrix has been assembled, a standard sparse solver package may be used to obtain the desired solution. For the present analysis, the ©PETSc solver package [241–243], was found to give a suitable interface to which the C++ linked-list can be exported, with a minimum computational penalty (the package provides a full interface to Fortran and ©Matlab).

C.1.1 Solution techniques

Numerical methods reduce the problem to a system of equations

$$Ax = b, \tag{C.4}$$

where, for discrete domain techniques such as the FEM, WED and finite differences, the square matrix A is very sparsely populated.

The techniques for solving equation C.4 fall into two main categories: direct and iterative. Direct methods solve equation C.4 exactly, obtaining a solution in a fixed amount of time, according to the size of the matrix A. This methods, which are very robust and stable, are usually based on a LU or Cholesky decomposition of A follow by back-substitution. However, this process requires not only to store the entire matrix, but produces new entries in A affecting the original sparsity of the matrix.

Iterative methods give as approximate solution of equation C.4 by iteratively minimising the residual error

$$r = b - Ax, \tag{C.5}$$

until a (given) minimum residual value is reached.

These methods do not require to store the matrix A, taking full advantage of its sparsity. On the other hand, the convergence of the solution to the desired residual, depends strongly on the conditioning and diagonal dominance of the final system matrix.

The iterative solution algorithms implemented in ©Petsc, are preconditioned Krylov solvers (see, e.g. [244]). In these methods the system C.4 is multiplied by another matrix in order to accelerate the convergence of the iterative algorithm. That is

$$(M_L^{-1} A M_R^{-1})(M_R x) = M_L^{-1} b, \tag{C.6}$$

where M_L and M_R indicate preconditioning matrices (or matrices from which a preconditioner is to be constructed). If $M_L = I$, where I is the identity matrix, then right preconditioning results, and the residual r

$$r = b - Ax = b - M_R^{-1} M_R x, \tag{C.7}$$

is preserved. In contrast, the residual is altered for for left ($M_R = I$) and symmetric preconditioning, as given by

$$r_L = M_L^{-1} b - M_L^{-1} Ax = M_L^{-1} r. \tag{C.8}$$

For symmetric systems with a clear diagonal dominance, there are well established algorithms, such as conjugate gradients (CG), which converge to the desire residual after a few number of iterations. For non-symmetric systems or systems for which the diagonal values are not dominant, variants of the CG method must be used [245], such as the bi-conjugate gradient (BiCG) or the generalised minimal residual (GMRES). The convergence of a given iterative algorithms depends strongly on the selection of a right preconditioner.